RADIO EMISSION OF THE EARTH AS A PLANET

A. Ye. Basharinov, A. S. Gurvich, and S. T. Yegorov

1. Report No. NASA TT F-16,078	2. Government Accession No.	3. Recipient's Catalog No.
4. Title and Subtitle RADIO EMISSION OF THE EARTH AS A PLANET		5. Report Date January 1975
		6. Performing Organization Code
7. Author(s) A. Ye. Basharinov, A. S. Gurvich, and S. T. Yegorov		8. Performing Organization Report No.
		10. Work Unit No.
9. Performing Organization Name and Address Leo Kanner Associates Redwood City, California 94063		11. Contract or Grant No. NASw-2481
		13. Type of Report and Period Covered Translation
12. Sponsoring Agency Name and Address National Aeronautics and Space Administration, Washington, D.C. 20546		14. Sponsoring Agency Code

15. Supplementary Notes
Translation of "Radioizlucheniye Zemli kak Planety," Moscow, "Nauka" Press, 1974, 188 pp.

16. Abstract The book presents the physical essentials of microwave sensing of the Earth and its atmosphere. Characteristics of the formation of microwave radiation in the system Earth's atmosphere-surface are examined. Principal emphasis is given to problems yielding a practical outcome: determining humidity, moisture content of clouds, continuity of ice cover, moisture content and temperature of land cover. The book sums up experience in satellite measurements in the microwave range. These measurements were made for the first time on the Kosmos 243 and Kosmos 384 satellites in 1968 and 1970. The treatment is based largely on the original results of the authors.

17. Key Words (Selected by Author(s))	18. Distribution Statement Unclassified - Unlimited

19. Security Classif. (of this report) Unclassified	20. Security Classif. (of this page) Unclassified	21. No. of Pages 215	22. Price

PRECEDING PAGE BLANK NOT FILMED

Radioizlucheniye Zemli kak planety /Radio Emission of the Earth as a Planet/, Basharinov, A. Ye., Gurvich, A. S., and Yegorov, S. T., Nauka Press, 1974, 187 pp.

The book presents the physical essentials of microwave sensing of the Earth and its atmosphere. Characteristics of the formation of microwave radiation in the system Earth's atmosphere-surface are examined. Principal emphasis is given to problems that yield a practical outcome: determining humidity, moisture content of clouds, continuity of ice cover, moisture content, and temperature of land cover. The book generalizes experience in satellite measurements in the microwave range. These measurements were made for the first time on the satellites Kosmos 243 and Kosmos 384 in 1968 and 1970 and provides new geophysical results and new methods of remote sensing. At the present time interest in microwave sensing has risen sharply both in our countries and abroad -- satellites with microwave radiometers began operating in the US in 1973. Based on the accumulated experience, promising functions of satellite and ground-based microwave sensing in a complex with other facilities are examined. The treatment to a large extent is based on original results obtained by the authors.

The book is written for specialists in geophysics, meteorology, and the study of natural resources from space and is of interest to a wide range of readers, including designers of remote sensing systems and specialists in radiowave propagation.

Chief editor: M. S. MALKEVICH

---

* Numbers in margins indicate pagination in the foreign text.

Observations of the conditions of the atmosphere, cloud
cover, and land surface made by meteorological satellites have
yielded a wealth of information necessary for the study of
atmospheric processes and solving problems in weather fore-
casting. However, the use on satellites of only optical and
infrared spectral regions markedly complicates the interpre-
tation of the observations, since the atmosphere and especially
clouds strongly absorb (electromagnetic waves in this range.
In order to increase the reliability of data on the condition
of the atmosphere and the ocean, which is particularly important
in achieving greater timeliness of predictions of weather changes,
it is necessary to expand the information on atmospheric and
oceanic processes obtained from satellites. Radioastronomical
methods based on measuring the outgoing radiothermal emission
of the system atmosphere-underlying surface opened up new
possibilities for acquisition of this information.

The advantage of remote sensing methods based on measuring
radiothermal emission is due above all to the transparency of
the Earth's atmosphere for centimeter and millimeter radiowaves.
The fairly high transparency of the atmosphere permits determining
the temperature and the condition of the ocean surface, and
obtaining an estimate of the continuity of ice cover in polar
regions from measurements of radiation in the centimeter wave-
length range, virtually independently of the presence of cloud
cover. In addition, the presence in the centimeter wavelength
range of quite intense absorption lines of water vapor and
weakly selective absorption lines in the liquid water of clouds
permits determining not only the characteristics of the under-
lying surface, but also atmospheric parameters, such as air
humidity and moisture content of clouds, and also tracing the
relationship between these parameters and total atmospheric
circulation.

The book presented to the readers is a generalization of the
results of measurements of thermal radio emission of Earth from
the satellites Kosmos-243 and Kosmos-384 that were first begun
in the Soviet Union in 1968 and showed the advantages of radio-
astronomical methods for investigating our planet from outer-
space.

The book examines the physical fundamentals of remote sensing
of the atmosphere and the underlying surface. Not only is a
substantiation provided for already implemented methods of   /4

determining geophysical parameters from measurements of thermal radio emission, but ways of extending the capabilities of these methods in solving other problems in geophysics, meteorology, and the study of natural resources from space are indicated.

Taking measurements from satellites required building a complex of automated radiometers satisfying the experimental conditions. Much space in the book is given to describing the principles of designing this equipment and the specific details of satellite measurements of thermal radio emission.

Of particular interest is a detailed description of the results obtained with the above-mentioned Kosmos satellites and their possible application in solving applied problems.

It should be noted that 4 years after the Soviet experiments, in December 1972 when the book had already been prepared for print, the Nimbus 5 meteorological satellite was launched in the United States; onboard the satellite instruments for measuring the thermal radio emission of Earth had also been installed. The first published results based on the materials of measurements from Nimbus 5 agreed with the data obtained in the Soviet Union.

It can be hoped that the successes of satellite experiments will spur further development of remote sensing of the atmosphere in the radiowave range along with other methods of sensing, and also the broader use of the results of satellite measurements in meteorology and other fields of practical application.

M. S. Malkevich

The use of artificial Earth satellites for investigations of the environment by remote sensing methods involves different sections of the electromagnetic spectrum. In this problem area radioastronomical methods of studying the radiothermal emission of Earth figure prominently.

Radioastronomical methods of investigation at the present time have reached a high degree of perfection, however their use for the study of Earth from artificial satellites requires the solution of a great many specific problems. In contrast to other space objects, a much greater body of information has been accumulated on our planet and therefore in remote sensing in the radiowave range it is necessary to be able to use all the available data in order to more reliably interpret results to acquire new information.

The first investigations of the Earth's atmosphere by radioastronomical methods were conducted by R. Dicke in 1946. Of high significance to the advancement of investigations of radiothermal radiation of the atmosphere and land and sea cover of Earth in the USSR are the studies by V. S. Troitskiy, S. A. Zhevkin, K. S. Shifrin, L. T. Tuchkov, and their coworkers. Several problems of the measurement of thermal radio emission of terrestrial cover and atmosphere are treated in monographs by K. Ya. Kondrat'yev, Yu. M. Timofeyev, and B. V. Vinogradov[1].

In the United States, an important cycle of studies was done by C. Tolbert, D. Hogg, D. Stilin, and W. Nordberg.

The range of geophysical problems associated with measurement of radiothermal emission of the Earth is determined, on the one hand, by the presence of selective-emission lines of water-vapor, oxygen, and ozone in the microwave range[2], on the one hand, the penetrating ability of microwave radiation provides quantitative information on the structure of the atmosphere,

---

[1] K. Ya. Kondrat'yev, and Yu. M. Timofeyev, Termicheskoye zondirovaniya atmosfery so sputnikov /Thermal Sensing of the Atmosphere from Satellites/, Gidrometeoizdat, 1970: B. V. Vinogradov and K. Ya. Kondrat'yev, Kosmicheskiye metody zemlevedeniya /Space Methods of Earth Resources Study/, Gidrometeoizdat, 1971.
[2] The microwave range includes frequencies from 300 MHz to 300 GHz (radiowave lengths from 1 m to 1 mm).

bodies of water, and continental cover both in the absence of cloud cover as well as when complex meteorological conditions are present.

Meteorogically, measurements in the microwave range are used for temperature sensing, determining the humidity of the atmo- sphere and the moisture reserve of clouds, and detecting zones of precipitation. It was found possible for hydrological purposes to determine the temperature and state of the sea surface, map the ice cover environment, and to estimate variations in the salinity of water.

Measurement of microwave radiation of continental cover permits determining the temperature and moisture content of soils and delineating the boundaries of zones of permafrost and snow thawing. The penetrating ability of microwave radiation can help provide data on the temperature and state of subsurface soil layers.

Microwave radiation of the atmosphere and regions of the Earth's surface can be made from aircraft and from artificial Earth satellites. The first experiments in measuring radiothermal emission of the Earth from space were conducted in the USSR on the Kosmos-243 artificial Earth satellite /AES/ in September 1968 and on the Kosmos-384 AES in December 1970. Interpretation of the results of these experiments yielded global data on the distribution of the moisture content of the atmosphere, the moisture reserve of clouds, the limits of ice fields, the temperatures of bodies of water and continents, and other data.

Further experiments on the radiothermal emission of the Earth from space are being developed in programs of experimental Earth satellites and space laboratories. For example, experiments on observations of radiothermal emission of the Earth in the United States have been conducted on the Nimbus 5 satellite in the United States, beginning in December 1972.

This monograph is an attempt to generalize data on the radiothermal emission of the Earth in a form accessible to a wide range of specialists in geophysics, meteorology, and study of environmental resources.

The authors did not strive for an exhaustive presentation of the status of the problem and deliberately did not present in close detail a number of key problems in microwave radiation studies of the Earth (as, for example, the radiative properties of films of petroleum and other oils on the sea surface, study of the microwave radiation of layers of ozone in the atmosphere, microwave radiative properties of ice-crystal clouds, and other areas).

A is the polarization vector of the secondary wave

a is droplet radius

$a_\lambda = \dfrac{2\pi a}{\lambda}$ is parameter of diffraction at water droplet

$B_{qq}; B_{TT}, B_{qT}$ are the correlation functions of meteorological parameters

$B_\nu; B_\lambda$ is blackbody spectral brightness

$b_n(\mathbf{r})$ is the correlation function of refractive index inhomogeneities

b_i is the bulk content of ice in an ice-water mixture

C is the air concentration in sea spume

c_o is the speed of light in vacuum

c_p is heat capacity

$E_\nu; E_\lambda$ is emissivity

E_T is the mean energy of thermal radiation in the time period τ

F (a) is the droplet size distribution function

f is the frequency of microwave vibrations used

G is front-to-back ratio

g is acceleration due to gravity

j is flare-use factor

H_W is characteristic cloud height

h is characteristic depth in ground, characteristic height in atmosphere

h is the Planck constant

I is rain intensity

J_λ is the spectral intensity of radiation flux

k is the Boltzmann constant

$k = \dfrac{2\pi}{\lambda}$ is wave number

K_T is coefficient of thermal conductivity

$\hat{K}p$ is the polarization factor

$\mathcal{K}(\lambda, p); \mathcal{K}_\lambda(h)$ is the kernel of an integral equation

L is the mean distance between layers

ℓ_e is the penetration depth of electromagnetic wave in solid cover

ℓ_H is length of heat wave

$\ell_{H.D}$; $\ell_{H.A}$ is wavelength of diurnal heat wave and wavelength of annual heat wave

ℓ is thickness of layer

M_t is a parameter characterizing the observability of a target

m is the unit vector of the secondary electromagnetic wave

m is the moisture content of rain

N is the mean number of inhomogeneities per unit volume

N_m is the mean number of layers per unit depth

n is the real part of a refractive index

n (a) is the number of droplets with radius a per unit volume

P is atmospheric pressure

$\hat{p}$ is the percentage content of water in soil (on mass basis)

Q is the integrated content of vaporous moisture in the atmosphere

$\hat{q}$ is specific moisture content

q_H is heat flux

q_m is the effective scattering cross-section of unit volume per unit solid angle in the direction **m**

R; R_λ is power reflection coefficient

$R_{\perp,\lambda}$ is reflection coefficient for horizontal polarization /8

$R_{\parallel,\lambda}$ is reflection coefficient for vertical polarization

R_s; R_p are reflection coefficients of soil and plant cover

r is the radius-vector of a scattering inhomogeneity

s is the salinity of sea water

S_t; S_s is the target area, and area of antenna beam spot on Earth's surface

T; T_o is the thermodynamic temperature of the environment, surface or antenna

$T_{b,\nu}$; $T_{b,\lambda}$; T_t^b is radiobrightness temperature of surface and of target

T_{ba}^b is the radiobrightness temperature of the space background

$T_{1,d}$; $T_{1,a}$ are the amplitudes of the first harmonics of the diurnal and annual fluctuations in ground surface temperature

T_a is antenna temperature

u is the frequency spectrum of fluctuations of brightness temperature

U is voltage at radiometer outlet

v is wind velocity

x

$V(p)$ is the one-dimensional Fourier-transform of a correlation function

$v(a)$ is the droplet fall rate

w is the error matrix

W is moisture content of cloud

z is altitude in atmosphere

β is the antenna scattering factor

Γ_o is the temperature gradient in air

γ_λ is the linear power absorption factor

δ is the delta-function

$\text{tg }\delta$ is the loss-angle tangent in a medium

$\varepsilon; \bar{\varepsilon}_\lambda$ is the complex dialectric constant

η is the efficiency of equipment components

θ is an angle characterizing the direction of radiation (or of the secondary incident wave) in the vertical plane

$\varkappa; \varkappa_\lambda$ is absorptivity (blackness factor)

$\varkappa^*$ is the imaginary part of the refractive index

λ is the wavelength of radiation

λ_s is the Debye relaxation parameter

μ is the degree of ice continuity

ν is the frequency of radiation oscillations

ξ is the fraction of an area covered by vegetation

ρ is density

ρ_a is density of air

ρ_v is density of water vapor

ρ_d is density of droplet liquid

σ^2 is dispersion of various parameters

σ_s is static conductivity

$\sigma_a; \sigma_s; \sigma_{ab}$ are the droplet attenuation, scattering, and absorption cross sections

τ_λ is optical thickness (integrated absorption of radiation)

τ_r is the relaxation time of molecules

τ is the period of observation during radiometric reception

$\Phi_n(p)$ is the three-dimensional Fourier transform of a correlation function

Υ is the fraction of the reflection coefficient associated with bulk scattering

$\varphi; \varphi_0$ is an angle characterizing the direction of radiation in the horizontal plane

$\psi_1; \psi_2$ are phase discontinuities during scattering and reflection

Ψ is the deviation from the mean-climatic profile of moisture content

Ω is a solid angle

$\omega = 2\pi f$ is cycle frequency

TABLE OF CONTENTS

RADIO EMISSION OF THE EARTH AS A PLANET

A. Ye. Basharinov, A. S. Gurvich, and S. T. Yegorov

CHAPTER ONE

THERMAL MICROWAVE RADIATION OF BODIES OF WATER

1. Quiet Water Surface

1-1) Measurement of thermal microwave radiation of bodies of water from satellites, aircraft, or from ships is as a rule carried out with fairly narrow-band radiometers with highly directional antennas. The surface of the water lies in the far zone of the antenna. Under these conditions an examination of the properties of thermal microwave radiation of a quiet water surface free of ice can proceed on the basis of Kirchhoff's law, and to calculated the required absorptivity by using Fresnel's formulas.

A rigorous derivation of formulas describing thermal microwave radiation from a plane interface, such as a quiet water surface, can be found in /I 7. Here we will only present some general results pertaining to equilibrium thermal radiation and show the relationship between the intensity of microwave radiation measured by radiometers (proportional to brightness temperature) and the parameters of the emitting medium, and also the geometry of the experimental setup. In the microwave range the long-wave asymptotic Planck formula -- the Rayleigh-Jeans law for the spectral brightness $B_\nu(T)$ of a blackbody[1] -- can be used to high accuracy:

$$B_\nu(T) = \frac{2kT\nu^2}{c_0^2},$$

(1.1)

where T is the temperature of the body and the radiation that is in equilibrium with it; ν is frequency; k is Boltzmann's constant; and c_0 is the speed of light in vacuum. Using Kirchhoff's law

---

[1] The thermodynamics of thermal radio emission is examined in detail in monographs on radioastronomy (see, for example: J. Posy and R. Brasuell, Radioastronomiya /Radioastronomy/, Moscow, 1958

$$\frac{E_\nu}{\varkappa_\nu} = B_\nu(T) \tag{1.2}$$

where E_ν is the emissivity; $\varkappa_\nu$ is the absorptivity of the interface (or blackness factor), we can introduce the concept of brightness temperature $T_{b,\nu}$:

$$T_{b,\nu} = E_\nu \frac{c_0^2}{2k\nu^2}, \tag{1.3}$$

which is equal to the temperature of a blackbody that has the brightness

$$B_\nu(T) = E_\nu(T_{b,\nu}). $$

After this conversion, we get the following relation from (1.1) for the brightness temperature $T_{b,\nu}$:

$$T_{b,\nu} = \varkappa_\nu T. \tag{1.4}$$

For a plane interface, $\varkappa_\nu$ is associated with the specular reflection coefficient R_ν (with respect to power) as follows:

$$R_\nu = 1 - \varkappa_\nu. \tag{1.5}$$

The reflection coefficient R_ν depends on the polarization of radiation and for a plane surface can be calculated by the Fresnel formulas for vertical polarization $R_{\|,\nu}$ and horizontal polarization $R_{\perp,\nu}$:

$$R_{\|,\nu} = \left| \frac{\varepsilon_\nu \cos\vartheta - \sqrt{\varepsilon_\nu - \sin^2\vartheta}}{\varepsilon_\nu \cos\vartheta + \sqrt{\varepsilon_\nu - \sin^2\vartheta}} \right|^2, \tag{1.6}$$

$$R_{\perp,\nu} = \left| \frac{\sqrt{\varepsilon_\nu - \sin^2\vartheta} - \cos\vartheta}{\sqrt{\varepsilon_\nu - \sin^2\vartheta} + \cos\vartheta} \right|^2, \tag{1.7}$$

where ε_ν is the complex dielectric constant of water at the frequency ($\varepsilon = 1$ is adopted); ϑ is the angle between the normal to the surface and the direction of radiation. The reflection coefficients $R_{\|,\nu}$ and $R_{\perp,\nu}$ correspond to two different polarizations: $R_{\|,\nu}$ is the electric vector of a wave parallel to the plane of incidence, and $R_{\perp,\nu}$ is the electric vector of a wave perpendicular to the plane of incidence. From (1.4) – (1.7) it is clear that the thermal radiation of a smooth water surface is polarized.

For observations at the nadir when $\theta = 0$, both reflection coefficients coincide:

$$R_{\perp,\nu} = R_{\|,\nu} = \left| \frac{\sqrt{\varepsilon_\nu} - 1}{\sqrt{\varepsilon_\nu} + 1} \right|^2.$$

In the following, if polarization is not indicated, the result pertains to arbitrary polarization.

Eqs. (1.5)-(1.7) are rigorous for a smooth interface surface, and the dependence of R_ν on frequency obtains only to the extent that the dielectric constant ν depends on ε_ν. A generalization of Eq. (1.5) to the case of a rough surface (for example, a wave-agitated sea) will be examined in the next section.

Referring to the relation between the wavelength or radiation λ and the frequency ν: $\lambda = c_0/\nu$, we can convert from the frequency distribution of energy $B_\nu(T)$ to the wavelength distribution $B_\lambda(T)$:

$$B_\lambda(T) = B_\nu(T) \left| \frac{d\nu}{d\lambda} \right| = \frac{c_0}{\lambda^2} B_\nu(T).$$

Converting to the wavelength distribution, as is clear from (1.4) /11 and (1.5), leads only to replacement of the subscript ν by λ in the expressions containing the coefficients of absorption and reflection, and brightness temperature. Therefore in the following this conversion will be carried out without special qualifications.

1-2) The dielectric constant of water ε_λ depends on the wavelength and also on the temperature and salinity of water. The dependence on wavelength λ and temperature T for fresh water in the centimeter wave range is described approximately by the Debye relaxation formula:

$$\varepsilon_\lambda = \varepsilon_0 + \frac{\varepsilon_s - \varepsilon_0}{1 + (\lambda_s/\lambda)^2} - i \frac{\lambda_s}{\lambda} \cdot \frac{\varepsilon_s - \varepsilon_0}{1 + (\lambda_s/\lambda)^2}. \tag{1.8}$$

The parameters appearing in (1.8): static dielectric ε_s and "optical" dielectric constant ε_0 and Debye relaxation parameter λ_s depend on temperature /2, 3/. A detailed listing of data for fresh water is given in /4/, where the range of temperature variation is from -8° C (supercooled water) to + 40° C and the wavelength range is from 1 mm to several meters.

3

The salinity of sea water can be referred to the centimeter range by adding to Eq. (1.8) the term

$$2i\sigma_s \frac{\lambda}{c_0},$$

where σ_s is the static conductivity of the electrolyte solution.

The presence of a salt dissolved in water changes the parameters ϵ_s and λ_s within slight limits. The working dependence of the parameters σ_s, λ_s, and ϵ_s on temperature and salinity is shown in Figs. 1.1 and 1.2 /5/.

Fig. 1.3 gives the blackness factor of a smooth water surface for nadir observations as working functions of the temperature and salinity of water. Presented in the same figure is the brightness temperature for four wavelengths as functions of water temperature, calculated for the salinity s = 35 per mil. From the data given in Fig. 1.3 it is clear that these functions have a complex course, caused by the dependence of the dielectric properties of water on temperature. The dependence of $T_{b,\lambda}$ on salinity within the limits of possible variations of salinity is weak, which can be seen from Fig. 1.4. Therefore the determination of salinity from radiation measurements in several wavelengths is impossible in principle, but in practice is an extremely complicated problem in the centimeter wavelength range.

To investigate variations in radiation intensity in several cases one must know the behavior of the derivative $\partial T_{b,\lambda}/\partial T_1$ which characterizes the sensitivity of radiobrightness to temperature changes. Fig. 1.5 presents the dependence of $\partial T_{b,\lambda}/\partial T$ on wavelength λ calculated in /6/. It is not difficult to see that in order to determine the thermal characteristics for nadir observations, the wavelength range $\lambda = 5$-10 cm in which

reaches a maximum is optimal.

1-3) The distribution of temperatures of the quiet surface of the Caspian Sea was measured from aircraft in 1964 /7/ at the wavelength $\lambda = 8.5$ cm. A prototype of a future satellite radiometer was used here. To reduce the measurement error associated with the tie-in of the radiometer to the absolute scale of radiobrightness temperatures, a reference point with known brightness (the area of Neftyanyye Kamny) was used in /7/, where the water temperature was measured by direct methods. The water temperatures were reconstructed from measurements of the increments of the brightness temperatures relative to the reference point. According to the flight conditions, the
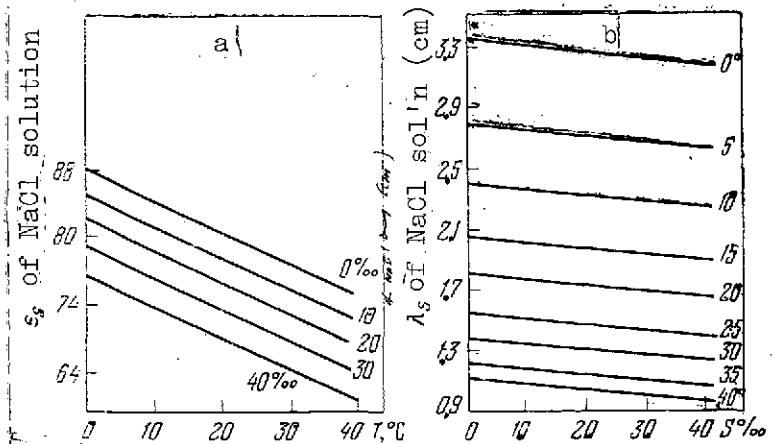
Fig. 1.1. Static dielectric constant ϵ_s (a) and relaxation wavelength λ_s (b) as functions of temperature and salinity [5]
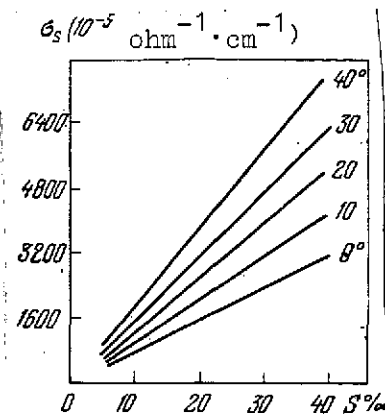
Fig. 1.2. Static conductivity σ_s as function of temperature and salinity [5]
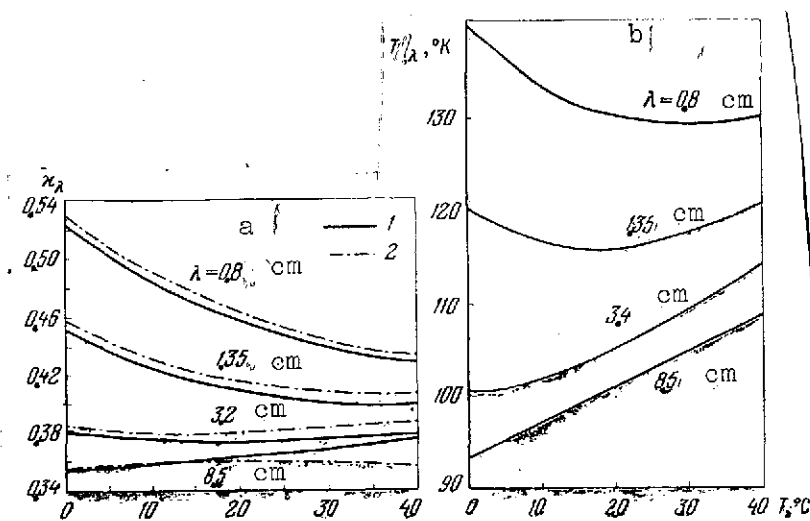
Fig. 1.3. Blackness factor [5] (a) and brightness temperature of water (b) as functions of temperature and wavelength
1. Fresh water
2. Sea water

measurements were not taken during heavy storms. Also, the use of a relatively long wavelength and nadir observations, as will be shown in Section 2, virtually precluded the effect of active sea states and changes in the blackness factor of the surface due to spume on the reconstruction of the water temperature. Fig. 1.6 presents one of the temperature profiles obtained in this study.

More detailed investigations were made of the surface temperature of the Caspian Sea in [8]. Fig. 1.7 presents a
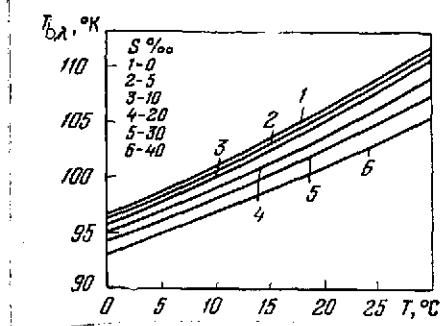
Fig. 1.4. Brightness temperature at wavelength 8.5 cm as a function of salinity and temperature of water.
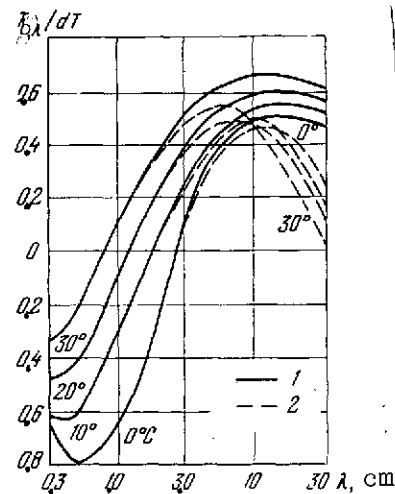
Fig. 1.5. $dT_{b,\lambda}/dT$ as function of wavelength $/6 7$
1. Fresh water
2. Sea water

map of the surface temperatures of the Caspian Sea obtained in the period from 9 to 19 December 1965. An estimate of the accuracy of these measures can be obtained by comparing remote measurements of temperatures from the aircraft and direct measure- /15 ments from a ship at points close to the aircraft route (Fig. 1.8). The root mean square deviation of the aircraft and shipboard data on the surface temperature was 0.8° K. Measurements of the water temperature from the aircraft made it possible in a short time (several days) to obtain a complete thermal pattern of the surface, which made it possible to analyze the relationship between the distribution of temperatures at the sea surface and the synoptic situation in December 1965 in the area of the Caspian Sea.

Several results of measurements of the water surface temperature on Lake Ladoga and the Caspian Sea made in 1966 by a technique analogous to that described in $/7 7$ are given in $/9 7$.

It should be noted that the thickness of the layer in which thermal microwave radiation is formed is determined by the value of the imaginary part of the refractive index $\sqrt{\varepsilon} = \varkappa *7$. Calculation for the centimeter range gives the result that $\varkappa*$ varies for water within the range 12-25 $/5 7$. Therefore, a layer thickness of $\lambda/\varkappa*2\pi,$ represents a fraction of the radiation wavelength in the medium.
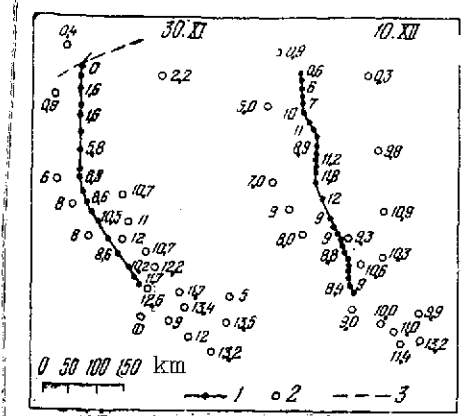
Fig. 1.6. Routes of flights over the Caspian Sea and surface temperatures reconstructed from radiometric data
1. Radiometric data
2. Shipboard data /7_7
3. Ice limits (the numbers refer to temperature in ° C)
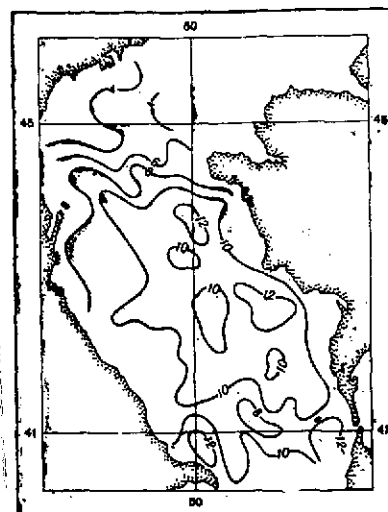
Fig. 1.7. Distribution of temperatures on the Caspian Sea surface from aircraft measurements /8_7
The numbers on the isotherms are temperatures in ° C
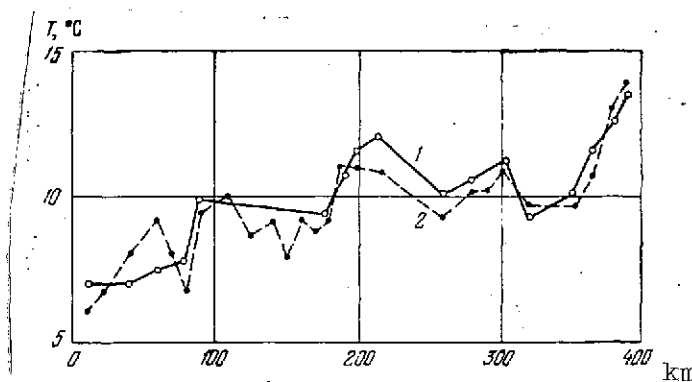
Fig. 1.8. Comparison of direct measurements of sea surface temperature (1) and results of remote sensing (2) /8_7.

2. Agitated Sea Surface

2-1) In actual conditions, the surface of bodies of water are very infrequently quiet. Waves of some intensity are virtually always present on a water surface. For a rough surface, which an agitated sea surface, in particular, is, it is required to refine the concept of blackness factor $\kappa|_\lambda$. In spite of the fact that Kirchhoff's law (1.2) is valid only in the approximation of geometrical optics, that is, when the ratio of radiation wavelengths to the dimensions of inhomogeneities tends to zero, Eq. (1.5) and the concept of the power reflection factor R_λ are generalized also to the case of a rough interface. Following /1_7, it can be shown that for a rough interface Eqs. (1.4) and (1.5) are valid if we assume that R_λ refers to the fraction of the power that is dissipated in the upper hemisphere when the

7

secondary plane electromagnetic wave propagating in the direction of the observation impinges at the interface. Since in the theory developed in /1_/ the reciprocity theorem is used, polarization of the secondary wave must identical to the polarization of the thermal radiation received. The secondary plane wave is necessary only for the calculation of scattering, and its introduction makes it possible to reduce the problem of thermal radiation to the problem of the electrodynamic theory of diffraction, and most importantly, makes it possible to employ approximate methods of diffraction theory.

A rigorous solution to the problem of reflection at a stochastically rough surface is extremely complicated /10/. Therefore in problems associated with thermal radio emission, one is usually limited to applying the Kirchhoff methods /11-16/, assuming that the reflected field can be calculated in the geometrical-optical approximation based on Fresnel's formulas from each surface element, by replacing it with a tangent plane. The power reflection factor R_λ is then found by adding the reflected waves.

A sufficiently large radius of curvature R of the roughnesses is the condition for the applicability of Kirchhoff's method for calculating reflection /10/:

$$\frac{2\pi}{\lambda} R \cos^3 \vartheta \gg 1,$$

(1.9)

where ϑ is the angle between the local normal to the surface and the direction of the incident secondary wave.

This condition is satisfied for large ocean waves and not overly large angles ϑ, however, for small waves of the ripple type, it appears doubtful that this condition is satisfied. To sidestep this difficulty, sometimes /16/ in calculations a distinction is made between major roughnesses, for which condition (1.9) is satisfied, and fine roughnesses, which are considered individually. Naturally, this approach is somewhat arbitrary.

Measurements /17/ conducted at the frequencies 1.41, 8.36, and 19.34 GHz showed that in high winds (up to 14 m/sec) the frequency dependence of both brightness temperature and polarization characteristics differs significantly from the calculated function obtained by Kirchhoff's method for an agitated surface. Without precluding the effect of spume that can occur during these observations, one can also advance the assumption that diffraction effects appeared in the experiment reported in /17/.

2-2). For the case when either the observational period is much longer than the period of the sea waves or else the characteristic dimension of the region from which the radiation is received is much larger than the length of the sea waves, one must calculate the mean value of the brightness temperature, taking the stochastic nature of the slopes into account.

The stochasticity of these slopes is described by the probability distribution for the direction of the local normal. In many calculations use is made of the distribution obtained by Cox and Munk in /18/ from an interpretation of measurements of sunlight reflected from ocean surface. This description is near-Gaussian and contains two characteristic parameters: dispersion of slopes g_x^2 and g_y^2 across and along the wind, respectively. Slope dispersions are associated with wind velocity v (m/sec) as follows:

$$g_x^2 = 0.003 + 1.92 \cdot 10^{-3}v \pm 0.002,$$
$$g_y^2 = 3.16 \cdot 10^{-3}v \pm 0.004.$$

The Cox-Munk distribution was obtained from observations in visible light, whose wavelength differs by four to five orders from radio waves and no serious substantiation was given for its application to calculations in the radiofrequency range, espe- /17 cially at large angles of incidence. Also, this distribution evidently describes a developed (steady-state) wind-driven seas, which is not uniquely possible. Therefore for model calculations use is made of a Gaussian distribution, or a distribution corresponding to purely trochoidal waves, or else more complicated distributions /20/.

However, the slope dispersion is usually small and therefore, whatever the slope distribution is taken as the basis for calculating the radiation, the result of calculating the mean radiation of the surface will be determined by the second moments of the distribution: by the dispersion of slopes in the perpendicular planes and by the correlation of slopes in these planes. It is precisely these parameters that can be determined as characteristics of the active sea states from observations of radiation in the microwave range from satellites.

2-3) Quite obviously, the results of calculating the radiation of the agitated surface depend on a large number of parameters: angle of incidence, polarization, position of the plane of incidence relative to the general direction of the propagation of waves, nature of active sea states, and so on. In order to have an idea of the order of magnitude of the variation in surface radiation due to the active sea states, let us examine a simplified scheme.

9

Referring to the results of calculations of reflection from an agitated ¡surface /11/, it can be assumed that to the surface radiation is added both radiation of the atmospheric layer between the surface and the detector as well as the specularly reflected radiation of the entire atmosphere. Therefore, for the brightness temperature at the wavelength λ when observations are taken from the altitude z at the angle ϑ to the normal, the following expression can be written:

$$T_{b,\lambda} = T_0(1-R_\lambda)\exp\left\{\frac{-\tau(z)}{\cos\vartheta}\right\} + \int\limits_0^{\tau(z)} T(z')\exp\left\{-\frac{\tau_\lambda(z)-\tau_\lambda(z')}{\cos\vartheta}\right\}\frac{d\tau_\lambda(z')}{\cos\vartheta} +$$
$$+ R_\lambda\exp\left\{\frac{-\tau_\lambda(z)}{\cos\vartheta}\right\}\int\limits_0^{\tau(\infty)} T(z')\exp\left\{-\frac{\tau(z')}{\cos\vartheta}\right\}\frac{d\tau_\lambda(z')}{\cos\vartheta},$$

(1.10)

Here $\tau_\lambda(z)$ is the integrated attenuation:

$$\tau_\lambda(z) = \int\limits_0^z \gamma_\lambda(z')\,dz',$$

where T_0 and $T(z')$ is the water temperature and air temperature; $\gamma_\lambda(z')$ is the linear absorption coefficient at the altitude z'.

Figs. 1.9 and 1.10 present the results of calculation of $T_{b,\lambda}$ as a function of the incident angle ϑ, wind velocity v, polarization, and wind direction relative to the plane of incidence. The calculations were made for the altitude z = 1 km and /18 a cloudfree atmosphere. Fig. 1.11 presents calculations for the altitude z = 1 km and for satellite observations. The calculations given in Figs. 1.9-1.11 were made for $T_0 = 290^\circ$ K and wavelength λ = 1.55 cm, for which $dT_{b,\lambda}/dT$ is near-zero (see Fig. 1.5).

First, we should note the weak effect of active sea states /19 on radiation for nadir observations. This fact, along with the use of detectors with circular antenna polarization (which, as it is not difficult to show, leads to the additional attenuation of the effect of active sea states), made it possible to determine the sea surface temperature during the flights described in /7, 8/. At the angles $\vartheta \approx 50^\circ$ for vertical polarization, the effect of active sea states on radiation from the system ocean-atmosphere is also small. For horizontal polarization, in contrast, at the angles $\vartheta \sim 50^\circ$ there is a marked increase in the brightness temperature when the active sea states become more
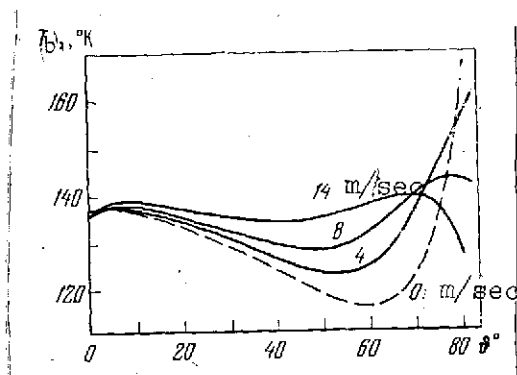
Fig. 1.9. Brightness temperature of agitated sea surface as function of observation angle |θ| and wind velocity v for horizontal polarization /12/
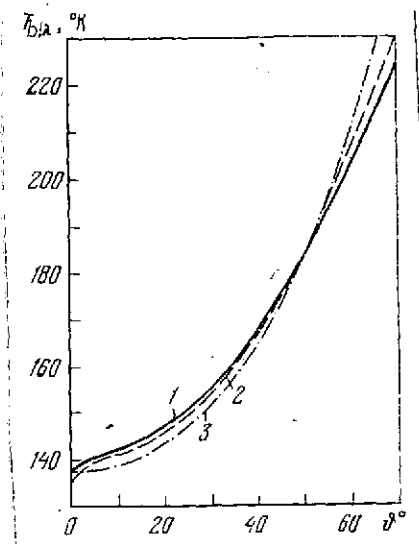
Fig. 1.10. Brightness temperature of agitated surface as function of observation angle |θ| at wind velocity v = = 15 m/sec for vertical polarization
1. Observation along wind
2. Across wind
3. Quiet surface /12/

intense, that is, with increase in the dispersion of the angles of the surface slope. From Fig. 1.11 it is clear that the rotation of the plane of incidence by 90° (for the Cox-Munk slope distribution) radiation changes only slightly. Changing the observation altitude when the sky is clear leads virtually only to an additive increment.

Waves on the surface of a body of water lead to a change in the degree of radiation polarization /19/. Fig. 1.12 presents the results of calculating the polarization factor

$$\hat{K}_p(\lambda) = \frac{\varkappa_{\perp,\lambda} - \varkappa_{\parallel,\lambda}}{\varkappa_{\perp,\lambda} + \varkappa_{\parallel,\lambda}}.$$

($\varkappa_{\perp,\lambda}$ is the blackness factor for horizontal polarization and $\varkappa_{\parallel,\lambda}$ is the blackness factor for vertical polarization) as a function of the incident angle and the root mean square value of the slope angles g_x^2 and g_y^2 for one-dimensional active sea states ($g_x^2 = 0$) and two-dimensional active sea states ($g_x^2 = g_y^2$).
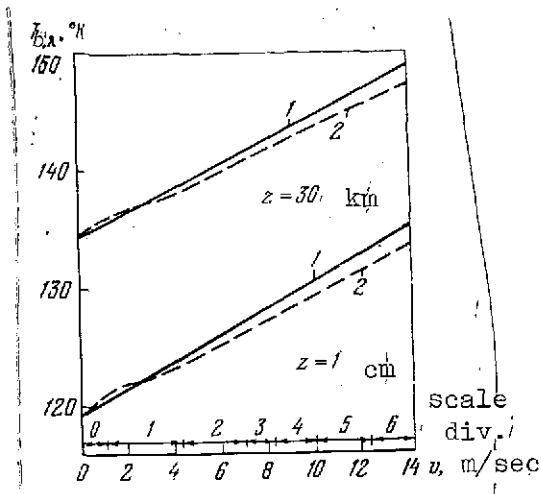
Fig. 1.11. Calculated dependence of brightness temperature $T_{b,\lambda}$ at 50° observation angle and for horizontal polarization at the wavelength 1.55 cm on wind velocity and state of active sea states in scale divisions for observation altitudes z ≞ 1 km and z = 30 km
1. Along wind direction
2. Across wind direction /12/

From these figures it is clear that appreciable depolarization occurs only for sufficiently large angles θ.

In spite of the extremely approximate nature of the calculations, from them we can conclude that measurements of radiation at angles close to the nadir and observations for different polarizations at angles θ of the order of 50° in the aggregate can yield information /20 on both the sea surface temperature as well as the dispersion of the surface slope angles and, therefore, the degree of active sea states. Additionally, measurements of the azimuthal dependence of the brightness temperature at angles θ of the order of 50° can in principle yield information on the wind direction or, more precisely, in a general direction of the propagation of the waves.
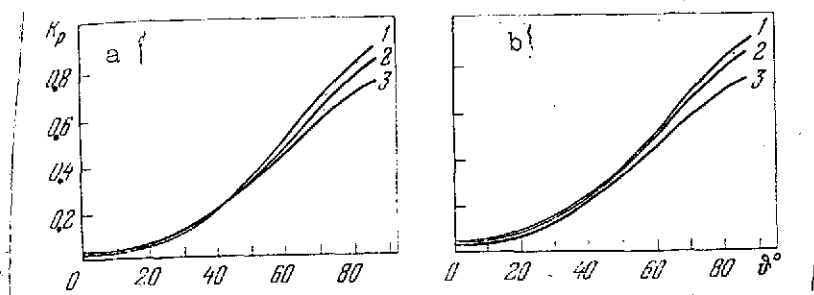
Fig. 1.12. Polarization due to active sea states as function of incident angle θ
a. One-dimensional active sea states
b. Two-dimensional active sea states
1. Quiet sea surface
2. Root mean square slope 5°
3. Root mean square slope 10° /19/
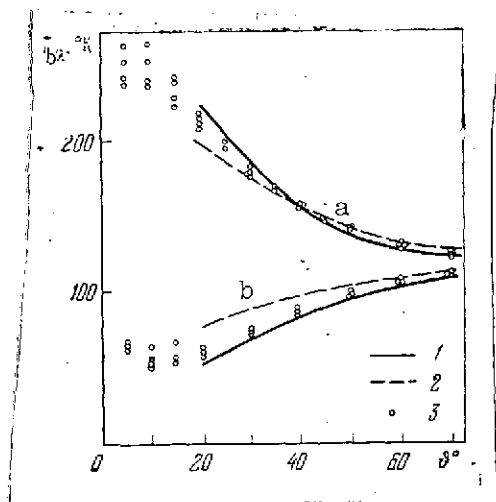
Fig. 1.13. Results of measuring angular dependence of brightness temperature $T_{b\mathfrak{u}\lambda}$ at wavelength

λ = 3.4 cm from shipboard
a. Vertical polarization
b. Horizontal polarization; active sea states to scale 3
1. Calculation /17/ for smooth surface
2. For agitated surface
3. Experiment
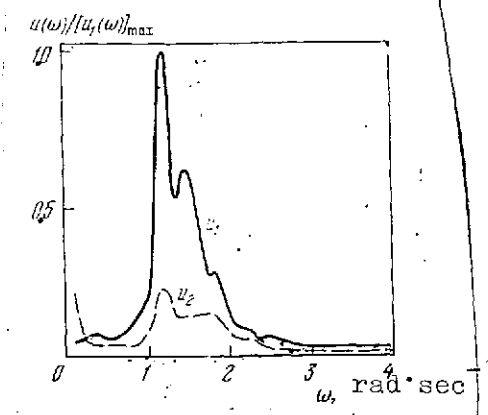
Fig. 1.14. Frequency spectrum of brightness temperature fluctuations

u_1. Observations across general direction of wave propagation
u_2. Observations along general direction of wave propagation; scale is normalized to maximum of u_1 spectrum

It should be noted that all the theoretical estimates of the effect of active sea states were made on the assumption that the active sea states change only the surface geometry. Actually, waves at a surface given sufficient amplitude or sufficiently strong wind become unstable, as is well known. Here the crests of the waves collapse, the tops are swept off by the wind, and other processes occur, which lead to the formation of spray and so-called spume -- an unstable mixture of air and sea water in different proportions. Spray and spume, whose effect on radio emission will be analyzed in the next section, greatly change the emissivity of the surface and therefore results of calculation and experimental data can be correctly compared only if there are not very active sea states. This restriction will be examined in greater detail also in the next section.

Fig. 1.13 presents experimental data from measurements of the angular dependence of radiation at the wavelength 3.4 cm taken onboard the research vessel Akademik Kurchatov during the 13th voyage in the Atlantic Ocean during sea states not exceeding

scale 3. Also plotted in this same figure are the calculated functions taken from /17/. A comparison of calculation and experiment indicates qualitative agreement.

2-4) Also of interest is the case when thermal radiation is integrated with a receiving antenna from an area much less than the length of the sea wave and the radiometer time constant is also small compared with the period of waves at the surface. Here, at the radiometer outlet, with suitably selected polarization and angle with respect to the horizon, a voltage is obtained, whose value is determined by the instantaneous slope averaged over the observation area. Measurements under these conditions permit detailed study of slope statistics.

Fig. 1.14 gives a frequency spectrum of fluctuations in brightness temperature $u(\omega)$ obtained from shipboard observations at an incident angle 50° and observations taken perpendicularly and parallel to the general direction of wave propagation. The measurements were recorded in vertical polarization at the wavelength 2.5 cm with a highly directional antenna and with a small radiometer time constant. From Fig. 1.14 it is clear that the frequency spectrum of fluctuations in radiobrightness temperature is relatively narrow and has a maximum at the frequency 0.2 Hz, which corresponds to the characteristic wave period of 5 sec. /21 Autocorrelations obtained by processing observations from shore equivalent to the frequency spectra are given in /19/. The possibility of remote measurements of slopes (in conditions of noncollapsing waves) is of undoubted interest to oceanological research.

3. Surface of Bodies of Water During Heavy Sea States

3-1) Measurements of thermal radioemission of a sea surface when the wind is sufficiently strong and active sea states are present yield a considerable rise in brightness temperature compared to the calculated value. Observations from aircraft at the wavelength 1.55 cm /21/ showed that regions of the sea covered with spume have a brightness temperature tens of degrees higher than follows from the calculation for the agitated surface free of spume.

The deviations of the results in /21/ from calculation are so large that the discrepancy cannot be accounted for by diffraction effects that were not considered. An entirely natural explanation can be found by considering the change in the emissivity of the surface due to spume, spray, and air bubbles in the surface layer produced when the stability of large waves is disturbed and when wave crests are swept off by the wind.

14
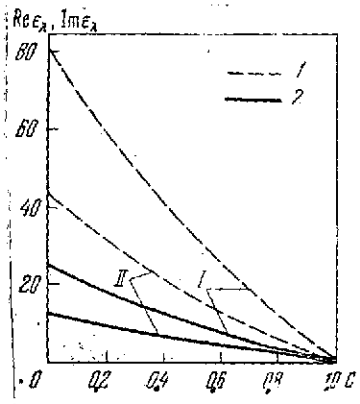
Fig. 1.15. Dielectric
constant ϵ_λ of water-
air mixture as a func-
tion of bulk concentra-
tion of air C /22/
I.   Re ϵ_λ

II. Im ϵ_λ

1. λ = 10 cm
2. λ = 1 cm
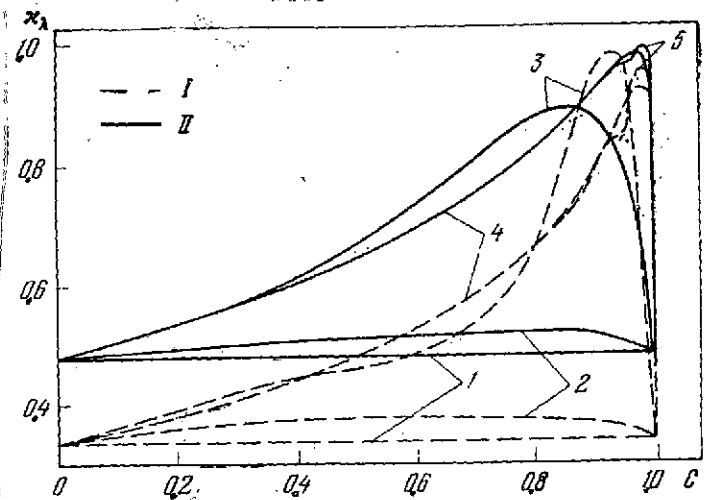
Fig. 1.16. Blackness factor of layer
of air-water mixture as a function of
bulk concentration of air C and thick-
ness of mixture layer h /22/
I. λ = 10 cm
II. λ = 1 cm
Layer thickness h in cm:
1.   0   4. 1.0
2.   0.01   5. 5.0
3.   0.1

At the present time it has not been possible to make a   /22
reliable quantitative analysis of the effect of spume on the
surface emission of bodies of water, since essential spume
parameters, such as relative content of water and air, distri-
bution of bulk content of water (or air) across layer thickness
and area, and finally, the actual microstructure of the spume
formations have been virtually uninvestigated.

Theoretical models are usually constructed based on schemes
that are far from reality: finely dispersed mixture /22/, and
thin films of water alternating with air interlayers /23/. In
spite of the obvious grossness of these models, they do afford
several qualitative estimates. A calculation of the dielectric
constant for a finely dispersed mixture of sea water-air made
in /22/ is shown in Fig. 1.15, while Fig. 1.16 presents a cal-
culated dependence of emissivity at the zenith on thickness h   /23
of a plane layer of an air-water mixture lying on the surface
of water, and as a function of the concentration of air in
mixture C for two wavelengths λ = 1 cm and 10 cm. Noteworthy
is the very strong dependence of the increment in emissivity
on concentration for low concentrations of water in the mixture.
This circumstance is associated with the very large difference

15

in dielectric properties of water and air in the centimeter range. Small oscillations that can be noted on some curves are associated with interference in the layer of the mixture and are due to the choice of model. The most important conclusions from the calculations whose results are presented in Fig. 1.16 is the increase in emissivity nearly to unity with a relatively thin layer of mixture and a low concentration of water in the mixture.

For air-saturated mixtures when $1 - C < 10^{-2}$, interference effects are virtually absent and the emissivity of water covered with a layer of this mixture can be estimated by the formula /22/

$$\varkappa_\lambda \approx 1 - R_\lambda e^{-2\tau_\lambda}.$$

where τ_λ is the optical thickness of the mixture, which is proportional to the water content per unit area and inversely proportional to the square of the wavelength in the centimeter wavelength range. In Fig. 1.17 is presented the increment of emissivity at the zenith as a calculated function of the water content $(1 - C)$ in the mixture for the wavelengths $\lambda = 0.8$, 1.35, 3.4, and 8.5 cm. From this figure it is clear that even negligible amounts of precipitated water -- tenths of a millimeter and even less -- strongly change emissivity and this change is manifested more in the shorter wavelengths. Similar conclusions can be drawn also from the results of the calculation in /23/, presented in Fig. 1.18 for a model with thin water films interlain with air.

Practically speaking, spume on the surface of bodies of water never forms a continuous homogeneous layer. Therefore even for estimational calculations one must know the distribution of the mixture as to thickness, concentration, and so on. This information is lacking at the present time. However, in the light of the preceding estimates it can be anticipated that when spume is present, there will be an increase in emissivity of the surface, which will be the greater, the shorter the wavelength. The dependence on wavelength to a large extent is determined by the distribution of the concentration and thickness of the layers. In the limiting case τ_λ is proportional to λ^{-2} for low optical thickness $\tau_\lambda \ll 1$ of a mixture on a water surface; for large values of τ_λ, the dependence of $\varkappa_\lambda$ on λ is weaker.

The effects of scattering in a water-air mixture by the surface of bodies of water have been virtually unstudied in the microwave range and require special consideration. Here it is appropriate to note that visual and photographic obser-

16

vations of spume based on the scattering of visible light,
whose wavelength is four to five orders smaller than centimeter
waves can give results markedly differing from microwave
measurements.
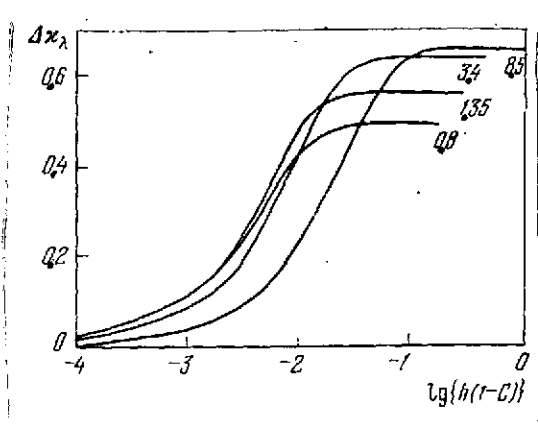
Fig. 1.17. Increment in black-
ness factor of spume for low
concentration of water as a
function of total moisture
content of mixture h (1 - C)
/22/
The numbers alongside the
figures represent wavelength
in cm
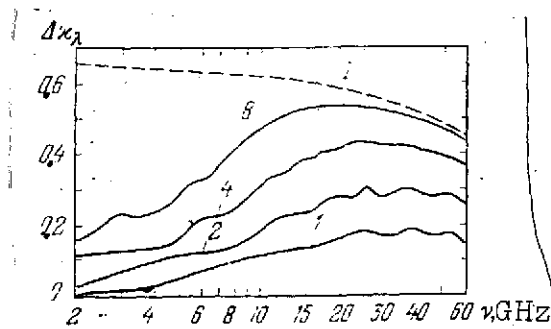
Fig. 1.18. Frequency depen-
dence of increment in black-
ness factor for the model
given in /23/
1. Difference in blackness
   factor of a blackbody
   and of a freewater
   surface; the numbers
   alongside the curves
   give the thickness of
   the spume layer in cm

3-2) Since statistical characteristics describing spume
on the ocean surface are determined mainly by the wind and sea
states, study of emission spectra at different angles to the
surface enables us to find a relationship between the sea state
parameters and wind velocity, on the one hand, and radiation
in the microwave range -- on the other.

Fig. 1.19 a presents a tracing of radiation (at the wave-
length 2.5 cm) of spume that is produced in the collapse of a
ship's wake. The measurements were taken on shipboard at an
angle of 45° to the horizon, and alternately sections covered
with foam and areas free of foam entered the field of view.
At the moments indicated by the markers on the recording,
photographs were taken of the section of the surface from which
the microwave radiation was measured. Radiation of the foamy
section (Fig. 1.19 b) is close to that of a blackbody, while
the section free of spume (Fig. 1.19 c) has a brightness that
is less by a factor of 1.5.

Fig. 1.20 /24/ shows the increment in brightness temperature (relative to the brightness temperature of a free sea surface) as a function of wind velocity v obtained from aircraft observations at the nadir at the wavelength 1.55 cm. Beginning at some critical velocity v ⌐ 6 m/sec, the brightness temperature increases roughly linearly with wind velocity. The critical velocity corresponds to the appearance of "froth" at wave crests. In /24/ it is noted that with increase in the angle of incidence, the dependence of lightening on wind velocity intensifies.

/26

Fig. 1.19. Recording of brightness temperature of foamy sea surface at wavelength λ = 2.5 cm (a) and synchronous photographs of surface with spume (b) and without spume (c) The markers 1 and 2 in the recording (a) correspond to photographs b and c
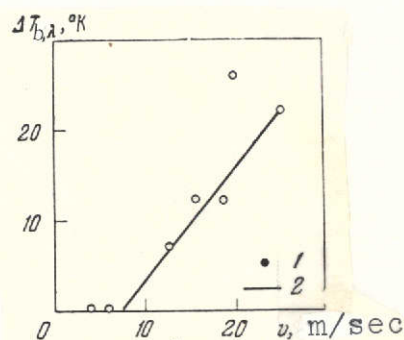
Fig. 1.20. Dependence of increment of brightness temperature at wavelength λ = = 1.55 cm on wind velocity /24/
1. Experimental data
2. Averaged dependence

Thus, an increase in wind velocity leading to instability and the collapsing of wave crests produces a large rise in the brightness of bodies of

18
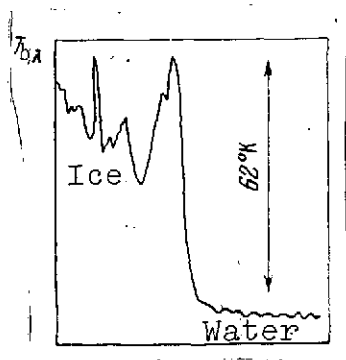
Fig. 1.21. Interference
beats in airborne measure-
ments at the wavelength
λ = 8.5 cm over the freezing
part of the Caspian Sea /7_/
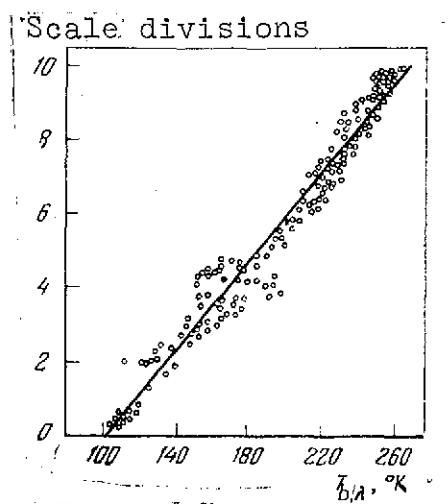
Fig. 1.22. Dependence of
brightness temperature on
ice continuity /31/

water. This brightening is more appreciable at short wave-
lengths. However, analysis of the relationship between micro-
wave radiation from a foamy sea surface and meteorological
conditions such as sea state scale, type of sea state, and
wind velocity is at its very beginning stage and in order to
more widely utilize this relationship for remote sensing of
bodies of water experimental data are needed above all.

4.   Bodies of Water in Polar Regions

4-1) In polar regions, in winter, and in the temperate
latitudes, ice floats on the water surface. The presence of
ice substantially alters the thermal emission of bodies of
water. The physical pattern of the formation of radiation
from an ice-water system is most graphically traced by looking
at the simplest case -- a plane sheet of ice floating on the
water surface /25, 26/. Since the dielectric parameters of
ice are intermediate in value between those of liquid water and
air and, which is particularly essential, attenuation of micro-
wave radiation in ice calculated at the wavelength of interest
is small, and in the intermediate ice layer wave reflected from
the air-ice and ice-water interfaces are subjected to inter-
ference.

The presence of loose dry snow reduces reflection from ice,
increases radiobrightness, and reduces the interference effects.

19

Conversely, the appearance of wet snow, and especially a thin water film on the ice surface, reduces the radiobrightness of the multilayer system /27/. It should be noted that polariza- tion characteristics of radiation from multilayer systems snow-ice-water can be calculated for plane-layered models, and the experiment reported in /28/ provides satisfactory agreement with the calculation. Model calculations of layered formations are discussed in Chapter Two. Density inhomogeneities in the ice bulk lead to additional scattering and, therefore, to a reduction in the emission factors. The effect of bulk scattering is more evident in emission from fresh ice in which there is much less absorption.

The problem of the effect of bulk scattering /29/ is ana-lyzed more closely in Chapter Two.

The high contrast between the emission of water and ice permits reliable detection of ice on a water surface /7, 30/. During flights over a continuous thin freshly frozen ice, oscillations of brightness temperature (Fig. 1.21) associated with the above-described interference effects can be easily seen in the recording of a radiometer directed in the nadir.

4-2) Measurements of radiobrightness of ice containing pools of open water permit estimating ice continuity. If we let μ stand for the continuity of ice in the radiometer field of view, then $(1 - \mu)$ is the relative area occupied by water, and the radiobrightness $T_{b, \lambda}$ measured by the radiometer will be

$$T_{b, \lambda} = \mu (T_{b, \lambda})_{_A} + (1 - \mu) (T_{b, \lambda})_{_W} . \tag{1.11}$$

Eq. (1.11) can be used for remote estimation of ice continuity, since the emission factor of sufficiently thick (more than several tens of centimeters) sea ice is close to unity, while water emits much more weakly than ice: $(T_{b, \lambda})$ of water is about $90-150^{\circ}$ K, depending on wavelength (see Fig. 1.3). Experiment /31/ on the synchronous measurement of icefield emission at the wavelength 3.4 cm and icefield photography (for different degrees of icefield continuity) demonstrated good agreement with calculation results based on Eq. (1.11) (Fig. 1.22).

The experiments in /32/ in which emission of annual and multiannual icefields was compared indicate a certain relation-ship between the age of sea ice and its emission factor. Evidently, the reason for this relationship lies in the differ-ence between the internal structure of ice density and the associated bulk scattering.

Scattering by ice density inhomogeneities can be a marked interference in the estimation of ice continuity based on Eq. (1.11). As will be shown in the next chapter, measurements over a fairly broad wavelength range reduce the effect of this interference. An additional source of interference when ice-field continuity is being determined can be a layer of water or wet snow on the ice surface during the warm time of the year. The presence of these layers, as will be shown below, severely reduces the emission, which leads to an apparent reduction in ice continuity. At low temperatures, continuity data obtained over a wide emission spectrum are quite reliable.

REFERENCES

1. Levin, M. L. and Ritov, S. M., Teoriya ravnovesnykh teplovykh fluktuatsiy v elektrodinamike /Theory of Equilibrium Thermal Fluctuations in Electrodynamics/, Moscow, Nauka Press, 1967.

2. Collie, C., Hasted, J., and Riston, D., Proc. Phys. Soc. 60/71, 145 (1948).

3. Hasted, J., Progress in Dielectric 3, 103 (1961).

4. Ray, P. S., Appl. Opt. 11/8, 1836 (1972).

5. Rabinovich, Yu. I., and Melent'yev, V. V., Trudy GGO /Transactions of the State Geophysical Observatory/, 235, 78 (1970).

6. Pereslegin, S. V., Izv. AN SSSR, seriya FAO 3/1, 47 (1967).

7. Gurvich, A. S., and Yegorov, S. T., Izv. AN SSSR, seriya FAO 2/3, (1966).

8. Matveyev, D. T., Izv. AN SSSR, seriya FAO 4/5, 508 (1968).

9. Rabinovich, Yu. I., Shchukin, G. G., and Melent'yev, V. V., Trudy GGO, 222, 49 (1968).

10. Shmelev, A. B., UFN 106/3, 459 (1972).

11. Shifrin, K. S., and Ionina, S. N., Trudy GGO, 222, 22 (1968).

12. Stogryn, A., IEEE, Trans. on. ant. and prop., AP-15/2, 278 (1967).

13. Hyatt, H. A., J. Quant. Spectr. Rad. Transfer 10/4, 217 (1970).

14. Shumko, A. M., Trudy GGO 222, 19 (1968).

15. Matveyev, D. T., Meteorologiya i gidrologiya 8, 36 (1970).

16. Wu, S. T., and Fung, A. K., J. Geophys. Res. 77/30, 5917 (1972).

17. Hollinger, J. P., IEEE, Trans. on geosci. electr. GE-9/3, 165 (1971).

18. Cox, C., and Munk, W., J. Opt. Soc. Amer. 44/4, 838 (1954).

19. Basharinov, A. Ye., and Shutko, A. M., Issledovaniye vsaimosvyazi kharakteristik polya teplovogo radioizlucheniya s sostoyaniyem poverkhnosti akvatoriy /Investigation of the Relationship Between the Characteristics of Thermal Radio Emission /Fields and the Surface State of Bodies of Water7, Preprint of the Institute of Radio Engineering and Electronics, USSR Academy of Sciences, Moscow, 1971.

20. Martsinkevich, L. M., Meteorologiya i gidrologiya, 10, 41 (1970). /29

21. Nordberg, W., Conoway, J., and Thadeus, P., Quart. J. Roy. Meteor. Soc. 95/404, 408 (1969).

22. Matveyev, D. T., Izv. AN SSSR, seriya FAO 7/10, 1070 (1971).

23. Rosenkranz, P. W., and Staelin, D. H., J. Geophys. Res. 77/33, 6528 (1972).

24. Nordberg, W., Conaway, J., Ross, D. B., and Wilheit, T., J. Atm. Sci. 28/4, 429 (1971).

25. Basharinov, A. Ye., Tuchkov, L. T., Polyakov, V. M., and Ananov, N. I., Izmeneniye radioteplovykh i plasmennykh izlucheniy v SVCh diapazone /Variation of Radiothermal and Plasma Radiation in the Microwave Range7, Moscow, Sov. radio Press, 1968.

26. Tuchkov, L. T., Yestestvennyye shumovyye izlucheniya v radiokanalakh /Natural Noise Radiation in Radio Channels7, Moscow Sov. radio Press, 1968.

27. Basharinov, A. Ye., Kolosov, M. A., Kurskaya, A. A., and Tuchkov, L. T., Trudy GGO 222, 159 (1968).

28. Kurskaya, A. A., Fedorova, L. V., and Yakovleva, G. D., Trudy GGO 222, 54 (1968).

29.
29. Gurvich, A. S., Kalinin, V. I., and Matveyev, D. T., Izv. AN SSSR, seriya FAO 9/12, 1247 (1973).

30. Seling, T. V., and Nance, D. K., Electronics 34/19, (1961).

31. Rabinovich, Yu. I., Shchukin, G. G., and Novoselov, A. N., Trudy GGO 235, 67 (1970).

32. Gloersen, P., Nordberg, W., Schmugge, T. J., and Wilheit, T. T., J. Geophys. Res. 78/18, 3564 (1973).

MICROWAVE RADIATION OF CONTINENTAL COVER AND ICE FORMATIONS

1. Background of the Problem

The basic difference between radiation of continental cover and ice formations from radiation of bodies of water is associated with the sharp difference between their electrical properties. Characteristic of solid cover, especially for dry soils and ice fields, is a much smaller absorption of microwave radiation. Therefore, thermal emission of solid cover is formed in a much thicker near-surface layer than in the case of a water medium. Here a key role begins to be played by both inhomogeneities of internal structure, in particular, inhomogeneities associated with the distribution of moisture, and by vertical temperature gradients in the emitting layer. If to this is added the wide diversity of forms of the air-soil interface and the presence of all kinds of vegetation, the full complexity of the pattern of microwave radiation formed by solid cover becomes evident.

To clarify the role of particular factors affecting microwave radiation of solid cover, it is expedient to examine simplified models in which some particular properties of the natural formations are singled out of the entire array of factors. The following such models are considered in this chapter:

1) a homogeneous medium with a smooth and a rough surface with the presence of a vertical temperature gradient;

2) a plane layer in a semi-infinite space;

3) a plane-layered medium with random electrical properties of the layers; and

4) a medium containing scattering inclusions.

Actual natural formations in rare instances are electrically homogeneous media. As a rule, they consist of different solid constituents with disseminated gas bubbles and also contain water or ice (in frozen soils). To simplify the analysis, these complex dielectrics have to be described as homogeneous by means of an equivalent complex dielectric constant, which can be estimated from the theory of binary mixtures /1, 2, 3/. Therefore, the actual data on the parameters of ice, snow, and also dry, moist, and frozen soils presented in this chapter have the significance of equivalent dielectric properties.

Unfortunately, at the present time these data are limited and their scatter reflects both the diversity of natural properties of soils as well as determination errors.

The most general approach to the solution of the problem of soil emission can be obtained on the basis of work done by S. M. Rytov and M. L. Levin /4, 5/. In several cases the application of methods of solving emission transport equations /6, 7/ along with other approximate methods leads to fairly exact results.

2. Model of Homogeneous Cover

2-1) The problem of the emission of an electrically homogeneous half space for the isothermal case was examined in detail in the preceding chapter and here the stress will be placed on the nonisothermal case when the temperature within the bounds of the emitting layer changes markedly. But the electrical properties of the medium described by its complex refractive index

$$\sqrt{\varepsilon_\lambda} = n_\lambda + i\varkappa_\lambda.$$ (2.1)

are assumed invariant within the emitting layer. The linear power coefficient of absorption in the medium γ_λ

$$\gamma_\lambda = \frac{4\pi}{\lambda}\varkappa^*$$ (2.2)

for weakly absorbing media in several cases is conveniently expressed in terms of the loss-angle tangent tg δ and the real part of the refractive index

$$\gamma_\lambda = \frac{4\pi}{\lambda} n_\lambda \operatorname{tg}\delta.$$ (2.3)

At the depth

$$l_e = \frac{1}{\gamma_\lambda}$$ (2.4)

the electromagnetic wave propagating in the direction normal to the interface is attenuated in power by e times. Therefore, l_e can be assumed equivalent to the thickness of the emitting layer.

The brightness temperature $T_{b,\lambda}(\vartheta)$ of the natural radiation of a plane cover-air interface in the direction ϑ is determined by the following expression:

$$T_{b,\lambda}(\vartheta) = [1 - R_\lambda(\vartheta)] \int_0^\infty \frac{\gamma_\lambda}{\cos\vartheta'} T(h) \exp\left\{-\frac{\gamma_\lambda h}{\cos\vartheta'}\right\} dh,$$ (2.5)

where the coefficient of reflection $R_\lambda(\vartheta)$ depends on the angle

and polarization; the angle ϑ' is associated with the angle ϑ by Snell's law: T(h) is the temperature at the depth h. In the iso-thermal case: $T(h) = T_0 = const$ and Eq. (2.5) with reference to Eq. (1.5) converts into Eq. (1.4).

For a smooth surface R_λ can be calculated from the Fresnel formulas (1.6) and (1.7). For a rough surface, the concept of the reflection coefficient can be carried out analogously as for an agitated sea surface. When the conditions for Rayleigh's cri-terion (1.9) are satisfied, reflection from surface elements can be calculated approximately from the formulas of geometrical optics, by using (1.6) and (1.7).

We note that emission from solid cover, as from a water sur-face, is appreciably polarized, and polarization attains its highest value when ϑ is close to Brewster's angle.

2-2) Let us examine the features of emission from a noniso-thermal homogeneous medium with the example of vertical sensing (that is, observations at the nadir) to which $\vartheta = \vartheta' = 0$ corres-ponds in Eq. (2.5). Considering that $(1 - R_\lambda) = \varkappa_\lambda$, for $\vartheta = 0$ we get

$$T_{b,\lambda} = \varkappa_\lambda \gamma_\lambda \int_0^\infty T(h) \exp\{-\gamma_\lambda h\}\, dh. \qquad (2.6)$$

From (2.6) it follows that the natural emission of a homogeneous medium with temperature distribution T(h) is equivalent to emis-sion of an isothermal medium with effective temperature T_b, defined as follows:

$$T_{e,\lambda} = \gamma_\lambda \int_0^\infty T(h) \exp\{-\gamma_\lambda h\}\, dh. \qquad (2.7)$$

The effective temperature depends on both the vertical profile T(h) and the radiation wavelength λ .

Special interest lies in the changes in temperature with increasing depth, associated with periodic fluctuations in surface temperature -- the diurnal and seasonal trends, for example. If the surface temperature varies according to a harmonic law with amplitude T_1 and frequency ω_1, the temperature T(h,t) at the depth h at the moment t is:

$$T(h, t) = T_{av} + T_1 \exp(-h/l_h) \sin\left(\omega_1 t - \frac{h}{l_h}\right), \qquad (2.8)$$

where $l_h = \sqrt{\dfrac{K_h \rho}{c_p} \dfrac{2\pi}{\omega_1}}$; K_h is thermal conductivity; c_p is heat

capacity; ρ is density; and T_{av} is the mean temperature of the emitting medium. From (2.8) it is clear that at the depth h, temperature varies also according to a harmonic law with period

$t_1 = 2\pi / \omega_1$ and amplitude $T_1 \exp \{-h/l_h)\}$. From (2.8) it is clear that l_h is the length of the heat wave attenuated by e times in amplitude at the depth $h = l_h$. Substituting (2.8) into (2.6), we get

$$\left| T_{b,\lambda} = T_0(1 - R_\lambda) + (1 - R_\lambda)\, \frac{T_1}{\sqrt{1 + 2\frac{l_e}{l_h} + 2\left(\frac{l}{l_h}\right)^2}}\, \sin(\omega_1 t + \varphi), \right.$$

$$\left. \mathrm{tg}\,\varphi = \frac{l_e}{l_h}\left(1 + \frac{l_e^2}{l_h^2}\right)^{-1}. \right| \tag{2.9}$$

From the linearity (2.6) in temperature it follows that, by expanding the diurnal and seasonal temperature changes in a Fourier series, we can, by using (2.9), calculate the harmonic components of the variations in brightness temperatures and the corresponding shifts in phase ϕ. For the diurnal variations, the characteristic values of the heat wavelength are $l_h = 10\text{-}40$ cm, and for the seasonal waves $l_h = 2\text{-}8$ m. From (2.8) it is clear that the amplitude of radiobrightness falls off with rise in the ratio l_e/l_h and when $l_e/l_h \geqslant 2$, it is less than 30 percent of the amplitude of the temperature fluctuations at the surface.

Estimates show that in the centimeter range the radiation mirrors diurnal fluctuations, while the seasonal variations are manifested in the decimeter radio wave range.

The presence of continuously active heat sources, which can be of either natural or artificial origin leads to the manifestation of temperature fields with the temperature gradient

$$\mathrm{grad}\, T = - q/K_h, \tag{2.10}$$

where q is the heat flux. In the simplest case of a constant heat flux from depth, $q = \mathrm{const}$, Eq. (2.10) changes into the equation

$$\frac{dT}{dh} = - q/K_h. \tag{2.11}$$

Calculation of $T_{e,\lambda}$ in the case of a constant temperature gradient leads to the formula

$$T_{e,\lambda} = T_0 + \frac{dT}{dh}\, l_e, \tag{2.12}$$

where T_0 is the surface temperature. In the case of the exponential temperature profile $T(h) = T_\infty(h) + \Delta T \exp(- h/h_h)$ with characteristic depth h_h, $T_\infty = T(h \gg h_h)$, $T_0 = T_\infty + \Delta T$ integration in Eq. (2.7) yields

$$T_{e,\lambda} = T_\infty + \Delta T \frac{h_h}{h_h + l} \cdot \qquad (2.13)$$

The limiting cases $h_h \gg l_e$ and $h_h \ll l_e$ thus leads, as can be seen from (2.13), to the isothermal case $T_{e,\lambda} \approx T_\infty + \Delta T = = T_0$ and to a small perturbation of the equivalent temperature $T_{e,\lambda} \approx T_\infty + \Delta T (h_h/l_e)$.

2-3) For soil with an uneven surface, one can introduce the concept of the reflection coefficient analogous to what was done in Chapter One where we analyzed radiation from an agitated sea surface. Characteristic of dry land is much greater surface roughness than for the sea and therefore its effect shows up stronger. The surface roughness of land produces partial (or total) depolarization of radiation and deformation of the angle-brightness functions.

In model descriptions of reflection at stochastically inhomogeneous surfaces, use is made of perturbation theory methods /8/ /34/ (for small shallow inhomogeneities) and the approximate Kirchhoff method /8, 9/ (for large inhomogeneities). In the geometrical-optics approximation, relatively simple relations can be obtained by representing large-scale surface irregularities as sets of randomly oriented area (facets). It is assumed that the number of facets is sufficiently large and that their reflective properties are roughly identical. The properties of a surface in the one-dimensional approximation are determined by the distribution function of the facet orientation angles $F(\vartheta') \, d\vartheta'$, where the angles ϑ' characterize the deviation of the facet normal from the mean normal to the surface.

The angle-brightness characteristic of the blackness factor of a surface in the direction ϑ , under Kirchhoff's law, is defined by the relation

$$\varkappa_\lambda = 1 - \int_{-\pi/2}^{+\pi/2} R_\lambda (\vartheta - \vartheta') F(\vartheta') \, d\vartheta', \qquad (2.14)$$

where $\int_{-\pi/2}^{+\pi/2} F(\vartheta') \, d\vartheta' = 1$ by the normalization condition, and $R_\lambda (\vartheta)$

is the power reflection coefficient with reference to polarization. The increase in facet dispersion "smooths" the angle-brightness functions.

3. Models of Inhomogeneous Cover

3-1) A plane layer having thickness l and lying in a homogeneous half-space is the simplest model of an inhomogeneous structure

of cover. In spite of the very high idealization, this model enables us to examine interference effects manifested, for example, in the radiation from systems such as ice on a water surface, films of petroleum or petroleum products on a water surface, snow on soil surface, and so on.

A sharp boundary between a layer (or layers) denotes physically that change in ε_λ occurs in some region much smaller than the wavelength of emission in the medium. If the region of change in ε_λ has a thickness comparable with the wavelength, or longer, to this structure there corresponds the model of a layered structure with transitional layers.

As will be shown below, in regular layered structures the presence of reflections from boundaries leads to strongly pronounced resonance effects, especially for small values of the loss-angle tangent in the medium. However, in actual conditions the thickness of the layer (or layers) is random, which leads to the manifestation of specific effects, for example, the blurring of oscillations or the manifestation of correlation of inhomogeneities when natural objects are under observation. The properties of a medium with random inhomogeneities will be examined for models of a random layered structure and a structure with random three-dimensional inclusions. All models of inhomogeneous structures in this section will be examined on the assumption that the temperature of the entire system is constant, if there will be no special reservations.

3÷2) Let us look at a plane homogeneous layer of thickness 1 located at the boundary of a homogeneous medium whose dielectric properties differ from the properties of the medium.

To calculate the radiation of this two-layer model in the direction ϑ_0, it is sufficient to calculate the power reflection R_λ of the secondary plane wave corresponding to the polarization $\underline{/4, 5/}$ in the direction ϑ_0. An elementary calculation $\underline{/10/}$ yields, for the blackness factor of the system $\varkappa_\lambda = 1 - R_{\lambda}$ (where R_λ is the total reflection coefficient of the system), the following expression:

$$\varkappa = \frac{[1 - R_{2,\lambda}\exp(-2\tau_\lambda)](1 - R_{1,\lambda})}{1 + R_{1,\lambda}R_{2,\lambda}\exp(-2\tau_\lambda) + \sqrt{R_{1,\lambda}R_{2,\lambda}}\,e^{-\tau_\lambda}\cos[2kl\cos\vartheta + \varphi_1 + \varphi_2]},$$ (2.15)

where $R_{1,\lambda}$ and $R_{2,\lambda}$ are the coefficients of reflection from the air-layer interface and from the layer-homogeneous medium interface, respectively; $\tau_\lambda = \gamma_\lambda l / \cos\vartheta$; γ is the coefficient of absorption in the layer; the angles ϑ_0 and ϑ are associated by Snell's law; $k = \dfrac{2\pi n_\lambda}{\lambda}$; n_λ is the index of refraction in the

layer; and the angles ϕ_1 and ϕ_2 are the changes in the phase of the wave upon reflection from the air-layer interface and the layer-homogeneous medium interface, which depend on the polarization and angle of incidence ϑ. In calculations based on Eq. (2.15), it is necessary to allow for the change in the polarization of the wave upon passage across the layer-air interface.

From Eq. (2.15) it follows that the dependence of $|\varkappa_\lambda|$ on the parameter kl is oscillatory in character. This circumstance is a consequence of the interference between the direct and reflected waves. L. T. Tuchkov $/10/$ was the first to point to the role of interference effects in radiation. From Eq. (2.15) it is also clear that absorption in the layer smooths out the oscillations.

Eq. (2.15) was derived for monochromatic radiation. For radiation in the band $\lambda, \lambda + \Delta\lambda$ the blackness factor $\varkappa_{\lambda,\Delta\lambda}$ can be easily calculated by the formula

$$\varkappa_{\lambda,\Delta\lambda} = \frac{1}{\Delta\lambda} \int_\lambda^{\lambda+\Delta\lambda} \varkappa_\lambda d\lambda.$$

Fig. 2.1 shows the calculated dependence of the brightness temperature on layer thickness for a model of a two-layer medium for the case of narrow-band reception (from data in $/7/$).

In wideband reception when $\Delta\lambda/\lambda \gg kl\cos\vartheta$, the oscillations are eroded even for weak absorption in a layer, and the emissivity of a two-layer medium is defined as

$$\varkappa_\lambda = \frac{[1 - R_{2,\lambda}\exp(-2\tau_\lambda)](1 - R_{1,\lambda})}{1 - R_{1,\lambda}R_{2,\lambda}\exp(-2\tau_\lambda)}. \qquad (2.16)$$

In the case when the primary medium has weak emissivity (as, for example, a water medium), the appearance of an absorptive layer leads to a monotonic rise in the blackness factor of the system with increase in absorption. The dependence of the blackness factor on absorption in the upper layer is shown in Fig. 2.2.

3-3) In nonisothermal cases, the shape of the radiobrightness temperature spectrum of a layered medium can have features that depend on the sign of the temperature gradient in the upper layer. The effect of change in radiobrightness temperature over the spectrum in the nonisothermal case is associated with the microwave emission in the upper layer that is dependent on the frequency of absorption.

Examples of integrated-absorption functions of the radiobrightness temperature of a model of a nonisothermal two-layer medium in conditions of averaging of interference oscillations are shown
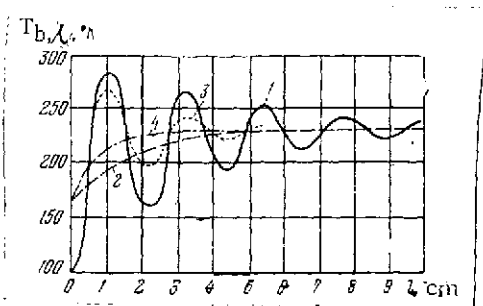
Fig. 2.1. Oscillations of radio-
brightness temperature of a model
of an ice-water medium when there
is a rise in the thickness of the
ice layer, according to $\underline{/7\underline{/}}$
(λ = 10 cm)

1. $T_{b,\lambda}$ when $\gamma = 15$ (nepers/m)

2. mean value of T_b,

3. $T_{b,\lambda}$ when $\gamma = 30$ nepers/meter

4. mean value of T_b,
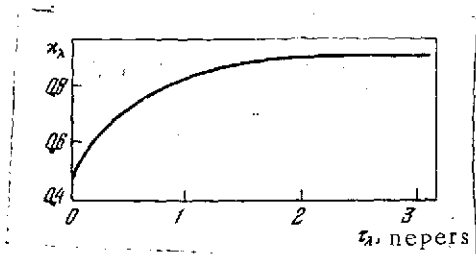
Fig. 2.2. Dependence of
blackness factor on absorp-
tion in intermediate layer
in an isothermal two-layer
        model
In the absence of the layer
  λ = 0.5; when the layer is
very thick, λ = 0.9.

in Fig. 2.3. As can be seen in Fig. 2.3, the radiobrightness
temperature of a layered medium, when the upper layer is poorly
conductive, can have either an ascending, or a descending branch,
depending on the sign that the temperature gradient has.

3-4) A model of layered structures with abrupt gradients
can be used in a limited number of cases, when the thickness of
the transitional layers does not exceed a fourth of a wavelength.
In several cases, the separation of the layers by abrupt bound-
aries does not occur and satisfactory approximation is attained
by using models of layered structures with transitional layers
in which the dielectric constant changes smoothly over the inter-
val of a wavelength or several wavelengths. The transitional   /37
layers with smoothly-varying parameters have a matching effect,
leading to a decrease in reflections at the boundaries and a smooth-
ing over of interference effects $\underline{/11\underline{/}}$.

This model with exponentially varying dielectric constant
of the transitional layer was examined by A. I. Kozlov. With the
representative example of a model where there is a transitional
layer between the upper layer with $\varepsilon_3 = 3$ and a substratum with
$\varepsilon_4 = 40$, A. I. Kozlov found that when the thickness of the
transitional layer exceeds a half-wavelength, nearly total absence
of reflections is achieved. In these conditions, the radiative
properties of the model proved to be close to the radiative pro-
perties of a half-space with upper-layer parameters. Irregular-
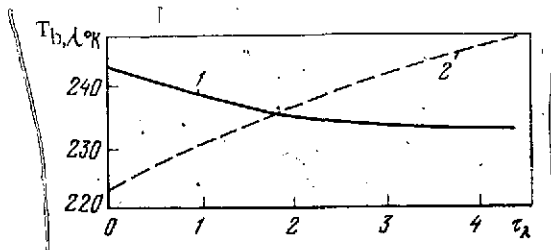ities at the interfaces cause scattering of radiation and lead to

Fig. 2.3. Dependence of radio-brightness temperature on absorption in intermediate layer in a nonisothermal two-layer model

$1 - T_1 = 270°$ K; $T_0 = 240°$ K; $R_{1\lambda} = 0,005$; $R_{2\lambda} = 0,1$;
$2 - T_1 = 240°$ C; $T_0 = 270°$ K; $R_{1\lambda} = 0,05$; $R_{2\lambda} = 0,1$

T_1 is the temperature of the lower interface of the intermediate layer

T_0 is the surface temperature

spatial variations of the effective layer thickness, which is accompanied by the smoothing of the oscillatory structure of the radiation field. Thus, for example, in the frame of reference of the facet model, a variation in the slope of the facets causes a change in the path length and variations in the phase shifts of the interference vibrations. In the calculation, the resultant interference structure must be averaged over a set of phase shifts.

The above-analyzed properties of regular plane-layered media are clearly manifested either in specially prepared laboratory specimens, or in extremely favorable conditions of full-scale experiments. In natural conditions, the random variations in thickness and dielectric properties of cover as a rule lead to the blurring of interference maxima and minima, especially for large spatial averaging.

3-5) Radiation characteristics of media containing random inhomogeneities of density and composition have features associated with the scattering of radiation by these inhomogeneities. Most solid natural formations are stochastically inhomogeneous, and statistical methods must be resorted to in calculating their emission. The electrodynamic theory of thermal fluctuations /4,5/ indicates an approach toward solution of the problem of /38 the radiation of a medium with random inhomogeneities: calculation of active losses of a secondary wave incident on the inhomogeneous medium. Calculation of active losses requires in turn the solutions of the diffraction problem. In the case of an isothermal medium, it is sufficient to calculate the fraction of power of the secondary wave scattered by the medium into the ambient space. This also necessitates a solution of the problem of diffraction and determination of the field outside the emitting medium. An exact solution in the general case cannot be obtained, and one must resort to approximate methods for solution of the diffraction problems.

Quite obviously, scattering by random inhomogeneities in bulk is equivalent to an increase in the coefficient of reflection from the boundary of a medium. Therefore, for a medium containing refractive index inhomogeneities, one can write the following expression associating the brightness temperature T_b,

with the temperature of the medium T_0:

$$T_{b.\lambda} = T_0 [1 - (R_\lambda + \Upsilon_\lambda)],$$ (2.17)

where R_λ is the coefficient of reflection from the medium-air interface; and Υ_λ is the coefficient describing bulk scattering and referring to the fraction of power of the secondary wave that is scattered by bulk inhomogeneities across the interface into the ambient space.

The simplest and most graphic result of calculating Υ_λ is obtained when in the solution of the diffraction problem one must be limited to single scattering and must use the perturbation method for randomly-inhomogeneous media /12, 13/. For simplicity of the analysis of the role of bulk effects, the interface of the medium can be assumed to be plane. In this case, it is possible to calculate Υ_λ in a fairly general form and investigate individual particular cases.

3-6) To calculate scattering by the perturbation method it is sufficient to know the spectral density of fluctuations of the real part of the refractive index n, which is a Fourier-transform of the structure function $D_n(r)$ of a random, locally homogeneous field $n(r)$:

$$(D_n \, r) = \overline{(n \, (r + r_1) - n \, (r_1))^2},$$

where $n(r)$ is the value of n at an arbitrary point r. However, qualitative analysis of the results is simplified if one is limited to examining not locally-homogeneous, but homogeneous fields for which there exist the mean value of the refractive index $\bar{n}$, the dispersion $\sigma_n^2 = \overline{(n - \bar{n})^2}$, and the correlation function

$$b_n \, (r) = \frac{\overline{(n \, (r_1) - \bar{n}) \, (n \, (r + r_1) - \bar{n})}}{\sigma_n^2} .$$

The geometry of bulk scattering is shown in Fig. 2.4.

Suppose that in an inhomogeneous medium the secondary plane is propagating in the direction of unit vector m. Then, as shown in /12/, the effective scattering cross section q_m per unit volume per unit solid angle in the direction m' is

$$q_m \, (m') = 2\pi k^4 \sigma_n^2 \Phi_n \, (k \, (m - m')) \sin^2 \chi,$$ (2.18)

where $\Phi_n(p)$ is the three-dimensional Fourier transform of the correlation function $b_n(r)$; and χ is the angle between the direction of polarization and the vector m', $|m| = |m'| = 1, k = 2\pi\bar{n}/\lambda,$ $k_0 = 2\pi/\lambda.$. Eq. (2.18) is derived without considering absorption in the medium and the refraction of the incident secondary wave
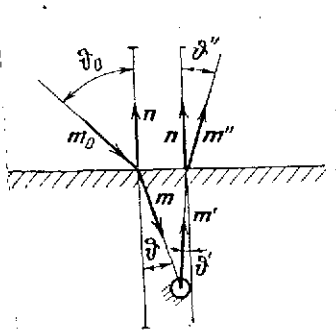
Fig. 2.4. Scheme of bulk
scattering (for the cal-
culation of   based on
Eqs. (2.18)-(2.20)

m_0, m, m' and m" are the
unit vectors of the inci-
dent secondary wave refracted
in the medium, scattered in
the medium, and the wave
emitted into the ambient
space, respectively;
$\vartheta_0, \vartheta, \vartheta'$ and ϑ'' are the
angles between the normal
to the surface and the
corresponding unit vectors:

$$\sin \vartheta_0 = \bar{n} \sin \vartheta;$$
$$\sin \vartheta'' = \bar{n} \sin \vartheta'$$

at the medium interface. With
reference to these factors,
the cross section of scattering
at the depth h (h < 0), $q_m(m',h)$
of the secondary wave incident
at the interface (h = 0) in
the direction m_0 can be written
as

$$q_{m_0}(m', h) = (1 - R_\lambda) \frac{\cos \vartheta_0}{\cos \vartheta} \cdot$$

$$\cdot \exp\{2k_0 \varkappa^* h / \cos \vartheta\} q_m(m'), \qquad (2.19)$$

where ϑ and ϑ_0 are the angles
between the normal to the surface
of the medium and the vectors
m and m_0, m_0, $\sin \vartheta_0 = \bar{n} \sin \vartheta$,
and * is the imaginary part of
the refractive index of the medium.
For the power of the secondary
wave backscattered across the
interface of the emitting medium,
Γ_λ can be calculated based on
the following formula:

$$\Gamma_\lambda = \cos \vartheta_0 \int_{-\infty}^{0} dh \int_{0}^{\pi/2} \sin \vartheta'' d\vartheta'' \int_{0}^{2\pi} d\varphi \frac{\cos \vartheta''}{\cos \vartheta'} (1 - R_\lambda') \times$$
$$\times \exp\{2k_0 \varkappa^* h / \cos \vartheta'\} q_{m_0}(m', h), \qquad (2.20)$$

where ϑ' is the angle between vector m' and the normal to the
surface of the medium $\bar{n} \sin \vartheta'' = \sin \vartheta'$. The reflection coeffi-
cient R_λ' appearing in (2.20) depends on the angle of incidence
ϑ' and on the polarization of the scattered wave. The direc-
tion of polarization is determined by the vector $m' [A m']$,
where A is the direction of polarization of the secondary wave
in the medium. From the conditions of the applicability of the
perturbation method (that is, the smallness of the scattered
field) it follows that Γ_λ must be small compared with unity.

/40

3-7) By substituting Γ_λ calculated by Eq. (2.20) into
(2.17), one can analyze the dependence of the radiobrightness of
the scattering medium on the direction, polarization of radiation,
and parameters of the medium. Carrying out this analysis is com-
plicated in the general case, however, one important general con-
clusion concerning the role of the scales of inhomogeneities making

the main contribution to scattering follows directly from (2.20). One can obtain the estimate of these scales if it is considered that the scattering vector k(m - m'), which is the argument of the spectral density of fluctuations in the dielectric constant in the integral (2.20), varies in absolute magnitude within the limits

$$2k \leqslant |k(m - m')| \leqslant k_0 \sqrt{2} [\bar{n}^2 - \sin^2 \vartheta_0 - (\bar{n}^2 - \sin^2 \vartheta_0)^{1/2} (\bar{n}^2 - 1)^{1/2}]^{1/2},$$

which corresponds to the scales of inhomogeneities from $\lambda/2\pi\bar{n}$ to $\lambda/2\pi\bar{n} \sqrt{2} [\bar{n}^2 - \sin^2 \vartheta_0 - (\bar{n}^2 - \sin^2 \vartheta_0)^{1/2} (\bar{n}^2 - 1)^{1/2}]^{1/2}.$ From this it is clear that inhomogeneities with these scales must be regarded as determinative in the analysis of the radiation of a randomly-inhomogeneous medium.

A graphical result is obtained from (2.20) for a layered-inhomogeneous medium. If the layers are elongated in the horizontal direction, the correlation of fluctuations falls off rapidly in the bulk and slowly along the horizontal. If in this case the extent of the layers is much greater than the wavelength, this medium scatters primarily in the specular direction, which makes it possible to approximately calculate the integrals in (2.20). The calculation leads to the following results for Υ_λ :

$$\Upsilon_{\perp, \lambda} = 2\pi (\bar{n}^2) \left(\frac{2\pi}{\lambda} \right)^2 V \left(\frac{4\pi\bar{n}}{\lambda} \cos \vartheta \right) \cos \vartheta_0 (1 - R_\lambda)^2 \sigma_n^2 l_e \qquad (2.21)$$

for the horizontal polarization and

$$\Upsilon_{\parallel, \lambda} = 2\pi (\bar{n})^2 \left(\frac{2\pi}{\lambda} \right)^2 V \left(\frac{4\pi\bar{n}}{\lambda} \cos \vartheta \right) \cos \vartheta_0 \cos^2 (2\vartheta)(1 - R_\lambda)^2 \sigma_n^2 l_e \qquad (2.22)$$

for the vertical polarization. The parameter $l_e = \lambda/4\pi\varkappa^*$ appearing in (2.21) and (2.22) is the equivalent thickness of the emitting layer. The function V(p) is a one-dimensional Fourier transform of the correlation function $b_n(r)$ with respect to the vertical coordinate.

From Eqs. (2.21), (2.22), and (2.17) it is clear that the presence of layered inhomogeneities leads to additional polarization effects.

The results obtained in the theory of random processes /14/ can be used in calculating the spectra V(p).

Let us examine by way of example a medium in which the properties vary with depth so that in each layer the refractive index differs from the mean value by $\pm \Delta n$, the thickness of each layer /41 is random and independent of the thicknesses of all the remaining layers, and the mean thickness of the layer is l_0. For this medium $\sigma_n^2 = (\Delta n)^2$ and $b_n(\zeta) = \exp(-\zeta/l_0)$

$$V(p) = \frac{1}{\pi} \frac{l_0}{1 + p^2 l_0^2} \cdot$$

In the simplest case, for observations at the nadir $(\vartheta = \vartheta_0 = 0)$ the expression for the radiobrightness temperature can be represented in the following form:

$$T_{b,\lambda} = T_0 (1 - R_\lambda) \left[1 - \frac{\pi^2 (\Delta n)^2 \bar{n}_\lambda}{\varkappa_\lambda / \bar{n}} \cdot \frac{\bar{n} \frac{l_0}{\lambda} (1 - R_\lambda)}{1 - \frac{16 \pi^2 \bar{n}^2 l_0^2}{\lambda^2}} \right] \cdot \qquad (2.23)$$

From Eq. (2.23) it is clear that the effect of scattering on the radiobrightness of the layered medium is manifested most strongly at the wavelengths $\lambda \approx 4 \pi \bar{n} l_0$, while at shorter and longer wavelengths the scattering plays a smaller role. This circumstance has a well-defined physical significance. For the waves with $\lambda \approx 4 \pi \bar{n} l_0$ most strongly evidenced are the resonance effects examined above in the model of a two-layer medium; however, owing to the statistical scatter of the layer thicknesses, the resonances are strongly blurred. For the long waves $\lambda \gg 4 \pi \bar{n} l_0$ the inhomogeneities are too small, the scattered waves are mutually cancelled, and the medium approximates the homogeneous medium in its scattering properties. A reduction of scattering for short waves $\lambda \ll \quad 4 \pi \bar{n} l_0$ is associated with the fact that the equivalent thickness of the layer $l_e = \lambda / 4 \pi \varkappa^*$ decreases proportionally to λ (if it is assumed that $\varkappa^*$ depends weakly on wavelength) and, accordingly, the number of scattering layers is reduced. Phase relations for short waves when layers are randomly distributed become random and this leads to incoherent addition of power scattered by each interface between layers.

3-8) For arbitrary inhomogeneities arranged chaotically, but at distances that are large compared with the wavelength, the phase relations between the waves scattered by each inhomogeneity do not play a major role and the value of Υ_λ within the applicability of single scattering can be estimated by the following formula

$$\Upsilon_\lambda = (1 - R_\lambda) \bar{q}_\lambda N l_e, \qquad (2.24)$$

where N is the mean number of inhomogeneities per unit volume; and $\bar{q}_\lambda$ is the mean effective diameter of scattering of an individual inhomogeneity in the upper hemisphere, with reference to the reflection of the scattered waves from the interface. As an example of estimates of Υ_λ based on Eq. (2.24), let us examine a finely layered medium with refractive index n in which layers having thickness l with somewhat different refractive index $n + \Delta n, \Delta n \ll n$ are disseminated. The distance between the layers L varies randomly and the variations of this distance ΔL are large:

$\overline{(kn\Delta L)^2} \gg 4\pi^2$, in addition, $L \gg l$. The coefficient of reflection from each of the layers can be calculated by using Eq. (2.15) and the Fresnel formulas (1.6) and (1.7). The smallness of $\Delta n/n$ makes it possible to assume that the coefficients of reflection from the interfaces $R_{1,\lambda}$ and $R_{2,\lambda}$ appearing in (2.15) are

$$R_{1,\lambda} = R_{2,\lambda} \approx \frac{1}{4}\left(\frac{\Delta n}{n}\right)^2 \ll 1.$$

(2.25)

By substituting (2.25) in (2.15) and using the smallness of $(\Delta n/n)^2$, we get the formula -- by neglecting absorption in the layer -- for reflection from the layer:

$$R_{c,\lambda} = \frac{1}{2}\left(\frac{\Delta n}{n}\right)^2 [1 - \cos(2knl\cos\vartheta + \varphi_1 + \varphi_2)].$$

Since scattering by the layer occurs in the direction of specular reflection, the mean coefficient of reflection of the layer is

$$\bar{R}_{c,\lambda} = \overline{\frac{1}{2}\left(\frac{\Delta n}{n}\right)^2 [1 - \cos(2knl\cos\vartheta + \varphi_1 + \varphi_2)].}$$

If the variations $\Delta n/n$ do not depend on the layer thickness l, then we have

$$\bar{R}_{c,\lambda} = \frac{1}{2}\left(\overline{\frac{\Delta n}{n}}\right)^2 [1 - \overline{\cos(2knl\cos\vartheta + \varphi_1 + \varphi_2)}].$$

(2.26)

To calculate $\overline{\cos(2knl\cos\vartheta)}$ we must know the distribution of the probabilities of the phase thicknesses of the layer knl. However, for two cases: for short waves when the variations in the layer thickness are large, $\overline{k^2n^2(l-\bar{l})^2} \gg 4\pi^2$ and for long waves, when $knl \ll 1,$ Eq. (2.26) can be simplified. In the case of short waves, it can be assumed that

$$\overline{\cos(2knl\cos\vartheta)} \ll 1,$$

and then

$$\bar{R}_{c,\lambda} = \frac{1}{2}\left(\overline{\frac{\Delta n}{n}}\right)^2, \qquad kn\overline{(l-\bar{l})^2}\cos^2\vartheta \gg 4\pi^2.$$

(2.27)

In the case of long waves, by expanding $\cos(2knl\cos\vartheta)$ in a series, we get

$$\bar{R}_{c,\lambda} = \frac{1}{2}\left(\overline{\frac{\Delta n}{n}}\right)^2 k^2n^2\bar{l}^2\cos^2\vartheta.$$

(2.28)

By substituting (2.27) into (2.24), with reference to the fact that $\bar{q}_\lambda = (1 - R_\lambda) \times N_c\bar{R}_{c,\lambda}$, we get the result that for short waves

$$\Upsilon_\lambda = \frac{1}{2}(1 - R_\lambda)^2\left(\overline{\frac{\Delta n}{n}}\right)^2 N_c l = \frac{1}{2}(1 - R_\lambda)^2\left(\overline{\frac{\Delta n}{n}}\right)^2 \frac{l_e}{L},$$

(2.29)

where N_c is the mean number of layer per unit depth, equal to $N_c = 1/\overline{L}$, $\overline{L}$ is the mean distance between the layers. The cofactor $(1 - R_\lambda)^2$ takes into account reflection from the cover interface /43 of both incident and scattered waves. For long waves, from (2.24) and (2.28) we get

$$\Upsilon_\lambda = \frac{1}{2}(1 - R_\lambda)^3 \left(\frac{\overline{\Delta n}}{n}\right)^2 N_c l_e k^2 n^2 \overline{l^2} \cos^2 \vartheta.$$

(2.30)

By substituting (2.29) and (2.30) in (2.17), it is easy to analyze the frequency dependence of the emission of a finely-layered medium and to see that this function is analogous to the function analyzed in the preceding section for a layered-inhomogeneous medium.

The above-analyzed examples involved strongly anisotropic inhomogeneities; however, the qualitative conclusions obtained do not lose their force even for an arbitrary form of inhomogeneities, including spherically symmetrical inhomogeneities.

It should also be noted that in all cases the effect of bulk inhomogeneities is the greater, the larger the effective depth l_e. Therefore, the inhomogeneity of internal structure must, to the greatest extent, affect the emission of dry soils and, especially, dry fresh ice floes, firn, snow, and so on. The effect of the inhomogeneous structure of glaciers on their emission /13/ will be examined more closely in Chapter Six when we analyze the results of measurements of radiation over the Antarctic.

4. Radiation Properties of Dry Soils

4-1) Dry soils with moisture content to 3 percent are encountered in the mid-latitudes and in arid regions of the equatorial zone when groundwater is at a depth of more than 10 meters and when vegetation is sparse. Dry soils are widely distributed in desert and semidesert regions, in brackish zones, and so on. Typical forms of soils include sands, clays, gravel beds, loams, limestone, chalk, dolomite, and others.

The physical properties of soils depend on the chemical composition and differ markedly in the cases of finely dispersed states (clays), coarsely dispersed states (sands), and moderately dispersed states (sandy loams and loams).

Moisture strongly affects soil properties (see Section 5).

The electrophysical properties of soils are determined by the complex dielectric constant, specific resistivity, and coefficient of linear attenuation of radio waves. The dielectric

constant of dry soil depends on soil porosity. The following
relation is satisfied for silicate rocks

$$n \simeq 1 + 0.5\rho,$$ (2.31)

where ρ is the density in g/cm^3. The values of the dielectric
constant and the loss-angle tangents of dry soils in the micro-
wave range from laboratory measurements $\angle 15, 16\angle$ are character- $\angle 44$
ized by the following values: for soils of sand and clay the
dielectric constant ε = 3-4, the loss-angle tangent tg δ =
= 10^{-2} - 10^{-3}, and specific conductivity σ_s = 10^{-4} - 10^{-2} (mho/m).
An increase in the conductivity is observed in soils of clay with
an admixture of iron and aluminum. The minimum loss angles and
the absorption of radio waves occur in sandy soil, where the
linear coefficient of absorption in the microwave range is esti-
mated by the approximation relations

$$\gamma \text{ [db/m]} \simeq \frac{0.4 + 0.5\rho}{\lambda \text{ [m]}},$$ (2.32)

where p is moisture content in percent.

According to the data presented, the blackness factor of dry
soils is about 0.9; the depth of penetration of an electromagnetic
wave in the decimeter range can reach several meters.

4-2) Heat transfer in soils is determined by thermal conduc-
tivity K_h, heat capacity c_p, and density ρ. The heat capacity
of soils is c = 0.15-0.22 cal/deg·g. The thermal conductivity of
compact dry soils with porosity values to 40 percent is $(1.5-4) \cdot$
$\cdot 10^{-1}$ cal/m·sec·deg. When the porosity is increased to 70 percent,
the thermal conductivity drops to 10^{-2} cal/m·sec·deg. From the
data in $\angle 17\angle$, the thermal conductivity of rocks varies in the
range 0.3-1.3 cal/m·sec·deg.

The vertical temperature profile in the surface zone to a
depth of several tens of meters is formed under the influence of
internal geothermal gradients and solar thermal fluxes causing
temperature waves. Let us estimate the contribution of the tem-
perature wave constituents for different electromagnetic wave
penetration depths.

In the active layer, the effective soil temperature accord-
ing to (2.9) can be represented as

$$T_{e, \lambda} \simeq T_0 + \frac{T_{1d}}{\sqrt{1 + 2\delta_d + 2\delta_d^2}} \sin(\omega_d t + \varphi_d) +$$

$$+ \frac{T_{1a}}{\sqrt{1 + 2\delta_a + 2\delta_a^2}} \sin(\omega_a t + \varphi_a) + \dots,$$ (2.33)

where

$$tg\,\varphi_d = \frac{\delta_d}{1+\delta_d^2}, \quad tg\,\varphi_d' = \frac{\delta_a}{1+\delta_a^2};$$

$\delta_d = l_e/l_{h.d}$; $\delta_a = l_e/l_{h.a}$ are the ratios of electromagnetic wave penetration in the diurnal $l_{h.d}$ or annual $l_{h.a}$ heat wave harmonics; T_{ld} and T_{la} are the amplitudes of the first harmonics of the diurnal and annual fluctuations in temperature at the surface.

With increase in the depth of the horizon being sensed in the active layer, the influence of diurnal temperature fluctuations diminishes and when $3l_{h.d} < l_e$ we have

$$T_{e;\,\lambda}(t) \simeq T_0 + \frac{T_{la}}{\sqrt{1+2\delta_a+2\delta_a^2}} \sin(\omega_a t + \varphi_a) + \Delta_{h,d} \qquad (2.34)$$

The contribution of diurnal fluctuations $\Delta_{h.d}$ does not exceed 20 percent of the temperature fluctuations at the surface. Therefore the effective temperature is determined by the mean-diurnal temperature in the selected season of observation and can be compared with the mean-monthly temperature.

When $2l_{h.d} < l_e$,

$$T_{e;\,\lambda}(t) \simeq T_0 + \Delta_{h,a} \qquad (2.35)$$

Here the effective temperature is determined mainly by the mean-annual temperature.

4-3) At depths greater than $l_{h.a}$ the thermal processes are determined by geothermal fluxes.

Geothermal fluxes are caused by radioactive decay, exothermal reactions of the oxidation of sulfide ore formations, combustion in coal shafts, and so on.

Thus, for example, in ore formations containing 1 percent pyrite, the heat flux in exothermic reactions is about 0.2 cal/m^2·sec.

From the data of measurements reported in /18/, thermal fluxes in shafts caused by oxidative reactions can have regular seasonal variations. The maximum values of zonal geothermal fluxes in the selected sites observed in /18/ were 3, 9, and 9-20 cal/m^2·sec.

TABLE 1.   GEOTHERMAL FLUXES AND GRADIENTS

Heat sources	Heat flux, cal/m^2·sec	Temperature gradient, deg/m
Interior of the Earth	0.015	0.01-0.05
Weak local sources	0.15-1.5	0.1-4.5
Sources of moderate intensity	1.5-15	1-15
Intense local sources	15 and higher	15-50
Sun	20	---

These heat fluxes are accompanied by marked vertical temperature gradients, which determines the possibility of their recording from microwave radiation.

Estimates of geothermal fluxes and geothermal gradients are given in Table 1.

The geothermal gradient depends on both the intensity of geothermal sources and on soil thermal conductivity. Therefore, the range of the gradients listed in Table 1 for different soils is found to be larger than the range of flux values.

4-3) Let us examine the sensitivity of the radiometric method of determining geothermal gradients.

To measure radiobrightness temperatures, let us select the region of the emission spectrum for which the effective thickness of the emitting layer exceeds the penetration depth of diurnal fluctuations. According to (2.12), the effective temperature of the layer with temperature linearly varying with depth is determined by the temperature at depth l_e:

$$l_e \simeq \frac{\lambda}{4\pi n_\lambda \, \text{tg}\, \delta} \cdot \qquad (2.36)$$

The difference of the effective temperatures ΔT_e^b for observations at two wavelengths λ_1 and λ_2 is proportional to the difference of the penetration depths of the selected waves:

$$\Delta T_e (\lambda_1, \lambda_2) = \Delta l_e \frac{\Delta T}{\Delta h} \cdot \qquad (2.37)$$

Assuming that in the spectral region selected the loss-angle tangent does not depend on wavelength, we get the following result, with reference to (2.36):

$$\Delta T_e(\lambda_1, \lambda_2) = (\lambda_1 - \lambda_2)\frac{\Delta T}{\Delta h}\frac{1}{4\pi n\,\mathrm{tg}\,\delta}. \qquad (2.38)$$

Considering the relation of the radiobrightness and effective temperatures, we get the following relation, on the assumption that $\varkappa_{\lambda_1} = \varkappa_{\lambda_2} = \varkappa_\lambda$:

$$\frac{\Delta T_b}{\lambda_1 - \lambda_2} = \varkappa_\lambda \frac{\Delta T}{\Delta h}\frac{1}{4\pi n\,\mathrm{tg}\,\delta}. \qquad (2.39)$$

Relation (2.39) enables us to estimate the sensitivity of the radiometric method when measurements are made of weak geothermal gradients.

Setting $\quad \varkappa = 0.9;\ \dfrac{1}{4\pi n\,\mathrm{tg}\,\delta} = 2 \div 5,\quad$ in (2.39), we get

$$\left[\frac{\Delta T}{\Delta h}\right]_{\min} \simeq (0.2 \div 0.5)\frac{[\Delta T_b]_{\min}}{(\lambda_1 - \lambda_2)}. \qquad (2.40)$$

When $\angle\ \Delta T_b 7_{\min} = 0.5°$, and $(\lambda_1 - \lambda_2) = 30$ cm, we get

$$\left[\frac{\Delta T}{\Delta h}\right]_{\min} - 0.3 \div 1 \text{ deg/m.} \qquad (2.41)$$

According to these estimates, the microwave radiometric method of estimating geothermal gradients enables us to record thermal geothermal fluxes whose value exceeds by 20–30 times the mean geothermal flux from the Earth's interior. The values of penetration depths of the thermal wave l_h as a function of duration of the perturbation process for nonstationary thermal sources are presented below.

/47

Δt, day	1	10	30
l_h, m	0.2–0.9	0.6–2.9	1.1–4.5

As can be seen from these estimates, the lag of the temperature waves in the ground limits the capabilities of the radiometric thermal sensing of nonstationary heat sources at great depths.

It should be emphasized that the number of factors determining the radiation properties of nonisothermal soils (even dry soils) is large. For an exact prediction of the radiobrightness values of various natural soils it is necessary to first broadly investigate their electrophysical properties.

5. Radiation Properties of Frozen Soils and Ice Cover

The physical properties of ice cover have a number of features that determine their specific radiation properties in the microwave range. As a rule, ice cover has a well-defined layered character. Wetting, porosity, and the presence of salt inclusions in sea ice strongly affect radiation properties.

The limited volume of microwave radiometric studies that have been conducted with ice cover yielded only some characteristic differences of microwave radiation properties of sea, freshwater, and continental ice formations, examples of which are discussed below.

5-1) The microstructure and properties of freshwater and sea ice experience changes dependent on the conditions of formation and growth. The thickness of multiannual sea ice can be as much as several meters. Young sea ice several decimeters thick has high bulk moisture content and increased salinity. Two-year and multi-annula ice more than one and a half meters thick has much lower moisture content. The upper layers of two-year and multiannual ice contains inclusions of air bubbles and dewatered caverns. The porosity of the ice is estimated by the bulk content of air. Thus, ice of moderate porosity contains up to 50 cm^3/kg air. When there is a high degree of porosity, the air content can climb to 200-400 cm^3/kg. The breakdown of porosity of ice fields is manifested in the form of cracks and open pools of water.

Continental ice formations (surface glaciers and permafrost) have multiannual periods of formation and range in thickness from tens of meters to several hundreds of meters. Processes of seasonal transformations are responsible for the layered nature of glacier structure. In glacier structure can be seen vertical spalling and cracks covered with a crust of firn and snow. There may be cases when lenses of sub-ice water have been preserved (taliks, nonmerging permafrost). The surface of ice formations and permafrost, as a rule, has a snow cover.

The dielectric properties of sea and freshwater ice depend on temperature, degree of wetting, salinity, and porosity of ice samples.

Allowing for the effect of wetting and salinity is carried out on the basis of working relations for multicomponent formations. For example, in determining the complex dielectric constant of wetted freshwater ice, the Wiener-Wagner relation $\underline{/}\,2\,\underline{/}$ can be used:

$$\frac{\varepsilon_{wi}-1}{\varepsilon_{wi}+u} \simeq \frac{\varepsilon_w-1}{\varepsilon_w+u}\beta_w + \frac{\varepsilon_i-1}{\varepsilon_i+u}(1-\beta_w), \qquad (2.42)$$

where ε_{wi}, ε_w, and ε_i are the dielectric constants of wet ice, water, and dry ice, respectively; β_w is the bulk content of water in the wet ice; and u is the shape factor ($2 \leqslant u \leqslant 10$).

Table 2 lists the calculated data according to [19] on the absorption index of wetted freshwater ice.

TABLE 2. DEPENDENCE OF ABSORPTION INDEX OF FRESHWATER ICE κ^* · 10^1 ON WAVELENGTH λ AND PERCENTAGE (BY WEIGHT) WATER CONTENT $\hat{p}$ PERCENT AT 0° C

λ, cm	$\hat{p}$, %				λ, cm	$\hat{p}$, %			
	0,4	0,8	1,2	1,6		0,4	0,8	1,2	1,6
0,86	13,4	21,7	30,0	38,3	11,0	5,9	6,7	7,4	8,1
3,2	7,7	10,2	12,7	15,2	17,0	5,7	6,1	6,6	7,1

Experimental data [20] show the marked dependence of the absorption index on temperature. When the temperature was lowered from 0 to -10° C, the absorption index fell by 3-4 times; over the -10 to 50° C temperature interval there was an additional drop of 1.5-2 times.

The dependence of the absorption index on ice density has a roughly linear trend.

Absorption rises with increase in the salinity of ice. The experimental data reported in [21, 22] show that at the wavelength of about 90 cm the absorption coefficient rises from 13/db/m to 37 db/m when the ice salinity is changed from 3 to 13 percent.

The data in Table 2 show that in the absence of wetting the linear coefficient of attenuation in fresh ice does not exceed the values given by the estimational formula

$$\gamma_\lambda \,[1/\text{m}] = \frac{4\pi n}{\lambda\,[\text{m}]}\,\text{tg}\,\delta \leqslant \frac{2\cdot10^{-2}}{\lambda\,[\text{m}]}\cdot \qquad (2.43)$$

For salt sea ice, the absorption coefficients rise to 20-26 db/m in the decimeter range and reach 34-35 db/m in the centimeter range.

The dielectric constant of nonwetted ice weakly depends on temperature ($n^2 \leqslant 3$); in conditions of wetting, the dielectric constant can increase somewhat. The thermal conductivity of ice is characterized by values of 1-10 cal/m·sec·deg.

The dielectric constants of continental glaciers are similar to the properties of freshwater ice and depend on density, porosity, and moisture content.

Absorption in frozen soils varies over a wide range, depending on the nature of the soil and its temperature. From the data in [23], the specific conductivity of frozen soils is (10^{-1} - 10^{-2}) mho/m.

5-2) Models calculations of microwave radiation characteristics of sea and freshwater ice show that the blackness factor for homogeneous layers of annual and multiannual ice is 0.9-0.95. For young ice, at thicknesses that are smaller than the depth of penetration of the electromagnetic wave, the dependences of the blackness factor and the polarization coefficient on thickness can be oscillatory.

Internal scattering of emission by air inclusions and inhomogeneities causes a reduction in the blackness factor in the short-wave part of the centimeter and millimeter ranges. Thus, for porous ice with a 200 cm^3/kg air inclusionscontent, when the mean diameter of an air bubble is 1-3 mm, testimates of the scattering effect show that in the wavelength range 2-0.5 cm the scattering effect can ccause a 10-20 percent reduction in the blackness factor.

Microwave radiation characteristics of continental glaciers (blackness factor, coefficient of polarization of radiation) depend on the dielectric constant of the material, the homogeneity of the glacier structure, the thickness of the snow cover, and the moisture content. The appearance of vertical cracks and spalling is reflected in the trend of the elevation-brightness characteristics.

Structural characteristics are found in shelf ice/forming in the sliding of continentall ice into littoral waters and reaching thicknesses of several tens of meters. The porous structure of shelf ice promotes the formation of vertical capillaries, due to which moisture can find its way up into the upper horizons.

The microwave radiation characteristics of shelf glaciers have anomalously low values of the blackness factor in the centimeter range. These characteristics are discussed in Chapter Six.

During experimental studies of the microwave radiation characteristics of sea and freshwater ice, oscillatory functions of the radiobrightness temperature, dependent on ice thickness were obtained [7, 24], along with radiobrightness spectra and the polarization characteristics of microwave radiation [25].

Fig. 2.5 presents an example of the oscillatory dependence of radiobrightness temperature on sea ice thickness, derived for observations on Dikson island [24].
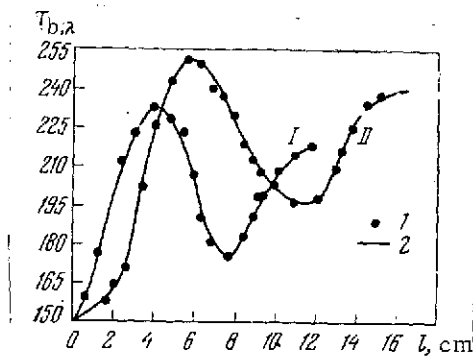
Fig. 2.5. Oscillations of radio-
brbrightness temperature with growth
in ice thickness 1 for sea ice
with salinity 11 permill
I -- λ = 30 cm
II -- λ = 50 cm after [24]
1 -- experimental data
2 -- smoothed function

From data of experimen
mental oscillatory depen-
dences of the blackness
factor on the thickness of
sea ice in [24], the dielec-
tric constant and the ab-
sorption coefficient of
the ice layer were deter-
mined. From measurements
at the 30 cm wavelength,
the following estimates
were obtained: $n^2 \cong 3-4$
(depending on the salinity
of the water); the coeffi-
cient of absorption
γ = 12-17 db/m (for 10
cm thick ice) and γ =
= 6-8.6 kg/m (for 10-20 cm
thick ice). The absorption coefficient was reduced to γ = 1-2
db/m for annual ice.

Measurements of the elevation-brightness characteristics of
the emission of ice cover [24] in vertical and horizontal polariza-
tions showed the marked effect of temperature and surface state
of the ice layer on the coefficient of polarization of microwave
radiation.

Measurements of the spectrum of radiobrightness temperatures
of annual and multiannual ice in the wavelength range 4 mm to 21
cm [26, 27] showed the characteristic differences in the shape of
the radiobrightness temperature spectrum in the cases of thin ice,
thick annual ice layers, and multiannual ice. Thus, for thin
young ice, in accordance with the theoretical conception of the
effect of the absorbing layer, the blackness factor is reduced
with increase in wavelength. For thick annual ice, the blackness
factor proved to be independent of wavelength. In the case of
multiannual ice, the blackness factor was observed to rise with
increase in wavelength. This spectral dependence of the black-   /51
ness factor in multiannual ice is accounted for by the effect of
internal scattering in the inhomogeneous and porous upper layers
of the ice that increases with shortening of the wavelength.

Observations of the radiobrightness temperature of glaciers
and permafrost soils in the wavelength range for which the depth
of penetration is commensurable with the depth of penetration of
the diurnal and seasonal temperature waves furnish estimates of
the mean-diurnal and mean-monthly temperatures at the glacier
surface (examples are given in Chapter Six) if here the possible
scattering by inhomogeneous structures is taken into account.

The blackness factor of continental glaciers, like that of multiannual ice, has a tendency to decrease in the short-wave part of the centimeter and millimeter ranges.

5-3) A marked effect on the radiation properties of soils is found for snow cover. The density of snow cover, a mixture of ice and air, can vary over a wide range: 0.01-0.6 g/cm³, depending on the time of snowfall and the layer bedding depth. Newly fallen snow undergoes compaction and forms firns with density 0.4-0.6 g/cm³.

The dielectric properties of snow cover are determined by the properties of the mixture of ice and water. A working relationship from the theory of binary mixtures is of the form [19]

$$\frac{\varepsilon_d - 1}{\varepsilon_d + u} \simeq \beta_i \frac{\varepsilon_i - 1}{\varepsilon_i + u},$$ (2.44)

where β_i is the bulk content of ice; u is the shape factor $(2 \ll u \ll 10)$. The effect of snow cover temperature and density on the dielectric constant is illustrated below by examples.

Values of the absorption index of snow as a function of density and temperature after [19] are shown in Table 3.

TABLE 3. CALCULATED VALUES OF $\kappa \cdot 10^4$ FOR SNOW
WITH VARIOUS DENSITY AND TEMPERATURE VALUES

ε, g/cm³	T, °C		
	0	−10	−18
0.03	0.416	0.143	0.11
0.01	0.138	0.047	0.035

The dependence of the absorption index of snow on density is near-linear. The effect of temperature is of the same kind as in the case of ice cover. The effect of the degree of wetting /52 on the absorption index of snow can be seen from the experimental data in [19] obtained at the wavelength λ = 10 cm when the snow density ρ was 0.4 g/cm³.

p, %	0	0.4	1.0	1.6
$\kappa \cdot 10^2$	5.2	26.2	73.4	134.0
γ [1/m]	$7 \cdot 10^{-2}$	0.3	0.9	1.6

Analysis of the working relations and the above-presented data shows that the penetration depth of microwave-range radio waves in snow cover as a function of the density and moisture content of snow can vary from a single to several tens of meters. The dielectric constant depends weakly on temperature and can vary with changes in snow density and moisture content from 1.5 to 8-10. The thermal conductivity of snow is estimated, according to [28], by the empirical relation

$$K_h \simeq 0.77\rho^2 / \quad \text{cal/m·deg·sec} . \quad (2.45)$$

Soils covered with snow layers can have marked differences between the temperature of the soil beneath the snow and the temperature of the near-ground air layer owing to the low thermal conductivity of the snow cover. The difference between the temperatures of the soil and the near-earth air layer shows up in the trend of the dependence of the radiobrightness temperature on wavelength and snow cover thickness. In experimental studies at the wavelengths 0.8, 2.2, and 6 cm, the dependence of radiobrightness temperature on snow cover thickness, as shown in Fig. 2.6 based on the data in [29], was observed.
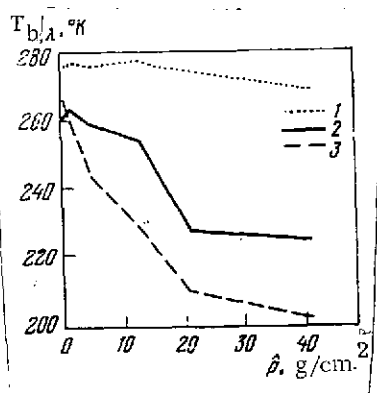
The nature of the resulting dependence of the blackness factor can be accounted for by the inclusion of the effect of bulk scattering (manifested at the wavelength 0.8 cm) and the temperature gradient in the snow cover.

Snow moisture content /53 strongly affects the blackness factor, experimentally confirmed in [29, 30].

Fig. 2.6. Experimental dependence of radiobrightness temperature of soil on snow cover thickness [29]
1 -- λ = 6 cm
2 -- λ = 2.2 cm
3 -- λ = 0.8 cm

These calculated and experimental data on the microwave radiation properties of frozen soils and ice formations indicate the fundamental potentialities of microwave sensing for acquisition of geophysical data, as for example:

1) estimates of the margins and integrity of ice fields;

2) estimates of thickness of sea and freshwater ice by an interference technique;

3) difference between annual and multiannual ice from the shape of the microwave radiation spectrum;

4) estimates of the thickness of the snow cover, temperature of soil beneath snow, and climatological temperature characteristics; and

5) determination of the margins of the ice thawing zone.

To increase the reliability of the data obtained, it is necessary to bring in the results of sensing in the visible and infrared radiation bands.

6. Radiation Properties of Wet Soils

Soil moisture contained in soil capillaries has a marked effect on microwave radiation properties of soils. An increase in soil moisture content can occur through seasonal wetting or through a rise in the groundwater level. The equilibrium level of moisture content is determined mainly by the processes of infiltration, condensation of water vapor, and evaporation. Excess soil water percolates into the water-impermeable layer and forms a perched water table, lying at the level of several meters from the surface, as well as ground water.

The paper [31] points to a correlation between soil moisture content and karst phenomena.

6-1) The complex dielectric constant of wet soils is determined by the Wiener-Wagner relation for binary mixtures and depends on the moisture content of the cover:

$$\frac{\varepsilon_s - 1}{\varepsilon_s + u} = \hat{p} \frac{\rho_s}{\rho_w} \cdot \frac{\varepsilon_w - 1}{\varepsilon_w + u} + (1 - \hat{p}) \frac{\rho_s}{\rho_b} \frac{\varepsilon_b - 1}{\varepsilon_b + u}, \qquad (2.46)$$

where ε_s, ε_b, and ε_w are the dielectric constants of wet soil, base, and water, respectively; p, (1 - p) are the values of the mass content of constituents; and u is the shape factor.

According to experimental data, the real and imaginary parts of the dielectric constant in the range of variations in moisture content from a few to several tens of percent can be approximated by linear functions. Thus, the value of the real part of the dielectric constant for sandy and clayey soils can be represented /54 in the form

$$\varepsilon_i (\hat{p}) = \varepsilon_0 + k_{p\lambda} \hat{p}, \qquad (2.47)$$

where the coefficient $k_{p\lambda}$ depends on the nature and size of soil particles. The derivative of the dependence of the dielectric constant on moisture content (2.47) is somewhat increased with increase in wavelength.

Thus, in the centimeter range an approximation of the experimental data in [16] gives the estimate

$$k_{p\lambda} = 0.55 - 0.57.$$

In the decimeter range a similar approximation yields the estimate

$$k_{p\lambda} = 0.62 \qquad \text{-- in the case of sand}$$

and

$$k_{p\lambda} = 1 \qquad \text{-- in the case of clay.}$$

The dependence of the absorption coefficient for radiowaves in the microwave range on moisture content in sandy soil obtained in [16] can be approximated in the form

$$\gamma \, [\text{db}/\text{m}] \simeq \frac{0.5 + 0.5\hat{p}}{\lambda \, [\text{cm}]}, \qquad (2.48)$$

where $\hat{p}$ is the soil moisture content in percent.

6-2) These approximational dependences of the dielectric constant of soils on the degree of wetting make it possible to represent the dependence of the blackness factor and the polarization coefficient of radiation on moisture content.

When observations are made in the vertical direction, the relation for the blackness factor is of the form

$$\varkappa_\lambda(\hat{p}) = 1 - \left(\frac{\sqrt{\varepsilon_0 + k_{p\lambda}\hat{p}} - 1}{\sqrt{\varepsilon_0 + k_{p\lambda}\hat{p}} + 1}\right)^2 = \frac{4\sqrt{\varepsilon_0 + k_{p\lambda}\hat{p}}}{(\sqrt{\varepsilon_0 + k_{p\lambda}\hat{p}} + 1)^2}. \qquad (2.49)$$

When $(\varepsilon_0 + k_{p\lambda}\hat{p}) > 8$, Eq. (2.49) can be expressed approximately by the function

$$\varkappa_\lambda(\hat{p}) \simeq \frac{4}{\sqrt{\varepsilon_0 + k_{p\lambda}\hat{p}} + 1}. \qquad (2.50)$$

Fig. 2.7 presents the dependences of cover blackness factor on moisture content typical of the centimeter range for vertical sighting. An estimate of the derivative of the blackness factor on moisture is $\overline{\Delta\varkappa_\lambda/\Delta\hat{p}} \simeq$ 0.13[1] percent, which corresponds to the derivative of the radiobrightness temperature

$$\frac{\Delta T_{b,\lambda}}{\Delta \hat{p}} \simeq 3 - 4 \ \text{deg/percent}.$$
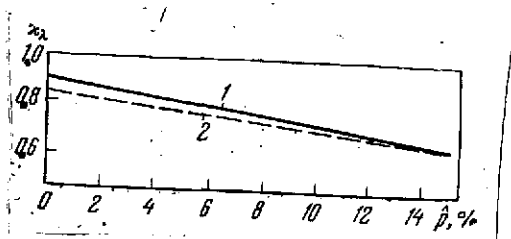

Fig. 2.7. Calculated dependence of blackness factor on moisture content of soil without plant cover
1 -- sand   2 -- clay

Experimental data of soil radiobrightness at the wavelength of approximately 21 cm as a function of moisture content [27] are shown in Fig. 2.8.

From averaged data, the quantity $\Delta T_b / \Delta \hat{p} \simeq$ 2.5 deg/percent, which is somewhat smaller than the value of this quantity based on calculated estimates. The scatter of experimental data shows that the effective error of the moisture content estimate in the experiment was about 3 percent. The calculated dependence of the polarization coefficient on soil moisture content is shown in Fig. 2.9.

6-3) These calculated dependences of the blackness factor of soil on the moisture content of the surface layer and available experimental data can be used for estimates of the sensitivity and accuracy of the radiometric method of measuring the moisture content. To estimate the sensitivity of the radiometric method, let us use the estimates of the derivative of the radiobrightness temperature with respect to moisture content. With reference to the reduced values $\Delta T_b / \Delta \hat{p}$ = 2-4 deg/percent, we get the result that the sensitivity of the radiometric moisture meters for exposed soils is about 1 percent.

In estimates of the accuracy of radiometric determinations moisture content, we must make allowance for methodological errors associated with the effect of the size of soil particles, chemical impurities, and vegetation.

Comparative experimental data on estimates of soil moisture content by means of contact measurements of specific conductivity and radiometric estimates at the wavelength 10 cm based on data in [32] are shown in Table 4.

Analysis of the calculated estimates in Table 4 and experimental data given in Fig. 2.8 can enable us to estimate the accuracy of radiometric measurements of soil moisture in the decimeter range.
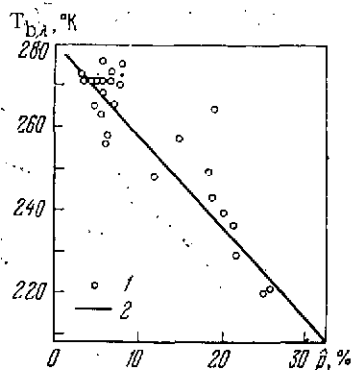
Fig. 2.8. Dependence of radio-brightness temperature on soil moisture content at wavelength 21 cm according to [27]
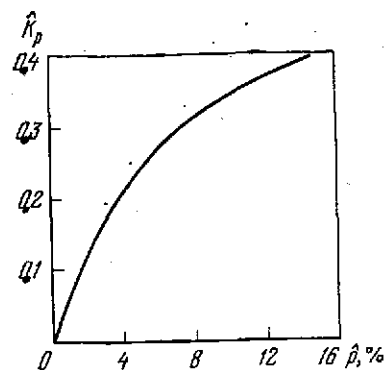1 -- experimental data
2 -- smoothed function

Fig. 2.9. Dependence of polarization coefficient of microwave radiation of soil on moisture content at a sighting angle of 60° with respect to the vertical

TABLE 4. ESTIMATE OF SOIL MOISTURE CONTENT $\hat{p}$, PERCENT

Method of Determination	Dry Soil	Wet Soil
From conductivity measurements	5	15
Radiometric estimates	2	10

Radiation characteristics of soils containing perched water table, ground water, and layers of increased moisture content at a shallow depth have a distinguishing feature in the form of a drop in the blackness factor in the decimeter range.

Results of model calculations of the blackness factor of a layered medium consisting of a sand layer with moisture to 3 percent and thickness 1 , beneath which lies a layer of water, are presented below ($\lambda = 100$ cm):

l [m]	1	2	4
$\dfrac{\varkappa_{s+w}}{\varkappa_s}$	0.79	0.92	1

These estimates show that the presence of layers of subsurface water can lead to a marked drop in the blackness factor of soil at the depths at which the water layer lies in the horizons 2-4 m from the surface.

The potentialities of detecting groundwater by the radiometric approach are determined by the minimum discernable contrast in radiobrightness temperature. Setting the threshold value of the radiobrightness contrast ΔT_{min} = 1° K, we get the result that the estimate of the depth at which groundwater can be detected from measurements in the decimeter range is 2-4 m.

6-4) The effect of plant cover has a screening action and lowers the contrast of the radiobrightness of soil expanses. To estimate the effect of plant cover, let us examine a model in which the cover parameters include the coefficient of reflection from the cover, attenuation in the cover layer, and the fraction of the soil area covered by vegetation. The blackness factor of /57 the soil covered by vegetation is estimated by the relation

$$\varkappa_\lambda \simeq (1 - R_{s,\lambda})(1 - \xi) + (1 - R_{p,\lambda})\xi(1 - e^{-\tau_\lambda}) + \\ + (1 - R_s)(1 - R_p)\xi e^{-\tau_\lambda},$$ (2.51)

where R_s and R_p are the coefficients of reflection of open soil and plant cover, respectively; ξ is the fraction of the area covered by vegetation; and τ_λ is the integrated attenuation in the cover layer, dependent on wavelength.

Absorption of radio waves in plant cover has the most marked screening effect in short-wave part of the microwave range, where the contrasts caused by the effect of moisture can be completely smoothed over. Experimental data characterizing the screening action of plant cover are presented in [27] (see also Section 2, Chapter Six).

REFERENCES

1. Wagner, K., Archiv fur Electrotechnic 2/1, 371 (1913).

2. Bogoroditskiy, N. P. et al., Teoriya dielektrikov /Theory of Dielectrics/, Moscow, Energiya Press, 1965.

3. Pearce, C. A., Brit. J. Appl. Phys. 6/10, 358 (1955).

4. Rytov, S. M., Teoriya elektricheskikh fluktuatsiy i teplovogo izlucheniya /Theory of Electrical Fluctuations and Thermal Emission/, USSR Academy of Sciences Press, 1953.

5. Levin, M. L., and Rytov, S. M., Teoriya ravnovesnykh teplovykh fluktuatsiy v elektrodinamike /Theory of Equilibrium Thermal Fluctuations in Electrodynamics/, Moscow, Nauka Press, 1967.

6. Sobolev, V. V., Perenos izlucheniya /v atmosferakh zvezd i planet /Transport of Radiation in Atmospheres of Stars and Planets/, Moscow, Gostekhizdat, 1956.

7. Basharinov, A. Ye., Tuchkov, L. T., Polyakov, V. M., and Ananov, N. I., Izmereniye radioteplovykh i plazmennykh izlucheniy v SVCh diapazone /Measurement of Radiothermal and Plasma Emission in the Microwave Range/, Moscow, Sov. radio Press, 1968.

8. Zubkovich, S. G., Statisticheskiye kharakteristiki radiosignalov, otrazhennykh ot zemnoy poverkhnosti /Statistical Characteristics of Radio Signals Reflected From the Earth's Surface/, Moscow, Sov. radio Press, 1968.

9. Shmelev, A. B., Uspekhi fiz. nauk 106/3, 459 (1972).

10. Tuchkov, L. T., Yesestvennykh shumovyye izlucheniya v radiokanalakh /Natural Noise Radiation in Radio Channels/, Moscow, Sov. radio Press, 1968.

11. Brekhovskikh, L. M., Volny v sloistykh sredakh /Waves in Layered Media/, USSR Academy of Sciences Press, 1957.

12. Tatarskiy, V. I., Rasprostraneniye voln v turbulentnoy atmosfere /Propagation of Waves in a Turbulent Atmosphere/, Moscow, Nauka Press, 1967.

13. Gurvich, A. S., Kalinin, V. I., and Matveyev, D. T., Izv. AN SSSR, seriya FAO 9/12, 1247 (1973).

14. Levin, B. R., Teoriya sluchaynykh protsessov i yeye primen-
    eniye v radiotekhnike /Theory of Random Processes and
    Its Applications in Radio Engineering/, Moscow, Sov.
    radio Press, 1957.

15. Ryazantsev, A. M., and Shabel'nikov, A. V., Radiotekhnika
    i elektronika 10/11, 1923 (1965).

16. Leshchanskiy, Yu. I., Lebedeva, G. N., and Shumilin, V. D.,
    Izv. vyssh. ucheb. zav., Radiofizika 14/4, 562 (1971).

17. Fedynskiy, V. V., Razvedochnaya geofizika /Prospecting Geo-
    physics/, Moscow, Nedra Press, 1967.

18. Ahmad, B., Ghosh, B., and Antalovich, N., Proc. of VII In-
    tern. Symp. on Remote Sensing of Environment, Univ. of
    Michigan, 1109, 1971.

19. Rozenberg, V. I., Rasseyaniye i oslableniye elektromagnit-
    nogo izlucheniya atmosfernymi chastitsami /Scattering and
    Attenuation of Electromagnetic Radiation by Atmospheric
    Particles/, Leningrad, Gidrometeoizdat, 1972.

20. Finkel'shteyn, M. I., Kozlov, A. I., and Mendel'son, V. L.,
    Radiotekhnika i elektronika 15/11, 2282 (1970).

21. Mendel'son, V. L., Kozlov, A. I., and Finkel'shteyn, M. I.,
    Izv. AN SSSR, seriya FAO 8/4, 396 (1972).   /58

22. Finkel'shteyn, M. I., and Glushnev, V. G., Dokl. AN SSSR
    203/3, 518 (1972).

23. Bogorodskiy, V. V., Trekov, G. V., Fedorov, B. A., and Khokh-
    lov, G. P., Izv. AN SSSR, Fizika Zemli 6, 86 (1971).

24. Basharinov, A. Ye., Kolosov, M. A., Kurskaya, A. A., and Tuch-
    kov, L. T., Trudy GGO im. A. I. Boyeykova, 222, 195 (1968).

25. Kurskaya, A. A., Fedorova, L. V., and Yakovleva, G. D., ibid.,
    222, 54 (1968).

26. Gloersen, P., Nordberg, W. and others, Rep. NASA, X-652-72-312
    (1972).

27. Schmugge, T., Gloersen, P. and others, Rep. NASA X-652-72-305
    (1972).

28. Bogorodskiy, V. V., Gusev, A. V., and Khokhlov, G. P., Fizika
    presnovodnogo l'da /Physics of Freshwater Ice/, Gidrometeo-
    izdat, 1971.

29. Meier, M., and Edgerton, A., _Proc. XII Intern. Symp. on Remote Sensing of Environment_, Univ. of Michigan, 1188, 1971.

30. Kennedy, J., and Sakamoto, R., _Primeneniye radioteplolokatsii v meteorologii i okeanologii_ /Radio Thermal Location in Meteorology and Oceanology/, a collection of articles, translated from the English under the editorship of Yu. I. Rabinovich, Gidrometeoizdat, 1969.

31. Hraby, R., and Edgerton, A., _Proc. VII Intern. Symp. on Remote Sensing of Environment_, Univ. of Michigan, 319, 1971.

32. Basharinov, A. Ye., and Shutko, A. M., _Meteorologiya i gidrologiya_, 9, 19 (1971).

CHAPTER THREE

MICROWAVE RADIATION OF CLOUD-FREE ATMOSPHERE

1. Absorption Spectrum of Atmosphere in the Wavelength Range $\lambda > 1$ mm

Water vapor and molecular oxygen are the main absorbing constituents. The remaining gases with polar molecules (ozone, oxides of nitrogen, and carbon dioxide) are at very low concentrations in the atmosphere, which along with the low intensities of the absorption lines, yields a negligible total contribution to total absorption. A highly detailed review /1 / of theoretical results and experimental data obviate the necessity of returning in this chapter to examining individual studies on the absorption of microwave radiation in atmospheric gases. In this section we will limit ourselves only to presenting the main results and indicate simple formulas suitable for practical estimational calculations.

1-1) The water molecule in the microwave range can be simulated by a rigid asymmetric gyroscope with dipole moment $1.84 \cdot 10^{-18}$ CGSE. The spectrum of the natural frequencies of this system contains a very large number of transitions occurring in the wavelength band $\lambda > 10$ /·m. At waves longer than one millimeter there are two lines with resonances at $\lambda = 1.35$ cm and $\lambda = 0.164$ cm. However, the major contribution to absorption is given by the wings of the intense lines belonging to the submillimeter band.

In a limited band of wavelengths, or far from the resonance of the intense lines or, in contrast, in the neighborhood of the intense line resonance, in calculating the coefficient of the absorption of water vapor molecules γ_λ it is convenient to use approximate formulas, which considerably simplify calculations. We can use the following formula

$$\Upsilon_\lambda(\text{db/km}) = 1.003 \cdot 10^5 \rho_V \frac{1}{\lambda^2} \cdot \frac{1}{T^{5/2}} [e^{-\frac{642.219}{T}} - e^{-\frac{643.283}{T}}] \times$$
$$\times \frac{\Delta v/c_0}{[0.5476 - \lambda^2] + 4\left(\frac{\Delta v}{c_0}\right)^2 \lambda^{-2}} + 4.465 \cdot 10^3 \rho_V \lambda^{-2} T^{-5/2} \frac{P}{760} \cdot \quad (3.1)$$

can be used for the wavelength range 0.4 cm $\leqslant \lambda \leqslant 3$ cm. In this formula the first term describes the resonance absorption at the wavelength 1.35 cm, and the second -- the contribution made by the wings of the high-frequency lines;

$$\Delta v / c_0 = 0.084 \ (P/760) \ (T/300)^{-0.626} / \text{cm}^{-1};$$

Δv is the line half-width; λ is wavelength in cm; T is temperature in $^{\circ}$K; P is pressure in mm Hg; and ρ_v is moisture content of air /60 in g/m^3. This formula gives an error not greater than 3 percent compared with the exact quantum-mechanical calculation in this wavelength range.

Besides absorption by isolated water vapor molecules, marked absorption by dimers -- short-lived molecules $(H_2O)_2$ -- can exist in the atmosphere. In the wavelength band 0.8-3 cm, the following approximational function is valid for absorption by dimers:

$$\gamma_\lambda (\text{db/km}) = 3.36 \cdot 10^{-3} \ \lambda^{-2} \ (\rho/7.5)^2 \ (T/318)^{-11.5}. \tag{3.2}$$

Eq. (3.2) does not contain resonance terms, since the dimer resonances can be resolved only at pressures P $\lesssim 50$ mm Hg, that is, at the altitudes where the water vapor content in the Earth's atmosphere and the contribution made by the dimers is virtually absent.

Fig. 3.1 gives the results of the calculation of the total absorption coefficient (one-dimensional and two-dimensional) in water vapor under standard conditions. Fig. 3.2 presents calculated values of the absorption coefficient at the altitudes 3, 10, and 20 km for the standard atmosphere /2_7.

Water vapor is a variable constituent of the Earth's atmosphere. Its content varies widely with temperature and altitude. Analysis of emission in the region of the resonances 0.164 cm and especially 1.35 cm is presently attracting interest owing to advances made in remote sensing of moisture content in the atmosphere.

1-2) Absorption of microwave radiation by molecular oxygen is associated with the magnetic moment of the O_2^{16} molecule. The system of absorption lines is associated with the quantum transitions corresponding to the fine structure of the molecular spectrum.

In the transitions corresponding to absorption or emission in the microwave range, the projection of the magnetic moment of the molecule in the direction of its rotational moment changes. This mechanism of transitions leads to a group of closely-lying, quite intense lines centered about $\lambda = 0.5$ cm, and one of these transitions gives an isolated line at 0.25 cm.

For the wavelength range $\lambda = 0.8-3$ cm outside the molecular oxygen absorption band, use can be made of the following approximate formula for calculating absorption in oxygen:

$$\gamma_\lambda = C_\lambda P^2 T^{-2.8} \,\text{db/km} , \tag{3.3}$$

in which the coefficient C_λ is a slowly-varying function of wavelength: $C_{0.8} = 0.662$, $C_{1.0} = 0.328$, $C_{2.0} = 0.131$, and $C_{3.0} = 0.108$. The dependence of C_λ on the wavelength is shown in Fig. 3.3. Eq. (3.3) is suitable at 300 mm Hg $\leqslant$ P $\leqslant$ 760 mm Hg, and 250° K $\leqslant$ T $\leqslant 310^\circ$ K; here it gives an error less than 3-4 percent. Outside this range of temperatures and pressures, and also at shorter wavelengths absorption in oxygen becomes so faint (< 0.1 db/km) that in estimational calculations as a rule it can /61 be neglected. However, it should be noted that the problem of absorption in oxygen at the wavelength $\lambda \geqslant 10$ cm at the present time has not been adequately studied /1 7. Though molecular absorption at long wavelengths is very small and extremely difficult to measure, this problem is of interest both for the theoretical study of intermolecular interaction as well as for a number of subtle radioastronomical studies.

At wavelengths $\lambda < 0.8$ cm, when absorption in molecular oxygen is calculated, one must take into account the entire system of lines belonging to the 0.5 cm absorption band. At sea level individual lines cannot be resolved and the dependence of absorption on wavelength is of the form shown in Fig. 3.4. Individual lines can be resolved, beginning at altitudes z = 20 km (Fig. 3.5). Absorption in the region of the line $\lambda = 0.25$ cm as a function of altitude is shown in Fig. 3.6.

Oxygen lines are caused by the magnetic moment of the mole- /64 cule and in the terrestrial magnetic field undergo Zeeman splitting. Calculations of the Zeeman effect /3, 47 show that it is of the order of 1-2 MHz in the terrestrial field and is manifested only at altitudes greater than 50 km. A map of the lines at these altitudes is complicated and depends on the orientation of the magnetic field with respect to the orientation of the propagation of microwave radiation and its polarization. Fig. 3.7 shows the splitting of one of the intense lines at altitudes of 50, 70, and 90 km.
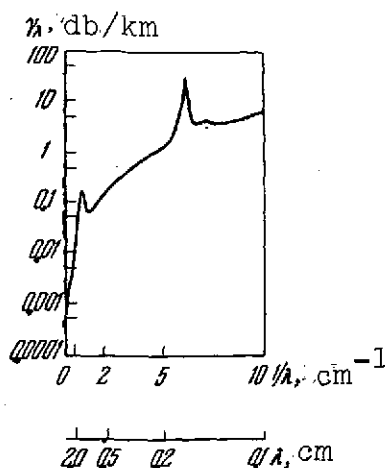
Fig. 3.1. Dependence of absorption coefficient in water vapor on wavelength under standard conditions $\underline{/1\_7}$
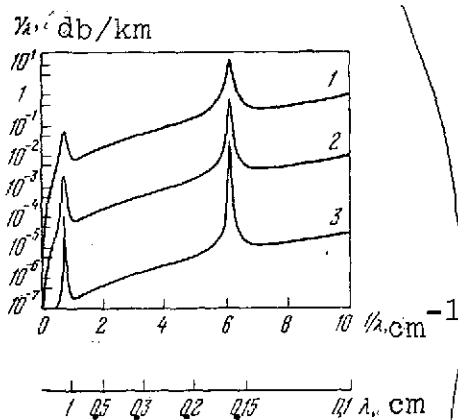$P = 760$ mm Hg
$T = 293^\circ$ K
$\rho_v = 7.5$ g/m^3

Fig. 3.2. Dependence of absorption coefficient in water vapor on wavelength at various altitudes for the standard atmosphere $\underline{/1\_7}$
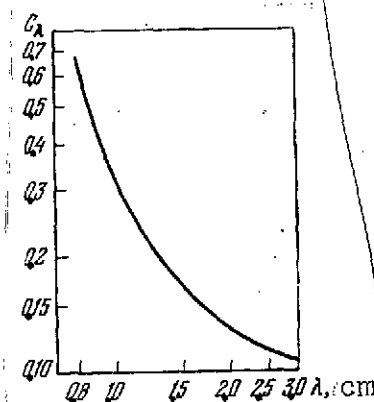1. z = 3 km
2. z = 10 km
3. z = 20 km

Fig. 3.3. Calculated coefficient C_λ for Eq. (3.3)

The percentage content of molecular oxygen in the atmosphere is virtually constant all the way to the altitudes 85-90 km. Therefore from the emission of molecular oxygen in the 0.5 cm band and the 0.25 cm absorption band it is possible to determine the vertical profiles of temperature in the atmosphere.

1-3) Total absorption in the atmosphere at pressures close to normal is made up of absorption in oxygen and water vapor. In Fig. 3.8 is shown the total calculated absorption in the atmosphere under standard conditions. Also plotted in this figure are the experimental results of various authors systematized in $\underline{/1\_7}$, shown by points.

/65

Resonances of the admixture gases O_3, N_2O, and CO were not scanned at high pressures at low altitudes. With a reduction in pressure, as the altitude is increased the lines are narrowed, absorption in the "windows" between oxygen resonance and water vapor resonance becomes less, and resonances of the admixture gases show up in these windows. Fig. 3.9, which presents the calculated absorption for a standard atmospheric model for the altitude 20 km
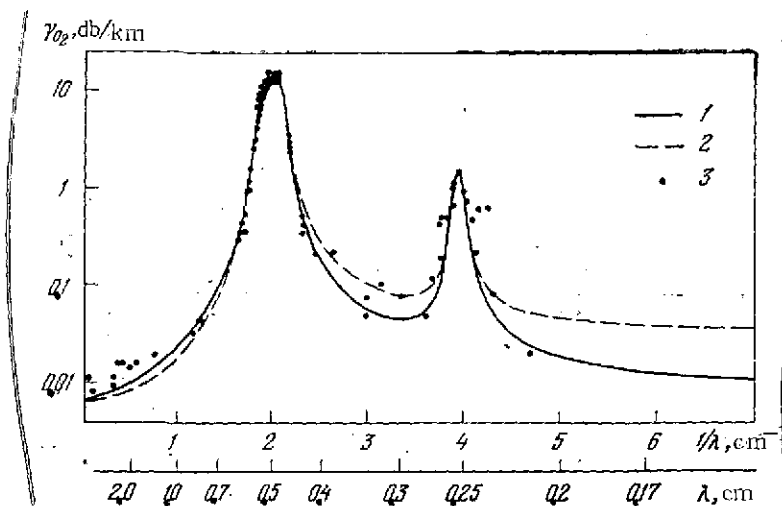
Fig. 3.4. Dependence of coefficient of absorption in oxygen on wavelength under standard conditions
1. Calculation by the Van-Fleck-Weiskopf formulas
2. By the kinetic equation in /1_7
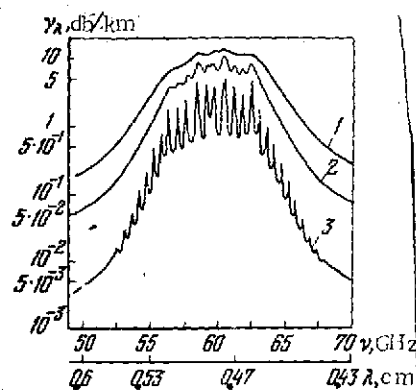3. Experimental data in /1_7

Fig. 3.5. Contour of 0.5 cm oxygen absorption band at different altitudes for standard atmosphere /1_7
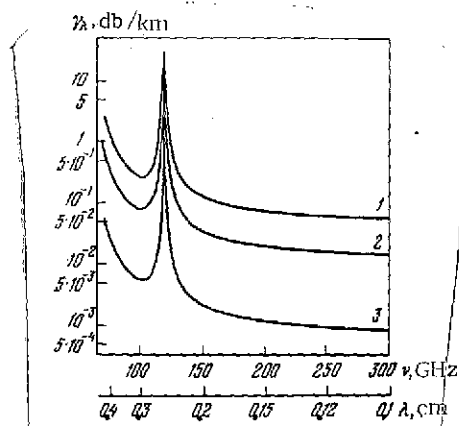1. z = 3 km
2. z = 10 km
3. z = 20 km

Fig. 3.6. Contour of oxygen absorption line λ = 0.25 /cm/ for standard atmosphere /1_7

Symbols are the same as in Fig. 3.5.

is an illustration of the fairly complicated absorption situation in the atmosphere at high altitudes. At the present time there are data indicating that absorption in admixture gases can be detected by radioastronomical methods /5_7.

2. Region of Water Vapor Resonance λ = 1.35 cm

Interest in the 1.35 cm absorption line is due to the fact that this line lies in the wavelength range in which fairly sensitive equipment with high spectral resolution necessary for scanning lines by frequency has already been developed. The optical thickness of the atmosphere in the resonance of this line as a rule does not exceed unity, and
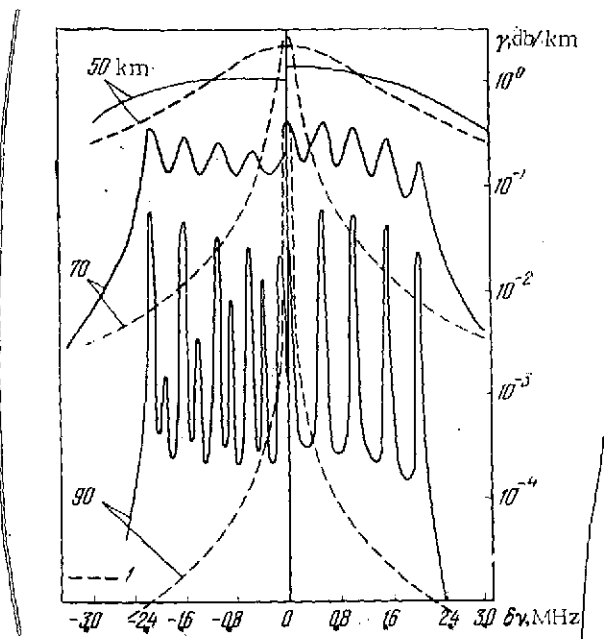
Fig. 3.7. Zeeman effect of oxygen line
Right -- observation along magnetic field, left -- across magnetic field
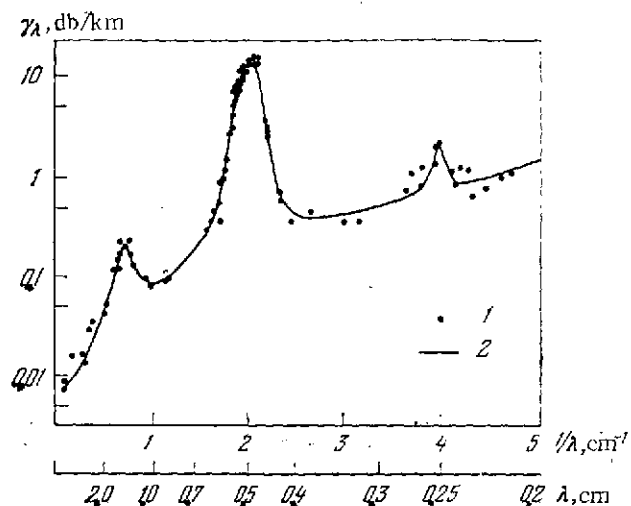1. Contour of line in absence of magnetic field /3_7

Fig. 3.8. Total absorption in atmosphere under standard conditions
1. Experimental data
2. Calculated data /1_7

therefore the atmosphere can assume to be semitransparent. In addition, absorption at the wavelength 1.35 cm is weak in clouds, which opens up the possibility of determining the water vapor content in the atmosphere when the cloud cover is present /6_7. Measuring the emission spectrum in the vicinity of the resonance makes it possible to determine the water vapor content at high altitudes /7, 8_7.

Of greatest interest at the present time is the determination of water vapor parameters in the lower atmospheric layers -- down to the level $P > 200-300$ mbar. Considerable advances have been achieved here /6, 9-17_7.

2-1) Knowing the vertical distribution of the pressure, temperature, and moisture content by altitude, it is not difficult to calculate the emission of the atmosphere in the vicinity of the 1.35 cm resonance. However, owing to the diversity of the atmospheric conditions, calculations of individual emission spectra
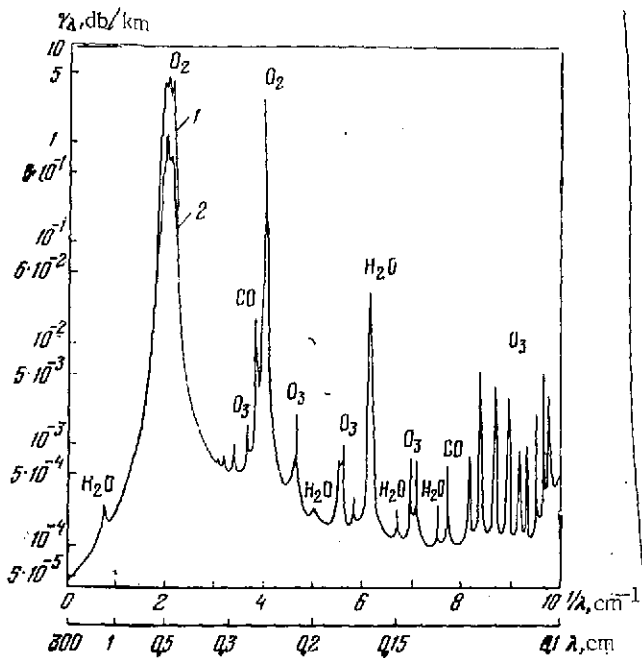
Fig. 3.9. Total absorption of
atmosphere at altitude 20 km
(calculated for standard atmo-
sphere)
1, 2. Envelopes of maxima
    and minima of 0.5 cm
    oxygen band /1_7

are not of high interest. Since
the vertical profiles -- distri-
bution of temperature T (z) and
moisture content ρ_v(z) by alti-
tude z -- can be considered as
a random function, the values
of the optical depthness

$$\tau_\lambda = \int_0^\infty \gamma_\lambda(z)\,dz$$
(3.4)

and the brightness temperature
(for zenith observations)

$$T_{b,\lambda} = \int_0^\infty \gamma_\lambda(z)\,T(z)\exp\left[-\int_0^z \gamma_\lambda(z')\,dz'\right]dz + T_{b,\phi}e^{-\tau_\lambda}$$
(3.5)

(where $T_{b,\phi}$ is the brightness
temperature of the outer space
background) are random functionals.
The mean value and the root-mean- /66
square deviation are the simplest
characteristics of these func-
tionals. The meaning and signi-
ficance of the mean values are
obvious; the root-mean-square
values give a quantitative
characteristic of the natural
variability of absorption and emission. The mean values are asso-
ciated mainly with geographical and climatical tie-ins and are
stable characteristics of an extensive region, latitude, season,
and so on. The root-mean-square values describe the effect of
random variability of meteorological conditions and are particularly
valuable for a quantitative estimation of the effect of weather on
microwave radiation for constant geographical and climatic factors.

To estimate the mean and root-mean-square values, it is
convenient to use the mean values of meteorological parameters and
correlation matrices of temperature and moisture content /18/.
For calculations associated with the atmosphere, it is desirable,
in computing the intervals (3.4) and (3.5) to convert from altitude
to pressure, by using the condition for static equilibrium in the
atmosphere:

$$dp = -\rho_a g\,dz$$

(where ρ_a is the density of air at the altitude z; g is acceleration due to gravity) and to convert from absolute moisture content ρ_v to specific moisture content $\hat{q} = \rho_v/\rho_a$.

Based on the natural assumption that variations in temperature $\delta T(z)$ and specific moisture content $\delta\hat{q}$ (z) are small, we can write equations for the mean values of optical depth $\bar{\tau}_\lambda$:

$$\bar{\tau}_\lambda = \int_{P_0}^{0} \gamma_\lambda [\bar{T}(P), \bar{\hat{q}}(P), P] \frac{dP}{\rho_a g},$$

(3.6)

and brightness temperature $\bar{T}_{b,\lambda}$:

$$\bar{T}_{b,\lambda} = \int_{P_0}^{0} \bar{T}(P)\gamma_\lambda [\bar{T}(P),\bar{q}(P),P]\exp\left\{-\int_{P_0}^{P} \gamma_\lambda [\bar{T}(P'),\bar{\hat{q}}(P'),P']\frac{dP'}{\rho_a g}\right\}\frac{dP'}{\rho_a g}.$$

(3.7)

Here the variations $\delta\tau_\lambda$ and $\delta T_{b,\lambda}$ can be written as

$$\delta\tau_\lambda = \int_{P_0}^{0}\left\{\frac{\delta\bar{\gamma}_\lambda}{\delta\hat{q}}\delta\hat{q}(P) + \frac{\delta\bar{\gamma}_\lambda}{\delta T}\delta T(P)\right\}\frac{dP}{\rho_a g},$$

(3.8)

$$\delta T_{b,\lambda} = \int_{P_0}^{0}\exp\left\{-\int_{P_0}^{P}\bar{\gamma}_\lambda(P')\frac{dP'}{\rho_a g}\right\}\frac{dP}{\rho_a g}\left\{\bar{T}(P)\frac{\delta\bar{\gamma}_\lambda(P)}{\delta\hat{q}}\delta\hat{q}(P) - \right.$$

$$- \bar{T}(P)\bar{\gamma}(P)\int_{P_0}^{P}\frac{\delta\bar{\gamma}(P')}{\delta\hat{q}}\delta\hat{q}(P')\frac{dP'}{\rho_a g} + \bar{\gamma}_\lambda(P)\delta T(P) +$$

$$\left. + \bar{T}(P)\frac{\delta\bar{\gamma}_\lambda(P)}{\delta T}\delta T(P) - \bar{T}(P)\gamma_\lambda(P)\int_{P_0}^{P}\frac{\delta\bar{\gamma}_\lambda(P')}{\delta T}\delta T(P')\frac{dP'}{\rho_a g}\right\},$$

where $\bar{\gamma}_\lambda(P) = \gamma_\lambda[\bar{T}(P), \bar{\hat{q}}(P), P].$

(3.9)

To estimate the root-mean-square values, it is necessary that Eqs. (3.8) and (3.9) be raised to the second power and averaged. Here in the expressions

$$((\overline{\delta T_{b,\lambda}})^2)^{1/2} \quad \text{и} \quad ((\overline{\delta\tau_\lambda})^2)^{1/2}$$

there appear the following correlations:

$$B_{\hat{q}\hat{q}}(P', P'') = \overline{\delta\hat{q}(P')\cdot\delta\hat{q}(P'')},$$

$$B_{TT}(P', P'') = \overline{\delta T(P')\delta T(P'')}.$$

$$B_{\hat{q},T}(P', P'') = \overline{\delta\hat{q}(P')\delta T(P'')}.$$

64

A listing of empirical values of $B_{\hat{q}\hat{q}}$, B_{TT}, and $B_{\hat{q},T}$ obtained from multi-annual radiosonde data can be found in $\underline{/18/}$.

TABLE 5. MEAN VALUES AND VARIATIONS OF OPTICAL DEPTH
AND BRIGHTNESS TEMPERATURE

Station co-ordinates		Time of meas.		$\bar{\tau}_\lambda$, db	$\sqrt{\overline{(\delta\tau_\lambda)^2}}$	$\bar{T}_{b,\lambda}$, °K	$\sqrt{\overline{(\delta T_{b,\lambda})^2}}$	Q, g cm
N. 47° lat.	W. 101° long.	July	00^h	0,76	0,22	49,1	8,7	2,49
47	101	Jan	00^h	0,19	0,10	14,7	5,5	0,67
53	35	July	12^h	0,62	0,24	39,5	11,2	2,04
53	35	"	00^h	0,26	0,14	18,9	7,7	0,92
35	48	"	00^h	0,73	0,21	50,0	9,0	2,58
45	41	"	00^h	0,59	0,24	49,9	11,6	2,66
53	36	"	00^h	0,46	0,24	30,8	11,4	1,59
63	33	"	00^h	0,42	0,19	28,2	9,8	1,44

As an example, Table 5 gives the estimates of the values $\bar{T}_{b,\lambda}$, $\bar{\tau}_\lambda$, $(\overline{(\delta T_{b,\lambda})^2})^{1/2}$ and $((\overline{\delta\tau_\lambda})^2)^{1/2}$, calculated in $\underline{/19/}$ from the data given in $\underline{/18/}$, for the characteristic conditions of continental (the first two rows) and oceanic stations, for winter and for summer, in the vicinity of the 1.35 cm resonance. Striking is the fact that the variations in optical depth as well as in brightness temperature are close to each other in order of magnitude at the different latitudes in the oceanic and continental conditions, in summer and winter, for different integrated content Q of water in the atmosphere.

The values of the variations in brightness temperature listed in Table 5 are a natural measure of the accuracy in formulating the requirements on the equipment. Actually, if the error of measurements is $((\overline{\delta T_{b,\lambda})^2})^{1/2}$, then these measurements have little /68 to give compared with apriori estimates obtained from mean-climatic data.

The effect of cloud cover or precipitation was not considered in the calculations of the data listed in Table 5. An examination of atmospheric emission when clouds are present is given in the next chapter, and here we will limit ourselves to the remark that cloud cover over the ocean introduces an additional absorption and increases both the mean brightness temperature as well as its variations.

It is shown in /19/ that the dependence of the mean brightness temperature on the mean amount of precipitable water $Q = \int \rho_V dz$ is closely approximated by a straight line (Fig. 3.10) with slope 19.1° K/g·cm^{-2}. The possibility of a linear approximation is a consequence of the small optical depth of the atmosphere (even in the vicinity of the 1.35 cm resonance) and the fact that the ratio T_λ/ρ_V varies with altitude much more slowly than does ρ_V (see /1_7/).

In Fig. 3.11 /9_7/ is presented the spectrum of radio emission descending at an angle 30° to the horizon in the vicinity of the 1.35 /cm/ resonance, calculated for the near-Earth temperature $T = 300°$ K, pressure $P_0 = 760$ mm Hg, temperature profile $T(z) = T_0 - \Gamma_0 z$ (where $\Gamma_0 = 6°/km$), and exponential distribution of water vapor with the characteristic altitude 2.2 km.

Since the incoming emission in the neighborhood of the 1.35 cm resonance is determined mainly by the amount of precipitable water, there is the possibility of determining the parameter Q from radiometric measurements of absorption τ_λ. Considering this low variation in T_λ/ρ_V with altitude, Eq. (3.4) can be written as follows:

$$\tau_{\lambda,Q} = \int_0^\infty \frac{T_\lambda(z)}{\rho_s(z)} \rho_s(z)\, dz = \overline{\Psi}_\lambda Q.$$

$$(3.10)$$

To calculate (3.10), use was made of the theorem of the mean and $\overline{\Psi}_\lambda$ is none other than T_λ/ρ_V at some point z. Strictly speaking, $\overline{\Psi}_\lambda$ is a functional, dependent on the distribution of temperature and moisture content in the atmosphere, and also on the wavelength of the radiation. However, detailed calculations /10/ showed that we can select a wavelength λ such that the coefficients Ψ_λ change little (by not more than 5 percent) within the limits of a very extensive region and are stable with respect to changes in meteorological conditions. Thus, for example, for $\lambda = 1.3$ cm, $\overline{\Psi}_\lambda = 0.24$ db·cm^2·g^{-1} for the content and $\overline{\Psi}_\lambda = 0.27$ db·cm^2·g^{-1} for the ocean.

Determinations of Q were made based on measurements of τ_λ /11-14/ over land and over sea. Here τ_λ was determined by scanning emission by angles. This technique /20/ makes it possible to avoid measuring absolute values of brightness temperatures, but
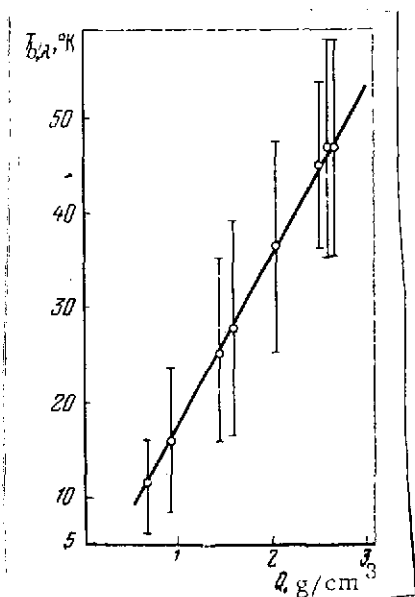
Fig. 3.10. Dependence of brightness temperature of atmosphere on water vapor integral Q
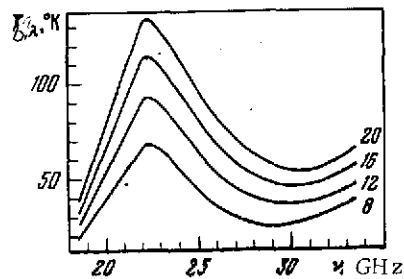Vertical lines are the root-mean-square deviations /19/

Fig. 3.11. Spectrum of brightness temperature of standard atmosphere for observation at local angle 30°
Numbers alongside curves are the values of the near-Earth moisture content $\rho_{v,o}$ in g/cm^3 /9_7

requires considerable time and relies on the assumption that the atmosphere is horizontally uniform. These measurements give the total optical depth of water vapor and oxygen, however the latter is small and can be considered on the basis of the standard atmospheric model in the interpretation of experimental data.

Fig. 3.12 is a correlation plot of the measurement of Q by radiometric and standard aerological methods /21/ in the area of the city of Gor'kiy. Measurements over a wide range of Q values agree well with each other. The technique of determining Q from absorption has found wide application in measurements onboard ships in the Atlantic Ocean /13, 14/.

Determinations of Q from measurements of $T_{b,\lambda}$ in the vicinity of λ = 1.35 cm from the Earth have also given results that are close to those obtained by radiosonde. Fig. 3.13. gives the results of calculations and measurements of brightness temperature $T_{b,\lambda}$ and of Q /15/, which also indicates good agreement of experimental and calculated data. In /15/ the following empirical

formula is suggested for the calculation of Q, g/cm^2 based on measurements of brightness temperature $T_{b,\lambda}$ °K:

$$Q = 0.056 \, T_{b,\lambda} - 0.16.$$

It should be noted that the coefficient 0.056 $g \cdot cm^{-2}/$° K agrees closely with the equivalent coefficient calculated in /19/ based on mean data: $(19.1°$ $K/g \cdot cm^{-2})^{-1} = 0.052$.

Determinations of Q from brightness temperature measurements and from measurements of the elevation gradient of brightness temperature /16/ also give results that agree satisfactorily /70 with aerological measurements.

In /16/, the problem of an objective measure of the value of the radiometric determination of Q is discussed, in relation to the fact that there is a correlation between the precipitable water Q and the near-Earth moisture content $\rho_{v,o}$. Measurements in /16/ during the summer over a period of a month in the central region of the European part of the Soviet Union showed that actually there is an extremely close relationship between Q and $\rho_{v,o}$ (Fig. 3.14). However, measurements over the Atlantic Ocean gave a much greater scatter in an analogous plot (Fig. 3.15). It is noted in /21/ that the coefficient of correlation between $\rho_{v,o}$ and Q can drop to 0.2. At the present time further investigations must be conducted to establish objective criteria for estimating the accuracy of ground radiometric data, which can appreciably increase the information on the content of water vapor in the atmosphere.

2-2) Outgoing emission in the neighborhood of the 1.35 cm resonance enables us to obtain reliable information on the moisture content in a cloud-free atmosphere over oceans. This becomes obvious when we analyze the equation for the outgoing emission for nadir observations $(\vartheta = 0)$:

$$T_{b,\lambda} = \varkappa_\lambda T_0 e^{-\tau_\lambda} + \int_0^\infty \gamma_\lambda(z) \, T(z) \exp\left\{ -\int_z^\infty \gamma_\lambda(z') \, dz' \right\} dz + $$

$$+ (1 - \varkappa_\lambda) e^{-\tau_\lambda} \int_0^\infty \gamma_\lambda(z) \, T(z) \exp\left\{ -\int_0^z \gamma_\lambda(z') \, dz' \right\} dz. \tag{3.11}$$

Fig. 3.16 presents the dependence of three terms of this equation on precipitable water /15/, and Fig. 3.17 gives the experimental dependence of $T_{b,\lambda}$ on precipitable water over a quiet sea /15/.

From these figures it is clear that the emission of the atmosphere and its reflection makes a marked contribution to the total radiation flux and has a near-linear dependence of $T_{b,\lambda}$ on Q for the standard atmospheric model. It should be stressed that an increase in the water vapor mass, generally colder than sea water, increases the outgoing emission. This is associated with the fact that sea water readily reflects and poorly emits in the microwave range[1].

Emission of continental cover examined in the preceding chapter is much more intense than emission from bodies of water and is marked by greater variegation. Therefore over continents the third term (reflected radiation) in Eq. (3.11) becomes small, and the isolation of the effect of the second term (atmospheric radiation) against the background of the first (emission of the surface attenuated by the atmosphere) is a complicated problem.
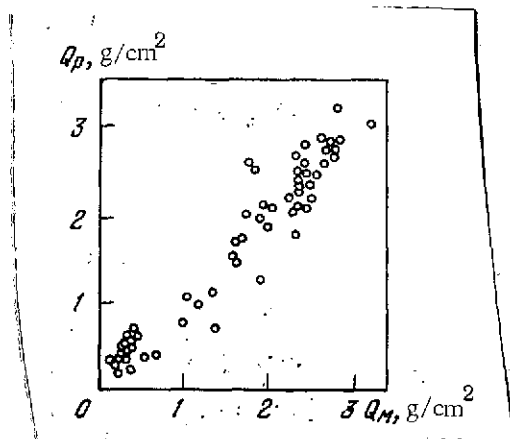
Fig. 3.12. Experimental data on the determination of Q by radiometric method from the Earth (Q_p) and by radiosonde (Q_M) /21/.
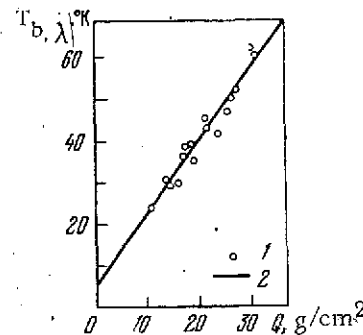
Fig. 3.13. Dependence of brightness temperature in the region of the 1.35 cm resonance on water vapor content.
1. Experimental data
2. Calculated data /15/

Fig. 3.18 presents the dependence of brightness temperature over oceans as a function of local latitude for observations at the nadir. The standard atmospheric model was used in calculating this curve. Variations of brightness temperature from polar to

[1] In the infrared band, where in contrast reflection from sea water is weak, an increase in absorption in the atmosphere reduces the outgoing emission.
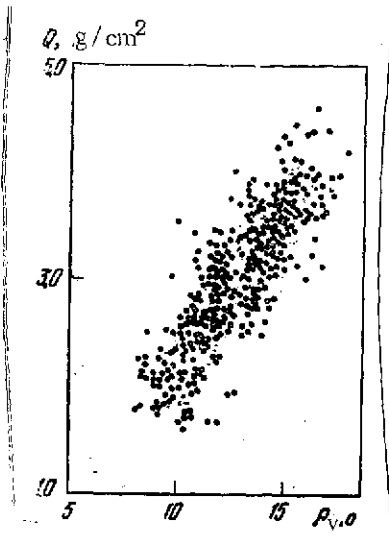
Fig. 3.14. Correlation between
Q and near-Earth moisture con-
tent $\rho_{v,o}$ over land /16/
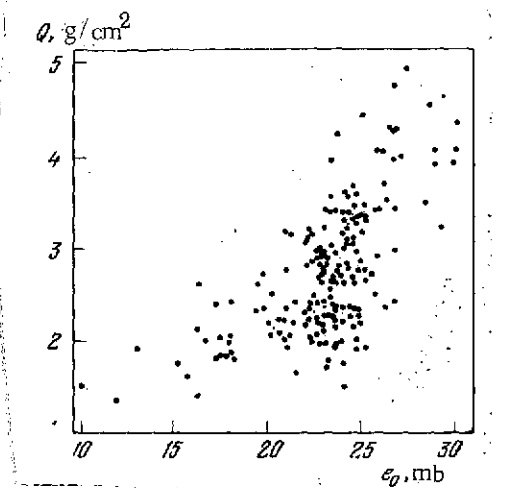
Fig. 3.15. Comparison of Q
with driven pressure of water
vapor e_o over ocean /14/
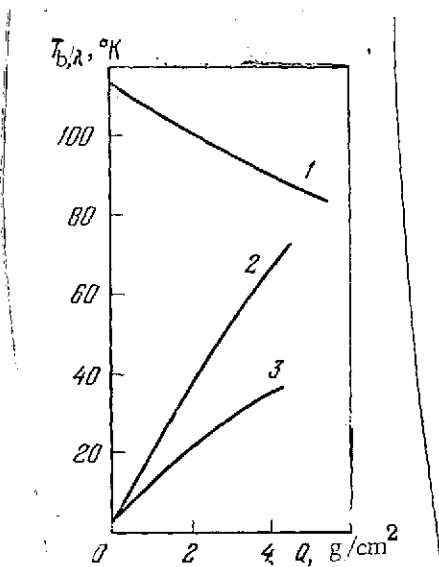
Fig. 3.16. Components of out-
going radiation in neighborhood
of 1.35 cm water vapor resonance
as a function of Q
1. Emission of water surface
   attenuated by atmosphere
2. Atmospheric radiation
3. Atmospheric radiation
   reflected from surface /15/
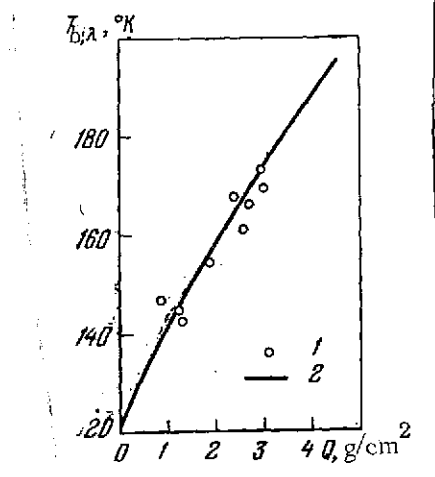
Fig. 3.17. Experimental
measurements (1) of radiation
in the water vapor resonance
from aircraft and calculated
data (2) /15/

Fig. 3.18. Estimate of contribution made by emission of water vapor dimers at wavelength $\lambda = 1.35$ cm as a function of geographical latitude
1. Calculation based on Eq. (3.1)
2. As above, considering dimers according to Eq. (3.2)
3. Calculation based on Eq. (3.1), but with one and a half times greater nonresonance term
4. As above, with reference to dimers according to Eq. (3.2) /22/
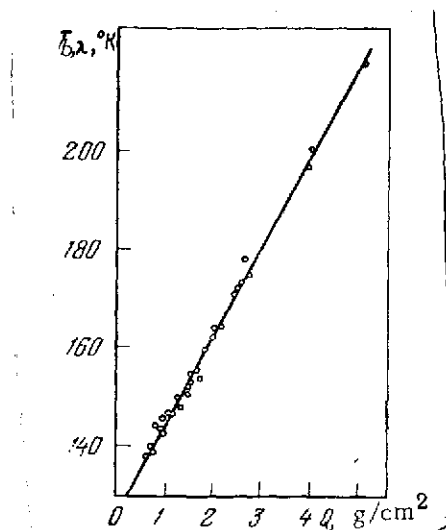
Fig. 3.19. Brightness temperature of outgoing radiation in neighborhood of 1.35 cm resonance as a function of Q (calculation based on radiosonde data)
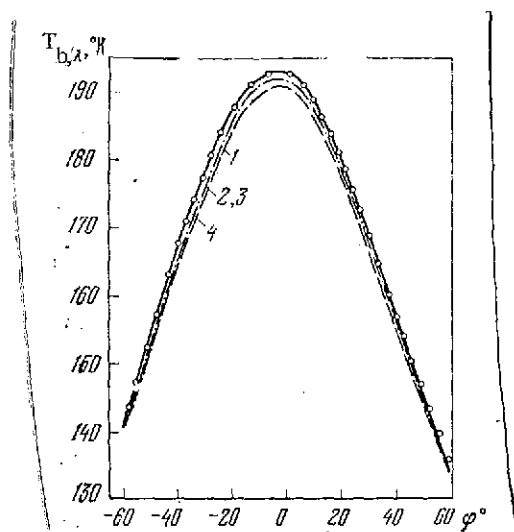Line is the regression line

equatorial latitudes at this wavelength (1.35 cm) are due to changes in the water vapor content. Also given in this figure are the data from the calculation of the effect of water vapor dimers on radiation in the neighborhood of the 1.35 cm resonance /22/. As can be seen from the data given in this figure, the addition of the dimer absorption is equivalent to a one and a half times increase in the nonresonance term that takes into account monomeric absorption of water vapor. Dimeric absorption has virtually no effect on the outgoing radiation over the entire globe.

In Fig. 3.19 is given the calculated dependence of the outgoing radiation at the wavelength $\lambda = 1.35$ cm on Q, obtained from actual soundings at different points of the globe over the ocean. This function, calculated for $\vartheta = 0$, is close to the straight line $T = 127 + 18$ Q and was used in interpreting the satellite measurements of Q described in Chapter Six.

3. Radiation in the "Window" Around $\lambda = 0.8$ cm and at the Wavelength $\lambda \geqslant 3$ cm

The "window" at around $\lambda = 0.8$ cm is located between the resonances of water vapor $\lambda = 1.35$ cm and molecular oxygen $\lambda = 0.5$ cm. Absorption in this window is equally determined by oxygen and water vapor. At the cutoff of the centimeter range, the atmosphere is quite transparent: the optical depth τ_λ varies from 0.06 in the polar regions with low water vapor content to 0.14 in the equatorial latitudes, where the content of precipitable water can rise to 5 g/cm^2.

Major interest in the investigation of radiation at $\lambda = 0.8$ cm is associated, in particular, with the fact that at the short-wave cutoff of the centimeter band there is a marked rise in absorption in clouds and a stronger dependence of the emission of the water surface on the presence of spume is noted. In addition, at the wavelength $\lambda = 0.8$ cm, at the present time fairly sensitive radiometers are available (see Chapter Five) and at short wavelengths for the same antenna sizes a higher spatial resolution can be achieved.
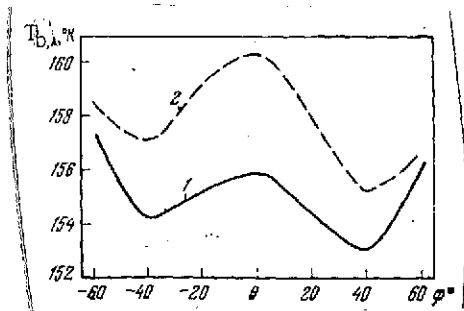
Fig. 3.20. EStimate of contribution made by dimers to radiation at wavelength $\lambda = 0.8$ cm as a function of geographical latitude /22/
1. Calculation based on Eq. (3.1)
2. As above, with reference to dimers based on Eq. (3.2)
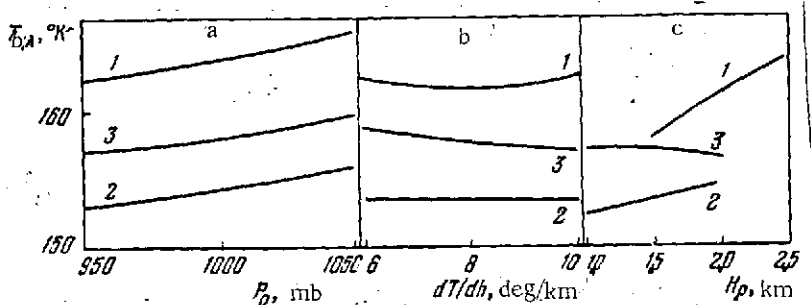
Fig. 3.21. Dependence of radiobrightness temperature of outgoing radiation at wavelength $\lambda = 0.8$ cm on near-Earth pressure P_0 (a), gradient of temperatures in troposphere dT/dh (b) and characteristic altitude of water vapor H_ρ (c)
1. Equatorial latitudes
2. For polar latitudes
3. For middle latitudes

Fig. 3.20 presents the calculated latitudinal dependence of
outgoing radiation at the wavelength $\lambda = 0.8$ cm /22/. From the
data in this figure it is clear that the latitudinal trend of
the radiation is weakly pronounced and comparable with the con-
tribution given by water vapor dimers.

Calculation of variations at the radiation at the wavelength
0.8 cm based on the technique presented in the previous section
shows that the root-mean-square deviations of the brightness
temperature of outgoing radiation over the ocean associated, when
the sky is free of clouds, with variations in the meteorological
parameters (mainly moisture content of air) is enclosed in the
limits 1.3° to 4.4° K, that is, much less than in the water vapor
resonance. In Fig. 3.21 are presented the results of model
calculations of variations in the brightness temperature of outgoing
radiation over the ocean when there is a change in the gradient
of temperatures in the troposphere, near-Earth pressure, and
characteristic altitudes of water vapor distribution. Of high
interest is the fact that the variations are small -- they do not
exceed several degrees. For this reason, radiometric measurements
at the wavelength 0.8 cm are quite free of atmospheric inter-
ferences in the diagnostics of clouds and precipitation (Chapter
Four), the condition of the sea surface when the sea state is
strongly agitated and spume is present (Chapter One), and also
the condition of continental cover (Chapter Two). In particular,
emission at the wavelength 0.8 cm also contains information on
the water vapor content and this information can be extracted
from the measurements. However, as will be shown in the next
section, in the diagnostics of water vapor it is more convenient
to use the region of water vapor resonance 1.35 cm in which
considerably greater sensitivity to water vapor is observed.

Synchronous measurements at the wavelengths 1.35 and 0.8 cm,
which as was shown in Chapter Six permit separate determination
of precipitable droplet water in clouds and the integral of water
vapor Q also give the possibility of reducing the error of the
determination of Q over a greatly agitated sea.

Absorption in a cloud-free atmosphere at wavelengths longer
than 3-5 cm is determined mainly by oxygen. In this range the
atmosphere is very transparent, its radiation is weak, and varia-
tions in radiation associated with changes in meteorological con-
ditions are tenths and hundredths of a degree. Therefore the
emission of the underlying surface in the long-wave portion of
the centimeter range is virtually undistorted by the atmosphere
and is determined mainly by the underlying surface.

4. Reconstruction of Temperature and Moisture Content Profiles in the Atmosphere

4-1) The presence of water vapor and oxygen resonances in the microwave range makes it possible to formulate the problem of determining the vertical profiles of temperature and water vapor content in the atmosphere. This problem is solved on the basis of general methods developed for the infrared band /23-26/. A specific feature of the microwave band is the possibility of resolving spectral lines and, accordingly, the kernels of the corresponding integral equations become narrower /23/, which increases the accuracy of the solution of the inverse problem -- -- reconstruction of profiles. In addition, interference by clouds in the microwave range is considerably less than in the infrared band, which is no small advantage for microwaves. Finally, in the reconstruction of the moisture content profile based on emission in the 1.35 cm resonance, there is no need to know exactly the distribution of temperatures, which simplifies the solution of the problem compared with the infrared band.

However, it would be incorrect to fail to note also specific disadvantages intrinsic to the microwave band in solving the problem of profile reconstruction. Above all they include a wavelength that is greater compared to the infrared band, which leads to the necessity of more carefully taking diffraction effects by receiving antennas into account. In addition, variations in the emissivity of the underlying surface and interference produced by precipitation limit the resolving capabilities of the microwave band.

4-2) The problems of determining the vertical distribution of atmospheric characteristics from the thermal radiation of the atmosphere in different spectral regions reduce, mathematically speaking, to solving Fredholm integral equations of the first kind. The difficulties in solving these problems, called inverse problems, are associated with the fact that they are improper in the classical sense, and until recent years there was no common approach to their solution. Only with the appearance of studies by A. N. Tikhonov /27/ and V. F. Turchin /28/, were two of the most general methods of the statistical regularization of improper problems outlined[2].

Reviews of studies on the solution of improper problems as applied to atmospheric sensing can be found in /23, 24/. We note that at the present time, essentially, all practical methods of

/76

---

[2] The methods suggested in /26, 29/ essentially coincides with the modifications /25, 30/ of the V. F. Turchin method.

74

solving inverse problems of atmospheric physics /17, 31-37/ are variants of the methods of statistical regularization based on work done by V. F. Turchin or Westwater and Strand.

In this section, we will give a brief review of studies on microwave sensing of the atmosphere, and in particular, reconstruction of moisture content and temperature profiles based on measurements of intrinsic atmospheric radio emission.

The emission and absorption of microwave radiation has been studied by numerous authors (see /1 7/), but only in the studies /7, 8, 38, 39/ were the capabilities of determining atmospheric characteristics from atmospheric microwave radiation examined for the first time. For example, in /7, 8/ a method is proposed for determining the water vapor content in the stratosphere based on ground measurements of atmospheric radiation at the frequency 22.235 GHz. In /38, 39/, an examination is made of the problem of the possibility of thermal sensing of the atmosphere in the molecular oxygen absorption band at 60 GHz, both from the Earth's surface as well as from various flight vehicles.

In /40/, a numerical experiment on reconstructing temperature profiles in the troposphere from ground measurements of atmospheric radiation in the wavelength range $\lambda = 0.55-0.60$ cm was presented, and the required accuracy of the measurements was indicated. In /33/, based on a numerical experiment, an analysis was made of the dependence of reconstruction errors on the size of measurement errors in sensing both from satellites as well as from the Earth's surface, and the method of selecting optimal sensing frequencies was proposed.

However, in spite of this theoretical "watershed" and the fact that in the microwave region of atmospheric radiation in principle sensing "through" clouds is possible, practical thermal location of the atmosphere began to develop only in recent years, after the appearance of narrow-band high-sensitivity radiometers.

An expression for the brightness temperature of the system underlying surface-atmosphere observed from a satellite at the nadir is of the form

$$T_{b,\lambda} = T_0(1 - R_\lambda)e^{-\tau_{0,\lambda}} + \int_P^{P_0} T(P)\gamma_\lambda(P)e^{-\tau_{0,\lambda}+\tau_\lambda(P)}dP +$$
$$+ R_\lambda e^{-\tau_{0,\lambda}} \int_P^{P_0} T(P)\gamma_\lambda(P)e^{-\tau_\lambda(P)}dP,$$

(3.12)

where T_o and R_λ are the temperature and coefficient of reflection of the underlying surface, respectively; $T(P)$ is the temperature profile; $\gamma_\lambda(P)$ is the coefficient of absorption of radiowaves, of wavelength λ, by atmospheric gases; and P_o is the pressure at the surface;

$$\tau_\lambda(P) = \int_P^{P_0} \gamma_\lambda(P')\,dP'; \qquad \tau_{0,\lambda} = \int_0^{P_0} \gamma_\lambda(P)\,dP.$$

We note that Eq. (3.12) is satisfied for the entire range of microwave radiation of the atmosphere given the condition that we have some ideal monochromatic receiver capable of receiving radiation at a single wavelength. A receiver with the 20–30 MHz band is close to the ideal if we limit ourselves to sensing all the way up to the altitudes $P = 5$–10 mb.

Since the coefficient of absorption $\gamma_\lambda(P)$ depends on the temperature profile $T(P)$ and moisture content profile $\hat{q}(P)$ of the atmosphere, $T_b(\lambda)$ is a function both of the characteristics of the underlying surface as well as the meteorological parameters of the atmosphere. Therefore an ideal experiment to determine atmospheric parameters of the atmosphere and the underlying surface must be an integrated experiment, making it possible from measurements of $T_{b,\lambda}$ in different sections of the emission spectrum to determine T_o, R_λ, $T(P)$, and $\hat{q}(P)$. However, since in this integrated formulation this experiment is thus far still difficult to carry out, at the present stage of progress in radiothermal location determining each of the unknown parameters of the atmosphere and the underlying surface on the assumption that the remaining parameters are known is of independent interest.

4-3) Let us examine the problem of finding the vertical distribution of moisture content in the atmosphere from measurements of atmospheric radiation in the neighborhood of the wavelength $\lambda = 1.35$ cm.

Absorption of dimeric molecules of water vapor and molecular oxygen doesonot have resonances near this wavelength. The resonance absorption line of monomeric molecules of water vapor $\lambda = 1.35$ cm is an isolated line. The half-width of this absorption line at sea level is ~ 2400 MHz, while the resolving capability of ordinary narrow-band radiometers is of the order of 10–20 MHz and smaller (Chapter Five). Given this ratio of receiver band and half-width of line, it can be assumed that a monochromatic reception of atmospheric radiation is realized.

It is shown in /34/ that in the neighborhood of the resonance line $\lambda = 1.35$ cm, variations in brightness temperatures caused by the redistribution of vapor in the atmosphere, for a fixed integrated moisture content, are so large that they can be used in determining the moisture content profile in the atmosphere.

Thus, assuming that for several λ near $\lambda = 1.35$ cm we know the parameters of the underlying surface T_o, R_λ, and the vertical profile of atmospheric temperature $T(P)$, from (3.12) we can determine the moisture content profile $\hat{q}$ (P).

Based on a familiar technique /41/, after substituting in (3.12) the sum of the corresponding mean-climatic profile $\bar{q}$ (P) and the deviations from it $\delta\hat{q}$ (P), instead of the profile $\hat{q}$ (P),

$$\hat{q}(P) = \bar{q}(P) + \delta\hat{q}(P)$$

(3.13)

and isolating the emission spectrum $\overline{T}_{b,\lambda}$ corresponding to the mean-climatic profile $\bar{q}$ (P), Eq. (3.12) can be linearized and reduced to the Fredholm integral equation of the first kind:

$$f(\lambda) = \int_{P_0}^{0} \mathscr{K}(\lambda, P)\,\psi(P)\,dP.$$

(3.14)

Here $f(\lambda) = T_{b,\lambda} - \overline{T}_{b,\lambda}$, $\psi = \delta\hat{q}(P)$. Eq. (3.14) is improper, since small errors in determination of $f(\lambda)$ can lead to as widely differing functions of $\psi(P)$ as the solutions to Eq. (3.14). And since the function $f(\lambda)$ owing to the presence of measurement and recording errors cannot be known precisely, the direct determination of $\psi(P)$ from (3.14) leads to results that are physically meaningless. To solve Eq. (3.14) we must introduce some additional information on the behavior of the unknown function $\psi(P)$ in order to leave among the possible solutions of Eq. (3.14) only those that are physically meaningful.

Referring readers interested in the details of the method to the studies /24, 28/, we present, on the example of the solution of Eq. (3.14), the essentials of the technique of statistical regularization using as the apriori information about the solution we seek the autocorrelation moisture content matrix.

First, we reduce Eq. (3.14) to a system of linear algebraic equations

$$f(\lambda_j) = \sum_{k=1}^{n} \mathscr{K}(\lambda_j, P_k)\,\psi(P_k), \qquad j = 1, \ldots, M,$$

(3.15)

where M is the number of wavelengths at which the measurements are taken, and n is the number of quadrature points in the computation of integral (3.14). Eq. (3.15) can be written in matrical form

$$f = \mathcal{H}\psi,$$

where f, $\mathcal{H}$ and ψ are matrices of size (M x 1), (M x n), and (n x 1), respectively. Since the vector f includes errors of measurement and recording, this equation is, strictly speaking, approximate.

We will assume that the measurement errors at different wavelengths are distributed according to the normal law, with zero mathematical expectation, are independent, and that we know the dispersions σ_i^2 of these errors. Then instead of Eq. (3.14), we can write the distribution function of the vectors f that can be obtained in the course of measurements at the specified vector ψ:

$$F(f/\psi) = C_1 \exp\left[-\frac{1}{2}(\psi^* \mathcal{H}^* w \mathcal{H} \psi) + \mathcal{H}^* w f \psi\right],$$

(3.16)

where w is the error matrix with the following elements

$$w_{i,j} = -\frac{1}{\sigma^2}\delta_{ij}; \quad \delta_{ij} = \begin{cases} 0 & \text{for } i \neq j, \\ 1 & \text{for } i = j. \end{cases}$$

The sign (*) denotes transposition of the matrix.

Let us assume a priori that the desired deviations of $\psi(P)$ of moisture content profiles from the mean-climatic profile $\bar{q}(P)$ are distributed according to the normal law with the matrix of second moments B coincident with the outer correlation moisture content matrix $B_{\hat{q}\hat{q}}$ plotted according to previously accumulated data from aerological sounding of the atmosphere. Then the a priori distribution of the profiles $\psi(P)$ will be of the following form:

$$F(\psi) = C_2 \exp\left\{-\frac{1}{2}(\psi^* B^{-1}\psi)\right\}.$$

(3.17)

And, finally, from distributions (3.16) and (3.17), based on the Bayes theorem, we get the aposteriori distribution of vectors ψ satisfying Eq. (3.14) for a known vector f:

$$F(\psi/f) = C_3 \exp\left\{-\frac{1}{2}\psi^*[\mathcal{H}^* w \mathcal{H} + B^{-1}]\psi + \mathcal{H}^* w f \psi\right\}.$$

(3.18)

The vector

$$\dot{\psi} = [\mathcal{H}^* w \mathcal{H} + B^{-1}]^{-1} \mathcal{H}^* wf,$$

(3.19)

being the mathematical expectation of the distribution of (3.18), is taken as the desired solution of Eq. (3.14). The diagonal elements of the matrix $[\mathcal{H}^* w \mathcal{H} + B^{-1}]$, being dispersions of the distributions (3.18) at the corresponding levels, will serve as a measure of the reconstruction errors.

In /34/, the possibility of reconstructing moisture content profiles from satellite measurements of atmospheric radiation in the vicinity of λ = 1.35 cm is verified by numerical experiment.

For the case of measurements from the Earth's surface of incoming atmospheric radiation, in Eq. (3.12) there remains only the second term and the expression for the brightness temperature /80 becomes

$$T_{b,\lambda} = \int_P^{P_0} T(P)\gamma_\lambda(P) e^{-\tau_{0,\lambda} + \tau_\lambda(P)} dP.$$

(3.12')

However, the method of solving Eq. (3.12') remains the same as for Eq. (3.12).

In /32/, based on actual ground measurements of atmospheric radiation, moisture content profiles in continental and oceanic conditions were reconstructed.

Examples of the reconstruction of moisture content profiles taken from /32, 34/ are shown in Figs. 3.22 and 3.23. Reconstruction errors for the levels P > 800 mb are 10-15 percent, while for the levels 500 < P < 800 mb, the reconstruction errors reach 40 percent, and for the levels P ⩽ 500 mb, where the actual moisture content values are low, the reconstruction errors can be 100 percent.

However, with all the common ground of the solution to problems of reconstructing moisture content profiles based on ground and on satellite measurements of atmospheric radio emission, there is a difference between them, namely that in ground measurements the value of the unknown function at the location of the receiving equipment can be measured directly and then used as additional apriori information in reconstructing the moisture content profile. Formulated this way, the problem was solved in /17/ for the case of measurements taken from Earth in continental and oceanic conditions. As we can see from Figs. 3.24 and 3.25, introducing the additional information improves the reconstruction of the
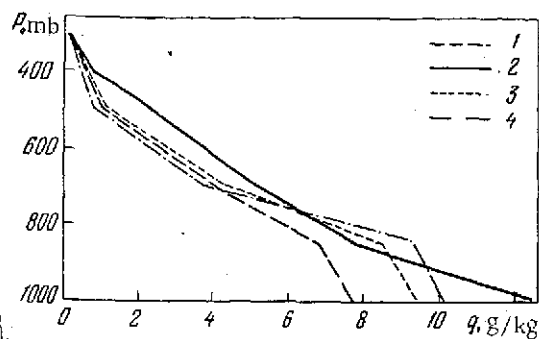
Fig. 3.22. Example of reconstruction of moisture content profiles from satellite measurements of spectrum in the region of the 1.35 cm resonance (numerical experiment)
1. Mean-climate
2. True profile
3. Its reconstruction based on "measurements" at three wavelengths
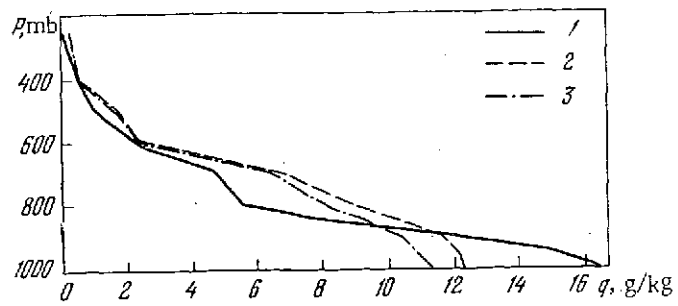4. As above, based on "measurements" at 31 wavelengths /34/

Fig. 3.23. Example of reconstruction of moisture content profiles from shipboard measurements of absorption spectrum in atmosphere in the 1.35 cm resonance region
1. Radiosonde measurements
2. Reconstruction based on open scheme
3. Reconstruction based on closed scheme /32/
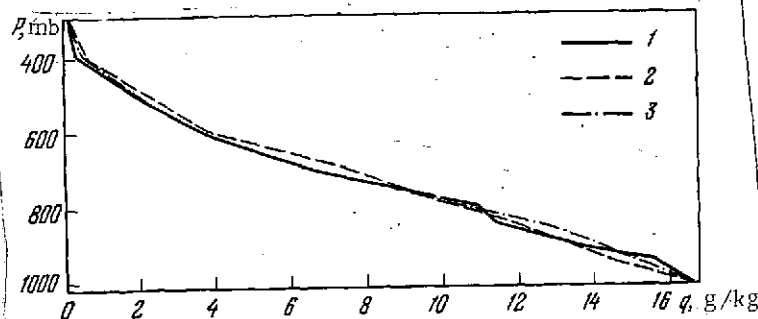
Fig. 3.24. Example of reconstruction of moisture content profile based on shipboard measurements of absorption spectrum in region of 1.35 cm resonance, taking driven moisture content into account.
1. Radiosonde measurements
2. Reconstruction based on open scheme
3. Reconstruction based on closed scheme /17/

moisture content profiles in the near-Earth layer. There is a marked improvement in the reconstruction of the moisture content profiles with large moisture content gradients in the near-Earth layer. It was possible to reconstruct also the inversion of moisture content in the near-Earth layer. As a whole, the reconstruction errors in the atmospheric layers from 1000 to 800 mb as a rule do not exceed 10 percent.

However, it was not /81 possible to reconstruct the inversions in the atmospheric layers when $P \approx 600-800$ mb, The point is that given the smoothness of the kernels $\mathscr{K}(\lambda, P)$ of Eq. (3.14) that

are realized in this wavelength range, the inversion similar to the one shown in Fig. 3.26 makes a minor contribution to brightness temperature values.

Summarizing studies on the reconstruction of moisture content profiles from radiometric measurements of atmospheric radiation, it should be remembered that in all the above-cited studies, in reconstructing the moisture content profiles measurements taken in cloud-free weather were used and, moreover, it was assumed that the temperature profile T (P) was known.

Some estimates show that the replacement of the actual temperature profile by the mean-climatic profile in the reconstruction of the moisture content profile does not lead to appreciable errors.
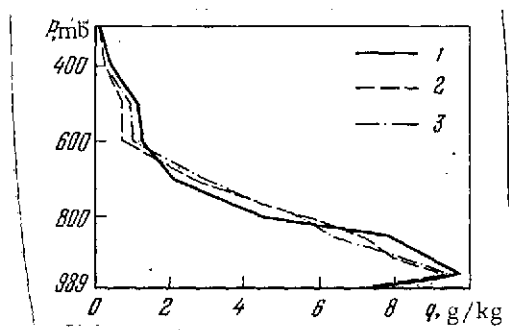
Fig. 3.25. Example of reconstruction of moisture content profile with ground inversion based on ground measurements of absorption spectrum in the vicinity of 1.35 cm resonance, with ground moisture content taken into account. The symbols are the same as in Fig. Fig. 3.24 /177/
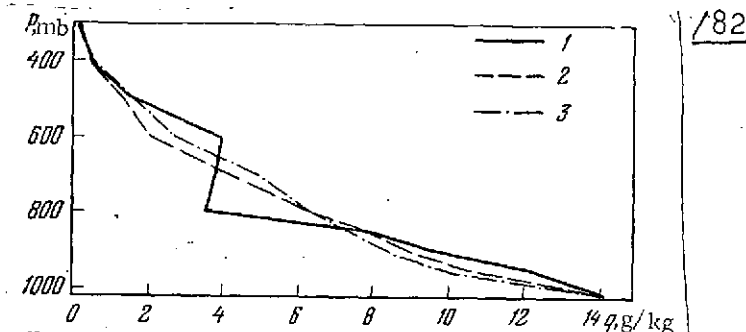
Fig. 3.26. Example of reconstruction of moisture content profile with altitude inversion Symbols are the same as in Fig. 3.24.

4-4) Formulation and solution of the problem of reconstructing the vertical temperature profile from microwave radiation of the atmosphere in the oxygen absorption band λ| = 0.5 cm in principle are entirely analogous to the formulation and methods of solving the above-considered problem of reconstructing the moisture content profile.

In the oxygen band absorption by water vapor is small and taking it into account from mean-climatic data is sufficient for
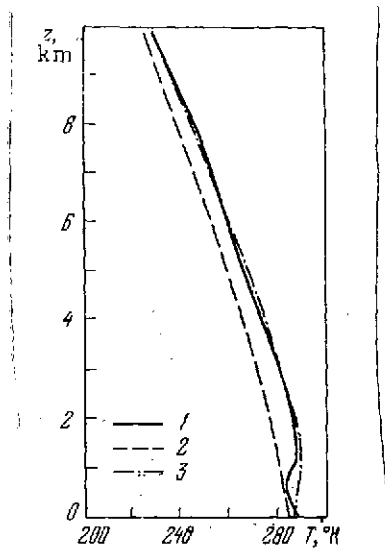
Fig. 3.27. Reconstruction of temperature profiles in troposphere for oxygen emission in three wavelengths
1. Radiosonde measurements
2. Mean-climatic profile
3. Reconstruction based on microwave radiation /37/
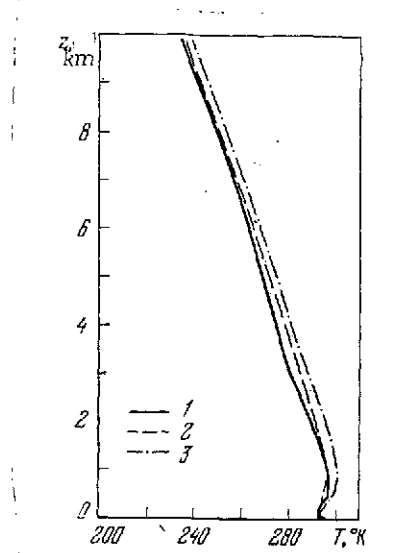
Fig. 3.28. Reconstruction of temperature profile in troposphere based on the measurements at five frequencies in the band λ = 0.5 cm
Symbols are the same as in Fig. 3.27 /37/

the first step. Further refinement can be based on determination of Q from measurements of radiation near the λ = 1.35 cm resonance.

Leaving outside our consideration the problem of the applicability of Eqs. (3.12) and (3.12') for actual receivers and assuming that there is an ideal monochromatic receiver available we can investigate the problem of the information content of the microwave radiation of the atmosphere in the oxygen band, the possibility of reconstructing temperature profiles from several values of $T_{b,\lambda}$ measured in this band, and the required accuracy of these measurement.

In part, these investigations were conducted in the above-studies already cited /33, 39, 40/.

We note that the reconstruction of the temperature profiles is carried out either from $T_{b,\lambda}$ the values measured at several wavelengths in this band for a fixed angle of observation, or /83 from $T_{b,\lambda}$ values measured at a single wavelength, but at different zenith angles of the axis of the receiving antenna, that is, at different angles of observation. Reconstructions of the temperature

profiles based on actual measurements of radiobrightness temperature of the atmosphere in the oxygen bands were carried out in /37/. In reconstructing the temperature profile, in this study use was made of ground measurements (at the zenith) of the microwave incoming radiation of the atmosphere in the 5-6 mm band. The accuracy of the measurements was 1-2° K. The measurements were taken at the station Oakland in the state of California in December 1967 and in August 1968. Simultaneously with the measurement of radiation, a meteorological sounding was carried out. The temperature profiles were reconstructed up to the altitude of 10 km based on $T_{b,\lambda|}$ data known for three to five wavelengths. The root-mean-square error of reconstruction was 2-5° K. Examples of true, reconstructed, and the corresponding mean-monthly profiles are given in Figs. 3.27 and 3.28. From these figures it is clear that the reconstructed profiles overall better reflect the trend of the true temperature profile than the corresponding mean-climatic profile.

The problem of reconstructing profiles based on microwave /84 radiation examined in subsections 4-3) and 4-4) of this section is far from its final solution. Further investigations on selecting optimal wavelengths and parameters of the measuring equipment are needed. We note that the high spectral resolution of the receiving microwave equipment, as well as the strong dependence of absorption in water vapor and oxygen on the profile of meteorological parameters make it possible to set up the problem of the integrated reconstruction of vertical profiles of temperature and moisture content through the simultaneous use of both faint ($\lambda| = 1.35$ cm) as well as intense ($\lambda| = 0.164$ cm, 0.25 cm, and 0.5 cm) resonances for altitudes up to 85-95 km.

4-5) Reconstruction of the parameters of the upper atmospheric layers has been examined in /42/. Analysis of the emission spectrum of oxygen showed that frequencies can be selected at which, when the atmosphere is being observed from the satellite "against the light" in the horizontal direction, the brightness temperature of radiation does not depend on the air temperature (in the possible range of its variations, of course) and is proportional to the density of the altitude corresponding to the "target" distance. Calculations given in /42/ showed that measurements of density by this technique can be carried out at altitudes from 30 to 60 km.

A method conceptually close to this technique, for determining moisture content profiles, was examined in /43/.

4-6) Advances made in the practical mastery of the submillimeter range of electromagnetic waves (see /1.7/) together with the progress made in space technology have stirred heightened interest in submillimeter radiometeorology. At the present stage, it appears useful to investigate the fundamental possibilities of radiometeorological measurements in this new wavelength band /44/.

First of all it should be noted that regular meteorological investigation from the Earth's surface in the submillimeter range are considerably hampered owing to the great optical depths /thicknesses/ of the Earth's atmosphere /45/. Therefore investigations of the atmosphere in submillimeter waves from topside (in particular, from satellites) are optimal.

The optical depth of the cloud-free atmosphere over sufficiently broad intervals of submillimeter radiowaves is determined by the rotational spectrum of water vapor. In the submillimeter band of radiowaves, we find also the resonance frequencies of such dipolar gases as CO, N_2O, NO, and NO_2, and so on. There

are particularly numerous rotational lines of ozone in the submillimeter wavelength band /46/. The concentration of these gaseous admixtures in the atmosphere is usually low ($\sim 10^{-7} - 10^{-4}$ percent). But given the adequate concentration of the corresponding constituents, the optical depth of the atmosphere in the resonance regions of the absorption can be determined by the contribution of the gases listed above, which in turn serves as a basis for /85 investigating their content by the techniques of submillimeter radiometeorology. However, the effect of these gases on the optical depth of the atmosphere is appreciably reduced outside the corresponding resonances and is negligibly small in the region of intense rotational resonances of water vapor absorption. Thus, one of the possible applications of submillimeter radiometeorology lies in investigating the moisture content of the atmosphere.

In /44/, calculations were presented concerning the optical depth of the cloud-free atmosphere caused by molecular absorption of water vapor, in the resonance regions of four intense absorption lines of monomeric molecules H_2O (see Fig. 2 in /1_7/): $2_{-2}-2_0$ ($1/\lambda_{ij} = 25.11$ cm^{-1}), $1_{-1}-1_1$ ($1/\lambda_{ij} = 18.58$ cm^{-1}), 3_1-4_{-3} ($1/\lambda_{ij} = 12.67$ cm^{-1}), and 4_0-5_{-4} ($1/\lambda_{ij} = 10.86$ cm^{-1}). In the calculations of the atmospheric

optical depth, use was made of the quantum-mechanical formula (6) in /1_7/ for the absorption coefficient of monomeric H_2O molecules. The contour of the spectral line described by Eq. (6) is caused by the molecular collisions, and Eq. (6), of course, is valid only at the altitudes at which the broadening of the spectral lines H_2O is determined by the appropriate collisions. Therefore, at greater altitudes (up to $z \cong 80$ km) an approximate correction for the effect of the Doppler broadening, after /8_7/, is introduced into the working formula.

The results of calculating the levels of the departure of outgoing thermal radiation H_λ determined by the condition

$$\int_{H_\lambda}^{H_{max}} \gamma_\lambda \, dz = 1$$

(where $\gamma|_\lambda|$ is the absorption coefficient at the wavelength $\lambda|$, H_{max} is the provisional upper atmospheric cutoff) obtained from the slopes of the corresponding absorption lines for a summer standard model (60° N)[3] are given in Table 6. In the actual resonance lines, the departure levels rise to very large values. The fact that the emission departure levels change markedly over the contour of the atmospheric absorption lines is the natural prerequisite for the possibilities of obtaining meteorological information in the corresponding spectral regions. This is further indicated by the changes in the brightness temperatures of the atmosphere as as function of wavelength (they are $\sim 30°$ K based on the contour /86 of the line for these atmospheric models) and the altitude changes in the weighting functions of the absorption coefficients $\Psi_\lambda|$.
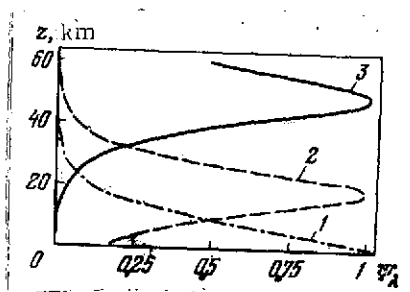
Fig. 3.29. Maximum-normalized weighting functions in the neighborhood of the resonance $4_o - 5_{-4}$ (10.86 cm^{-1}) for submillimeter waves
1. $\lambda|$ = 0.95 mm
2. $\lambda|$ = 0.92 mm
3. $\lambda|$ = 0.9208 mm /44/
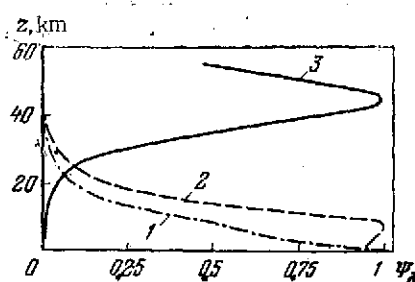
Fig. 3.30. Maximum-normalized weighting functions in the neighborhood of the resonance $1_{-1} - 1_{11}$ (18.58 cm^{-1})
1. $\lambda|$ = 0.52 mm
2. $\lambda|$ = 0.535 mm
3. $\lambda|$ = 0.5382 mm /44/

---

[3] In the calculations, the atmospheric models were supplemented by specifying the vertical distribution of moisture content up to the altitude $z = 80$ km, $\hat{q}(z) = \tilde{\hat{q}}_o e^{-a_o z}$ for $0 \leqslant z \leqslant 16$ km and $\hat{q}(z) =$ = const at altitudes 16 km $< z < 80$ km ("dry" stratosphere), or $\hat{q}(z) = \hat{q}_1 e^{-a_1(z-16)}$ for 16 km $< z < 30$ km ("moist" stratosphere), followed by the rapid reduction in the specific moisture content down to the values of q corresponding to the "dry" model ($\hat{q}_o =$ = $9.4 \cdot 10^{-3}$ g/g in summer, and $1.5 \cdot 10^{-3}$ g/g in winter, $\alpha_o = 0.48$ km^{-1}, and $\alpha_1 = 0.24$ km^{-1}).

TABLE 6. CALCULATED VALUES OF DEPARTURE LEVELS OF TERRESTRIAL ATMOSPHERIC RADIATION NEAR THE WATER VAPOR RESONANCES IN THE SUBMILLIMETER WAVE BAND

λ, mm	H_λ, km	λ, mm	H_λ, km	λ, mm	H_λ, km	λ, mm	H_λ, km
0,38	6,5	0,52	8,8	0,75	3,4	0,90	2,6
0,39	8,7	0,53	10,2	0,77	4,6	0,91	3,6
0,40	12,8	0,54	15,8	0,79	11,5	0,92	6,8
0,41	7,8	0,55	10,0	0,81	4,4	0,93	4,0
0,42	6,2	0,56	8,4	0,83	2,9	0,94	2,6

Figs. 3.29 and 3.30 present the corresponding weighting functions ψ_λ, each of which is normalized for 1, for the two quantum transitions of H_2O: $4_0 - 5_{-4}$ and $1_{-1} - 1_1$.

In the submillimeter wavelength band, the brightness temperatures can be calculated based on the formula that is the customary one for the centimeter and millimeter bands, for the Rayleigh-Jeans approximation $2\pi h \, c_0 \, \lambda|^{-1} \ll kT$ (h and k are the Planck and Boltzmann constants, respectively, and c_0 is the speed of light) is satisfied in the terrestrial conditions at wavelength $\lambda| \gtrsim 0.36$ mm. Broadening of the spectral water vapor lines is determined in the terrestrial atmosphere by molecular collisions in the submillimeter wavelength band to the altitude $z \cong 55\text{-}60$ km. Thus, for the line $4_0 - 5_{-4}$ ($1/\lambda|_{ij} = 10.86$ cm^{-1}), the ratio of the half-width of the /87 line caused by collisions to the Doppler half-width $\Delta\nu_{st}/\Delta\nu_d = 2.5$ at the altitude $z = 60$ km. For the line $1_{-1} - 1_1$ ($1/\lambda|_{ij} = 18.58$ cm^{-1}) a similar relation obtains at the altitude $z = 55$ km. In the resonance of the $4_0 - 5_{-4}$ line, the contribution made by the atmospheric layers $z = 60\text{-}80$ km to the optical depth is ~ 0.1. For the resonance of the line $1_{-1} - 1_{\pm 1}$ the level of the radiation departure in summer is about 60 km, while in the winter conditions it drops to 48 km. The optical depth of the atmospheric layers from 55 to 80 km is of the order of $\tau \sim 0.2$. The relative contribution to the optical thickness of the atmosphere made by layers at which the Doppler line broadening is substantial decreases rapidly with increase in separation from the resonance and when mistunings $\delta_\lambda| \gtrsim 0.002$ mm are present does not exceed even fractions of a percent.

These results are applicable for the analysis of possible measurements of submillimeter radiation with narrow-band receivers (with band not more than 1-2 MHz). When the resolving capability of the equipment is poorer, one must reckon with averaging of the effects of the entire receiving band. Modern submillimeter receivers at the sensitivity of $\sim 1-2^\circ$ K thus far have very broad bands (several hundreds of megahertz). However, compared with the longer-wave bands, the submillimeter band has the advantage for radiometeorological studies in that it can yield information on the higher atmospheric layers (see the values of the radiation departure levels in Table 6). These factors evidently must simulate developments in submillimeter radio-meteorology.

REFERENCES

1. Zhevakin, S. A., and Naumov, A. P., Izv. vyssh. ucheb. zav. Radiofizika 10/9-10, 1213 (1967).

2. Tablitsa standartnoy atmosfery. GOST 4401-64 /Table of Standard Atmosphere, State Standard 4401-64/.

3. Demin, V. V., Izv. Vyssh. ucheb. zav., Radiofizika 12/4, 512 (1969).

4. Lenoir, W. B., J. of Geophys. Res. Space Physics 73/1, 361 (1968).

5. Voronov, V. N., Kuslyakov, A. G., Kukina, E. P., and Naumov, A. P., Izv. ANsSSR, seriya FAO 8/1, 29 (1972).

6. Basharinov, A. Ye., Yegorov, S. T., Kolosov, M. A., and Kutuza, B. T., Trudy GGO, 222, 153 (1968).

7. Barret, A. H., and Chang. V. K., J. of Geophys. Res. 67/11 (1962).

8. Croom, D. L., J. of Atm. and Terr. Phys. 27, 217 (1965).

9. Toong, H. D., and Staelin, D. H., J. of Atm. Sci. 27/5, 781 (1970).

10. Naumov, A. P., Izv. AN SSSR, seriya FAO 4/2, 170 (1968).

11. Plechkov, V. M., Izv. AN SSSR, seriya FAO 5/9, 85 (1969).

12. Naumov, A. P., and Plechkov, V. M., Izv. AN SSSR, seriya FAO 7/3, 352 (1971).

13. Plechkov, V. M., Gurvich, A. S., and Snopkov, V. G., Dokl. AN SSSR 193/5, 1041 (1970).

14. Plechkov, V. M., Romanov, Yu. A., and Snopkov, V. G., Dokl. AN SSSR 200/5, 1081 (1971).

15. Rabinovich, Yu. I., and Shchukin, G. G., Trudy GGO, 222, 62 /88 (1968).

16. Gorelik, A. G., Kalashnikov, V. V., and Frolov, Yu. A., Trudy TsAO /Transactions of the Central Aerological Observatoory/, 103, 5 (1972).

17. Yershov, A. T., Naumov, A. P., and Plechkov, V. M., _Izv. vyssh. ucheb. zav., Radiofizika_ 15/4, 5]0 (1972).

18. Popov, S. M., _Izv. AN SSSR, seriya FAO_ 1/1, 18 (1965).

19. Gurvich, A. S., and Time, N. S., _Izv. AN SSSR, seriya FAO_ 2/8, 814 (1966).

20. Kislyakov, A. G., _Radiotekhnika i elektronika_ 13/7, 1161 (1968).

21. Gurvich, A. S., Yershov, A. T., Naumov, A. P., and Plechkov, V. M., _Meteorologiya i gidrologiya_, 5, 22 (1972).

22. Demin, V. V., Zhevakin, S. A., and Naumov, A. P., _Izv. AN SSSR, seriya FAO_ 7/2, 145 (1971).

23. Kondrat'yev, K. Ya., and Timofeyev, Yu. M., _Termicheskoye zondirovaniye atmosfery so sputnikov_ /Thermal Sensing of the Atmosphere From Satellites/, Leningrad, Gidrometeoizdat, 1970.

24. Turchin, V. F., Kozlov, V. P., and Malkevich, M. S., _UFN_ 102/3, 345 (1970).

25. Turchin, V. F., Malkevich, M. S., and Gorchakova, I. G., _Izv. AN SSSR, seriya FAO_ 5/449 (1969).

26. Strand, O. N., and Westwater, E. R., _J. Assoc. Comp. Mach._, 15/1, 100 (1968).

27. Tikhonov, A. N., _Dokl. AN SSSR_ 153/1, 49 (1963).

28. Turchin, V. F., _ZhVMMF_ 7/6, 1270 (1967).

29. Strand, O. N., and Westwater, E. R., _J. Assoc. Comp. Mach._ 15/1, 100 (1968).

30. Turchin, V. F., and Nozik, V. Z., _Izv. AN SSSR, seriya FAO_ 5/1, 29 (1969).

31. Gorchakova, I. A., Malkevich, M. S., and Turchin, V. F., _Izv. AN SSSR, seriya FAO_ 6/6, 565 (1970).

32. Gorchakova, I. A., Malkevich, M. S., Naumov, A. P., and Plechkov, V. M., ibid., 7, 731 (1971).

33. Westwater, E. R., and Strand, O. N., _J. of Atm. Sci._ 25/9, (1968).

34. Gorchakova, I. A., Demin, V. V., and Yershov, A. T., _Izv. AN SSR, seriya FAO_ 7/8, 841 (1971).

35. Pakhomov, L. A., Timofeyev, Yu. M., Shklyarevskiy, V. G., and Pokrovskiy, O. M., _Meteorologiya i gidrologiya_, 12, 25 (1971).

36. Pokrovskiy, O. M., and Timofeyev, Yu. M., _Meteorologiya i gidrologiya_, 1, (1972).

37. Miner, G. T., Thornton, D. D., and Welch, W. J., _J. of Geophys. Res. Oceans and Atm._ 77/6, 975 (1972).

38. Meeks, M. L., _J. of Geophys. Res._ 66, 3749 (1966).

39. Meeks, M. L., and Lilley, A. E., ibid., 68/6, 1683 (1963).

40. Westwater, E. R., _J. Res. NBS_ 69 D, 1201 (1965).

41. Malkevich, M. S., and Tatarskiy, V. I., _Kosmicheskiye issledovaniya_ 3/3, 444 (1965).

42. Gurvich, A. S., _Izv. AN SSSR, seriya FAO_ 5/10, 985 (1969).

43. Gurvich, A. S., ibid., 7/10, 1023 (1971).

44. Gurvich, A. S., and Naumov, A. P., ibid., 8/5, 543 (1972).

45. Zhevakin, S. A., and Naumov, A. P., _Izv. vyssh. ucheb. zav., Radiofizika_ 8/6, 1100 (1965).

46. Gora, E. K., _J. Molec. Spectroscopy_ 3/1, 78 (1959).

MICROWAVE RADIATION OF CLOUDY ATMOSPHERE

1. Characteristics of Atmospheric Cloud Cover and Precipitation

1-1) In a cloudy atmosphere various states are possible, differing in the phase structure of clouds, altitude and thickness of cloud strata, precipitation, and other features. Microwave absorption and emission spectra arising during the transport of radiation in cloud formations depend on the phase structure of clouds, their temperature, and their spatial configuration.

In terms of phase structure, a distinction is made between droplet, ice-crystal, and mixed clouds. Stratus droplet (St) and stratocumulus droplet (Sc) clouds are formed at altitudes to 10 km and differ in their bulk content of water (moisture content), vertical size (thickness), droplet microstructure, and temperature /1, 2/. Depending on the kind of formation, the moisture content of droplet clouds is 0.1-0.5 g/m³, but in rare cases can be as high as 5 g/m³. The thickness of droplet clouds varies from hundreds of meters to several kilometers (the thickness of nimbostratus and cumulonimbus clouds can be 5-7 km). The microstructure of droplet clouds is determined by droplet size distribution. Droplet size distribution as a function of cloud layer altitude has a maximum in the 5-20 μm range and covers the range 1-40 μm. Droplet shape is near-spherical.

The temperature of droplet clouds occupies the range 0+30° to -40° C, depending on altitude and conditions of formation. Clouds made of ice crystals are formed at below-zero temperatures at altitudes to 20 km. The moisture content of ice-crystal clouds (Ci, Cs) does not exceed 0.1 g/m³. A combination of droplet and ice-crystal states is possible in nimbostratus (Nb), altostratus (As), and altocumulus (Ac) clouds.

1-2) Droplet precipitation (rain) and solid-phase precipitation (hail and snow) differ in phase structure. In droplet precipitation droplet sizes are in the range 0.05-6 mm. Droplet shape is a flattened spheroid and, to the first approximation, can be assumed to be spherical.

Rain intensity is characterized by the column of water falling on per unit area per unit time:

$$I \text{ (mm/hr)} = 15.1 \int_0^{a_{max}} N(a)v(a)a^3 da,$$ (4.1)

where a is droplet radius in mm; $N(a)$ is the number of droplets with radius a per unit volume $(1/m^4)$; and v_a is the droplet fall velocity in m/sec.

The intensity of weak drizzling rain is not higher than 1 mm/hr; moderate rain has an intensity of 1-20 mm/hr, while heavy showers have an intensity of 40-60 mm/hr. As a rule, droplet sizes increase with rain intensity.

Several kinds of approximation functions characterizing droplet size distribution in rainfall are used.

By the Marshall-Palmer distribution /3_7:

$$N(a) = N_0 e^{-xa},$$ (4.2)

where $N_0 = 8 \cdot 10^{-2}$ cm^{-4}; x (cm^{-1}) = 82 I$^{-0.21}$ (mm/hr). Best /4_7 suggested empirical formulas for droplet size distribution and moisture content:

$$F(a_0) = 1 - e^{-\left(\frac{a_0}{a_e}\right)^{v_0}},$$ (4.3)

$$m = C_0 I^{f_0},$$ (4.4)

where $F(a_0)$ is the fraction of moisture content with droplet size less than a_0; $a_e = \alpha_0 I^{\beta_0}$ is the effect of droplet size in cm; m (g/cm^2) is the moisture content of the rain; and C_0, f_0, v_0, α_0, and β_0 are parameters. The mean values of parameters according to Best's data /4_7 are as follows: $C_0 = 6.7 \cdot 10^{-8}$ (g/cm^3), $f_0 = 0.846$, $v_0 = 2.25$, $\alpha_0 = 0.13$ (cm), and $\beta_0 = 0.232$.

Solid-phase precipitation in snow and hail form has dimensions from tenths of a millimeter to several millimeters. In rare cases the sizes of hail particles and snowflakes are as high as several centimeters. The density of snowfalls averages 0.01 g/cm^3, while the density of hail particles is up to 1 g/cm^3.

2. Transport of Microwave Radiation in an Inhomogeneous Atmosphere

2-1) The transport of microwave radiation in clouds is accompanied by effects of absorption and scattering by individual droplets and by secondary emission of droplets.

In calculations of energy absorption and scattering in individual droplets, diffraction theory equations are used. For spherical droplets, the relations determining the attenuation cross section σ_a, scattering cross sections σ_{sc}, and absorption cross sections σ_{ab} in the form of dimensional quantities have several series containing Bessel functions and their derivatives (see /5, 6, 7/). The relative cross sections of attenuation Q_a, scattering Q_{sc}, and absorption Q_{ab} in dimensionless form are defined as follows:

$$Q_a = \frac{\sigma_a}{\pi a^2} ; \qquad Q_{sc} = \frac{\sigma_{sc}}{\pi a^2} ; \qquad Q_{ab} = \frac{\sigma_{ab}}{\pi a^2} . \tag{4.5}$$

Calculations of attenuation and scattering cross sections were not too small values of diffraction parameters $a_\lambda = 2\pi a/\lambda$ and na_λ requires retaining dozens of terms of the series and are performed on digital computers. Examples of droplet attenuation and scattering calculations are given in the monographs cited /6-8/; several additional calculations of Q_a and Q_{sc} for the microwave range are to be found in /9 /.

For small values, $a_\lambda \ll 1$, $na_\lambda \ll 1$, we can use the approximation in the form of the first three terms of the expansion in the small parameter a_λ:

$$\sigma_a \simeq \frac{\lambda^2}{2\pi} a_\lambda^3 (C_1 + C_2 \cdot a_\lambda^2 + C_3 \cdot a_\lambda^3). \tag{4.6}$$

where

$$C_1 = \frac{6\varepsilon''}{(\varepsilon' + 2)^2 + (\varepsilon'')^2} ; \tag{4.7}$$

$$C_2 = \frac{\varepsilon''}{15} \left[\frac{3[7(\varepsilon')^2 + 4\varepsilon' - 20) + 7(\varepsilon'')^2]}{[(\varepsilon' + 2)^2 + (\varepsilon'')^2]^2} + \frac{25}{(2\varepsilon' + 3)^2 + 4(\varepsilon'')^2} + 1 \right], \tag{4.8}$$

$$C_3 = \frac{4}{3} \frac{(\varepsilon' - 1)^2 (\varepsilon' + 2)^2 + (\varepsilon'')^2 [2(\varepsilon' - 1)(\varepsilon' + 2) - 9] + (\varepsilon'')^4}{[(\varepsilon' + 2)^2 + (\varepsilon'')^2]^2} . \tag{4.9}$$

The real ε' and imaginary ε'' parts of the dielectric constant of the water droplets, according to the Debye dipole theory (see Eq. (1.8)) are defined in the form

$$\varepsilon' = \varepsilon_0 + \frac{\varepsilon_s - \varepsilon_0}{1 + \left(\frac{\lambda_s}{\lambda}\right)^2} , \tag{4.10}$$

$$\varepsilon'' = - \frac{\lambda_s (\varepsilon_s - \varepsilon_0)}{\lambda \left[1 + \left(\frac{\lambda_s}{\lambda}\right)^2\right]},$$ (4.11)

where $\lambda_s = 2\pi c_0 \tau_r$; τ_r is the relaxation time of the dipolar molecules, $\varepsilon'(\lambda) = \varepsilon_s$ as $\lambda \to \infty$, and $\varepsilon'(\lambda) = \varepsilon_0$ as $\lambda \to 0$. Eqs. (4.10) and (4.11) determine the dependence of the real and imaginary parts of the dielectric constant on wavelength $\lambda = v/c_0$. The behavior of the real and imaginary parts of the dielectric constant of the water in the microwave range has been studied quite completely. At the present time there are reliable experimental data on the temperature functions of relaxation time and parameters ε_0 and ε_s for the range of temperatures above the thawing point and in the supercooling region /7_7.

The quantity λ_s, according to /7_7, can be approximated by the analytic function

$$\lambda_s = 1.466 e^{-0.0634T} + 0.000136T^2 - 0.02729T + 1.873511,$$ (4.12)

where T is expressed in ° C (also see Figs. 1.1 and 1.2). A more gross approximation of the temperature dependence of the relaxation time used in /10/ is also possible. The coefficients C_1 and C_2 in (4.6) tend to zero in the absence of losses in the liquid ($\varepsilon'' = 0$).   /92

The fraction of scattered radiation for waves in the millimeter and centimeter ranges in cloud formations when $na_\lambda \ll 1$ is extremely small and as a rule can be neglected. The second term in (4.6) can also be neglected. In this approximation the absorption cross section of droplets according to (4.6) can be represented as

$$\sigma_{ab} \simeq \frac{\lambda^2}{2\pi} a_\lambda^3 C_1 = \frac{4\pi^2 a^3}{\lambda} \frac{6\varepsilon''}{(\varepsilon' + 2)^2 + (\varepsilon'')^2}.$$ (4.13)

2-2) Linear absorption in water droplets $\gamma_{\lambda, w}$ can be obtained by summing the absorption cross sections of individual droplets contained in a unit volume:

$$\gamma_{\lambda, w} = \int_0^\infty \sigma_{ab}(a, \lambda) N(a) \, da.$$ (4.14)

In the Rayleigh approximation, by substituting (4.13) into (4.14), we get

$$\gamma_{\lambda, w} = \frac{3\pi}{\rho_d \lambda} W C_1(\lambda),$$

(4.15)

where W is the moisture content of a cloud:

$$W = \int_0^\infty \frac{4\pi}{3} a^3 \rho_d N(a)\, da,$$

(4.

ρ_d is the density of the droplet liquid.

The dependence of $\gamma_{\lambda, W}$ on wavelength and temperature can easily be derived from (4.15), (4.7), (4.10), and (4.11). From these formulas it follows that at long wavelengths the linear absorption is proportional t to λ^{-2}. Thus, when $\lambda \gg \lambda_s$ and T = 291° K, we can use the following formula to a good approximation:

$$\gamma_{\lambda, W} \ (db/km) = 0.41 \ W \ (g/cm^3) \lambda^{-2} \ (cm).$$

(4.16)

For shorter wavelengths, $\lambda_s / \lambda \leqslant 1$, the dependence of $\gamma_{\lambda, W}$ on wavelength is weaker. The dependence of $\gamma_{\lambda, W}$ on droplet temperature is a consequence of the variation of the dielectric parameters of water ε_s, ε_0, and λ_s with temperature. Fig. 4.1 in which the dependence of $\gamma_{\lambda, W}/W$ on wavelength and on temperature is presented as a parameter gives an idea of the behavior of $\gamma_{\lambda, W}$ for liquid-droplet clouds in the centimeter and millimeter wavelength ranges.

In the case of ice-crystal clouds, the absorption coefficient for equivalent water content is approximately two orders less than the absorption coefficient in droplet clouds. In ice-crystal clouds, owing to the weak dependence of the dielectric constant of ice on frequency in the microwave range, the linear absorption coefficient is approximated by the following linear dependence on /93 λ^{-1}:

$$\gamma_{i, \lambda} (db/km) = k_i \frac{W(g/m^3)}{(cm)},$$

(4.17)

where the coefficient $k_i = (9 \cdot 10^{-4} - 7 \cdot 10^{-3})$. The values that k_i takes depend on cloud temperature and droplet shape.
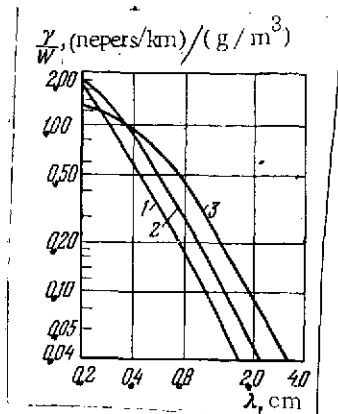
Fig. 4.1. Effect of temperature on shape of normalized droplet cloud absorption spectrum
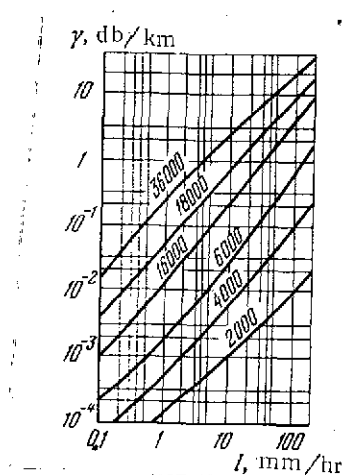1. t = 10° C
2. t = 0° C
3. t = 20° C

Fig. 4.2. Dependence of absorption coefficient of microwave radiation in rainfall on precipitation intensity
The numbers along the curves are frequencies in MHz.

2-2) For rain droplets, the condition that the diffraction parameters a_λ and na_λ be small is not satisfied even in the centimeter range. Therefore to calculate the relative cross sections of attenuation, scattering, and absorption one must sum the corresponding series obtained in diffraction theory. The linear absorption coefficient $\gamma_{\lambda W}$ can be expressed in terms of Eq. (4.14), in which we must substitute the absorption cross section and rain droplet radius distribution. The well-known distributions of Marshall-Palmer, Best, and others can be used as this distribution. Estimates of absorption obtained for different distributions were found to be close to each other, as can be seen from comparing the results of the calculations in /8, 9, 11/.

The calculated estimates of the dependence of the absorption coefficient on rain intensity according to /8_/ are given in Fig. 4.2.

A quantitative estimate of the increase in absorption due /94 to diffraction can be expressed by a factor G, indicating by how many times the actual absorption in rain is greater than the calculation in the Rayleigh approximation provides. Estimates of the factor G are given in Table 7 for three wavelength intervals and three rain intensity levels. The data in Table 7 were obtained from calculations given in /8_/.

TABLE 7. VALUES OF FACTOR G

Intensity of rain precipitation	Limits of spectral regions in wavelength, cm		
	0.8-1	1-2	2-4
Gentle rain, I < 2 mm/hr	5-6	4-5	2-4
Moderate rain, I < 10 mm/hr	5-7	7-10	3.5-7
Heavy and shower-intensity rain, I < 16 mm/hr	7-8	8-10	10-20

TABLE 8. VALUES OF SCATTERING COEFFICIENT Q_{sc}/Q_{ab}

I, mm/hr	λ, cm		
	0,8	1,35	3,2
2	0,31	0,14	0,05
5	0,36	0,20	0,06
16	0,42	0,28	0,08
40	0,46	0,34	0,10
90	0,49	0,39	0,13

When rain precipitation becomes more intense, the influence of resonant effects shifts from the millimeter to the centimeter radio-wavelength range. The data in Table 7 show also that in the short-wave section of the centimeter range and in the millimeter range the role of resonant mechanisms is very significant.

In calculating the emissivity of rain layers in several cases one must make allowance for the contribution of scattering fields. The influence of scattering effects is conveniently described by the coefficient of scattering per unit volume ("probability of survival of a quantum") and by the shape of the scattering indicatrix. The scattering coefficient is equal to the ratio of the scattering and absorption cross sections calculated per unit volume. Calculations of the scattering indicatrix for the polydispersion model given in /9_7 show that the shape of the indicatrix in the centimeter range is close to the Rayleigh form. The calculated estimates of the scattering coefficient in the elementary volume based on the data in /9_7 are presented in Table 8 as a function of wavelength and rain intensity.

/95

The data in Table 8 show that for the millimeter wavelengths the contribution made by the scattering fields must be taken into account for rain precipitation over the entire range of rain intensity. The effect of scattering is much weaker for centimeter waves than for millimeter waves, however in the case of intense rainfall neglecting scattering can lead to marked errors.

3. Spectrum of Outgoing Microwave Radiation

3-1) To find the main features of the emission spectrum of a cloudy atmosphere observed by satellite, let us examine the simplest model: the atmosphere over a quiet water surface. The calculations will be made for observations at the nadir, without allowing for scattering effects in the atmosphere. Some complications of the model will be examined shortly in subsection 3-2) of this section.

For the atmosphere model adopted, the expression for brightness temperature takes on its familiar form:

$$T_{b,\lambda} = (1 - R_\lambda) T_0 \exp\left\{-\int_0^\infty \gamma_\lambda(h')\,dh'\right\} +$$
$$+ \int_0^\infty \gamma_\lambda(h)\, T(h) \exp\left\{-\int_h^\infty \gamma_\lambda(h')\,dh'\right\} dh +$$
$$+ R_\lambda \exp\left\{-\int_0^\infty \gamma_\lambda(h')\,dh'\right\} \int_0^\infty T(h) \exp\left\{-\int_0^h \gamma_\lambda(h')\,dh'\right\} \gamma(h)\,dh. \tag{4.18}$$

In contrast to the case of a cloudless atmosphere, the linear coefficient of absorption γ_λ in (4.18) consists of three terms:

$$\gamma_\lambda = \gamma_{\lambda,O_2} + \gamma_{\lambda,H_2O} + \gamma_{\lambda,W.} \tag{4.19}$$

Actually, (4.18) is a complex functional, dependent on the vertical distribution of air temperature and humidity, altitude distribution of droplet water, and so on. The presence of droplet water in clouds leads to unusual features in the spectrum of outgoing microwave radiation. Fig. 4.3 presents examples of the calculation of the spectrum of brightness temperatures for a 1 km thick model of a cloud layer, with a total content of droplet water $W = 1$ kg/m^2. In the calculation it is assumed that the middle of the cloud layer is at the altitude $H_W = 1$ km and 2.5 km. The temperature and humidity distribution correspond to the standard atmosphere.

First we note that the presence of cloud cover increases the brightness temperature of the water surface, and the tem-

perature rise proves to be greater at shorter wavelengths. This
consequence is natural, since the rise in absorption in droplets
is proportional to λ^{-2}. A more subtle effect of cloud cover is
that the increase in cloud altitude and, thus, a decrease in cloud
temperature lead to a marked rise in the brightness temperature of
the entire system. The rise in the brightness temperature with
cloud ascent is associated with the fact that the increase in the
optical density of the cloud $\tau_{\lambda w} = \int \gamma_{\lambda w} dh$ dominates over its
temperature drop. We also note that in the area of the oxygen
resonance where absorption is very high, the cloud cannot be
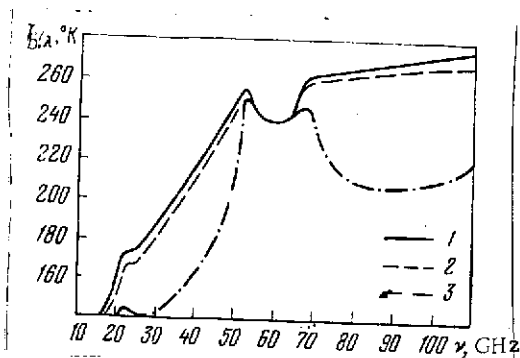scanned when observations are taken from above.

Fig. 4.3. Spectra of outgoing
radiation of cloudy atmosphere
over quiet water surface
1. H_W = 2.5 km
2. H_W = 1 km
3. Cloudfree atmosphere

3-2) The spectrum of radio-
brightness temperatures of a
cloudy atmosphere in a precipi-
tation zone has features asso-
ciated with the influence of the
weakly selective effects of micro-
wave radiation absorbed and
scattered by droplets with
dimensions exceeding tenths of
a millimeter.

As shown by estimates (see
Table 8), the scattering coeffi-
cient per unit volume of rain
precipitation is 5-50 percent,
depending on the intensity of
the precipitation and the
selection of the spectral region
of observation. An estimate of
the effect of scattering on the
radiobrightness temperature in
the precipitation zone, made by use of radiation transport
equations, showed /12/ that when the integrated absorption is
more than 0.5 neper /, scattering corrections must be introduced
when the scattering coefficient is more than 10 percent. There-
fore in the calculation of radiobrightness in the 0.1-3 cm range
during periods of rain, one must allow for the reduction in
radiobrightness temperature due to droplet scattering.

3-3) The effect of the temperature and state of the under-
lying surface becomes most strongly evident in the long-wave
section of the centimeter range and in the decimeter range,
where absorption in the atmosphere is low even during rainfall.

The reflecting properties of the underlying surface directly
affect the sensitivity of the spectrum of radiobrightness tempera-

tures to variations in atmospheric parameters. When observations are made of continental cover where the power reflection coefficient does not exceed 10 percent, the sensitivity of the spectrum of radiobrightness temperatures to variations in atmospheric parameters in the centimeter range and in the long-wave section of the millimeter range is reduced by more than fivefold compared to observations of a quiet water surface.

Tables presenting the results of calculations of outgoing radiation for different scattering intensities in precipitation and for different reflectivities of the underlying surface are given in /9, 12/.

3-4) The characteristic changes in the shape of the spectrum of outgoing microwave radiation associated with changes in the condition of the underlying surface and the atmosphere are conveniently found by grouping the states of the atmosphere and the Earth's surface. Let us single out the following typical ensembles differing in microwave radiation properties for sea surface, continental cover, and cloud cover:

a) for a sea surface: 1) the free sea surface (when wind velocity does not exceed 5 m/sec); 2) the surface with moderate sea state (when wind velocity is not above 8 m/sec and foaming is limited); and 3) a surface with intense sea state and foaming;

b) for continental cover: 1) dry soil with moisture not exceeding 5 percent; 2) moderately moist soils with moisture to 12 percent; 3) waterlogged soils; 4) frozen soils and glaciers; and 5) soils covered with vegetation; and

c) for cloudy atmospheric states: 1) ensembles of single-layer cloud cover (clouds of the lower, middle, and upper tiers); 2) ensembles of vertically developed clouds; and 3) ensembles of clouds with falling precipitation.

The arbitrary nature of this preliminary classification is admitted and it can be assumed that as data on the microwave radiation characteristics of the Earth accumulate, this classification will be refined.

3-5) The presence of the atmospheric-state dependence of the intensity of outgoing microwave radiation from the system underlying surface-atmosphere makes it possible to solve various inverse problems of determining the meteorological parameters of the atmosphere. As applied to a cloudy atmosphere, two kinds of inverse problems can be examined: problems of determining the integrated parameters (total mass of water vapor, moisture reserve of clouds, precipitation intensity, and so on) and problems of determining the vertical profiles of temperature and humidity.

The solution of the inverse problems as applied to a cloudy atmosphere is conveniently done in two stages: the stage of classification (distinguishing an ensemble) and the stage of estimating the parameters characteristic of the ensemble selected.

In distinguishing an ensemble of states, it is suggested to use integrated observations incorporating photographic data and data on radiation temperatures in the IR /infrared/ and microwave ranges.

Let us examine several possibilities of elucidating charac-   /98
teristic features of cloud ensembles over a quiet water surface.

1. Ensembles of one-layer cloud cover with different tier altitude differ in the radiation temperatures in the infrared range. The thickness of cloud layers is estimated from the moisture reserve.

2. An ensemble of clouds of vertical development and multi-layer structures are distinguished from the feature of the combination of significant altitude of the cloud top, 6-8 km, and a marked increase in the radiobrightness temperature due to the high moisture reserve in clouds.

3. An ensemble of clouds with falling precipitation is characterized by a sharp increase in the radiobrightness of the system underlying surface-atmosphere owing to radiation from large droplets and the appearance of polarization effects owing to flattening of the droplets.

At the stage of estimating meteorological and hydrological parameters for a selected ensemble, models of the states of the atmosphere and the underlying surface are brought into considera-tion. The number of parameters in the models is arbitrary to some extent and can vary, depending on the complex of observa-tional facilities.

The following problems in microwave sensing representative of a cloudy atmosphere can be presented by way of example:

1) a three-parameter model where the temperature of the underlying surface, the total mass of water vapor in the atmo-sphere, and the moisture reserve of clouds are determined;

2) a four-parameter model, in which additionally the altitude of the cloud layer centered from the moisture content distribution is estimated; and

3) multiparameter models containing parameters of vertical profiles of humidity, temperature, and intensity of precipitation.

4. Determination of Integrated Meteorological Parameters

4-1) The relatively low optical thickness values of the atmosphere in the microwave range (with the exception of course of oxygen resonances) make it possible, even when cloud cover is present, to formulate the problem of determining several integrated meteorological parameters from measurements of the brightness temperature spectrum /13, 15-18/. First of all, these parameters include the integrated content of water vapor $Q = \int\limits_0^\infty \rho_v (h)\, dh$ and droplet water in clouds $W = \int\limits_0^\infty \rho_d (h)\, dh$, as well as the effect of cloud altitude H_W.

Since the ratio of the absorption coefficient in water vapor /99 to the density of water vapor $\gamma_{\lambda,Q}/\rho_v$ varies with altitude much more slowly than $\rho_v(h)$ (see (3.1)), total absorption in water vapor $\tau_{\lambda,Q}$ can be described analogously to (3.10) as follows

$$\tau_{\lambda,Q} = \int\limits_0^\infty \gamma_{\lambda,Q}\, dh = \overline{\psi}_\lambda Q. \tag{4.20}$$

As shown in section 2 of this chapter (see (4.15)), to the Rayleigh approximation the absorption $\gamma_{\lambda,W}$ is proportional to W. The coefficient of proportionality $C_1(\lambda)$ depends on temperature (since the dielectric constant of the droplet liquid depends on temperature). As can be seen from Fig. 4.1, this function can be assumed, approximately, to be linear:

$$C_1(\lambda) = C_1(\lambda, T_0)\left[1 + a_\lambda \frac{T - T_0}{T_0}\right] \tag{4.21}$$

where $C_1(\lambda, T_0)$ is the value of $C_1(\lambda)$ at temperature T_0; a_λ is a coefficient whose value can be estimated if we know the dependence of ε_s, ε_0, and λ_s on temperature.

Referring to (4.15) and (4.21), we get the result, by using the theorem of the mean:

$$\tau_{\lambda,W} = \frac{3\pi C_1(\lambda, T_0)}{\rho_d \lambda} W\left(1 + a_\lambda \frac{T_W - T_0}{T_0}\right), \tag{4.22}$$

102

where T_W is the effect of cloud temperature. Assuming that the temperature in the troposphere falls off linearly with altitude with gradient Γ_0, from (4.22) we get

$$\tau_{\lambda,W} = \Theta_\lambda W + \mathcal{E}_\lambda W H_W,$$

(4.23)

where $H_W = (T_W - T_0)/\Gamma_0$ is the effect of cloud altitude. Expressions for the coefficients in (4.23) become obvious upon comparison of (4.22) and (4.23). Since total absorption in oxygen can be calculated with sufficient accuracy, then by determining the total absorption

$$\tau_\lambda = \tau_{\lambda,O_2} + \tau_{\lambda,Q} + \tau_{\lambda,W}$$

(4.24)

at several wavelengths, we can get estimates of the integrated parameters.

4-2) In order to relate the integrated parameters to the brightness temperature spectrum, let us write out Eq. (4.18) in the following form:

$$T_{b,\lambda} = (1 - R_\lambda) T_0 e^{-\tau_\lambda} + T_\lambda^* [1 - e^{-\tau_\lambda}] + T_\lambda^{**} R_\lambda (1 - e^{-\tau_\lambda}) e^{-\tau_\lambda}.$$

(4.25)

The effect of temperature T* and T** in (4.25) are defined as follows:

$$
\begin{aligned}
T^* &= \frac{\displaystyle\int_0^\infty \gamma_\lambda(h)\, T(h)\, \exp\left\{-\int_0^\infty \gamma_\lambda(h')\, dh'\right\} dh}{\displaystyle\int_0^\infty \gamma_\lambda(h)\, \exp\left\{-\int_h^\infty \gamma_\lambda(h')\, dh'\right\} dh}, \\[3mm]
T^{**} &= \frac{\displaystyle\int_0^\infty \gamma_\lambda(h)\, T(h)\, \exp\left\{-\int_0^h \gamma_\lambda(h')\, dh'\right\} dh}{\displaystyle\int_0^\infty \gamma_\lambda(h)\, \exp\left\{-\int_0^h \gamma_\lambda(h')\, dh'\right\} dh}.
\end{aligned}
$$

(4.26)

The temperatures T* and T** have the same physical significance as the $T_{e,\lambda}$ introduced in Chapter Two for a homogeneous cover. The difference between T* and T** characterizes the manifestation of atmospheric nonisothermicity in outgoing and incoming radiation.

In conditions when τ_λ is small, the difference between T* and T** is of the order of $\frac{1}{2}\,\tau_\lambda\Gamma_0 h_\tau,$ while T* and T** are of the order of $\Gamma_0 h_\gamma$ (where h_γ is the characteristic altitude for the absorption coefficient). For oxygen $h_\gamma \cong 5$ km, and for water vapor $h_\gamma \cong 2$ km /147.

4-3) To get estimates of Q, W, and H_W from brightness temperature measurements, to the first approximation we will assume that T* = T**, and we will denote

$$\Delta T_\lambda = T_0 - T^*.$$

Under this condition, from (4.25) we get

$$\tau_\lambda = -\ln\left[\frac{(1-R_\lambda)\,\Delta T_\lambda}{2R_\lambda\,|T_0-\Delta T_\lambda|}\pm\right.$$
$$\left.\pm\sqrt{\frac{(1-R_\lambda)^2\,(\Delta T_\lambda)^2}{4R_\lambda^2\,(T_0-\Delta T)^2}+\frac{T_0-T_{n,\lambda}-\Delta T_\lambda}{R_\lambda\,(T_0-\Delta T_\lambda)}}\right].$$

(4.27)

The sign "+" is taken for

$$\tau_\lambda \leqslant \ln\frac{(1-R_\lambda)\,\Delta T}{2R_\lambda\,(T_0-\Delta T)}.$$

Assuming that R_λ and T_0 are known in advance (or have been determined from radiometric measurements at long wavelengths), and ΔT have been obtained, for example, from mean-climatic data, we can determine τ_λ for several wavelengths and then solve the the system of equations:

$$\tau_\lambda - \tau_{\lambda,O_2} = \Psi_\lambda Q + \Theta_\lambda W + \mathcal{E}_\lambda W H_W.$$

(4.28)

The selection of wavelengths in the system of equations (4.28) is made so that the determinant of the system[1] reaches a maximum. One of these wavelengths must deliberately lie within the neigh- /101 borhood of the 1.35 cm resonance in order to get estimates of Q.

---

[1] System (4.28) can be viewed as a system of linear equations if we introduce the additional unknown $\widehat{WH_W} = \overline{WH_W}.$

The system (4.28) can be used only to determine Q, and this case was analyzed more fully in Chapter Six where we discussed the results of determining Q from satellites.

To determine Q, W, and H_W, we need as broad a range of wavelengths as possible in order that in the measurements the dependence of the coefficient a_λ introduced in (4.21) on wavelength can be manifested. Otherwise, the system (4.28) degenerates and the determination of W and H_W becomes impossible. In this case, to find W we must independently determine the effective cloud temperature T_W by using, for example, apriori information on the cloud cover type. The error in determining the integrated parameters associated with the assumption of the equality $T^* = T^{**}$ and with their indeterminacy can be somewhat reduced by iteration, by using the values of Q, W, and H_W calculated in the first approximation for revising the values of T^* and T^{**}. The estimates obtained for calculated models show that the iteration reduces the error of determining T^* and T^{**} down to 3-4° K.

4-4) The system of equations (4.28) allows us to obtain estimates of errors associated with the errors in measuring brightness temperature, the indeterminacy of the blackness factor of the surface, and other external parameters. However, a more graphical result giving a general idea of the possibilities of determining integrated parameters can be realized at small τ_λ from Eq. (4.25) linearized in τ_λ. By expanding exp $(-\tau_\lambda)$ and by limiting ourselves to first-order terms in τ_λ, we get

$$T_{b,\lambda} - T_0(1 - R_\lambda) = [2R_\lambda T_0 - (T_0 - T^*) - R_\lambda(T_0 - T^{**})]\tau_\lambda \quad (4.29)$$

By dropping the last two terms in the brackets as being inessential for the analysis of the errors of measuring brightness temperature, we get the system of equations

$$\Psi_\lambda Q + \Theta_\lambda W + \mathscr{E}_\lambda \widehat{WH_W} = (2R_\lambda T_0)^{-1}(T_{b,\lambda} - T^0_{b,\lambda}), \quad (4.30)$$

where $T^0_{b,\lambda} = T_0(1 - R_\lambda) + 2R_\lambda T_0 \tau_{\lambda, O_2}$. The solution of the system of equations (4.30) for the unknowns Q, W, $\widehat{WH_W}$ with the right-hand parts obtained from measurements at three wavelengths λ_1, λ_2, and λ_3, can be written by using the matrix $\|M_{ij}\|$ that is the inverse of the matrix of Eq. (4.30). Let us use the matrix $\|M_{ij}^{-1}\|$ to estimate the effect of the errors in measuring $T_{b,\lambda}$,

which are characterized by the dispersions $\sigma^2_{\lambda_1}, \sigma^2_{\lambda_2}, \sigma^2_{\lambda_3}$. By assuming the errors of measurement at each wavelength to be independent, and their dispersions to be σ^2_T, the estimates of the dispersions $\sigma^2_Q, \sigma^2_{W_2}$ and $\sigma^2_{\widehat{WH}}$ can be expressed as follows:

$$
\begin{aligned}
\sigma^2_Q &= (M^2_{11} + M^2_{12} + M^2_{13})\, \sigma^2_T, \\
\sigma^2_W &= (M^2_{21} + M^2_{22} + M^2_{23})\, \sigma^2_T, \\
\sigma^2_{\widehat{WH}} &= (M^2_{31} + M^2_{32} + M^2_{33})\, \sigma^2_T.
\end{aligned}
\tag{4.31}
$$

4-5) In order to obtain a quantitative idea of the effect /102 of errors in measurement of radiobrightness temperatures on the determination of the integrated parameters, a model with single-tier cloud cover 1 km thick at altitude from 0.5 to 3 km above a quiet water surface was considered, with the other atmospheric conditions taken as standard. The moisture reserve of the cloud cover W varied from 0.3 to 3 kg/m^2. Table 9 gives the characteristic values of the noise error coefficients calculated by A. N. Tsvetkov and M. S. Krylova defined as the ratio $\sigma_Q/\sigma_T, \sigma_W/\sigma_T,$ and $\sigma_{\widehat{WH}}/W\sigma_T$ for several triples of wavelengths (the frequencies $f = c_0/\lambda$ is indicated in the table). In each triplet there is included a wavelength in the region of water vapor resonance. The data given in the table show that use of radiation at the wavelength $\lambda \geqslant 0.8$ cm (f ≈ 37.5 Hz), when the error of measurement of brightness temperature values is $T_{b,\lambda} \geqslant 1°$ K, provides virtually no additional information on the effective cloud altitude H_W for clouds with moisture reserve W ⩽ 0.6 kg/m^2 (for which the estimate scheme examined here is valid). In order to obtain by the above-described method, data on altitude H_W, it is desirable to use shorter wavelengths, in the range $\lambda \sim 0.4$ cm, given the condition that the measurement of the brightness temperatures of the order of 1° K is exact. The measurements to this precision in the 0.4 cm range at the present time pose certain technical difficulties.

The linearization of Eq. (4.25) and the conversion from system (4.30) to (4.31) also introduces approximation errors. Use of Eqs. (4.30) by virtue of their simplicity in several cases proved to be preferable, given the condition that the coefficients Ψ_λ, Q_λ and $\mathcal{E}_\lambda$ constituting the matrix of system (4.30) were selected from a set of apriori data. In addition, depending on

106

TABLE 9   COEFFICIENTS OF NOISE ERRORS

f_1 (GHz)	18	22.2	22.2	22.2
f_2 (GHz)	22.2	27.5	30	37.5
f_3 (GHz)	37.5	45	45	70
σ_Q/σ_T (g/cm$^2\cdot$deg)	0.12	0.11	0.10	0.087
σ_W/σ_T (kg/m$^2\cdot$deg)	0.12	0.055	0.057	0.028
$\sigma_{WH}/W\sigma_T$ (kg/deg)	1.0	0.6	0.58	0.27

the type of radiation spectrum, here the meteorological situation is determined in the zone of measurements and the particular matrix in Eq. (4.30) is appropriately selected. Estimates show that a set of two matrices makes it possible to reduce by several times the approximation error compared with a single matrix.

4-6) The solution of the problem of zones where precipi-
tation can possibly appear can be carried out in two stages: the first involves detection of precipitation and the second involves estimation of Q and rain intensity.

At the stage of detection, estimates are made of the radio-brightness temperatures over sections of about 0.8, 1.6, and 3 cm and the resulting estimates are compared with threshold values adopted as criteria for the detection of the zones of falling precipitation. In the second stage, the dependence of absorption on precipitation intensity was used for estimating the integrated meteorological parameters, including the estimate of precipitation intensity.

When the problem of determining the integrated parameters was examined, it was assumed that the blackness factor of the surface $\kappa_\lambda = 1 - R_\lambda$ was known. However, even over the ocean this para-meter can change owing to agitated sea states and the presence of spume (see Chapter One) within certain limits. Therefore, κ_λ requires independent determination. Polarization measurements with slant sensing can be used to determine κ_λ. Estimates of the errors in determining Q for sensing at two wavelengths at the nadir are examined in Chapter Six.

5. Reconstruction of Temperature and Humidity Profiles When Cloud Cover is Present

5-1) The problem of reconstructing vertical profiles of humidity and temperature in a cloudfree atmosphere was examined in the preceding chapter. The solution to this problem, when cloud cover is present, becomes considerably complicated by the circumstances that absorption in clouds is weakly selective by wavelength, while the cloud cover parameters -- moisture content and its distribution by altitude -- vary so significantly that the mean-climatic data cannot be used.

Let us write Eq. (4.18) as

$$T_{b, \lambda} = \int_0^\infty T(h) \mathcal{K}(\lambda, h) \, dh; \quad T(0) = T_0. \tag{4.32}$$

When cloud cover is present, an unknown absorption in clouds appears in the kernel of this equation. Therefore formally it is not possible to solve Eq. (4.32) for the desired temperature profile T(h). Similar difficulties arise also in the reconstruction of the humidity profile.

However, for an actual cloudy atmosphere, the situation of the reconstruction of the vertical profiles from measurements of radiobrightness in the microwave range does not appear so hopeless. First of all, ice-crystal clouds practically speaking are not a source of interference for operation in the microwave range, and it is here that its advantage over the infrared range lies. Secondly, conditions can be determined in which the moisture reserve of clouds is not too high and in this case we can outline /104 a realistic way of canceling out the effect of cloud cover on the reconstruction of vertical profiles of meteorological parameters.

5-2) In order to quantitatively estimate the effect of cloud cover on the emission spectrum in the oxygen absorption band, let us examine a cloud layer model whose upper boundary is at the altitude H_{max}, and its lower -- H_{min}. We will assume the layer to be thin, that is, $H_{max} - H_{min} \ll (H_{max} + H_{min})/2$. We will let H_W stand for the mean altitude of the cloud.

This model is quite closely reflects the characteristics of the effect of cloud cover and enables us to obtain quantitative estimates. Schematization greatly simplifies the algebraic operations and enables us to represent the estimates obtained in a quite compact form.

Let us write the expression for brightness temperature (4.18) in the following form:

$$T_{b,\lambda} = (1 - R_\lambda)\, e^{-\tau_\lambda} T_0 + \int_0^\infty T(h) \exp\left(-\tau_\lambda + \tau_\lambda(h)\right) \frac{d\tau_\lambda}{dh}\, dh +$$

$$+ R_\lambda \int_0^\infty T(h) \exp\left(-\tau_\lambda - \tau_\lambda(h)\right) \frac{d\tau_\lambda}{dh}\, dh;$$

$$\tau_\lambda(h) = \int_0^h \gamma_\lambda(h')\, dh', \qquad \tau_\lambda = \int_0^\infty \gamma_\lambda(h)\, dh. \tag{4.33}$$

Since in the following we will find the effect of cloud cover, let us single out in (4.33) the linear absorption in the cloud $\gamma_{\lambda,W}$, denoting the absorption of a cloudfree atmosphere by γ_λ^0. Similarly, we introduce notation for optical thickness:

$$\tau_\lambda = \tau_\lambda^0 + \tau_{\lambda W}, \qquad \tau_\lambda(h) = \tau_\lambda^0(h) + \tau_{\lambda W}(h).$$

Let us estimate the difference in brightness temperatures of a cloudy atmosphere $T'_{b,\lambda}$ and a cloudfree atmosphere $T^0_{b,\lambda}$ for the same distribution of temperature and humidity. when we get, to a precision of the order of $\tau_{\lambda W}$, the following expression for the unknown difference $T_{b,\lambda} - T^0_{b,\lambda}$

$$\mathcal{F}_\lambda \simeq \tau_{\lambda W} e^{-\tau_\lambda^0} \left\{ T(H_W)\, e^{\tau_\lambda^0(H_W)} [1 + R_\lambda e^{-2\tau_\lambda^0(H_W)}] + \right.$$

$$+ \left[-T_0(1 - R_\lambda) - \int_0^{H_W} T(h)\, e^{\tau_\lambda^0(h)} \gamma_\lambda^0(h)\, dh - \right.$$

$$\left. - R_\lambda \int_{H_W}^\infty T(h) \times e^{-\tau_\lambda(h)} \gamma_\lambda^0(h)\, dh - R_\lambda \int_0^\infty T(h)\, e^{-\tau_\lambda^0(h)} \gamma_\lambda^0(h)\, dh \right] \right\}. \tag{4.34}$$

From (4.34) we can see that the manifestation of cloud cover, owing to the presence of the cofactor $e^{-\tau_\lambda^0}$ will be most substantive in the wings of the absorption band when $\tau_\lambda^0 \leqslant 1-3$, /105 that is, precisely at the wavelength λ where measurements yield information on the distribution of temperatures in the troposphere.

The first term in the braces describes the contribution made by the cloud to radiation, and the second, always negative, is derived from the attenuation of surface and atmosphere emission by cloud cover. Over a fairly wide range of wavelengths, reflection
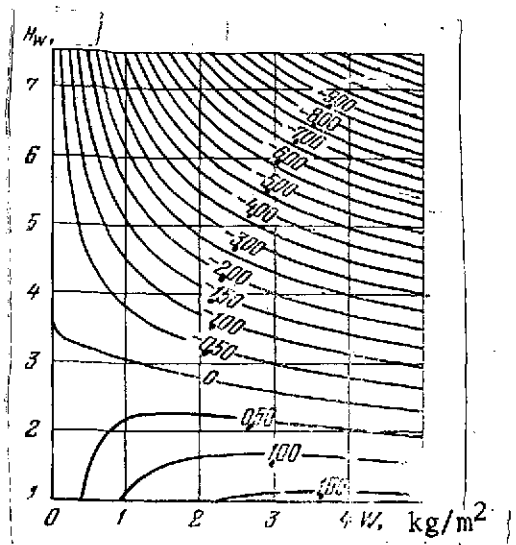
Fig. 4.4. Calculated dependence of difference $|\mathcal{J}_\lambda| = T_{b,\lambda} - T^O_{b,\lambda}$ on mean cloud altitude H_W and moisture reserve W of cloud 1.5 km in thickness-/18/ The numbers alongside the curves represent $T_{b,\lambda} - T^O_{b,\lambda}$ in °K

coefficients, and possible variations in the temperature profile T(h), the value of the difference $\mathcal{J}_\lambda$ tends to zero for certain values of H_W. This conclusion is valid not only for small $\tau_{\lambda W}$, which is indicated by the results of numerical calculations in /18/ shown in Fig. 4.4. Calculations in /18/ were made for the wavelength $\lambda = 5.592$ mm (frequency 53.65 GHz), for a standard atmosphere, and for clouds with different moisture reserve, whose optical thickness $\tau_{\lambda W}$ reaches several units. The data given in Fig. 4.4 reveal that for the standard atmosphere clouds over an ocean at the altitude $H_W \approx 3$ km do not become manifest in the radiation at this wavelength, for which $\tau^0_\lambda \simeq 2.$

Eq. (4.34) can be used to solve the problem of reconstructing the vertical temperature profile T(h). To do this, let us represent it in the following form:

$$T_{b,\lambda} - \mathcal{J}_\lambda = \int_0^\infty T(h)\,\mathcal{H}^0(\lambda,h)\,dh, \qquad (4.35)$$

where $\mathcal{H}^0$ is the kernel of the integral equation (4.18) without considering cloud cover. The quantity measured is T_b, and Eq. (4.35) differs from analogous equations examined in the preceding chapter by the presence of the additional term $\mathcal{J}_\lambda$, which must be independently measured. From (4.34) it is clear that only the integrated cloud cover parameters appear in the added term $\mathcal{J}_\lambda$ its altitude H_W and optical thickness $\tau_{\lambda W}$. The possibility of independently determining these parameters from measurements outside the resonance region was examined in the preceding section.

Let us estimate the error of calculating $\mathcal{J}_\lambda$ associated /106 with the inaccuracy of the determination of H_W. Differentiating (4.34) in H_W, we find

$$\frac{\partial \mathcal{J}_\lambda}{\partial H_W} = \tau_{\lambda, W}\left\{\frac{dT(H_W)}{dH_W} e^{-\tau_\lambda^0 + \tau_\lambda(H_W)}[1 + R_\lambda e^{-2\tau_\lambda(H_W)}]\right\} \cdot \qquad (4.36)$$

In order to gain an idea of the size of the error, let us substitute into (4.36) reasonable estimates: $dT(H_W)/dH_W = 6\text{-}8$ K/km, $-\tau_\lambda^0 + \tau_\lambda^0(H_W) = -1$, $\tau_\lambda^0(H_W) = 0.5$; and $R_\lambda = 0.4$. Then we get

$$\frac{\partial \mathcal{J}_\lambda}{\partial H_W} = (2.5 - 3.4)\,\tau_{\lambda, W} \,{}^\circ K/\text{km}$$

that is, when $\tau_{\lambda|W} < 0.2\text{-}0.3$, the error of the determination of $\mathcal{J}_\lambda$ due to the imprecision of determining H_W in 1 km does not exceed $0.5\text{-}1^\circ$ K. We note that the optical thickness $\tau_{\lambda|W} = 0.3$ at the wavelength $\lambda = 0.55$ cm corresponds to a quite appreciable moisture reserve of the cloud: $W = 0.2$ kg/m^2.

We note that the estimates for models where no assumption of small cloud thickness and low moisture reserve was made lead to similar results.

5-3) This examination of the cloud cover model enables us to outline the following approach in solving the problem of reconstructing vertical temperature profiles from measurements of microwave radiation when cloud cover is present. Let us represent the kernel $\mathcal{H}(\lambda, h)$ and the temperature profile $T(h)$ in Eq. (4.32) in the form

$$\begin{aligned}
\mathcal{H}(\lambda, h) &= \overline{\mathcal{H}}(\lambda, h) + \delta\mathcal{H}(\lambda, h), \\
T(h) &= \overline{T}(h) + \delta T(h),
\end{aligned} \qquad (4.37)$$

where $\overline{\mathcal{H}}(\lambda, H)$ is the kernel of the integral equation corresponding to the cloudfree atmosphere with mean-climatic temperature distribution $\overline{T}(h)$; $\delta T(h)$ are the temperature variations we seek; $\delta\mathcal{H}(\lambda, h)$ is a small addition to the equation kernel that is to be determined. Substituting (4.37) into (4.32), we get

$$T_{b, \lambda} - \int_0^\infty \overline{T}(h)\overline{\mathcal{H}}(\lambda, h) = \int_0^\infty \delta T(h)\overline{\mathcal{H}}(\lambda, h)\,dh +$$
$$+ \int_0^\infty \overline{T}(h)\delta\mathcal{H}(\lambda, h)\,dh + \int_0^\infty \delta T(h)\delta\mathcal{H}(\lambda, h)\,dh. \qquad (4.38)$$

In the first stage of the calculations, the last term on the right=hand side of (4.38), being of the second order of smallness, can be dropped. The second term

$$\mathcal{Y}_\lambda = \int\limits_0^\infty \bar{T}(h)\, \delta \mathcal{H}(\lambda, h)\, dh$$

can be calculated when $\tau_{\lambda W} \leqslant 1$ based on (4.34) with $T(h) = \bar{T}(h)$ and with the values of $\bar{\tau}_{\lambda, W}$ and H_W determined from measurements outside the absorption band. Whatever the value of $\mathcal{Y}_\lambda$ is determined, the equation

$$T_{\text{я.}\lambda} - \int\limits_0^\infty \bar{T}(h)\, \mathcal{H}(\lambda, h)\, dh - \mathcal{Y}_\lambda = \int\limits_0^\infty \delta T(h)\, \mathcal{H}(\lambda, h)\, dh$$

can be solved with respect to $\delta T(h)$ by methods examined in the preceding chapter.

In the second stage, iteration can prove useful in refining the solution.

The scheme of allowing for cloud cover in the solution of problems of reconstructing the vertical profile has been outlined above only in the most general terms. In the following, much work remains to be done in revising the limits of applicability of this scheme with reference to both actual atmospheric conditions as well as possible variations in the radiation from the underlying surface. However, preliminary estimates show that if the optical thickness of clouds $\tau \leqslant 0.3$, we can anticipate the successful reconstruction of the temperature profile. This optical thickness at the wavelength 0.55 cm corresponds to a cloud cover with a moisture reserve equal to about $W = 0.2$ kg/m^2, or a moisture reserve of a cloud of 0.2 g/m^3 for a 1 km thick cloud.

The above-developed approach to solving the problem of reconstructing the vertical temperature profile can in principle be also used in reconstructing the humidity profiles when cloud cover is present. However, in this direction further research is also needed.

REFERENCES

1. Khrgian, A. Kh., Fizika atmosfery /Atmospheric Physics/, Gidrometeoizdat, 1969.

2. Shishkin, N. S., Oblaka, osadki i grozovoye elektrichestvo /Clouds, Precipitation, and Lightning Electricity/, Gidrometeoizdat, 1964.

3. Marshall, T., and Palmer, W., J. Meteor. 5/4, 165 (1948).

4. Best, A., Quart. J. Meteor. Soc. 80, 522 (1954).

5. Shifrin, K. S., Rasseyaniye sveta v mutnoy srede /Scattering of Light in a Turbid Medium/, Gostekhizdat, 1950.

6. Van-der-Hulst, H., Rasseyaniye sveta malymi chastitsami /Light Scattering by Small Particles/, translated from the English, edited by V. V. Sobolev, Foreign Literature Publishing House, 1961.

7. Rozenberg, V. I., Rasseyaniye i oslableniye elektromagnitnogo izlucheniya atmosfernymi chastitsami /Scattering and Attenuation of Electromagnetic Radiation by Atmospheric Particles/, Gidrometeoizdat, 1972.

8. Rasprostraneniye ul'trakorotkikh voln /Propagation of Ultra-short Waves/ Translated from the English, edited by B. A. Shillerov, Moscow, Sov. radio Press, 1954.

9. Shifrin, K. S., and Chernyak, M. M., Trudy GGO im. A. I. Voyeykova /Transactions of the Main Geophysical Observatory imeni A. I. Voyeykov/, 222, 74 (1968).

10. Basharinov, A. Ye., Tuchkov, L.T., Polyakov, V. M., and Ananov, N. I., Izmereniye radioteplovykh i plazmennykh izlucheniy v SVCh diapazone /Measurement of Radiothermal and Plasma Radiation in Microwave Range/,Moscow, Sov. radio Press, 1968.

11. Shifrin, K.S., Rabinovich, Yu. I., and Shchukin, G. G., Meteorologiya i gidrologiya, 6, 10 (1969).

12. Volchok, B. A., and Chernyak, M. M., Trudy GGO im. A. I. Voyeykova, 222, 93 (1968).

13. Basharinov, A. Ye, Yegorov, S. T., Kolosov, M. A., and Kutuza, B. G., Trudy GGO im. A. I. Voyeykova, 222, 153 (1968).

14. Troitskiy, V. S., Zhevakin, S. A., and Tseytlin, N. M., Izv. vyssh. ucheb. zav. Radiofizika 1/2, 19 (1958).

15. Rabinovich. Yu. I., Shchukin, G. G., and Chernyak, M. M., Trudy GGO im. A. I. Voyeykova, 222, 149 (1968).

16. Rabinovich, Yu. I., and Shchukin, G. G., Trudy GGO im. A. I. Voyeykova, 291, 63 (1972).

17. Alibegova, Zh. D., and Shchukin, G. G., Trudy GGO im. A. I. Voyeykova, 291, 72 (1972).

18. Rosenkranz, P., Barath, F., et al., J. Geophys. Res. 77/30, 5833 (1972).

PRINCIPLES OF CONSTRUCTION OF ONBOARD RADIOMETERS

1. Formulation of Problem

Equipment intended for receiving and measuring fluxes of radiant energy in the corresponding ranges of the electromagnetic spectrum must have the following obvious properties:

1) they must be able to receive radiation with a specific spatial resolution;

2) they must have high sensitivity;

3) they must be capable of estimating quantitatively radiation fluxes to a high precision; and

4) they must make it possible to uniquely tie-in (within the limits of resolution) the fluxes measured to the spatial coordinates of the corresponding emitting elements.

Accordingly, microwave radiometers intended for remote measurements in the radio-frequency range must include at least three indispensible components:

1) an antenna system providing spatial directivity of the measured flux and its conversion into a directly measurable quantity -- antenna temperature;

2) a radiometer detector capable of measuring the antenna temperature with a given sensitivity and precision; and

3) a mapping device for uniquely comparing the position of the emitting element in space with its radiation intensity.

The different functions dictate essentially different forms of radiometer design and different approaches to radiometer construction depending on the following:

1) whether the equipment is to be placed on a stationary platform or on a mobile vehicle;

2) whether the equipment is to be operated by personnel or whether its operation is to be purely automatic; and

3) whether it is required to obtain conveniently perceivable qualitative patterns of the presence and the relative arrangement of variations in radiation intensity (gradient reception) or whether a more or less exact measurement of the absolute radiation intensities at points in the given region of space is required.

Below we will examine the general characteristics of radiometers, we will estimate their potential capabilities, and we will determine the limiting values of radiometer parameters and methods of approaching them. /110

The requirement of high sensitivity to variations in the radiobrightness temperature and the precision of their measurement when there is a constraint on the time needed to scan a certain region of space unfortunately contradicts the requirement of detailed scanning of the given region. Accordingly, when each specific problem is being solved, first one must solve the problem of the amount of detail and completeness of the information obtained, which is most intimately bound up with the method of scanning space and the method of achieving the spatial resolution.

Owing to the physical features of the specific functions, sometimes successive or simultaneous measurements at different frequencies can be necessary. In particular, when studying the atmosphere, its physical parameters, and its hydrometeorological state, several problems as was indicated above, can be solved by using a multichannel radiometer. Here several radiometer detectors must simultaneously receive radiation from general spatial elements at several frequencies.

2. Relations Between Antenna and Radiobrightness Temperatures

2-1) As indicated above, antennas in radiometers of any type must transform in as great detail as possible and as uniquely as possible the radiobrightness temperature of some spatial element, which is a measure of the intensity of its energy flux in a given direction, into the antenna temperature measured by the radiometer receiver.

Since the emitting elements in the general case as a rule are distributed continuously in space, forming some radiobrightness terrain T^b (θ, ϕ) in all the possible directions, and any actual antenna exhibits nonideal directivity properties, that is, it receives radiation energy not from one, but to some extent from all directions, which quantitatively is expressed by the front-to-back ratio G ($\theta - \theta_0$; $\phi - \phi_0$), and the antenna temperature T_a only approximately maps the radiobrightness temperature in the given direction.

The antenna temperature T_a is determined by the familiar
/1/ expression

$$T_a = \iint T^b(\theta; \varphi) \, G(\theta - \theta_0; \varphi - \varphi_0) \, d\theta \, d\varphi. \qquad (5.1)$$

Hence it follows that the mapping error depends on the position
of the axis of the antenna radiation pattern $(\theta_0; \varphi_0)$ and the
changes along with it.

Only in rare cases of investigation is it required to
measure the radiobrightness temperature in some single fixed
direction. Much more often it is necessary to investigate the
distribution of radiobrightness temperatures along some contin-
uous sequence of elements of space ("profiles") or within some
solid angle (when scanning a given two-dimensional region of
space).

Various types of antennas can be used for remote measure-
ments of radiobrightness temperature in a given direction, along
some trajectory, or within a certain region: from the
simplest -- single-element -- to complicated multi-element
antennas, with different methods of mutual multi-element
processing of signals. Single-element antennas for detailed
reproduction of radiobrightness terrain must provide for
variation in space of the location of their radiation pattern --
-- they must carry out scanning; but multi-element antennas can
in principle reproduce the radiobrightness terrain with fixed
radiation patterns owing to some program of processing signals
from different elements /2/.

Owing to a number of fundamental difficulties, multi-element
antennas thus far have found use only in radioastronomy. In
systems for investigating surfaces and the atmosphere of the
Earth and planets from flight vehicles, principally single-
element antennas with rigidly fixed beams are used in obtaining
"profiles", and with mechanical or electronic control of beam
position -- when it is necessary to scan.

As can be seen from Eq. (5.1), in theory one can reconstruct
the distribution $T^b(\theta, \phi)$ if one knows $T_a(\theta_0, \phi_0)$ and $G(- \phi_0;$
$\phi - \phi_0)$.

2-2) Let us examine three idealized cases when the solution
of the problem reduces to simple calculations.

a) If the antenna radiation pattern is ideal, infinitely
narrow, and free of side or back radiation, then

$$G(\theta - \theta_0; \varphi - \varphi_0) \equiv \delta(\theta - \theta_0) \cdot \delta(\varphi - \varphi_0),$$

where δ is the delta-function, and Eq. (5.1) yields

$$T_a(\theta_0; \varphi_0) = \iint\limits_{(4\pi)} T^b(\theta; \varphi)\, \delta(\theta - \theta_0)\, \delta(\varphi - \varphi_0)\, d\theta\, d\varphi = T^b(\theta_0; \varphi_0),$$

that is, as a result of scanning with an infinitely narrow beam free of side and rear lobes, the radiobrightness terrain is reproduced absolutely exactly, without distortions.

b) If the antenna radiation pattern is an ideal isotropic sphere, then,

$$G(\theta - \theta_0; \varphi - \varphi_0) = \frac{1}{4\pi},$$

and from Eq. (5.1) we get

$$T_a(\theta_0; \varphi_0) = \frac{1}{4\pi} \iint\limits_{(4\pi)} T(\theta, \varphi)\, d\theta\, d\varphi = (T^b)_{av},$$

that is, during scanning the antenna temperature remains constant, equal to the mean value $(T^b)_{av}$ of the radiobrightness temperature of the entire ambient space.

c) If the antenna radiation pattern is a spatial conical cone with finite width Ω_{be} with constant gain A and zero side and back lobes, then

$$G(\theta - \theta_0; \varphi - \varphi_0) =$$
$$= \begin{cases} A = \dfrac{1}{\Omega_{\pi}} & \text{for } |\varphi - \varphi_0| < \dfrac{\Delta\varphi}{2};\ |\theta - \theta_0| < \dfrac{\Delta\theta}{2}, \\[2mm] 0 & \text{for } |\varphi - \varphi_0| \geqslant \dfrac{\Delta\varphi}{2};\ |\theta - \theta_0| \geqslant \dfrac{\Delta\theta}{2}. \end{cases}$$

Here we must examine an important, often-encountered case, when the object of observation (target) with a radiobrightness temperature T^b_t visible from the antenna side at the solid angle Ω_t less than the antenna beam Ω_t is located against the background with constant radiobrightness temperature T^b_ϕ, that is

$$T^b(\theta, \varphi) = \begin{cases} T^b_\phi(\theta, \varphi) & \text{for } \Omega \in (\Omega_{be} - \Omega_t), \\ T^b_T(\theta, \varphi) & \text{for } \Omega \in \Omega_t. \end{cases}$$

where $\Omega = \Omega(\theta, \varphi)$.   Then Eq. (5.1) yields

$$T_a(\theta_0; \varphi_0) = A \int\limits_{\left(\theta_0 - \frac{\Delta\theta}{2}\right)}^{\left(\theta_0 + \frac{\Delta\theta}{2}\right)} d\theta \int\limits_{\left(\varphi_0 - \frac{\Delta\varphi}{2}\right)}^{\left(\varphi_0 + \frac{\Delta\varphi}{2}\right)} T^b(\theta; \varphi) d\varphi = \frac{1}{\Omega_{be}} \int\limits_{(\Omega_{be} - \Omega_t)} T^b_\phi(\Omega) d\Omega +$$

$$+ \frac{1}{\Omega_{be}} \int\limits_{\Omega_t} T^b_t(\Omega) d\Omega,$$

where $d\Omega = \sin\theta \, d\theta \cdot d\varphi$.   If, in addition, $T^b_\phi(\theta, \phi) = T^b_\phi = \text{const}$ and $T^b_t(\theta, \phi) = T^b_t = \text{const}$, then

$$T_a(\theta_0, \varphi_0) = \frac{T^b_\phi}{\Omega_{be}}(\Omega_{be} - \Omega_t) + \frac{T^b_t}{\Omega_{be}}\Omega_t = T^b_\phi + (T^b_t - T^b_\phi)\frac{\Omega_t}{\Omega_{be}}. \qquad (5.2)$$

Thus, in this case the antenna temperature is added from the background temperature and the temperature rise due to the object lying in the antenna beam. If the ratio of solid angles is replaced with the ratio of object area S_t to antenna beam- /113 spot area S_s, and the difference $(T^b_t - T^b_\phi)$ is the contrast $\Delta T^b_{t.\phi}$ of the target with respect to the background, we get the target parameter M_t /3_7:

$$M_t = \Delta T^b_{t.\phi} \frac{S_t}{S_s} \quad /\overline{s}po\underline{t}7 \;,$$

in terms of which it is convenient to express the antenna temperature in this case when $S_t < S_s$. In the general case of a real complex object with arbitrary distribution of radiobrightness temperature over its visible surface, the target parameter will obviously be expressed as follows:

$$M_t = \frac{1}{S_s} \int\limits_{S_t} T^b_t(\Omega) d\Omega.$$

When an object entirely fills a beam, that is, $\Omega_t \geqslant \Omega_{be}$ or $S_t \geqslant S_s$, the increment of antenna temperature due to the object will be precisely equal to the brightness temperature of the object.

2-3) In the general case, as can be seen from (5.1), the problem of reconstructing the distribution of radiobrightness terrain from the measured relief of the antenna temperature reduces to solving the Fredholm integral equation of the first kind, for which a small change in the value of T_a (for example, measurement error) can entail large changes in the unknown distribution T^b (θ, ϕ).

Introducing corrections into the quantity T_a being measured in order to bring it closer to T^b can be done from the measurements of antenna temperature in some vicinity around the point being corrected or by use of apriori information on the distribution of temperatures in this vicinity.

In those cases when operational acquisition of data on a real-time basis is needed, introducing corrections into the quantity T_a being measured in order to bring it closer to the true value of T^b is virtually impossible, and it is best to pose the problem differently: what requirements must be imposed on the antenna radiation pattern in order that the distortions of the quantity T_a being measured compared with the true value of T^b be assumed to be insignificant and acceptable.

From this point of view, the effect of the uncontrolled and random (owing to the effect of the vehicle) part of the antenna radiation pattern beyond the limits of the principal lobe and the random, in the general case, nonstationary distribution of temperatures in space is best reduced to some random, nonstationary noise at the antenna output. Statistical characteristics of this noise will be determined by the specific kind and conditions of use of G $(\theta - \theta_0, \varphi - \varphi_0)$, and also by the specific assignment of the statistical parameters T^b (ϕ, θ). Here the signal of the output of the antenna, that is, the antenna temperature, can be represented as follows:

$$
\begin{aligned}
T_a(\theta_0, \varphi_0) &= \iint\limits_{\Omega \text{pr}} T^b(\theta, \varphi) \cdot G(\theta - \theta_0, \varphi - \varphi_0) \sin\theta \, d\theta \, d\varphi + \\
&\quad + \iint\limits_{(4\pi - \Omega_{\text{pr}})} T^b(\theta, \varphi) \cdot G(\theta - \theta_0, \varphi - \varphi_0) \sin\theta \, d\theta \, d\varphi = \\
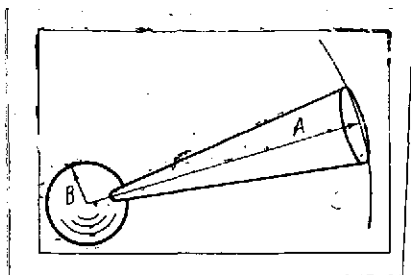&= T_{a.\text{pr}}(\theta_0, \varphi_0) + \delta T_a(\theta_0, \varphi_0).
\end{aligned}
$$

Fig. 5.1. Model of antenna radiation pattern of radiometer system

Now the signal $T_{a.pr}$ distorted by the random additive noise δT_a will be useful. Statistical properties of this noise will be determined by the structure of the antenna radiation pattern outside the principal lobe and by the distribution of brightness temperatures in the entire space around the element being resolved, which is sighted at the given instant principally by the main beam of the antenna radiation pattern. Obviously, these conditions will vary both during scanning of space by the beam of an antenna located at some fixed antenna point, as well as in the absence of scanning, but with a change in the antenna site.

The model of an antenna radiation pattern in the form of a spatial conical principal beam Ω_{be} and an isotropic spherical body in the rest of the region of space, as shown in Fig. 5.1, has gained fairly wide acceptance.

Here

$$G(\Omega) = \begin{cases} A & \text{for } \Omega \in \Omega_{be} \\ B & \text{for } \Omega \in (4\pi - \Omega_{be}). \end{cases}$$

From the condition of normalization

$$\int_{4\pi} G(\Omega)\, d\Omega = 4\pi$$

we get

$$A\Omega_{be} + B(4\pi - \Omega_{be}) = 4\pi. \tag{5.3}$$

Here the relative value of the second term is, by definition /4_7, the scattering coefficient of the antenna β:

$$\beta = \frac{B(4\pi - \Omega_{be})}{4\pi}, \tag{5.4}$$

having the physical significance of the fraction of energy
received by the antenna radiation pattern beyond the limits of
the principal lobe, with respect to total energy received by
the antenna, given the condition that the distribution of radio-
brightness temperatures in the ambient space is isotropic.

From (5.3) and (5.4) we find the model parameters:

$$A = \frac{4\pi(1-\beta)}{\Omega_{be}}, \qquad B = \frac{4\pi}{4\pi - \Omega_{be}}\beta.$$

We note that the scattering coefficient β is associated
with the flare-use factor j employed in the antenna equipment
by the simple relation

$$j = 1 - \beta.$$

When the radiobrightness temperature T_t^b is being measured
from an object with area S_t that is small compared with the area
of the antenna beam spot S_s located against a background with
brightness temperature T_Φ^b, and when the radiobrightness tempera-
ture $T_{\Phi.sc}^b$ falls in the scattering region of the antenna radiation
pattern, the antenna temperature $T_{a.sc}$ with reference to scattering,
instead of the Eq. (5.2) examined earlier, will be defined by the
relation

$$T_{a.sc} = \beta \cdot T_{\Phi.sc}^b + (1 - \beta) \cdot \angle \overline{T}_\Phi^b + \Delta T_{t,\Phi}^b \frac{S_t}{S_s} \angle =$$

$$= \angle \overline{T}_\Phi^b + \beta(T_{\Phi.sc}^b - T_\Phi^b \angle + (1 - \beta)M_t. \qquad (5.5)$$

From (5.5) it follows that owing to scattering in the antenna
temperature, the contribution made by background radiation rises
and the effective contrast of the target diminishes.

2-4) The presence of inevitable ohmic losses in the antenna
components leads to the external signals arriving at its output
attenuated by η_a times, where η_a is the system efficiency
-- defined as the ratio of signal power at output of an actual
antenna to signal power at the output of an ideal, loss-free,
antenna.

Chaotic charges and currents of a thermal nature, arising in
antenna components such as reflector, waveguide assemblies, and
so on, owing to the finite conductivity of the material, lead to
the appearance of noise fields of radiation, whose summation makes
it possible to find the natural antenna temperature, proportional
to active losses in the antenna and its kinetic temperature T_o.

If one considers the losses, the antenna temperature proves
to be associated with the radiobrightness temperatures of the
backgrounds and the object analogously, but in a somewhat more
complicated manner:

$$T_a = \eta_a \cdot T_{a.sc} + (1 - \eta_a) \cdot T_0 = \{T_0 + \eta_a [T_\phi^b - T_0] \beta (T_{\phi.sc}^b - T_\phi^b)\} + \\ + [\eta_a (1 - \beta) M_t].$$

(5.6)

Hence it follows that to find the brightness temperature of an $/116$
object T_t^b based on the antenna temperature T_a measured in real
conditions, we must know the value of η_a and β of the antenna,
its kinetic temperature T_0, and the brightness temperatures of
the background: the background lying in the antenna scattering
zone -- $T_{\phi.sc}^b$ and in the principal beam T_ϕ^b. We note that when
the target completely fills the main beam of the antenna, the
following conditions are satisfied:

$$\Omega_{be} = \Omega_t \text{ or } S_s = S_t \quad \text{and} \quad T_\phi^b = 0,$$

and Eq. (5.6) becomes

$$T_a = \eta_a (1 - \beta) \cdot T_t^b + \eta_a \beta \cdot T_{\phi.sc}^b + (1 - \eta_a) T_0.$$

(5.7)

2-5) Thermal radiation by its nature is chaotically
polarized. But on passing through interfaces with differing
dielectric properties, the radiation becomes more or less
polarized. The polarization is commonly estimated by the
polarization coefficient $\hat{K}_p$:

$$\hat{K}_p = \frac{T_\parallel^b - T_\perp^b}{T_\parallel^b + T_\perp^b},$$

where $T_\parallel^b$ and $T_\perp^b$ are the radiobrightness temperatures of the
surface under study upon reception of two components of polarized
radiation, vertical and horizontal, respectively.

In many cases of remote sensing of surfaces (cover),
receiving and measuring radiobrightness temperatures in two
independent polarization is of interest (see Chapter Two).

Since in onboard conditions the use of separate antennas for receiving polarization components of radiothermal emission is difficult, it becomes necessary to separate the total radiation energy into two components in the same antenna and to ensure the maximum possible decoupling during the reception of these two components.

Considering that the energy of the radiation received is proportional to the band of the simultaneously received frequencies and, therefore, as this band becomes larger the sensitivity of the radiometric measurements increases, often stricter requirements can be imposed on the antenna system of the radiometers as to their broad-band capacity.

Finally, when several frequency channels are used simultaneously, beams in space may have to be combined for the different wavelengths used.

3. Types of Radiometer Receivers, Their Maximum Sensitivity, /117 and Accuracy of Antenna Temperature Measurements

3-1)   A radiometer of any type is a device which, as part of a radiometer system, is designed to measure antenna temperature T_a with highest possible sensitivity and accuracy.

Since $/5/$ the measurements are taken in some finite frequency band $\Delta \nu$ and during some finite time interval τ, we can speak of the mean value of the measured energy E_τ:

$$E_\tau = \frac{h\nu}{e^{\frac{h\nu}{kT_a}} - 1} \Delta \nu \tau.$$

Owing to the statistical nature of thermal emission, the energy measured by the radiometer in the band $\Delta \nu$ in the time τ will be a random variable with the following dispersion:

$$\overline{\sigma_{E_\tau}^2} = E_\tau \left[h\nu + \frac{\overline{E_\tau}}{\Delta \nu \tau} \right].$$

The δT_a that satisfies the relation

$$\delta E_\tau = \frac{\partial E_\tau}{\partial T_a} \cdot \delta T_a.$$

can obviously be taken as the measurement error and system sensitivity.

Assuming that the maximum error of energy measurement is determined by its dispersion, let us find the condition

$$\delta E_\tau = \sigma_{E_\tau},$$

which, when the above-indicated expressions are taken into account, will yield the familiar result /5, 6/:

$$\delta T_{\mathrm{a}} = \frac{T_{\mathrm{a}}}{\sqrt{\Delta\nu\tau}} \; \frac{\mathrm{Sh}\left(\frac{h\nu}{2kT_{\mathrm{a}}}\right)}{\left(\frac{h\nu}{2kT_{\mathrm{a}}}\right)} \tag{5.8}$$

for the minimum possible error (and sensitivity) when measurements are taken of thermal noise in the band $\Delta\nu$ in the time τ.

From the equality

$$E_\tau = \sigma_{E_\tau}$$

we can find the minimum energy measured in the time τ in the frequency band $\Delta\nu$:

$$(E_\tau)_{\min} = h\nu \left[1 - \frac{1}{\Delta\nu\tau}\right]^{-1}.$$

As $\Delta\nu\tau \to \infty$, we get the obvious result: the minimum measured /118 error is one quantum. From (5.8) we can find the minimum possible measured temperature $(T_{\mathrm{a}}^{\cdot})$:

$$(T_{\mathrm{a}})_{\min} = \frac{h\nu}{k \ln (\Delta\nu\tau)}. \tag{5.9}$$

It should be noted that the minimum error of temperature measurement $(\delta T_{\mathrm{a}})_{\min}$ is found when $T_{\mathrm{opt}} > (T_{\mathrm{a}})_{\min}$, where T_{opt} is defined by the equality

$$\mathrm{th}\,\frac{h\nu}{2kT_{\mathrm{opt}}} = \frac{1}{2}\,\frac{h\nu}{2kT_{\mathrm{opt}}} \quad \text{or} \quad T_{\mathrm{opt}}\,[^\circ \mathrm{K}] = 1.25\cdot10^{-11}\nu\,(\mathrm{Hz}) \tag{5.10}$$

and depends on the frequency ν and the product $\Delta\nu\tau$:

$$(\delta T_a)_{min}[°\text{ K}] = \frac{T_{opt}}{\sqrt{\Delta v\tau}} \text{Sh} \frac{\left(\dfrac{h\nu}{2kT_{opt}}\right)}{\left(\dfrac{h\nu}{2kT_{opt}}\right)} = \frac{2.166 \cdot 10^{-11}}{\sqrt{\Delta v\tau}} \nu \bigg/ (\text{Hz}). \quad (5.11)$$

The dependence of the maximum sensitivity (and precision) of the measurement of thermal noise δT_a on level T_a, with reference to the constraint (5.9) and the extremum condition (5.10) and (5.11) is shown in Fig. 5.2.

When actual receivers are used, one must consider the additional noise produced by ohmic losses in the antenna and the line, and also the intrinsic receiver noise recalculated for the input.

In this case, the total energy arriving in the band Δf at the radiometer input E_τ will be

$$E_\tau = (1 - \eta_\ell) \cdot E_{\tau,\ell} + \eta_\ell E_{\tau,a} + E_{\tau,n},$$

where η_ℓ is the efficiency of the antenna-feeder line; $E_{\tau,a}$ is the energy of noise received by the antenna; $E_{\tau,\ell}$ is the energy of noise excited in ohmic losses of antenna and line; and $E_{\tau,n}$ is the energy of the intrinsic receiver noise, where the following relations obtain for all cases of practical importance:

$$E_{\tau,a} = kT_a \Delta f/\tau; \quad E_{\tau,\ell} = kT_\ell \Delta f/\tau; \quad E_{\tau,n} = kT_n \Delta f/\tau.$$

Now if it is assumed that

$$\delta E_\tau = \frac{\partial E_\tau}{\partial T_a} \cdot \delta T_a = \sigma_{E_\tau},$$

we easily get

$$\delta T_a = \frac{\eta_\ell T_a + (1 - \eta_\ell) \cdot T_\ell + T_n}{\sqrt{\Delta f/\tau}}. \quad (5.12)$$

If the line losses are neglected, that is, if we assume $\eta_\ell \to 1$, we get an expression that takes into account only noise in the high-frequency part of the receiver:

$$\delta T_a = \frac{T_a + T_n}{\sqrt{\Delta f/\tau}}. \quad (5.13)$$
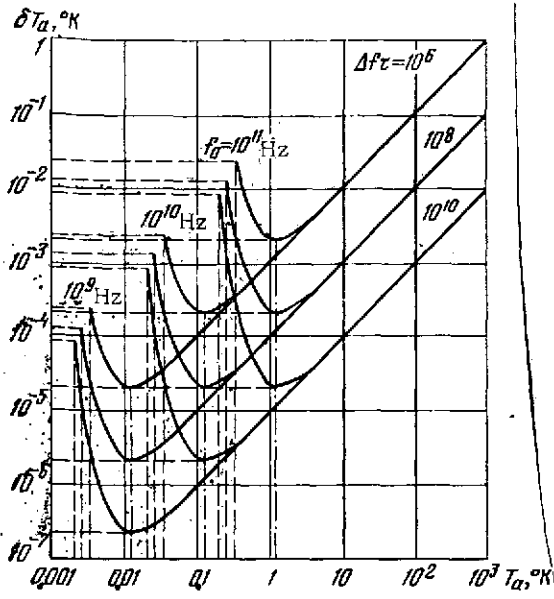
Fig. 5.2. Maximum sensitivity and accuracy of measurement of thermal radio emission

If it is assumed that there /119·) is no noise in the high-frequency part of the receiver and its square-law detector /7_/ and that intrinsic receiver noise is due only to the low-frequency line, recalculation of low-frequency noise into the equivalent temperature at the high-frequency receiver input leads to the relation

$$\sigma_{E_\tau}^2 = \sigma_{E_{\tau,a}}^2 + \sigma_{E_{\tau,n}}^2,$$

and with reference to this, we get

$$\delta T_a = \frac{\sqrt{T_a^2 + T_n^2}}{\sqrt{\Delta f \tau}}. \tag{5.14}$$

By thus examining various schemes of radiometer receivers known in the literature /8_/ (see Fig. 5.3), we arrive at relations analogous to (5.12) - (5.14), which are collected in Table 10. All these relations can be obtained by the single method indicated above and do not differ from those previously known.

3÷2) Circuits of radiometer receivers containing a reference temperature T_r irradiator connected close to the receiver input (circuits in Fig. 5.3 d, f, h, and i) have the advantage that a calibration point can be obtained in the radiometer to scale (see subsection 4÷4 of this chapter).

In addition, the value $T_r \approx T_a$ enables us to use the zero /122 method of measurement, optimizing the accuracy of the procedure; this same condition in the case of modulation methods shown in Fig. 5.3 d, f, i leads to the reduced effect of variations in the gain of the radiometer line on radiometer sensitivity /9_/.

From considerations of simplicity and operational reli- \ ability of the reference irradiators, particularly important in onboard conditions, it is convenient to use in the automated radiometer systems either $T_r \approx 0°$ K (horn oriented toward the sky) or $T_r \approx 300°$ K (matched load placed within the receiving block) as the T_r.
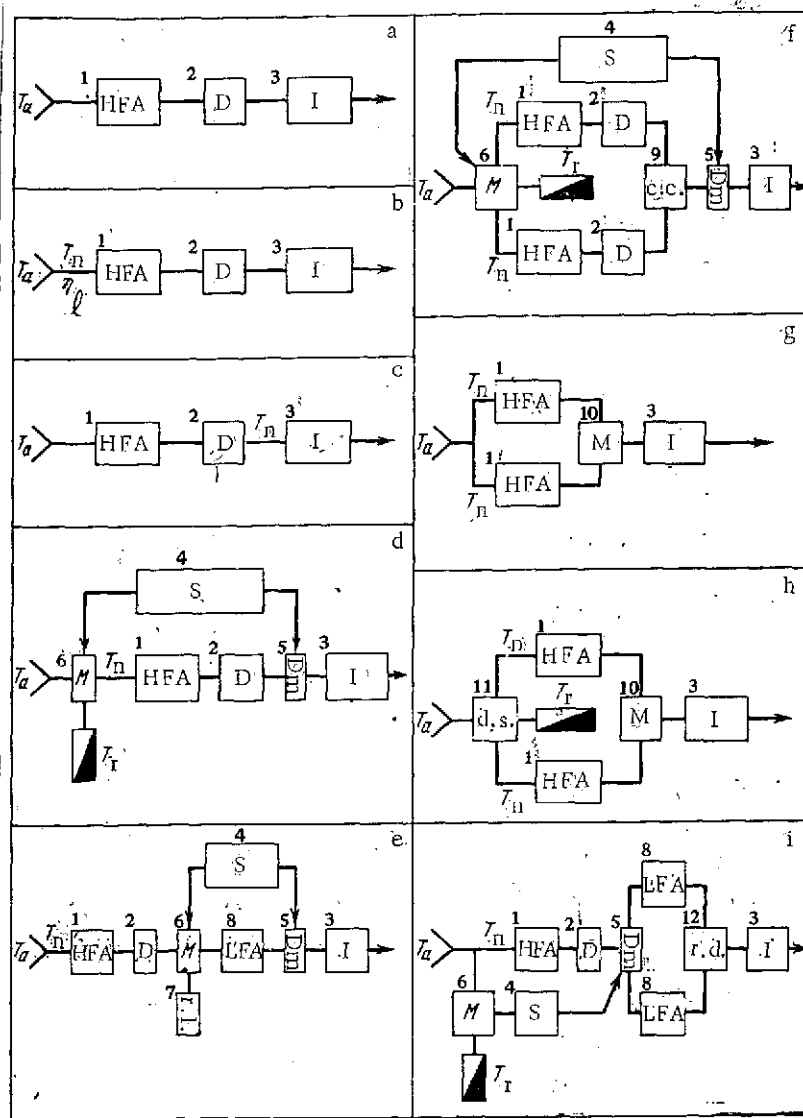
Fig. 5.3. Block diagrams of radiometer receivers
1.   HFA -- high-frequency amplifier
2.   D -- detector
3.   I -- integrator
4.   S -- synchronizer
5.   Dm -- demodulator
6.   M -- modulator
7.   r.l. -- reference load
8.   LFA -- low-frequency amplifier
9.   c.c. -- canceling circuit
10.   M -- multiplier
11.   d.s. -- difference summator
12.   r.d. -- ratio detector

TABLE 10. SENSITIVITY AND ACCURACY OF VARIOUS RADIOMETER SCHEMES /121

Nr.	Type of radiometer	Block diagram in Fig. 5.3	Sensitivity and accuracy of measurements: $\Delta = \frac{\delta T_a}{T_a}\sqrt{\Delta f \tau}$
1	Ideal noise-free power detector	a	$\Delta = \dfrac{Sh\,\frac{hf_0}{2kT_a}}{\frac{hf_0}{2kT_a}}$
2	Power detector with equivalent input noise and losses in line	b	$\Delta = (1 - \eta_\ell)\,\frac{T_\ell}{T_a} + \eta_\ell + \frac{T_n}{T_a}$
3	Power detector with equivalent input noise but without line losses	b	$\Delta = 1 + \dfrac{T_n}{T_a}$
4	Power detector with noise-free HFA and detector	c	$\Delta = \sqrt{1 + \left(\dfrac{T_n}{T_a}\right)^2}$
5	Modulation radiometer in general case	d	$\Delta = \sqrt{\left(1 + \dfrac{T_n}{T_a}\right)^2 \dfrac{\tau_1 + \tau_2}{\tau_1} + \left(\dfrac{T_r}{T_a} + \dfrac{T_n}{T_a}\right)^2 \dfrac{\tau_1 + \tau_2}{\tau_2}}$
6	Modulation radiometer when $\tau_1 = \tau_2 = \frac{1}{2}\tau$	d	$\Delta = 2\cdot\sqrt{\left(1 + \dfrac{T_n}{T_a}\right)^2 + \left(\dfrac{T_r}{T_a} + \dfrac{T_n}{T_a}\right)^2}$
7	Modulation radiometer under optimal conditions*	d	$\Delta = 1 + \dfrac{T_r}{T_a} + 2\cdot\dfrac{T_n}{T_a}$
8	Radiometer with post-detector modulation in the general case	e	$\Delta = \left(1 + \dfrac{T_n}{T_a}\right)\sqrt{1 + \dfrac{\tau_2}{\tau_1}}$
9	Radiometer with post-detector modulation when $\tau_1 = \tau_2 = \frac{1}{2}\tau$	e	$\Delta = \sqrt{2}\left(1 + \dfrac{T_n}{T_a}\right)$

TABLE 10 (continued)

Nr	Type of radiometer	Block diagram in Fig. 5.3	Sensitivity and accuracy of measurements: $\Delta=\dfrac{\delta T_a}{T_a}\sqrt{\Delta f\tau}$
10	Two-channel modulation radiometer in general case	f	$\Delta=\dfrac{1}{\sqrt{2}}\sqrt{\left(1+\dfrac{T_n}{T_a}\right)^2\dfrac{\tau_1+\tau_2}{\tau_1}+\left(\dfrac{T_r}{T_a}+\dfrac{T_n}{T_a}\right)^2\dfrac{\tau_1+\tau_2}{\tau_2}}$
11	Two-channel modulation radiometer when $\tau_1=\tau_2=\dfrac{1}{2}\tau$	f	$\Delta=\sqrt{\left(1+\dfrac{T_n}{T_a}\right)^2+\left(\dfrac{T_r}{T_a}+\dfrac{T_n}{T_a}\right)^2}$
12	Two-channel modulation radiometer under optimal conditions*	f	$\Delta=\dfrac{1}{\sqrt{2}}\left(1+\dfrac{T_r}{T_a}+2\dfrac{T_n}{T_a}\right)$
13	Correlation radiometer with common antenna	g	$\Delta=\dfrac{1}{\sqrt{2}}\sqrt{1+\left(1+\dfrac{T_n}{T_a}\right)^2}$
14	Difference-summator radiometer	g	$\Delta=\dfrac{1}{\sqrt{2}}\sqrt{1+\left(1+\dfrac{T_n}{T_a}\right)^2+2\dfrac{T_r}{T_a}\left(\dfrac{T_r}{T_a}+\dfrac{T_n}{T_a}\right)}$
15	Radiometer with addition of reference noise at input	h	$\Delta=2\cdot\left(1+\dfrac{T_n}{T_a}\right)\left(1+\dfrac{1+\dfrac{T_n}{T_a}}{\dfrac{T_r}{T_a}}\right)$

* $\dfrac{\tau_1}{\tau_2}=\dfrac{T_a+T_n}{T_r+T_n}.$

The antenna temperatures observable in practice usually lie either close to $T_a\approx 0^\circ$ K (radioastronomical observations) or $T_a\approx 150^\circ$ K (observations of bodies of water), or else close to $T_a\approx 300^\circ$ K (surface of continental land masses).

$$lg\left(\frac{\delta T_a}{T_a}\sqrt{\Delta f \cdot \tau}\right)$$
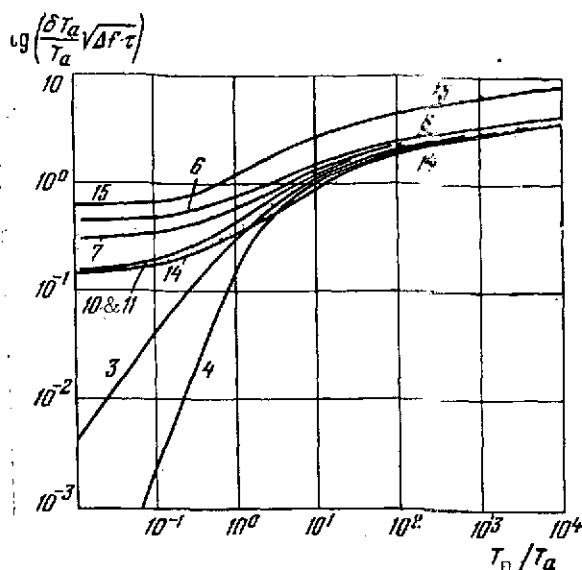
Fig. 5.4. Sensitivity and accuracy of measurement of antenna temperatures using different types of radiometer receivers
The numbers alongside curves refer to the locations in Table 10

Thus, from the practical standpoint it is best to examine the sensitivity of radiometer receivers of the types 6, 7, 11, 12, 14, and 15 from Table 10, when T_n/T_a undergoes variation over fairly broad limits for four possible cases: $T_r \approx 0^\circ$ K;

$T_r \approx 1/2\ T_a$; $T_r \approx T_a$; and $T_r \approx 2T_a$.

The corresponding expressions for Δ:

$$\Delta = \frac{\delta T_a}{T_a}\sqrt{\Delta f \tau},$$

-- relative maximum sensitivity and accuracy of temperature measurement using these schemes -- had been collected in Table 11, and the characteristic shape of the corresponding curves for the case $T_r \approx T_a$ is shown in Fig. 5.4. Also given in this figure, for comparison, is the dependence of the sensitivity of the block diagram with noise-free HFA and detector, and the block diagram with noise only in high frequencies (positions 4 and 3 in Table 10).

A closer examination of this problem shows that:

1) as T_n increases compared to T_a (for example, in radioastronomy) differences in radiometer schemes are smoothed over, and, conversely, when relatively high antenna temperatures T_a are being measured (for example, in scanning the Earth's surface) using low-noise receivers, selection of the radiometer type becomes increasingly substantive;

2) in the case of low-noise receivers (that is, when $T_n \ll T_a$), it is advantageous to select as T_r the lowest possible values; this increases the specific sensitivity and accuracy of measurements (if, of course, this is not interfered with by variations in the radiometer line gain); /125

3) two-channel radiometer schemes (such as f and g or h in Fig. 5.3) increase sensitivity compared with the corresponding single-channel radiometers; and

TABLE 11. SENSITIVITY AND ACCURACY OF RADIOMETERS CONTAINING REFERENCE STANDARD LOAD

Radiometer type	Position in Table 10	Block diagram in Fig. 5.3.	$\Delta = \dfrac{\delta T_a}{T_a} \cdot \sqrt{\Delta f \cdot \tau}$			
			$T_r = 0$	$T_r = \frac{1}{2} T_a$	$T_r = T_a$	$T_r = 2T_a$
Single-channel modulation radiometer for $\tau_1 = \tau_2 = \frac{1}{2}\tau$	6	d	$2\cdot\sqrt{1+2\frac{T_n}{T_a}+2\left(\frac{T_n}{T_a}\right)^2}$	$2\cdot\sqrt{1.25+3\frac{T_n}{T_a}+2\left(\frac{T_n}{T_a}\right)^2}$	$2\sqrt{2}\cdot\left(1+\frac{T_n}{T_a}\right)$	$2\cdot\sqrt{5+6\frac{T_n}{T_a}+2\left(\frac{T_n}{T_a}\right)^2}$
Single-channel modulation radiometer with optimal τ *	7	d	$1+2\frac{T_n}{T_a}$	$1.5+2\frac{T_n}{T_a}$	$2\cdot\left(1+\frac{T_n}{T_a}\right)$	$3+2\frac{T_n}{T_a}$
Two-channel modulation radiometer for $\tau_1 = \tau_2 = \frac{1}{2}\tau$	11	f	$\sqrt{1+2\frac{T_n}{T_a}+2\left(\frac{T_n}{T_a}\right)^2}$	$\sqrt{1.25+3\frac{T_n}{T_a}+2\left(\frac{T_n}{T_a}\right)^2}$	$\sqrt{2}\cdot\left(1+\frac{T_n}{T_a}\right)$	$\sqrt{5+6\frac{T_n}{T_a}+2\left(\frac{T_n}{T_a}\right)^2}$
Two-channel modulation radiometer for optimal τ *	12	f	$\frac{1}{\sqrt{2}}\left(1+2\frac{T_n}{T_a}\right)$	$\frac{1}{\sqrt{2}}\left(1.5+2\cdot\frac{T_n}{T_a}\right)$	$\sqrt{2}\left(1+\frac{T_n}{T_a}\right)$	$\frac{1}{2}\left(3+2\cdot\frac{T_n}{T_a}\right)$
Difference-summator radiometer	14	h	$\sqrt{1+\frac{T_n}{T_a}+\frac{1}{2}\left(\frac{T_n}{T_a}\right)^2}$	$\sqrt{1.25+1.5\frac{T_n}{T_a}+\frac{1}{2}\left(\frac{T_n}{T_a}\right)^2}$	$\sqrt{2+2\frac{T_n}{T_a}+\frac{1}{2}\left(\frac{T_n}{T_a}\right)^2}$	$\sqrt{5+6\frac{T_n}{T_a}+\frac{1}{2}\left(\frac{T_n}{T_a}\right)^2}$
Radiometer with addition of reference noise at input	15	i	∞	$2\cdot\left[3+5\frac{T_n}{T_a}+2\left(\frac{T_n}{T_a}\right)^2\right]$	$2\cdot\left[2+3\frac{T_n}{T_a}+\left(\frac{T_n}{T_a}\right)^2\right]$	$2\cdot\left[1.5+2\frac{T_n}{T_a}+\frac{1}{2}\left(\frac{T_n}{T_a}\right)^2\right]$

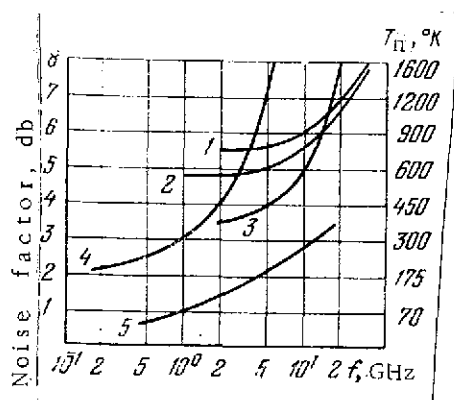$* \quad \dfrac{\tau_1}{\tau_2} = \dfrac{T_a+T_n}{T_r+T_n}$

Fig. 5.5. Dependence of
noise temperature of
various microwave receivers
on frequency
1. Point diodes
2. Schottky diodes
3. Tunnel diodes
4. Transistors
5. Parametric amplifiers

4) the scheme of a difference-summator radiometer, beginning at some value of T_n/T_a, is preferential for any T_r; this circumstance is all the more substantial, in that losses in difference-summator microwave elements can be made less than in modulators.

These relations (Table 11) and the corresponding graphical representations can also solve the problem of choosing the microwave radiometer, from among those available commercially, that is the most suitable for a specific application of the input device.

As an example, in Fig. 5.5 are presented plots of the frequency dependence of the noise temperature of various microwave receivers /10/.

Comparison of the data in Figs. 5.4 and 5.5 (or similar figures) permits a straight-forward optimal selection of the design scheme of a particular frequency channel.

4. Calibration of Radiometer Equipment

4-1) Calibration is required for the interpretation of the results of radiometric measurements, that is, establishing a mutually-unique correspondence between the brightness temperature of an element in space under scrutiny and the output readings of the radiometer system.

The most adequate calibration method involves an array /126 of space elements corresponding precisely to the spatial resolving power of the system and exhibiting different known radiobrightness temperatures in the range being measured. This method could experimentally establish the kind of dependence between the intensity of output system readings and the corresponding radiobrightness temperatures -- it could formulate the radiometer scale. However, in practice this procedure is difficult to realize.

The resolved areas in the radio range under actual ranges used can be several meters to tens of kilometers. Therefore constructing a system of these artificial "elements" with precision values for the various radiobrightness temperatures is a technically extremely complicated task, as well as unquestionably most expensive.

Natural objects suitable in size and contrast can be used for calibration purposes -- so-called external calibration; however, even under the most favorable conditions there are difficulties in finding the necessary number of objects with the required degree of contrast. Moreover, nonuniformity of radiobrightness temperature within the area, and the effect on radiobrightness temperature of meteorological conditions, as well as the inconstancy of its emission characteristics with time affect the precision of the calibrations thus obtained.

Transforming radiobrightness temperatures into the output response of the radiometer system, as was shown earlier, involves forming by means of the antenna, at the receiver input, a signal whose intensity is called the antenna temperature, followed by the transformation of the signal into the output voltage (or current) whose value is recorded with a meter or recorder.

Therefore calibrating a radiometer system in principle can proceed component by component: separately for the antenna system and separately for the radiometer receiver. This procedure of calibration is especially sound in those cases when the equipment must operate for a more or less prolonged period without direct human participation of a human operator in the measurement process, particularly for an automatically operating radiometer installed on space vehicles. Artificial "reference" radiotemperatures and "reference" natural objects with known radiobrightness contrasts are used for "external" calibrations, and also for checking and refining the componentwise calibrations and for "tying" them into actual working conditions of the radiometer system.

4-2) Let us look at the problems of calibrating antenna systems /11/.

As we can see from the expression for the antenna temperature (5.7), calibrating an antenna reduces to determining its /127 efficiency η_a and the scattering coefficient β. In the case of uniform ambient radiobrightness temperature when $T^b_{pr} = T^b_{\Phi.sc} = T^b_z$ (below we will show that it is useful to select this temperature equal to the zenith temperature T^b_z), Eq. (5.7) becomes

$$T_a = \eta_a T^b_z + (1 - \eta_a) T_o,$$
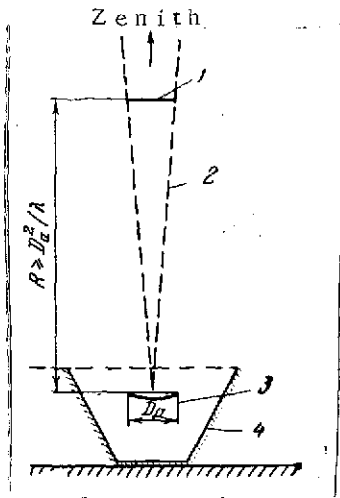
134}

Fig. 5.6. Antenna
calibration scheme
1. Absorbing emitter disk
2. Principal lobe of
    antenna radiation
    pattern
3. Antenna being cali-
    brated
4. Conductive shield

and from this we can find the
value η_a:

$$\eta_a = \frac{T_0 - T_a}{T_0 - T_z^b}.$$

In addition, as this expression
shows, the measurement accuracy
will be higher, the lower we
select T_z^b compared with T_0.

Actually, T_{pr} and $T_{\phi.sc}^b$ can
be made extremely close to each
other and small in magnitude if
the antenna is placed over a
curved, well-conductive surface
in such a way that the sky
radiation from the region of
zenith angles with zenith tem-
perature T_z^b would be reflected
into the region of side and rear
lobes of the radiation pattern
of the antenna system (see Fig.
5.6).

For the zenith sky temperatures to be low, calibration must
be carried out as far as possible under clear atmospheric condi-
tions. Obviously, when working in the wavelength ranges close
to the absorption lines of atmospheric gases (these include the
inevitable water vapor and oxygen in the radio range), it may
prove useful to perform the calibrations in mountainous locales,
at sufficient elevations above sea level and at low humidities.

The zenith temperature T_z^b can be measured with high accuracy
by reference standard horns with standard gain /12/ or else the
zenith temperature can be calculated theoretically from the known
temperature, humidity, and pressure in the experimental location
/13/.

It should be noted that owing to the nondependence of
active losses on antenna temperature, repeating the measurements
at different T_0 can be done to refine the measured value η_a.

Now, β also can be determined from the same equation, if   /128
the region of the principal lobe of the antenna radiation pattern
at the level of the first nulls is filled with an emitter having

known brightness temperature, as can be seen in Fig. 5.6. Naturally, this emitter must be at the distance R from the antenna, where the lobe structure of the antenna radiation pattern is already quite well defined, that is, R must satisfy the condition

$$R \gg \frac{D_a^2}{\lambda}.$$

where D_a is the antenna diameter.

It is simplest to use as the emitter a material that is absolutely absorptive at the given wavelength (an absolute blackbody) with brightness temperature equal to its kinetic temperature T_{em}, which can be measured to high accuracy over the entire surface of the material using temperature sensors, then averaged. The position of the emitter in the principal lobe can be found from the antenna temperature maximum $(T_a)_{max}$, and the accuracy of this position proves not to be highly critical, since the edge of the emitter falls in the region of the null level of the principle antenna lobe.

Then, based on (5.7), the antenna temperature of the system can be associated with the remaining parameters by the following expression:

$$(T_a)_{max} = \eta_a (1 - \beta) \cdot T_{em} + \eta_a \beta \cdot T_z^b + (1 - \eta_a) \cdot T_o,$$

from which we can find the single unknown, β:

$$\beta = \frac{\eta_a \cdot T_{em} + (1 - \eta_a) \cdot T_o - (T_a)_{max}}{\eta_a (T_{em} - T_z^b)}.$$

When once measured, the values of η_a and β for an entire system can change: η_a can change when there is a change in the surface conductivity of the material of which the antenna system is made, and β can change when the components of the antenna are shifted with respect to each other or when there are changes in the position of the antenna with respect to the body of the space vehicle (for example, during scanning).

From the foregoing there follows the vital importance of the technological (especially with respect to the coatings) and design development of the antenna, its components, and their placement on the space vehicle from the standpoint of subsequent interpretation of the resulting experimental data.

4-3) Let us look at the calibration of radiometer receivers. Calibration of a radiometer receiver is intended to find a relationship between the amplitude of the output signal and the antenna temperature which arrives at the input of the receiver.

The antenna temperature -- a quantity proportional to the microwave power /14/ brought to the receiver input -- undergoes linear amplification and subsequent detection in the channel, and considering the actual power levels of thermal microwave signals, the detection can always be assumed to obey the square law. But the response of a square-law detector (in the form of current or voltage) is proportional to the high frequency power applied at its input /15/.

Thus, in principle, a linear relationship of the following type must exist between antenna temperature T_a at the input of a radiometer receiver and the amplitude of its output signal U:

$$U = aT_a + b.$$

Here, as shown by detailed studies, the initial point on the scale is determined generally by the nonideality of matching between the various components of the high frequency part of the radiometer receiver /16/, which can change due to various factors and, in particular, when there is a change in the frequency of the signal being received. Also, since the quality of matching the high frequency lines as a rule is degraded with expansion of the band of frequencies received, instability of heterodyne frequency is one of the main causes of variations in b for broad-band superheterodyne radiometer receivers.

The curvature of scale a is determined mainly by the gain of the antenna components and by losses in the passive elements of the receiver line and thus variations of curvature arise when there are numerous variable external influences on these components and elements.

To eliminate the effect of variations in a and b on the reference accuracy of the antenna values, the scale must be calibrated (that is, the determination of the instantaneous values of the curvature and the starting point of the scale) periodically, at time intervals shorter than the correlation time of the corresponding variations.

In principle, based on the linear relationship between U and T_a, to calibrate a radiometric scale it is sufficient to periodically connect two emitters with precisely known temperatures

T_{a1} and T_{a2} to the input of the radiometer receiver and then to record the corresponding output signals U_1 and U_2. On the condition that in this calibration the signals pass through the entire line, from the line input (including the antenna emitter) to the output, the coefficients a and b can be readily found in the form

$$a = \frac{U_1 - U_2}{T_{a1} - T_{a2}}, \quad b = \frac{T_{a1}U_2 - T_{a2}U_1}{T_{a1} - T_{a2}},$$

and by reading the signal U obtained when the unknown temperature /130 T_a is measured, its value can be found uniquely:

$$T_a = \frac{(T_{a1} - T_{a2})U + (T_{a2}U_1 - T_{a1}U_2)}{U_1 - U_2}.$$

To increase the accuracy when there are marked changes in the parameters a and b, in the two successive calibrations it is best to use their interpolated values. However, when the equipment is used onboard, this calibration method can encounter serious difficulties.

In aircraft conditions, especially when an operator is onboard, his access to the input elements of the complete receiver line (that is, essentially, to the antenna emitter), during the flight proves to be impossible and therefore the problem of remote connection and disconnection of the reference standard temperatures at the times of calibration arises.

In the case of unmanned flight vehicles, this problem is complicated by the necessity of the total automation of calibration.

In several cases providing two precision temperature reference standards and their matching at the input during switchings can become a serious problem. Sometimes these difficulties are insurmountable and compromises must be resorted to -- simplified engineering solutions must be found at the cost of lowered calibration accuracy.

4-4) One variant of this simplified calibration system is the employment at reference temperatures of the low sky temperature (or the space temperature) obtained by means of a weakly directional horn oriented at the zenith or into free space, and the temperature of a well-matched load built in close to the receiver by design /17/.

Since of the above-examined types of radiometer receivers (see subsection 3-2), modulation radiometers have several technical and operational advantages, they are used much more often than the others.

Let us examine the main problems associated with calibrating a modulation radiometer receiver placed on a space vehicle.

Clearly, the receiving antenna and the reference horn must be placed outside the body of the space vehicle and connected to the receiver located within the body with more or less long lines exhibiting the inevitable ohmic losses. Also, it is obvious that the lines connecting the receiving antenna and the reference horns with the receiver can have different kinetic temperatures over its sections: outside the vehicle -- the external temperature T_{ex}, within the vehicle, from its walls to the receiver housing -- the internal temperature T_{in}, and within the receiver, due to heating from heat-releasing elements -- the receiver temperature T_r.
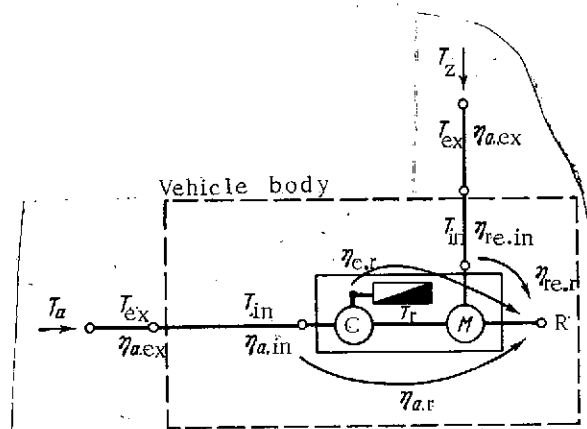
Fig. 5.7. Scheme of distribution of losses and temperatures in elements of high frequency line of modulation radiometer
C = commutator
M = modulator
R = receiver
The remaining symbols are explained in the text.

By singling out within each line (antenna line "a" and reference line "re") the sections that are at these indicated temperatures and by characterizing the losses in these sections with the appropriate deficiencies, as is shown in the scheme in Fig. 5.7, we can find the conditions under which the radiometer scale can be calculated and we can find the factors affecting calibration precision /187.

Using the rule of temperature reconversion /19/ when a signal passes through loss-exhibiting elements, as was done in the left-hand side of the double equation (5.6), we get the result that in the working regime the temperature T_a is recalculated from the antenna input of the radiometer to the receiver input

to point R (see Fig. 5.7), as $T_{a.r}$:

$$T_{a.r} = \{[T_a\eta_{a.ex} + (1 - \eta_{a.ex}) \cdot T_r]\eta_{a.in} + (1 - \eta_{a.in})T_{in}\}\eta_{a.r} + \\ + (1 - \eta_{a.r})T_r. \tag{5.15}$$

where $\eta_{a.ex}$, $\eta_{a.in}$, and $\eta_{a.r}$ are the efficiencies of the external, internal, and commutation parts of the antenna line, respectively.

Similarly, for the zenith temperature T_z^b recalculated across the reference line at the receiver input to the point R, we get $T_{z.r}$

$$T_{z.r} = \int [T_z^b \eta_{re.ex} + (1 - \eta_{re.ex}) \cdot T_{ex}]\eta_{re.in} + (1 - \eta_{re.in})$$
$$T_{in} \int \eta_{re.r} + (1 - \eta_{re.r})T_r, \tag{5.16}$$

where $\eta_{re.ex}$, $\eta_{re.in}$, and $\eta_{re.r}$ are the efficiencies of the external, internal, and commutation parts of the reference line, respectively.

In the calibration mode, when instead of the antenna, we connect to the modulator M by means of commutator C the matched load, usually within the limits of the high-frequency head of the receiver and therefore at the temperature T_r, at point R we get the temperature $T_{c.r}$:

$$T_{c.r} = T_r\eta_{c.r} + (1 - \eta_{c.r})T_r = T_r, \tag{5.17}$$

where $\eta_{c.r}$ is the efficiency of the commutation part of the line in the calibration mode.

Bearing in mind, further, that in a modulation radiometer receiver, the output signal U is linearly associated not with the actual temperature being measured, but with the difference between the values of the measured and reference temperatures at the modulator output, that is, at point R, we find that when the antenna is connected the output signal will be U_a:

$$U_a = S[T_{a.r} - T_{z.r}] + U_o, \tag{5.18}$$

and in the calibration mode, when the matched load is connected the output signal will be U_c:

$$U_c = S\,[T_{c.r} - T_{z.r}] + U_{re},$$ (5.19)

where the curvature of the scale S and the initial value of signal U_{re} at the output of the receiver are assumed identical in both measurements.

When taking the voltage from a variable voltage modulator from the reference generator, at the output of the modulator we obtain conditions that are equivalent to the situation where $T_{c.r} - T_{z.r} = T_{a.r} - T_{z.r} = 0$. Therefore, at this recorded modulation the output signal gives us the value U_{re}, which thus becomes known to us.

Using relations (5.15) – (5.19) and introducing for brevity the notation

$$\eta_a = \eta_{a.ex}\,\eta_{a.in}\,\eta_{a.r}, \qquad \eta_{re} = \eta_{re.ex}\cdot\eta_{re.in}\cdot\eta_{re.r},$$

we can find the measured quantity T_a:

$$
\begin{aligned}
T_a = \frac{U_a - U_{re}}{U_c - U_{re}}\Bigg[&(T_{ex} - T_z)\frac{\eta_{re}}{\eta_a} + (T - T_{ex})\frac{\eta_{re.in}\,\eta_{re.r}}{\eta_a} + \\
&+ (T_r - T_{in})\frac{\eta_{re.r}}{\eta_a}\Bigg] + \Bigg[T_z\frac{\eta_{re}}{\eta_a} - T_{in}\left(\frac{\eta_{re}}{\eta_a} - 1\right) - \\
&- (T_{in} - T_{ex})\frac{\eta_{re.in}\,\eta_{re.r} - \eta_{a.in}\,\eta_{a.r}}{\eta_a} - \left(T_r - T_{in}\right)\frac{\eta_{re.r} - \eta_{a.r}}{\eta_a}\Bigg].
\end{aligned}
$$ (5.20)

Here the expression in the first brackets corresponds to the scale curvature, and in the second -- to the initial temperature.

Thus, the antenna temperature under this calibration system is determined not only by the measured values of the output readings of the radiometer and the temperature sensors, but also by the losses in individual sections of the lines.

If all the losses in the lines are absent, then $\eta_a = \eta_{re} = 1$ and

$$T_a = \frac{U_a - U_{re}}{U_c - U_{re}}[T_r - T_z^b] + T_z^b.$$

If there are losses, but the entire line is at a constant tempera-ture, that is, $T_{ex} = T_{in} = T_r = T_{re}$, then

$$T_a = \frac{U_a - U_{re}}{U_c - U_{re}} \left[(T_{re} - T_z^b) \frac{\eta_{re}}{\eta_a} \right] + \left[T_{re} - (T_{re} - T_z^b) \frac{\eta_{re}}{\eta_a} \right]$$

and only the loss ratio η_{re}/η_a will affect the determination of T_a.

4-5) When equipment is used in actual conditions, there are variations in the losses due to random external actions. The following can have the strongest effect in the case of satellite equipment:

1) the effect, with time, of the actual atmosphere on the physicochemical condition of the coatings and their conductivity;

2) periodic changes in the external temperature, leading to variable deformations of lines and subsequent residual effects;

3) vibrational and linear mechanical stresses during trans-porting of the equipment and its launch; and

4) mechanical stresses and deformations that arise when there are pressure drops within and outside the satellite body in the various stages of its use.

Accordingly, it is of interest to estimate the possible variations of losses in lines, the effect of variations on the error of measuring the antenna temperature, and to find the conditions under which the effect of variations is brought to a minimum.

In the simplified case we are considering, the structure of the expression enables us to draw appropriate conclusions concerning the optimal conditions of operation without special analysis.

If we regroup the terms in the second square bracket of (5.20) in the way indicated below:

$$\begin{aligned}
T_a = \frac{U_a - U_{re}}{U_c - U_{re}} &\left[(T_{ex} - T_z^b) \frac{\eta_{re}}{\eta_a} + (T_{in} - T_{ex}) \frac{\eta_{re.in}\eta_{re.r}}{\eta_a} + (T_r - T_{in}) \frac{\eta_{re.r}}{\eta_a} \right] - \\
&- \left[(T_{ex} - T_z^b) \frac{\eta_{re}}{\eta_a} + (T_{in} - T_{ex}) \frac{\eta_{re.in}\eta_{re.r}}{\eta_a} + (T_r - T_{in}) \frac{\eta_{re.r}}{\eta_a} \right] + \\
&+ \left[T_{ex} + (T_{in} - T_{ex}) \frac{\eta_{a.in}\eta_{a.r}}{\eta_a} + (T_r - T_{in}) \frac{\eta_{a.r}}{\eta_a} \right],
\end{aligned} \qquad (5.21)$$

then it becomes clear at once that working with the temperature of the matched load, equal to the antenna temperature (the earlier-noted null regime) yields

$$\frac{U_a - U_{re}}{U_c - U_{re}} = 1,$$

and the first two bracketed terms in Eq. (5.21) are mutually cancelled out. Here the effect of three loss ratios: η_{re}/η_a, $\eta_{re.in}\eta_{re.r}/\eta_a$, and $\eta_{re.r}/\eta_a$ is eliminated, and the measurement error will be determined by the last square brackets in Eq. (5.21).

It can easily be seen that equalizing the temperatures $T_{ex} = T_{in} = T_r$ eliminates the effect also of the remaining two loss ratios in the lines $(\eta_{a.in}\eta_{a.r})/\eta_a$ and $(\eta_{a.r})/\eta_a$.

The ideal conditions of null measurements and the isothermicity of all the equipment components is scarcely realized in practice, but the effect of measurement errors due to random variations in the loss ratios in the lines can be appreciably reduced if the following two conditions are satisfied:

1) the temperature of the matched load is taken equal to the mean value of the possible range of the antenna temperatures measured; and

2) as far as possible, an effort is made to equalize the temperatures of the equipment components housed within and without the satellite body.

5. Satellite Equipment for Observing and Measuring Microwave Radiation of the Earth

Four frequency channels with the following operating wavelength $\lambda_1 = 8.5$ cm, $\lambda_2 = 3.4$ cm, $\lambda_3 = 1.35$ cm, $\lambda_4 = 0.8$ cm, were proposed for measurements of the radiothermal emission of Earth cover and Earth atmosphere from outer space.

As was already indicated above, this set of wavelengths makes it possible to acquire data on the temperature and condition of the underlying surfaces, on the integrated humidity of the atmosphere, and on the moisture content of cloud formations and precipitation.

A block diagram of the equipment is shown in Fig. 5.8. The functional connections within each frequency channel are identical for the most part, and so only the 3-centimeter channel is shown in detail in the diagram.

The received antenna signal of thermal radio emission travels via the external waveguide (a coaxial cable for a channel with $\lambda_1 = 8.5$ cm) into the internal hermetized satellite compartment. Along the internal waveguides (or the coaxial cables, in accordance with the channel wavelengths) the signal arrives via a slow-acting commutator C that serves for periodic calibration of the radio- /135 metric scale of the channel at a fast-acting commutator-modulator M. Continuously, the modulator compares at a high frequency the noise temperature of the signal arriving from the antenna with the temperature of signal arriving from the reference line (RL), which consists of a weakly directional horn oriented continuously toward free outer space, and external or internal waveguides or coaxials.

A modulated noise signal arrives at the output of the modulator during measurements; the intensity of this noise signal changes from the value corresponding to the reference line temperature, up to the value corresponding to the antenna temperature to be measured.

Through the decoupler (Dec) this signal arrives at the input of the superheterodyne receiver, built in the form of two modules by design: a high-frequency head and a low-frequency block.

The high-frequency head includes the slow- and fast-acting commutators, matched load, balance mixer M, klystron heterodyne H, and the intermediate frequency, low-noise-generating preamplifier -- IFPA. Photographs of the high-frequency heads of channels with $\lambda_1 = 8.5$ cm and $\lambda_4 = 0.8$ cm are shown in Figs. 5.9 and 5.10, respectively, and give an idea of their size and design.

To improve the mechanical characteristics, the high-frequency heads with all of their elements were coated with foam-epoxy resin, forming a monolithic block. The strongly heating klystron hetero- /138 dyne was mounted to the monoblock from the external side.

144
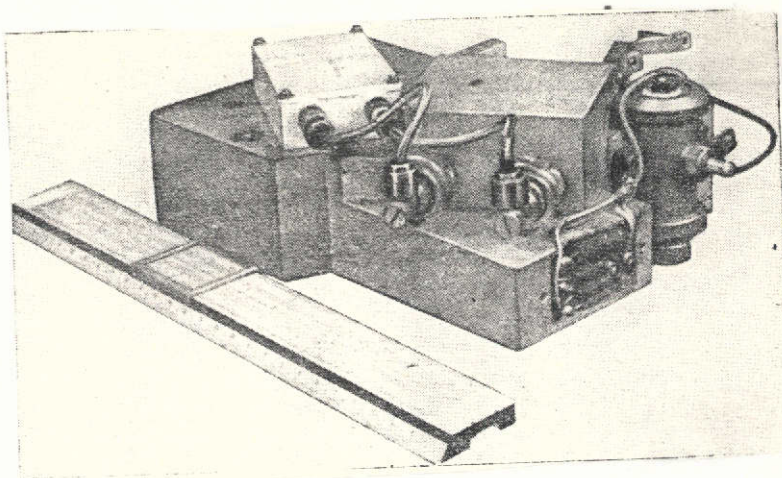
Fig. 5.9. High-frequency head of channel with λ_1 = 8.5 cm
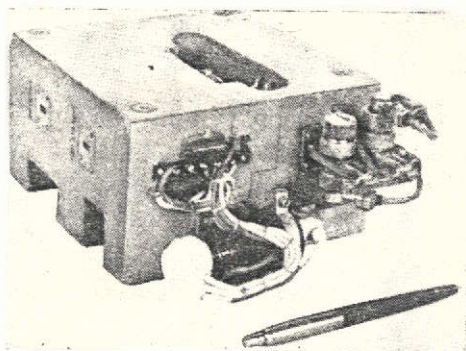
Fig. 5.10. High-frequency head of channel with λ_4 = 0.8 cm
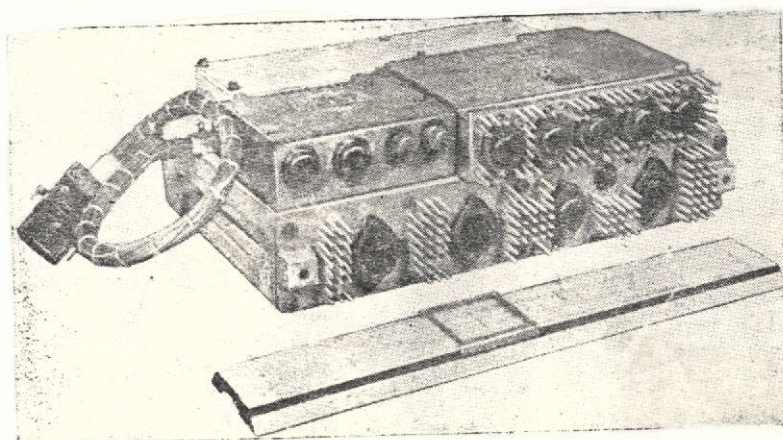
Fig. 5.11. Low-frequency block
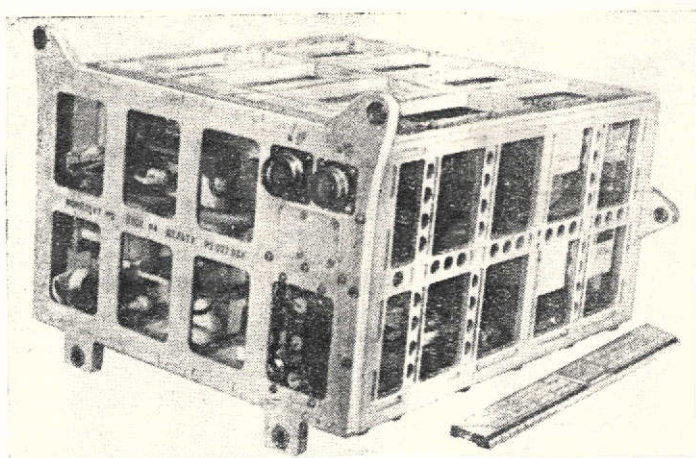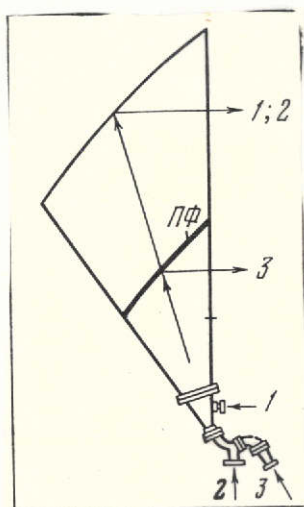
Fig. 5.12. Layout of two short-wave radiometers

Fig. 5.13. Scheme of combined three-range antenna
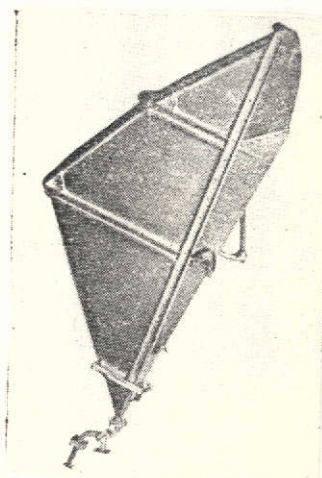Numbers represent channel numbers; ПФ is the polarization filter
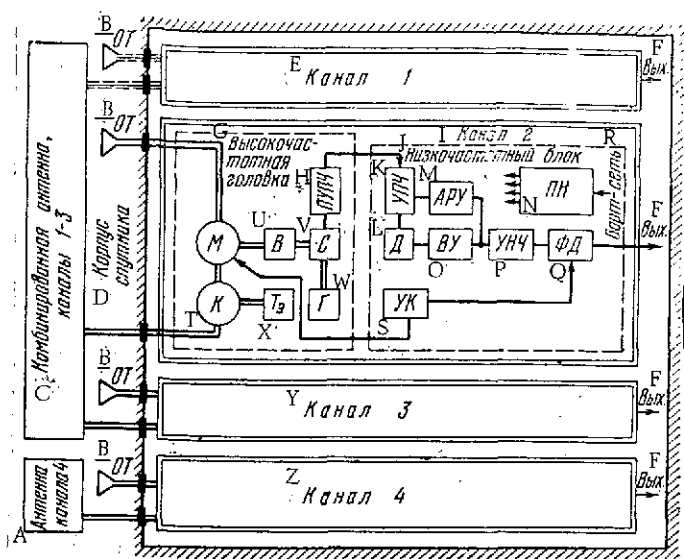

Fig. 5.14. Combination three-range antenna

Fig. 5.8. Block diagram of a satellite radiometer

KEY:
- A. Antenna of channel 4
- B. RL -- reference line
- C. Combined antenna, channels 1-3
- D. Satellite body
- E. Channel 1
- F. Output
- G. High-frequency head
- H. IFPA -- intermediate frequency, low-noise-generating preamplifier
- I. Channel 2
- J. Low-frequency block
- K. IFA -- intermediate frequency amplifier
- L. D. Detector
- MM. AGC -- automatic gain control
- N. VC -- voltage converter
- O. VA -- video amplifier
- P. LFA -- low-frequency amplifier
- Q. PD -- phase detector
- R. Onboard power line
- S. CU -- commutation unit
- T. C -- commutator
- U. Dec -- decoupler
- V. M -- mixer
- W. H -- klystron heterodyne
- X. T_{ref} -- reference temperature
- Y. Channel 3
- Z. Channel 4

The low-frequency block includes a voltage converter (VC) of the onboard line in the voltage ratings necessary to power all the electronic circuits, the primary intermediate frequency amplifier IFA with a second detector D, a video amplifier VA, and the automatic gain control circuit (AGC), a modulation frequency amplifier LFA /low-frequency amplifier/ with phase detector (PD), and a commutation unit CU synchronizing the operation of the modulator at the channel input with the phase detector at its output.

A photograph of the low-frequency block is shown in Fig. 5.11. Each low-frequency block, for the same considerations of mechanical strength, is coated with foam-epoxy resin or foam polyurethane.

Pairwise, the radiometer channels (two long-wave channels with λ_1 = 8.5 cm and λ_2 = 3.4 cm, and two short-wave channels, with λ_3 = 1.35 cm and λ_4 = 0.8 cm) are connected with light metal frames, which are mounted within the satellite body.

Fig. 5.12 shows a photograph of the frame connecting two short-wave radiometers.

For economy of space and alignment of the radiation pattern axes, the antenna for the first
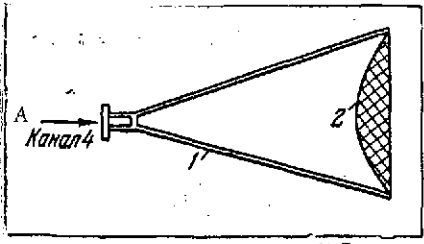
Fig. 5.15. Diagram of horn-lens antenna for the 8 mm range
1. Horn
2. Lens (block polystyrene)
KEY: A. Channel 4

three long-wave channels is made in common, a combined antenna.

The design principle of the combined antenna is clear from Fig. 5.13. It is a horn-parabolic antenna with a special polarization semitransparent near-filter (ПФ) installed in a bellmouth. The primary mirror and the polarization filter are segments of confocal paraboloids of revolution. Polarization of channels

TABLE 12. MAIN PARAMETERS OF EQUIPMENT INSTALLED ON
KOSMOS 243 AND KOSMOS 384 SATELLITES

Equipment parameter	Channels			
	1	2	3	4
Wavelength, cm	8.5	3.4	1.35	0.8
Width of antenna radiation pattern	8.6	4.0	3.6	4.0
Scattering coefficient, percent	20	15	24	5
Active losses, percent	5	3	1	6
Working sensitivity of receiver, $^{\circ}$K	0.7	0.5	0.9	1.3

with λ_1 = 8.5 cm and λ_2 = 3.4 cm is orthogonal to the polarization of the channel with λ_3 = 1.35 cm, and therefore the radiation pattern of the first three channels is formed by the primary mirror, while the pattern of the third channel is formed upon reflection from the mirror-filter.

In the first range the antenna is fed with a pin mounted in the standing-wave voltage antinode in a pyramidal horn, and in the second and third waves the antenna is fed with waveguides of the appropriate cross section.

A polarization plate is installed in the feeding junction for mutual decoupling between the second and third channels.

A photograph of the three-range antenna is given in Fig. 5.14. /139

The antenna of the fourth range with $\lambda_4 = 0.8$ cm is built separately in the horn-lens scheme: a metal horn with a dielectric lens in its flare. This scheme is shown in Fig. 5.15.

The main parameters of the equipment are listed in Table 12.

Equipment with these parameters made it possible in 1968 and 1970 to conduct the world's first study of the radio emission of the Earth's atmosphere and its cover from artificial Earth satellites.

REFERENCES

1. Levin, M. L., ZhTF 25/13, 2313 (1955).

2. Tseytlin, N. M., Radiotekhnika i elektronika 5/3, (1970).

3. McGillen, C. D., and Selin, T. V., IEEE, Trans., MLT-7, 296 (1963).

4. Tseytlin, N. M., Primeneniye radioastronomicheskikh metodov v antennoy tekhnike /Radioastronomical Methods in Antenna Engineering/, Moscow, Sov. radio Press, 1964.

5. Kaplov, N. V., and Prokhorov, A. M., "Maximum Sensitivity of Electromagnetic Radiation Receivers," Radiotekhnika i elektronika 9/12, (1964).

6. Krasovskiy, A. A., and Zuykov, V. N., "Maximum Sensitivity Threshold for Reception of Thermal Radio Emission," Radiotekhnika i elektronika 5/4, (1960).

7. Siegman, A. E., Microwave J. 4/3, 4, 5 (1961).

8. Tiuri, M. E., IEEE, Trans. MIL-8, 246 (1964).

9. Strum, P. D., Proc. of the IRE 46/1, (1958).

10. Nachrichtentechnik, 3/87, (1972).

11. Kuz'min, A. D., and Salomonovich, A. Ye., Radioastronomicheskiye metody izmereniy parametrov antenn /Radioastronomical Methods of Measuring Antenna Parameters/, Moscow, Sov. radio Press, 1964.

12. Hogg, D. C., and Semplak, R. A., B.S.T.J. 15, 1331 (1961).

13. Weger, E., J. of Meteor. 17, April (1960).

14. Basharinov, A. Ye., Tuchkov, L. T., Polyakov, V. M., and Anakov, N. I., Izmereniye radioteplovykh i plazmennykh izlucheniy v SVCh diapazone /Measurement of Radiothermal and Plasma Radiation in the Microwave Range/, Moscow, Sov.radio Press, 1968.

15. Gumkin, L. S., Lebedev, V. L., and Siforov, V. I., Radio-priyemnyye ustroystva /Radio Receivers/, Part 1, Moscow, Sov. radio Press, 1961.

16. Medd, W. J., and Covington, A. E., Proc. of the IRE 46/1, (1958).

17. "Microwave Camera Spy in the Sky," Microwaves, December (1969).

18. Haroules, G. G., and Brown, W. E., Rev. Sci. Instr. 38, August (1967).

19. Stelzried, C. T., IEEE, Trans. MTT-13/1, (1965).

RESULTS OF MEASURING MICROWAVE EMISSION OF THE
EARTH FROM SPACE

Measurements of microwave emission of the Earth from space
were first made from the Kosmos 243 satellite and were continued
on the Kosmos 384 satellite. Radiometers described in the preceding
chapter with receiving antenna oriented at the nadir were installed
on the satellites. The Kosmos 243 satellite was launched 23
September 1968 into an orbit with apogee 319 km, perigee 210 km,
and inclination to the equator of 71.3° /1-3/, and Kosmos 384
was launched 10 December 1970 into an orbit with parameters 314
km and 212 km and 72.9°, respectively /4-6/. Also installed on
these satellites were infrared radiometers receiving radiation in
the 10-12 μm band.

1. Temperature and State of Ocean Surface

This section deals with an analysis of measurements from
Kosmos 243 made over the oceans at long wavelengths (8.5 and 3.4
cm) for remote determination of the temperature and state of the
ocean surface, and also analysis of the ice situation. Measure-
ments at shorter wavelengths, including the infrared range, were
resorted to in order to provide uniqueness of the interpretation.

1-1) The brightness temperature for the long-wave ranges
can be written in the following form (4.26):

$$T_{b,\lambda} = T_0 \varkappa_\lambda e^{-\tau_\lambda} + T^* (1 - e^{-\tau_\lambda}) + T^{**} e^{-\tau_\lambda} (1 - e^{-\tau_\lambda})(1 - \varkappa_\lambda). \qquad (6.1)$$

Here T* and T** are several mean-weighted atmospheric temperatures
not differing widely from T_0, the temperature of the sea surface.
Using the smallness of $_\lambda$, Eq. (6.1) can be transformed to the
following form:

$$T_{b,\lambda} = \varkappa_\lambda T_0 + (\Delta T_1)_\lambda + (\Delta T_2)_\lambda, \qquad (6.2)$$

where ΔT_1 is an addition to ocean emission due to absorption in
the atmosphere without regard to clouds:

$$(\Delta T_1)_\lambda = (\tau_{\lambda, O_2} + \tau_{\lambda, H_2O}) [T^* + T^{**}(1 - \varkappa_\lambda) - \varkappa_\lambda T_0] \qquad (6.3)$$

$(\tau_{\lambda;O_2}$ and τ_{λ,H_2O} is the optical thickness of oxygen and of water vapor), and ΔT_2 is the addition to emission due to absorption in clouds:

$$(\Delta T_2)_\lambda = \tau_{\lambda,\mathrm{cl}} \, [T^* + T^{**}(1 - \varkappa_\lambda) - \varkappa_\lambda T_0], \qquad (6.4)$$

$(\tau_{\lambda,\mathrm{cl}}$ is the optical thickness of clouds). It should be noted that the additions ΔT_1 and ΔT_2 are small, even in the case of /141 moderate rain they do not exceed 10-15 degrees at the wavelength 3.4 cm. The analysis made in Sections 2 and 3 of Chapter One showed that the effect of spume on the ocean surface on emission decreases with increase in wavelength. Considering the smallness of the values (ΔT_1) and (ΔT_2), we can neglect the variations in $\varkappa_\lambda$ (for $\lambda = 8.5$ cm and $\lambda = 3.4$ cm) in the expressions within the brackets in (6.3) and (6.4) associated with spume formation, since these variations give corrections of the next order of smallness in τ_λ. Within the scope of this assumption, measurements at the two wavelengths $\lambda = 8.5$ cm and $\lambda = 3.4$ cm enable us to obtain two equations with two unknowns, since τ_{λ,O_2} and τ_{λ,H_2O}

were calculated to high accuracy based on mean-climatic data, and $\tau_{\lambda_2 \mathrm{cl}} / \tau_{\lambda_1 \mathrm{cl}} = (\lambda_2/\lambda_1)^2$ (see Chapter Four). One of the unknowns in this system is $\varkappa_\lambda T_0$. By determining it and by assuming that $\varkappa_\lambda$ corresponds to the emission of the ocean surface without the presence of spume, we can obtain an estimate of the water surface temperature. This possibility is illustrated by the results presented in Fig. 6.1 and 6.2. The first of these figures presents the latitudinal dependence of brightness temperature at two wavelengths $\lambda_1 = 3.4$ cm and $\lambda_2 = 8.5$ cm obtained during the over-flight of a satellite over the Pacific Ocean. /2_7. The breaks in the curve correspond to the moments of calibration. Also presented in this figure is the mean-climatic brightness temperature for the month of September. Striking is the brightenings, particularly noticeable at the shorter wavelength at about 30° and 15° N. Lat. and between 50° and 60° N. Lat.

By applying Eq. (6.2) and the above-presented scheme of calculation, the values of $\varkappa_\lambda T_0$ and then T_0 were calculated on the assumption that $\varkappa_\lambda$ corresponds to a surface free of spume. Fig. 6.2 presents T_0 values thus calculated, which closely reflect the latitudinal change in ocean temperature. The brightenings associated with intense precipitation (precipitation was indicated

by an analysis of measurements at the wavelength 0.8 cm and by synoptic data) in the region 15° N. Lat. was virtually not manifested in the latitudinal trend of T_0. At the same time, the brightenings around 30° N. Lat. and between 50° and 60° N. Lat. were manifested in the latitudinal trend. Analysis of measurements at the shorter wavelengths indicated that in these regions no precipitations were observed at the moment of measurements. Evidently, the increase in T_0 obtained from radiometric measurements was caused by a rise in the emission coefficient of the ocean surface due to a storm, which judging from the synoptic background ₁was highly probable in these regions.

Further investigations using longer wavelengths and improved sensitivity and stability of the radiometers will permit more reliable measurements of ocean surface temperature from AES /artificial Earth satellites/.

1-2) To solve the problem of delimiting the storm zone and determining variations in ocean surface temperature, the emission spectra of the ocean have to be studied during a storm. Based on currently available data, the blackness factor of the surface (for /142 observations at the nadir) depends on the presence of spume and spray even in the long-wave portion of the centimeter range. However, at shorter wavelengths, changes in the blackness factor during a storm period are more strongly manifested.

Fig. 6.3 presents the emission spectra of storm regions recorded by Kosmos 243 /8_7; in these regions, judging from measurements in the infrared range and at the wavelength λ = 0.8 and 1.35 cm no precipitation and significant cloud cover were observed. To isolate the variations in radiobrightness tempera-   /143 ture, in the figure are plotted $\Delta T_{b,\lambda}$ values -- increments of radiobrightness temperature compared with mean-climatic temperature. In all the spectra, if we pass over individual measurements at the wavelength λ = 1.35 cm (water vapor resonance), a monotonic increase in brightening with shortening of wavelength is observed. The dependence on wavelength in these spectra can be approximated by an exponential law with an exponent close to (-1). Absorption in clouds would lead to an exponent of (-2). This marked difference in exponent enables us to detect storm zones and to estimate the characteristics of active sea states from changes in the emission coefficient of the ocean surface during a storm.

It should be emphasized that the characteristics of the emission spectrum of the ocean surface during a storm and the polarization characteristics of an agitated sea surface enable us to detect storm regions through cloud cover. Because the
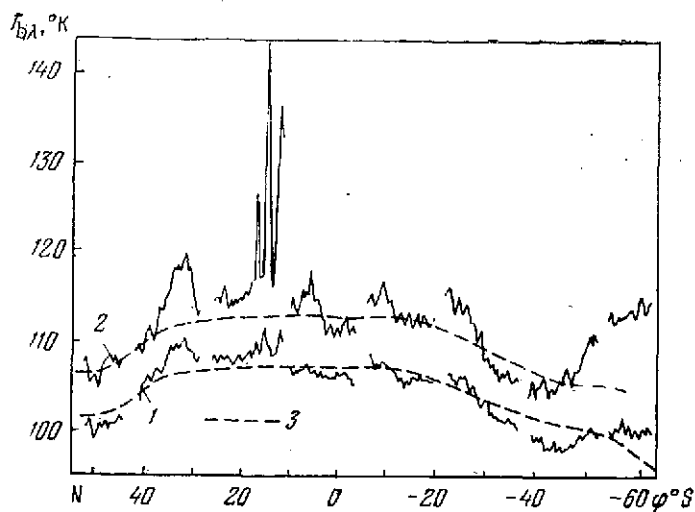
154)

Fig. 6.1. Latitudinal profile of radiobrightness temperatures along an orbit over the Pacific Ocean
1. λ = 8.5 cm
2. λ = 3.4 cm /2_7
3. Mean-climatic radiobrightness temperatures for the same wavelengths

period of revolution of Kosmos 243 was approximately 1.5 hours, projections of the orbits at an interval of a day were close to each other, and this made it possible not only to detect the storm zones, but also to trace their development with time. This work was done in /9_7, where brightenings of the ocean surface at the wavelength λ = 3.4 cm (with respect to the mean-climatic data) were compared with the wave heights calculated from synoptic data in eight nonoverlapping regions of the Pacific Ocean over a period of 3 days. When the brightenings were analyzed at the wavelength λ = 3.4 cm, regions with considerable cloud cover and precipitation based on measurements at the wavelength λ = 0.8 cm were
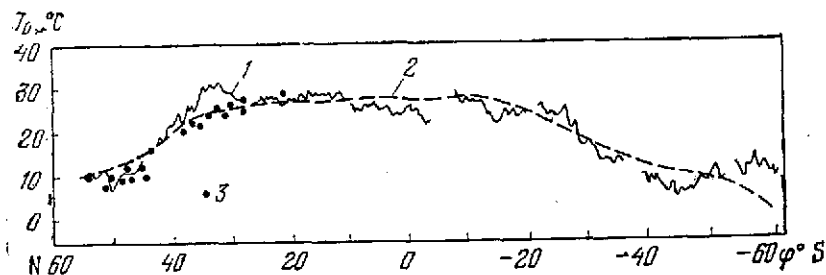
Fig. 6.2. Profile of surface temperatures of the Pacific Ocean reconstructed from measurements at wavelengths λ = 8.5 and λ = 3.4 cm
1. Reconstructed temperature
2. Mean-climatic temperature
3. Shipboard data /7_7

dropped. To simplify the comparison of the brightenings with wave height, the given quantities were represented in discrete form: four gradations of increment in brightness temperature were selected $\Delta T_{b,\lambda}$ = 0-3°, 3-6°, 6-9°, and 9-12° and correspondingly, four gradations for the calculated wave heights h = = 0-1.5 m, 1.5-3 m, 3-4.5 m, and 4.5-6 m. Shown in Fig. 6.4 is the temporal trend of brightenings and wave heights, expressed in the above-adopted relative units. From the plots shown in these figures it is clear that the buildup and weakening of active sea states as a whole is closely reflected in the brightening values. It is not precluded that the noncorrespondence of the total absence of brightenings with considerable wave height in the region 2-1 over a period of 3 days was caused by inadequate reliability of the synoptic information in this region of the southern hemisphere.

It was of interest to attempt to relate wind velocity (in those cases when it was known at the satellite track point) with brightening at the wavelength λ = 8.5 cm /10/. The wind velocity dependence of brightening shown in Fig. 6.5 indicates, in spite of the large scatter, the presence of a relationship between emission and wind velocity. A similar dependence obtained from aircraft measurements of radiobrightness at the wavelength λ = = 1.55 cm was discussed in Chapter One. At identical wind velocity, the contrast of radiobrightness at the wavelength λ = 8.5 cm is much less than at λ = 1.55 cm (see Fig. 1.20). Nonetheless, we cannot make a clear preference for short wavelengths in determining storm zones. As the wavelengths are shortened, the effect of droplet water in the atmosphere (especially of rain) on the emission of the ocean-atmosphere system becomes increasingly evident. Therefore, unique diagnostics of the ocean surface state requires multi-wavelength and polarization measurements in the microwave range. This viewpoint finds confirmation both in the results of satellite observations presented in this section as well as results of analysis of aircraft and ground-based experiments and calculations presented in Section 3 of Chapter One.

1-3) The contrast of the brightness temperatures of the free surface of water and ice floating at the water surface exceeds 100° K, and was noted above (Section 4, Chapter One), enables us to estimate the continuity of the ice. In AES observations, the emission is averaged over a large spot, whose size is determined by the antenna radiation pattern and the satellite altitude. Therefore interference effects that show up clearly in laboratory and model measurements and even in aircraft observations are not manifested during satellite measurements. Blurring of interference patterns in sea ice is also promoted by the relatively absorption
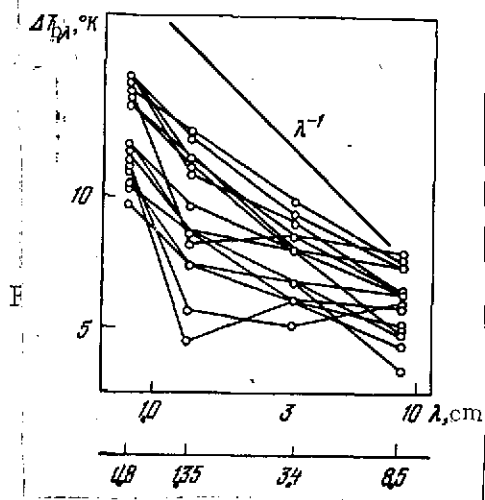
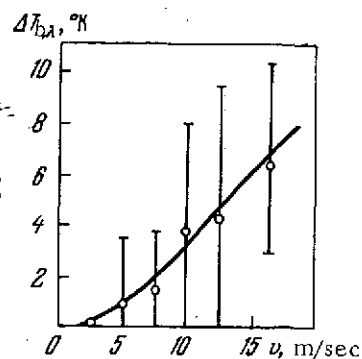Fig. 6.3. Spectra of radiobrightness temperatures over storm regions

Fig. 6.5. Comparison of brightening at wavelength λ = 8.5 cm with wind velocity in satellite track point /10/
Vertical segments correspond to the root-mean-square error of measurement of $\Delta T_{b,\lambda}$
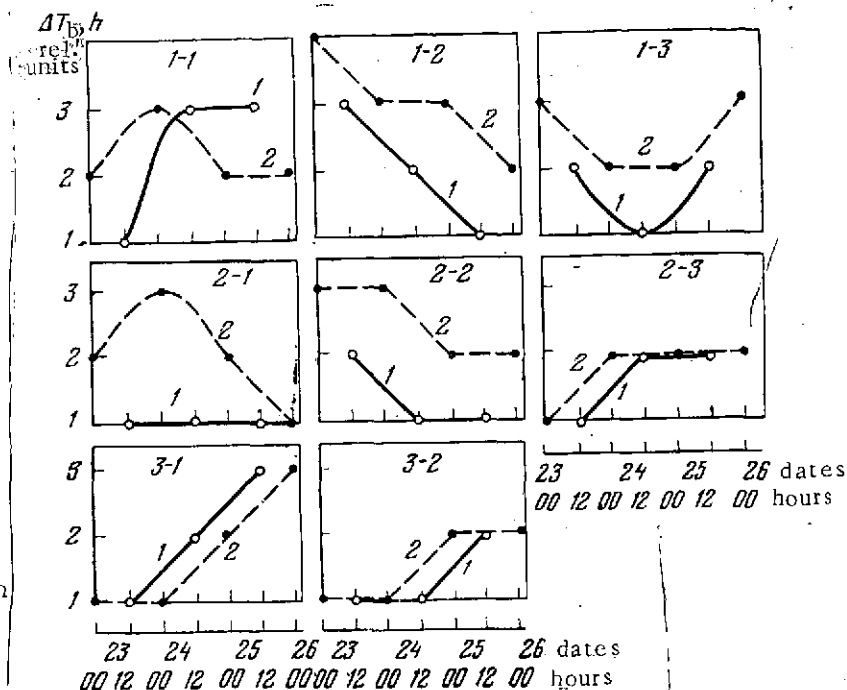

Fig. 6.4. Variation with time, during 23-26 September 1968, of the altitude of wind-driven waves and radiobrightness at the wavelength λ = 3.4 cm over eight different regions of the Pacific Ocean /9/
1. Increment in radiobrightness
2. Wave height (both are given in relative units)

of microwave radiation in sea ice. Therefore to the first approximation it can be assumed that the response of a radiometer installed on a satellite will be a linear function of ice continuity in the spot from which the emission is being received.

It should be noted that satellite determinations of ice continuity by observation of its thermal microwave emission can contain errors caused by a feature

157/

of emission formation in this complex system, represented by floating sea ice, which may even be covered with snow. If we consider the low probability of the appearance of clouds with high moisture reserve and intense rainfall in the polar regions, the main interference during the determination of ice continuity will be the appearance on the ice surface of water or water-soaked snow during the spring-summer period. The appearance of liquid water in any particular form on the ice surface sharply lowers its emission and, therefore, it can lead to an apparent reduction in continuity. A second factor also tending to reduce emission is the scattering by bulk inhomogeneities of density and inclusions of air bubbles or salt water in the ice interior. /146 Scattering effects most strikingly manifested in the emission of shelf glaciers of the Antarctic /11/ are discussed in the next section. It can be assumed that using emission spectral features associated with scattering can yield information not only on continuity but also on the internal structure and age of ice.
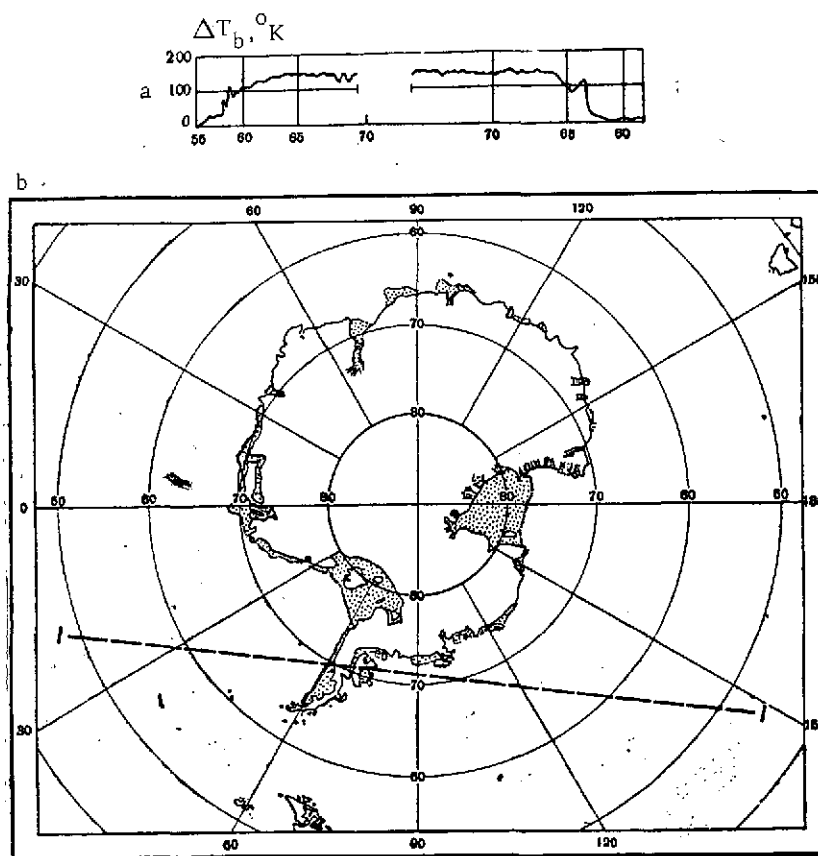
Fig. 6.6. Profile of increment in brightness temperatures at the wavelength $\lambda = 3.4$ cm in the transition from ocean to solid ice fields (a) and the trajectory (I - I) of the satellite track point (b).
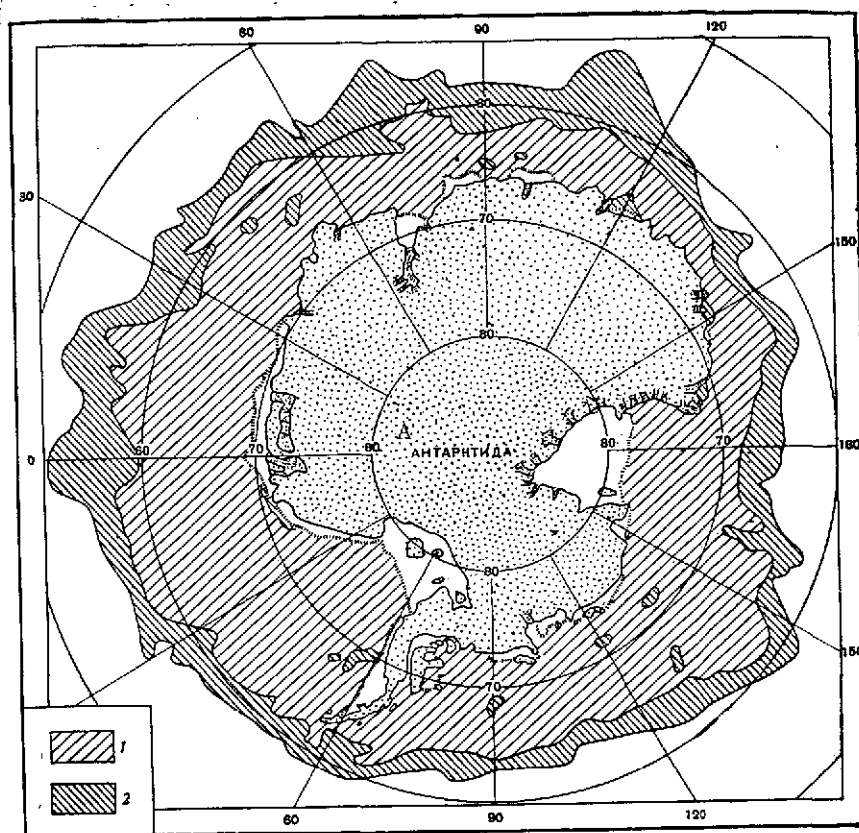
Fig. 6.7. Map of ice continuity from Kosmos 243 satellite measurements
1. Continuity greater than scale 5;
2. Continuity less than scale 5 /12/
KEY: A. Antarctica

Fig. 6.6. shows the trend of the variation in radiobrightness temperature at the wavelength λ = 3.4 cm as the satellite track point (observation point) passes from the open sea to ice. In the polar zone the projections of successive satellite orbits pass close to each other, gradually shifting from day to day, therefore the southern polar region in a short time was covered with a dense network of data sufficient to plot an ice continuity map around the Antarctic /1 /

Ice continuity μ for the plotting of the map was calculated /147 by the formula

$$\mu = \frac{\underline{/}\overline{T}_{b,\lambda} - (T_{b,\lambda})_{\text{water}}\underline{/}}{\underline{/}(T_{b,\lambda})_{\text{ice}} - (T_{b,\lambda})_{\text{water}}\underline{/}}$$

in which $(T_{b,\lambda})_{\text{water}}$ was calculated for the water temperature $T_o = 273^\circ$, and $(T_{b,\lambda})_{\text{ice}}$ was calculated for the mean-climatic temperature and the emission coefficient $\varkappa_\lambda = 0.96$.

A map with two continuity gradations constructed from measurements at wavelength $\lambda = 8.5$ cm and $\lambda = 3.4$ cm is shown in Fig. 6.7. We note that the polar night is not a barrier for the determination of parameters of ice floes, while television tracking during this time of the year is powerless to provide information. During the sunlit time, television tracking does /148 provide much greater resolution in the study of ice continuity. However, cloud cover is an insurmountable obstacle in obtaining ice pictures. The combination of television and microwave-range observations can considerably broaden the possibility of investigation compared with using only one of these means. Measurements from Kosmos 384 were taken during the polar day in Antartica. During this same time television images from the Meteor satellite were also taken. Fig. 6.8 shows the results of determining ice continuity from television images and from microwave-radiation measurements /13/. Where results of observations from both satellites are available, they coincide within reasonable limits. In some regions, owing to the presence of cloud cover, the ice continuity maps had to be plotted only from microwave observations.

It should be noted that bulk scattering in ice at the wavelengths $\lambda = 8.5$ cm and $\lambda = 3.4$ cm is manifested much less than at the shorter wavelengths $\lambda = 1.35$ cm and $\lambda = 0.8$ cm. Therefore the range $\lambda = 8.5$ cm and $\lambda = 3.4$ cm is optimal for determining the degree of ice continuity.

2. Variations in Temperature and Characteristics of State of /149
    Solid Cover

2-1) Measurements of microwave radiation of continental cover revealed a considerable scatter of the blackness factor in the range 0.6 to 0.95 associated with a difference in the dielectric constant of the soil material, the effect of wetting, and the effect of plant cover. Actual data based on the results of experiments on Kosmos 243 and Kosmos 384 are given in /1, 3-6, 13-15/. During observations made over homogeneous cover, it was
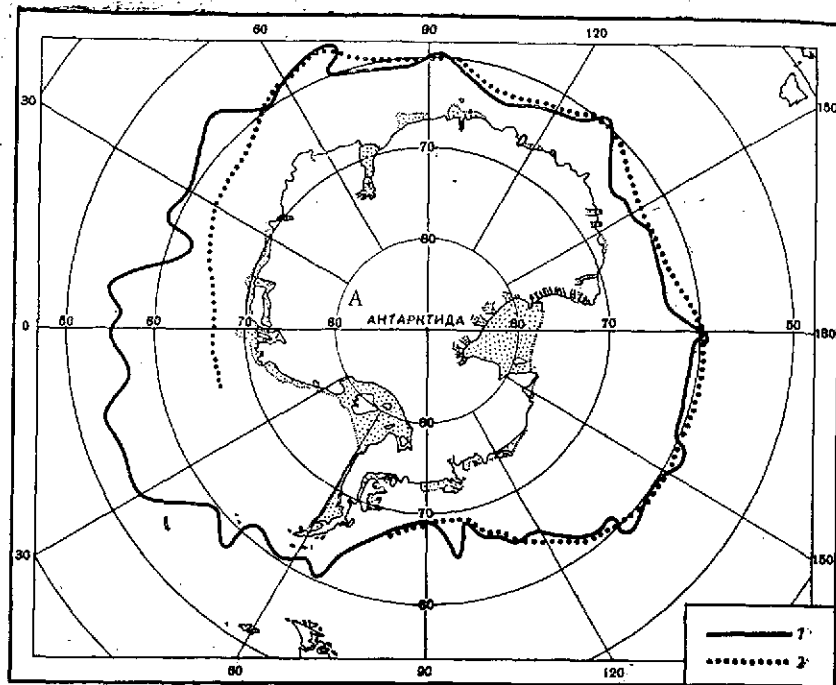
Fig. 6.8.   Icefield margins around Antarctica
1. From radiometric measurements of Kosmos 384
2. From television images from the Meteor satellite /13/
KEY: A. Antarctica

possible to record latitudinal variations in radiobrightness temperature dependent on the effective soil temperature[1]. The measured variations in effective soil temperature then were compared with the latitudinal variations of the mean-diurnal and mean-monthly temperatures.

For example, as the field of view of the radiotelescope passed over Australia from the southern coast to the northern coast, the measured values of the difference in the radiobrightness temperature at the wavelength 8.5 cm (Fig. 6.9) were 16-18° C, while the difference in the mean-monthly temperatures based on meteorological station data was about 13°.

---

[1] The concept "effective temperature" is defined in Section 2 of Chapter Two.

Fig. 6.10 presents a profile of the radiobrightness temperature at the wavelength 3.4 cm obtained during the flight of Kosmos 384 over West Africa and also reflecting changes in soil temperature recorded by meteorological stations. In Fig. 6.10 characteristic regions can be observed: region 1 where a smooth decrease in temperature from the coastline (8° N. Lat.) to the northern tropics is observed; region 2 (the northern part of the Sahara) where the temperature changes slowly; and region 3, extending over a mountainous region along the coast of the Mediterranean Sea.

These data show that the measured variations in radiobrightness temperature at the wavelength 8.5 cm image the latitudinal variations of the averaged soil temperatures.

Processing of data from multi-wavelength measurements of radiobrightness temperatures in regions well provided with meteorlogical stations established $/\overline{15}/$ that at the wavelength 0.8 cm the best correlation is obtained between radiobrightness temperature $T_{b,\lambda}$ and the measured soil temperature T_s. The results of these measurements obtained over the section of the orbit from the Black Sea to the Northern Urals are shown in Fig. 6.11 $/\overline{15}/$. The coefficient of correlation of radiobrightness temperatures and soil temperatures from the data in Fig. 6.11 is 0.92.

The points of intersection of the ascending and descending orbits with a time difference of about half a day were used to make estimates of the diurnal variations in radiobrightness temperature. Diurnal variations of radiobrightness observed for the desert regions of the Sahara and Australia at the wavelength 0.8 cm were several degrees, which is much less than the variations in air temperature in the near-Earth layer.

As the field of view passed over the mountainous regions, a drop of several tens of degrees in the radiobrightness temperature was recorded. These changes in radiobrightness temperature associated with the measurement of the effective soil temperature at high elevations was observed in the areas of the Himalayas, Tibet, Andes, and other mountain ranges. In Fig. 6.12 is shown a radiobrightness temperature profile during a pass over the Himalayas. For comparison, also shown in Fig. 6.12 is an elevation profile of the range. As we can see by comparing these profiles, changes in radiobrightness temperature correlate well with changes in elevation above sea level.

2-2) Measurements of microwave radiation of continental cover in the high-altitude zones revealed spectral features of the radiative properties of glaciers associated with latitudinal
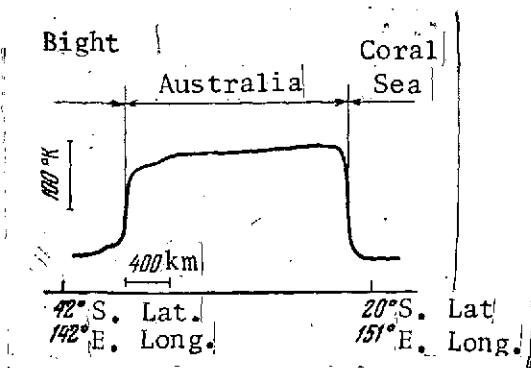
Fig. 6.9. Radiobrightness temperature profile of the Australian continent at wavelength λ = 8.5 cm, 24 Sep 1968 /5_7
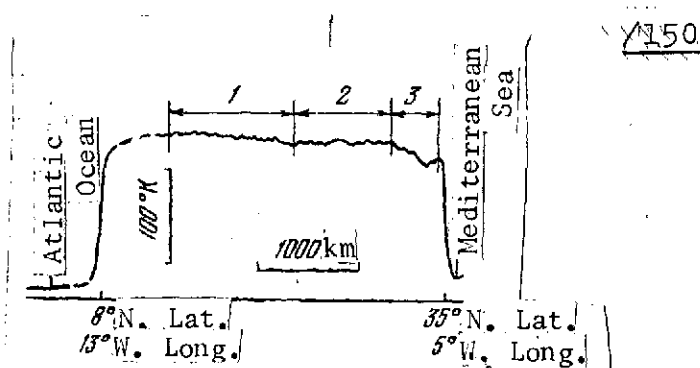

Fig. 6.10. Radiobrightness temperature profile of the African continent at wavelength λ = 3.4 cm, 10 Dec 70 /6_7

variations in temperature and with spectral changes in the blackness factor. Measurements during a pass of Kosmos 243 over the Antarctic yielded a wealth of material on the emission of ice formations.'

A characteristic profile of radiobrightness temperatures at wavelengths λ = 1.35 cm and λ = 3.4 cm obtained during a transect of the Antarctic continent[2] is shown in Fig. 6.13. It is clear /151 from the figure that the radiobrightness of continental ice falls off with decrease in wavelength. This is observed somewhat less for sea ice. In the profile in Fig. 6.13 we can see small local changes in radiobrightness that may be caused by a variation in both the temperature and the blackness factor of the glacier surface.

The radiobrightness profile shown in Fig. 6.14 was obtained during a pass of the satellite over ice shelfs. In this figure it is clear that in several cases (for the Amery and Lazarev)ice shelfs) the dependence of radiobrightness on wavelength is somewhat different from over continental ice: radiobrightness at the wavelength λ = 3.4 cm is less than at the wavelength 1.35 cm.

---

[2] At low temperatures the water vapor content in the atmosphere was low and in measurements made over ice in the polar regions distortions in the brightness of the underlying surface due to absorption in the region of the resonance λ = 1.35 cm were slight.

An idea of the emission spectrum of continuous sea ice is given by Fig. 6.14, where we should particularly note the section of the pass over Ross Sea. In this sea ice continuity is known to be close to scale 10, and thus the effect of open pools of water on the radiobrightness is precluded. A reduction in radiobrightness with decrease in emission wavelength is also readily detectable over the Ross Sea in the emission spectrum.

Just as mottled a radiation pattern as the one noted over the Antarctic was evidenced also in the northern hemisphere. Fig. 6.16 shows the results of measurements of $T_{b,\lambda}$ at the wavelength $\lambda = 3.4$ cm during one of the orbits over Greenland. A region with reduced radiobrightness can be seen in this figure.

In some regions of the Antarctic continent sections quite homogeneous in their radiation parameters were encountered. Fig. 6.17 presents data of measurements taken over such a homogeneous section in the absence of clouds. These data were obtained from simultaneous measurements by Kosmos 384 of radiobrightness T_b, at wavelength 0.8 cm and radiation temperature T_r in the infrared 10-12 μm window. The general trend of variation in both radiobrightness and radiation temperature follows the mean-monthly temperature plotted on this same graph. A correlation graph (Fig. 6.18) gives a more detailed idea of the relationship between T_r and $T_{b,\lambda}$ and indicates relative constancy of the emissivity of the glaciers (at the wavelength 0.8 cm) over fairly extended sections.

In Fig. 6.19 is presented a comparison of the brightness temperatures at the wavelength $\lambda = 1.35$ cm with the mean-monthly air temperatures for extensive regions of continental glaciers. In spite of the large scatter of data, this plot enables us to estimate the mean blackness factor for $\lambda| = 1.35$ with the value $\bar{\varkappa}_\lambda| = 0.85$.

Features of the radio emission spectrum of ice are illus- trated by the correlation plot in Fig. 6.20, where measurements are compared at two wavelengths $\lambda = 3.4$ cm and $\lambda = 1.35$ cm, classified by different types of ice formations. First of all we should note that the experimental data pertaining to different geographical regions do not overlap in the plot in Fig. 6.20. For sea ice, and especially for continental ice, radiobrightness at wavelength $\lambda = 1.35$ cm is much less than at the wavelength $\lambda = 3.4$ cm. For ice shelfs radiobrightness values at these wavelengths are close to each other, while the absolute radiobrightness values at a given wavelength are much lower than for continental
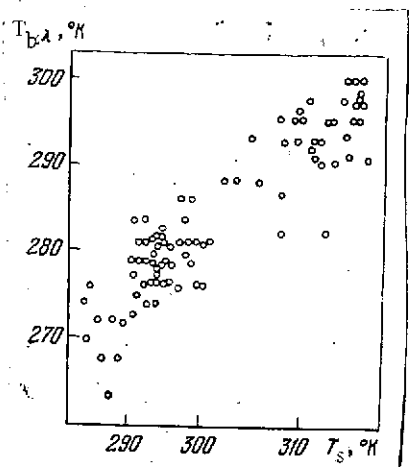
Fig. 6.11. Correlation diagram
of relation between radiobright-
ness temperature at wavelength
λ = 0.8 cm and thermodynamic
soil temperature (according to
/15/)

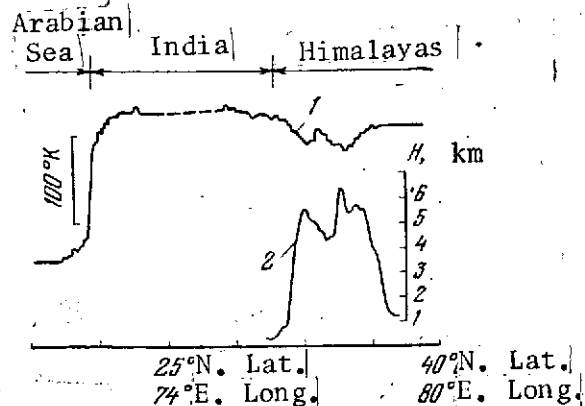Fig. 6.12. Radiometric (1) and
elevation (2) profiles of Hima-
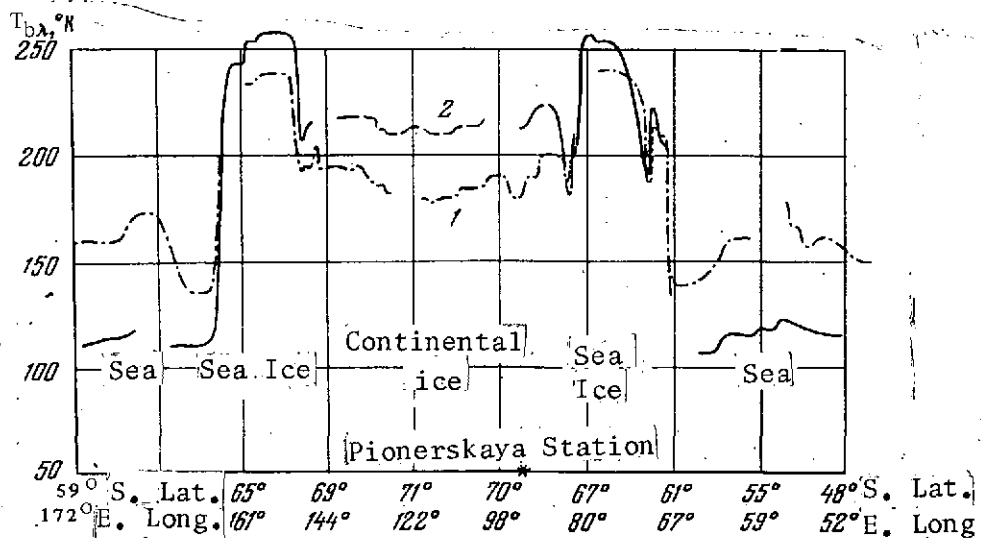layas-Tibet region at wavelength
λ = 3.4 cm, 24 Sep 68 /5_7

Fig. 6.13. Radiobrightness temperature profiles of
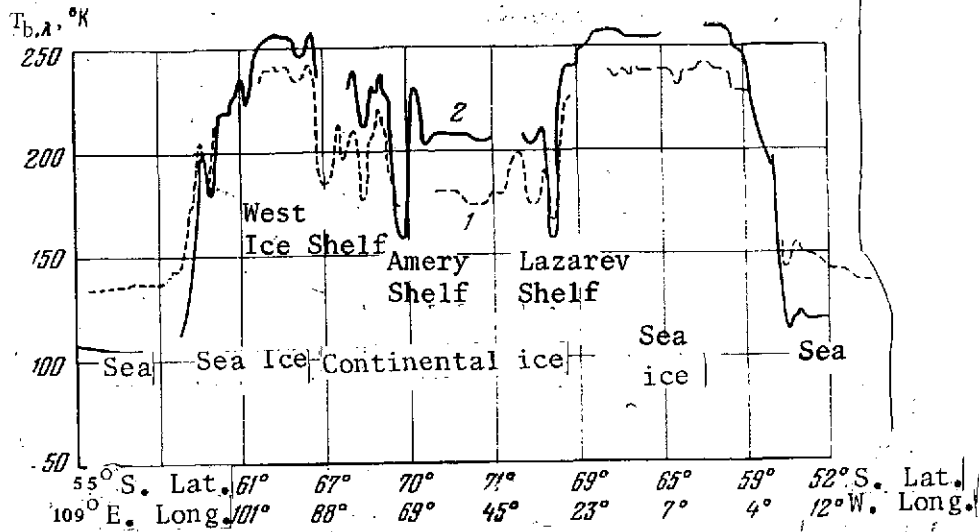continental and sea ice of Antarctica /5_7
1.   λ = 1.35 cm
2.   λ = 3.4 cm

Fig. 6.14. Radiobrightness temperature profiles of Antarctica over regions of ice shelfs /5_7
1. λ = 1.35 cm
2. λ = 3.4 cm
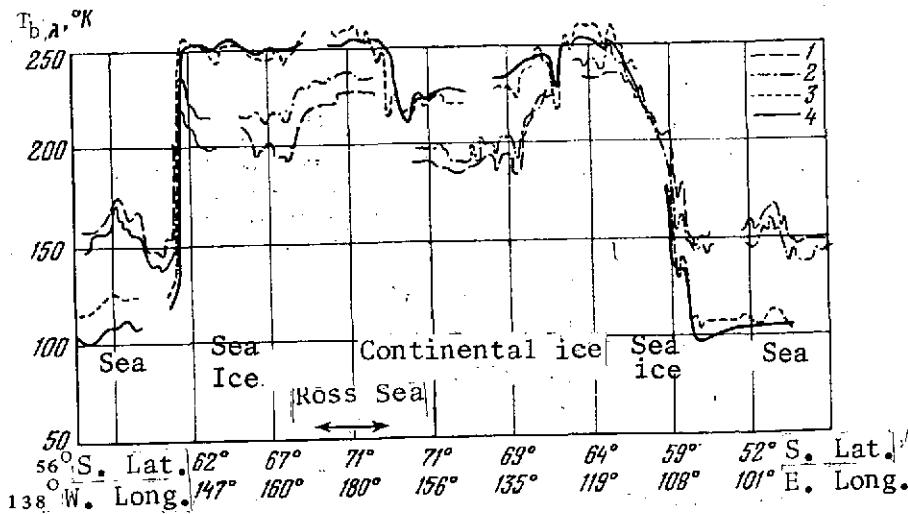
Fig. 6.15. Radiobrightness temperature profiles of continental and sea ice of the Antarctic at four wavelengths /5_7
1. λ = 0.8 cm   3.   3.4 cm
2. λ = 1.35 cm   4.   8.5 cm
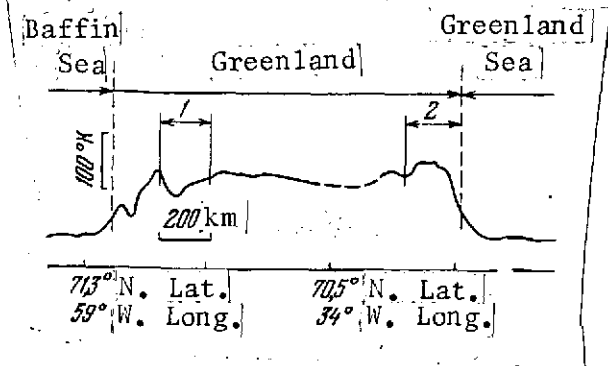
Fig. 6.16. Radiobrightness temperature profile at the wavelength $\lambda = 3.4$ cm of continental and sea ice of Greenland on 23 Sep 68 /5 /
1. Region of continental ice with reduced blackness factor
2. Region of ice floes
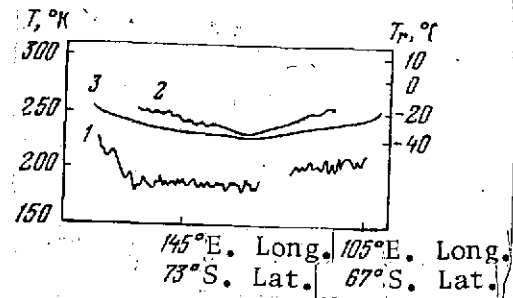
Fig. 6.17. Profiles of radio-brightness temperature ($\lambda = 0.8$ cm) (1), radiation temperature ($\lambda = 10$ μm) (2), and mean-monthly temperature (3) of Antarctic ice shelfs /13/
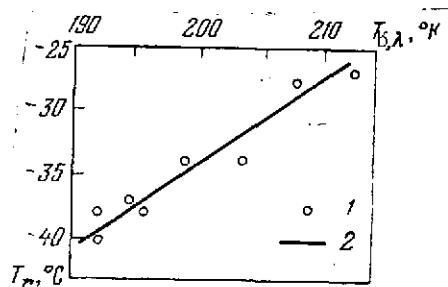
Fig. 6.18. Correlation plot of relation between radio-brightness temperature ($\lambda = 0.8$ cm) and radiation temperature ($\lambda = 10$ μm) of Antarctic ice shelfs
1. Experimental data
2. Averaged function
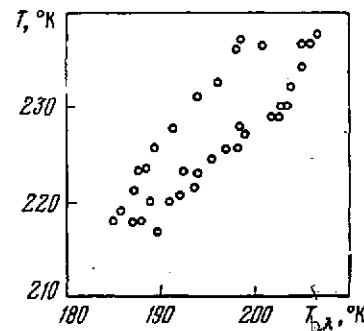
Fig. 6.19. Correlation diagram of relation between radiobright-ness temperatures $T_{b,\lambda}$ for $\lambda = 1.35$ cm and mean-monthly thermodynamic temperatures T

and sea ice. The estimate of the brightness factor $\varkappa_\lambda$ for ice shelfs gives, for short waves ($\lambda = 0.8$ cm and $\lambda = 1.35$ cm) $\varkappa_\lambda \simeq 0.7$ and for the wavelength $\lambda = 3.4$ cm, $\varkappa_\lambda$ drops to $\varkappa_\lambda = 0.6$.
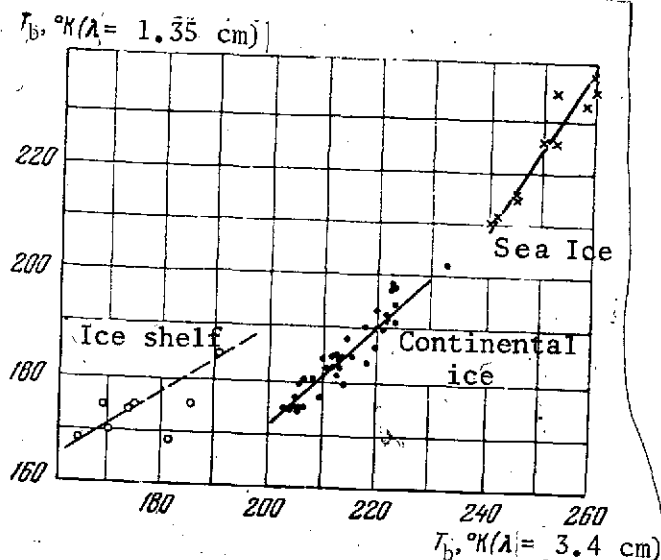
Fig. 6.20. Correlation functions of radiobrightness temperatures at wavelengths λ = 3.4 and 1.35 cm /5_/

The feature observed in the spectral function of the blackness factor of ice shelfs can be caused by several factors. Because of the relatively high porosity of the structure in ice shelfs, intrashelf water can be formed, collecting in lenses of meltwater and lenses impregnated with firn water /16, p. 74/. The reflectivity of firn when these lenses are present can increase over the wavelength interval 1 cm to 3 cm.

Scattering by structural inhomogeneities of the ice shelf formations is the probable common cause responsible for the low /156 values of the blackness factors of the ice shelf formations. Random density variations from layer to layer, air inclusions in continental ice, or inclusions of brine bubbles in sea ice, and so on are these kinds of inhomogeneities. The emission of weakly absorbing media, which include continental and shelf glaciers, when inhomogeneities are present, was examined in Chapter Two, Section 3. Also established there is a relationship between the emission spectrum and the parameters characterizing the random structure of glaciers. Measurements of emission spectra from Kosmos 243 make it possible to compare the results of calculation with experimental data /11/.

Fig. 6.21 gives examples of radiobrightness spectra for shelf and continental glaciers. These spectra, obtained from synchronous measurements at four wavelengths, graphically reflect the nonmonotonic dependence of radiobrightness on wavelength. In spite of the large scatter of absolute radiobrightness values $T_{b,\lambda}$ (the extreme values are taken for illustration), in Fig. 6.21 we can note that they are virtually all much lower than the values corresponding to the homogeneous firn structure and that the radiobrightness minimum is shifted toward the side of longer wavelengths for ice shelfs.

In Fig. 6.22 the averaged experimental data are compared with calculated data based on Eq. (2.23). In spite of the large scatter of experimental values, it can be noted that the calcu- /157
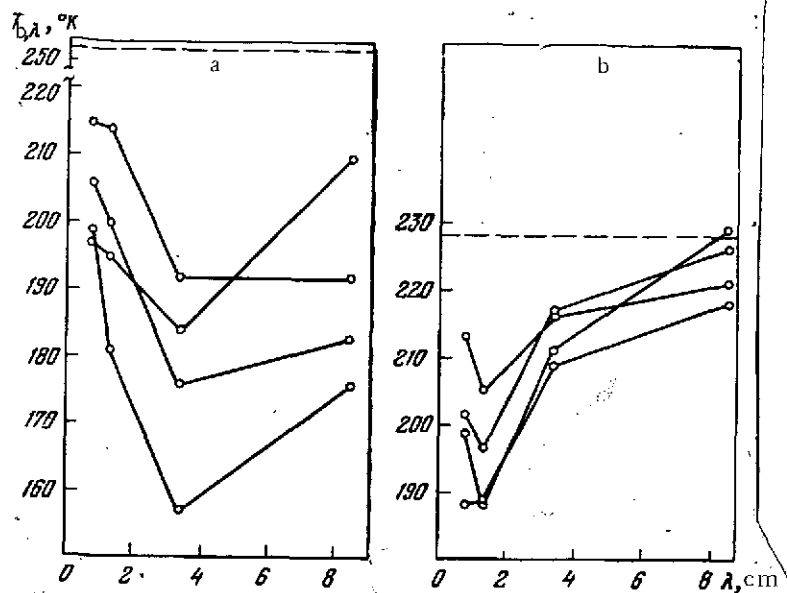
Fig. 6.21. Radiobrightness spectra of shelf
(a) and continental (b) ice of Antarctica
The dashed line represents calculated radio-
brightness values of shelf (a) and continen-
tal (b) glaciers without reference to
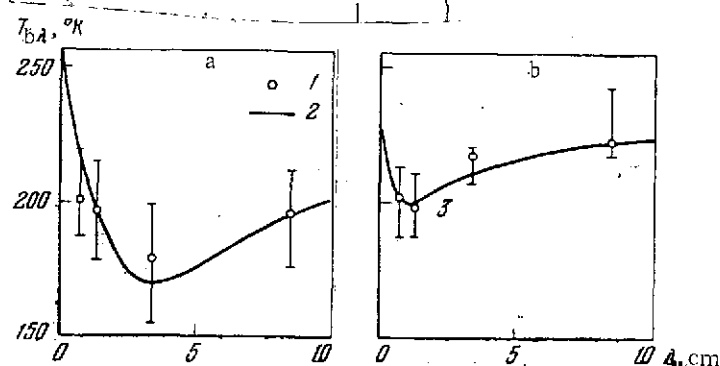scattering by inhomogeneities /11/

Fig. 6.22. Comparison of averaged meas-
ured spectra of radiobrightness (1) with
reference to (2) for random-inhomogeneous
medium (based on Eq. (2.23) [11]
a. shelf glaciers   b. continental glaciers

lation quite closely
conveys the trend of
the spectral function
and gives radio-
brightness values
that are in agree-
ment with measure-
ments. Comparison
with calculation
permits an estimate
of the root-mean-
square deviation of
the firn density for
the less homogeneous
ice shelfs σ_ρ = 2.7 ·
· 10^{-2} g/cm^3 and for
the more homogeneous
continental glaciers
σ_ρ = 1.5 · 10^{-2} g/cm^3.
These values agree
closely with the
independent estimates
that can be obtained
from the data given
in /16/.

2-3) Zones of
wet soils that have
linear dimensions
commensurable with
the dimensions of
the field of view
were reliably
recorded from the
satellites based
on radiobrightness
contrasts. Examples
of these observations
are in Figs. 6.23 and
6.24.

Fig. 6.23 shows
a profile of the
radiobrightness
temperature at the
wavelength 8.5 cm
obtained over a wet

zone in the lower reaches of the Orinoco River in South America. From estimates made on the basis of the moisture content dependence of the radiobrightness temperature (Section 6, Chapter Two), soil moisture content in this region is 25-30 percent. In Fig. 6.24 the radiobrightness temperature profile can detect zones with 12-16 percent soil moisture on the African continent. In the region marked by number 2, the wetting was evidently caused by heavy tropical showers.

Comparison of the data of radiometric measurements with direct measurements of soil moisture by agrometeorological stations was made in /15/ for two projections of trajectories of AES extending from the Black Sea to Obskaya Guba on 23-24 September 1968. It was found that the mean value of the derivative of the moisture dependence of the soil blackness factor is close to zero at the wavelength 0.8 cm and increases with increase in wavelength.　　/158
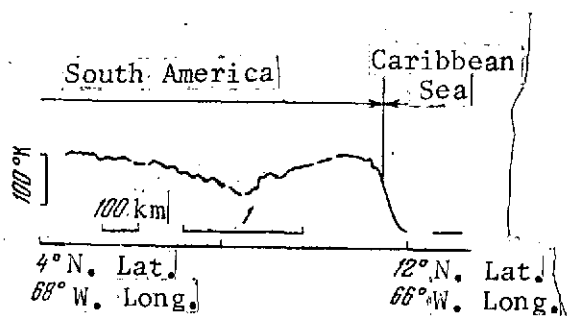

Fig. 6.23. Radiobrightness temperature profile at the wavelength λ = 8.5 cm for the area of South America covering the lower reaches of the Orinoco River (24 Sep 68)
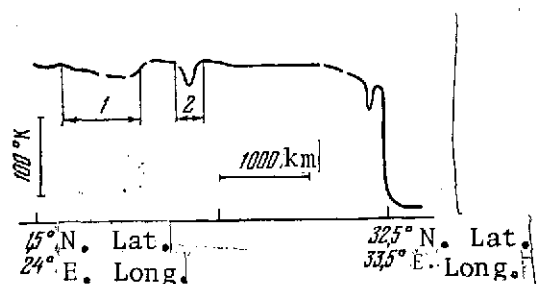1. Zone with increased soil moisture

Fig. 6.24. Radiobrightness temperature profile at the wavelength λ = 8.5 cm of the area of the African continent covering the equatorial region (23 Sep 68) /5_7/
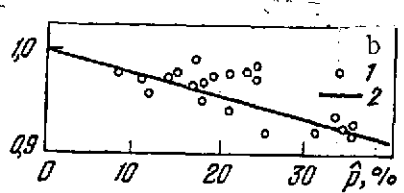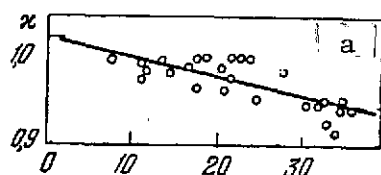1,2. Zones with increased soil moisture

, g. 6.25.
Fig. 6.25. Dependence of blackness factor at wavelength λ = 3.4 cm (a) and 8.5 cm (b) on soil moisture characteristics (according to data in /15_7/)
1. Experimental data　　2. Averaged data

The effect of the reduced influence of soil moisture on emissivity observed in the short-wave section of the centimeter range is accounted for by the screening action of plant cover. In Fig. 6.25 we present data of this comparison for the longest of the wavelengths used (λ = 3.4 cm and λ = 8.5 cm), for which the influence of moisture on the blackness factor is most marked.

A comparison of experimental data (Fig. 6.25) with calculated estimates (see Fig. 2.7, Chapter Two) shows a nearly twofold drop in the slope of the experimental function compared with the calculated function. This discrepancy is evidently caused by the screening action of plant cover and by the roughness of the actual underlying surface. The masking action of vegetation on the determination of soil moisture is especially strongly evident when observations are made from space in the millimeter wavelength range.

3. Water Vapor Content in Atmosphere Over Oceans

In Chapters Three and Four it was shown to be possible to determine the content of precipitable water from emission measurements at the wavelength 1.35 cm and 0.5 cm. In this section we will examine the determination of water vapor from satellite measurements and we will present some statistical results obtained from measurements taken with Kosmos 243; we will also analyze the relationship between the synoptic situation and the distribution of the integrated water vapor content over oceans.

3-1) The dependence of the brightness temperature of outgoing emission at the wavelength 1.35 cm on the integrated water vapor content /17/ is:

$$T_{b,\lambda} = 18Q \ (g \ cm^{-2}) + 127, \tag{6.5}$$

which was discussed in Chapter Three; this function can be used in determining the water vapor content from brightness temperature measurements. We note that in /18/, based on altogether independent material, a calculation was also made of a linear function, whose coefficients agree to an accuracy of 2 percent with Eq. (6.5).

When liquid-droplet cloud cover is present, which shows up clearly in radiometer readings at the wavelength 0.8 cm, Eq. (6.5) cannot be used and we must introduce a correction that takes absorption in clouds into account.

The optical thickness of a cloudfree atmosphere at the wavelength λ = 0.8 cm can be calculated by the approximate formula

$$\tau_{\lambda, O_2} + \tau_{\lambda, H_2O} = 0,060 + 0,014Q,$$

which ensures an accuracy of 0.01 neper for actual conditions over the oceans. For the wavelength 1.35 cm, by processing radiosond data, the following formula is obtained:

$$\tau_{\lambda, O_2} + \tau_{\lambda, H_2O} = 0,015 + 0,08Q. \qquad (6.7)$$

The optical thickness of clouds in the Rayleigh approximation is inversely proportional to the square of the wavelength in the wavelength range $\lambda > \lambda_s$ (see Section 2, Chapter Four). With reference to the temperature dependence of the dielectric parameters of water, we can obtain the following function for the ratio of the optical thicknesses of cloud cover $\tau_{b, cl}$ at the wavelength 0.8 cm and 1.35 cm:

$$\tau_{1,35, cl} = A(T_{cl})\tau_{0,8, cl}. \qquad (6.8)$$

The coefficient $A(T_{cl})$ depends on the cloud temperature $/19/$: $A(20°$ C$) = 0.34$; $A(0°$ C$) = 0.36$; and $A(-20°=C).=30.43$. For calculations in the processing of satellite, to the first approximation the value $A = 0.36$ was adopted, since the true temperature of droplets in the absorbing portion of a cloud was unknown. Measurements in the infrared region, taken by the satellite, could /160 give only the temperature of the top of the cloud cover.

The approximate relation

$$T_{b, \lambda} = T_0 \varkappa_\lambda e^{-\tau_\lambda} - \Delta T (1 + R_\lambda) e^{-\tau_\lambda} (1 - e^{-\tau_\lambda}), \qquad (6.9)$$

in which $R_\lambda = 1 - \varkappa_\lambda,$ and ΔT is the correction for the nonisothermicity of the atmosphere can be used in determining the total absorption of water vapor, oxygen, and droplet water from brightness temperature measurements. It can be assumed with sufficient accuracy that $\Delta T \approx 0,1 T_0,$ where T_0 is the temperature of the ocean surface. Eq. (6.9) does not make allowance for the scattering of radiation that is insubstantial in clouds, and this equation can be considered as an equation in τ_λ. The solution (6.9) can be written as follows:

$$\tau_\lambda = -\ln \frac{\varkappa_\lambda \Delta T \pm \sqrt{(\varkappa_\lambda \Delta T)^2 + 4R_\lambda (T_0 - \Delta T)(T_0 - T_{b, \lambda} - \Delta T)}}{2R_\lambda (T_0 - \Delta T)} \qquad (6.10)$$

The plus sign is taken for $\tau_\lambda \leqslant -\ln \dfrac{x_\lambda \Delta T}{2R_\lambda(T_0-\Delta T)},$ otherwise the

minus sign is used. Over the ocean the value $\tau = 3\text{-}4$ corresponds to the sign change for $l \geqslant 0.8$ cm.

Thus, by determining the values of τ_λ from measurements according to Eq. (6.10), we can, by using the system of equations (6.6), (6.7), and (6.8), calculate Q when cloud cover is present.

3-2) Before we proceed to set forth the results of the experiment conducted on Kosmos 243, it is of interest to discuss the possible sources of errors that are implicitly contained in the above-presented scheme of the calculation of Q. First of all, they include the following: a) indeterminacy of the coefficients R_λ and $x_\lambda = 1 - R_{\lambda,}$ which depend on the state of the sea

surface, and b) indeterminacy of the vertical distribution of water vapor by altitude. The indeterminacy of cloud temperature is more strongly reflected in the determination of the total content of droplet water in the clouds. Also, the deviation from the Rayleigh law of scattering and absorption in precipitation, especially for the shortest wavelengths /20/ introduces an appreciable error.

The indeterminacy associated with the variations in emissivity was analyzed in /21/, where it was shown that if the variations of the reflection coefficients δR_λ depend on the wavelength,

therefore in this way a certain error is introduced into the determination of Q. As discussed in Section 3 of Chapter One and in Section 1 of this present chapter, the coefficient of reflection of water drops off when spume forms on its surface. The spectral dependence of the reflection coefficient when spume is present has not been studied in detail, however, it was established that the effect of spume is more strongly evident at shorter wavelengths. Therefore, by specifying the simplest model of the exponential dependence of variations in the reflection coefficient on wavelength

$$\delta R_{\lambda_1} = (\lambda_1/\lambda_2)^{-n}\,\delta R_{\lambda_2},$$
(6.11)

we can estimate the order of magnitude of the error δQ in deter- /161 mining the integrated moisture content at two different wavelengths 0.8 cm and 1.35 cm.

Some substantiation for the exponential function is represented by experimental data on the emission of storm regions shown in Fig. 6.3, from which there follows a function for δR_λ

that is close to the exponential with exponent n = 1. If we take δR_λ = 0.07 at the wavelength λ = 1.35 (which evidently is the

upper estimate on the condition that averaging is taken over a large spot), the error in determining the moisture content for different n can be obtained from the following calculated data:

n	0	1	2	3
δQ g/cm^2	−0.4	−0.15	0	+0.15

When n = 2, the error is absent, for in this case the effect of variations in the coefficient reflection is indistinguishable from the manifestation of cloud cover. When the exponent n = 1, which evidently is close to the actual situation, the error δQ = −0.15 g/cm^2 is small, several times less than the root-mean-square variations in Q associated with change in weather.

The indeterminacy in the vertical distribution of water vapor leads to the fact that the coefficient of 0.08 in Eq. (6.7) actually can change somewhat, but not more than by 6 percent. In turn, this will lead to the same relative error in the determination of Q. This error, if one considers that variations can exceed 50 percent of the mean value can be recognized as insubstantial in the first stage of investigations. Spectral measurements in the vicinity of the resonance, discussed in Chapters Three and Four, can refine the vertical distribution and, thus, reduce the indeterminacy in the reconstruction of Q from radiometric measurements associated with this distribution.

Departures from the Rayleigh law of scattering and absorption for radiation with $\lambda \geqslant$ 0.8 cm can occur during rainy periods. Moving somewhat ahead of ourselves, we note that probable areas of rainfall were delimited by the abrupt rise in the absorption of microwave radiation, leading to a readily noticeable rise in brightness temperature not only at the wavelengths 0.8 cm, but also at the wavelengths 3.4 cm and even 8.5 cm. However, this delimitation was nonunique owing to the presence of stormy regions, where a similar rise in brightness was caused by a change in the coefficient of reflection to the spume.

A detailed discussion of this problem based on satellite measurements can be found in Section 1 of this chapter. In addition, during precipitation absorption becomes so intense that the reconstruction of τ_λ from measurements of $T_{b,\lambda}$ proceeds with high error. The range of problems associated with the source of error discussed in this section is quite broad and at the present time no reliable estimates of the determination errors are available[3]. /162

A specifically satellite aspect of the origin of the error[3] in the determination of Q when precipitation is present bears noting. During satellite measurements, the brightness temperature is averaged over the antenna radiation pattern. The size of the corresponding spot on the Earth's surface can markedly exceed the dimensions of the precipitation area of the most intense precipitation. Owing to the strongly nonlinear relation between $T_{b,\lambda}$ and τ_λ (6.9), when $\tau_\lambda \gtrsim 1$, the mean brightness temperature $T_{b,\lambda}$ no longer will correspond to the optical thickness τ_λ that is averaged over the radiation pattern. We can show that the effects associated with this situation understate the value of Q obtained from radiometric measurements.

The necessity of taking into account numerous factors when solving the simplest inverse problem of satellite atmospheric sensing -- determining water vapor content in the vertical column of unit cross sections -- requires careful handling of the problems of equipment calibration and subsequent monitoring of the results of reconstruction based on independent measurements.

To determine the water vapor content, absolute values of brightness temperatures are needed. When preparing an experiment, the radiometer sensitivity (coefficient of proportionality between antenna temperature and the output signal of the radiometer) was determined from laboratory calibration, and then the calibration was monitored by built-in sources -- noise generators. However, to obtain reliable absolute values of the brightness temperature it was required to tie in the radiometer scales during the flight. The tie-in involved finding the scale zero point. One possible method of tying in radiometer readings is based on mean-climatic atmospheric data /17/. Since in one orbit the Kosmos 243 satellite took measurements twice in the belt from 71.3° N. Lat. to 71.3° S. Lat., in a fairly short period, for example, in one 24-hour day, a large number of measurements N could be acquired, for which the brightness temperatures will be independent. Then, by using mean-climatic data, one can tie in the satellite radiometer readings to the absolute scale. This tie-in was conducted based on measurements only in cloud-free regions and in the absence of storms. The accuracy of the tie-in based on mean-

climatic data was $\overline{((\delta T_{b,\lambda})^2)^{1/2} \cdot N^{-1/2}},$ where $((\delta T_{b,\lambda})^2)^{1/2}$ is the root-mean-

---

[3] We note that, evidently, an insufficiently correct recording of absorption in droplet precipitation led most likely to the overstated values of Q: higher than 6 g/cm^2 (see /22/), which are obtained, respectively, for large brightness temperatures at the wavelength 0.8 cm.

square deviation of the brightness temperature $T_{b,\lambda}$ from its mean-climatic value. An idea of the magnitudes of $\overline{((\delta T_{b,\lambda})^2)^{1/2}}$ is given by Table 13, which contains the results of calculation of the brightness temperature of outgoing radiation based on correlation matrices of air temperature and humidity over the ocean. In the calculation of $T_{b,\lambda}$, use was made of formulas from Section 1, Chapter Three for the absorption coefficients with dimers taken into account. These play a marked role only at the wavelength 0.8 cm.

/163

TABLE 13. MEAN BRIGHTNESS TEMPERATURES $T_{b,\lambda}$ AND ROOT-MEAN SQUARE DEVIATIONS $\overline{((\delta T_{b,\lambda})^2)^{1/2}}$ CALCULATED FROM CORRELATION MATRICES OF RADIOSONDES FROM WEATHER SHIPS

Coordinates of Station and Season	$\lambda = 0.8$ cm		$\lambda = 1.35$ cm	
	$T_{b,\lambda}$ °K	$((\delta T_{b,\lambda})^2)^{1/2}$ °K	$T_{b,\lambda}$ °K	$((\delta T_{b,\lambda})^2)^{1/2}$ °K
62° N.Lat. 33° W.Long. January	156	1.35	151	13.9
53° N.Lat. 36° W.Long. January	156	3.54	138	6.6
July	159	2.52	173	9.0
44° N.Lat. 41° W.Long. January	156	2.42	144	8.9
July	160	3.10	162	12.9
35° N.Lat. 48° W.Long. January	157	3.21	172	10.5
July	162	4.41	178	13.7

The sections free of clouds over the ocean were delimited from readings of an infrared radiometer with a 10-12 μm band filter installed on the AES /23, 247. During the first day 80 such regions were delimited, more or less uniformly distributed latitudinally. Over these sections, a tie-in of scales was carried out, which essentially amounted only to correcting the attenuation in the antenna-waveguide line. The correction only somewhat increased the error of laboratory measurements of attenuation in the line.

Fig. 6.26 presents the calculated dependence of brightness temperature on time for one orbit of the satellite track, and the points refer to experimental values of the brightness temperatures for the delimited cloud-free sections with reference to the tie-in. The root-mean-square deviation of the experimental values

of the brightness temperatures at the wavelength $\lambda = 1.35$ cm was 11° K in good agreement with Table 13. A similar tie-in procedure was conducted also for the wavelength 0.8 cm and led to a root-mean-square deviation from the mean-climatic function of 5.3° K, which is also in agreement with the estimate from Table 13 when the fluctuational sensitivity of the equipment is taken into account. Use of these 80 independent sections permits estimating /164 the accuracy of the tie-in to the order of 1° K for the 0.8 and 1.35 cm ranges.

Delimitation in subsequent days of cloud-free sections demonstrated the stability of radiometer performance.

The above-described tie-in method is quite cumbersome and of course not the only one. The scale can be calibrated by individual points over land and over sea, for which points all the required meteorological parameters are known, without resorting to specifically laboratory calibrations. However, the tie-in method based on mean-climatic data with correction of equipment parameters based on these data has definite advantages.

First of all, using mean-climatic data does not require reference points with well-known meteorological parameters and, rather, these points can be used for monitoring.

Secondly, the method is based on relatively stable and well-studied mean-climatic functions and closely studied characteristics of the sea surface. Calibration based on the land-sea gradient is made difficult by the indeterminacy of the coefficient of emission of the continental surface.

Finally, the statistical nature of the method permits both a reduction in the influence of random errors in measurements and in data transmission, as well as the neglect of small-scale and short-lived variations of atmospheric parameters that can distort the conversion from calculated parameters at the reference point to satellite instrument readings.

To verify the accuracy of the determination of Q from satellite data, vertical temperature and humidity profiles were collected, obtained on weather ships and island meteorological stations.

From these, it was possible to collect 38 realizations in 3 days: 33 in the northern and 5 in the southern hemispheres, which were measured not farther than 150 km from the satellite track and were shifted in time by no more than 3 hours from satellite measurements. Generally, measurements in two wave-

lengths -- 0.8 cm and 1.35 cm -- were used in determining Q. At large $\tau_{0.8} > 1.0$, measurements at the wavelength 3.4 cm were resorted to in monitoring the observance of the function $\frac{\tau_{\lambda_1}}{\tau_{\lambda_2}} = \left(\frac{\lambda_2}{\lambda_1}\right)^2$

Fig. 6.27 is a correlation plot of the comparison of the Q_{AES} values measured from the satellite and the Q_{SON} values obtained by integrating radiosonde profiles. The good agreement between these measurements, which were entirely independent, can be noted. The coefficient of correlation between the results of the radiosonde and satellite measurements was 0.98. The root-mean-square deviation of the difference of these measurements was 0.2 g/cm^2 as Q was varied from 0.6 to 5.2 g/cm^2. It should be noted that when precipitation is present, the accuracy of the measurements will be less than the value relating to mean conditions.
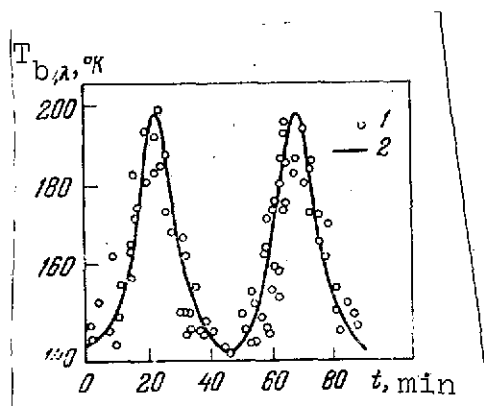
Fig. 6.26. Calculated mean-climatic trend of brightness temperature at wavelength $\lambda = 1.35$ cm for September (1) and experimental values (2) obtained in cloud-free regions /17/
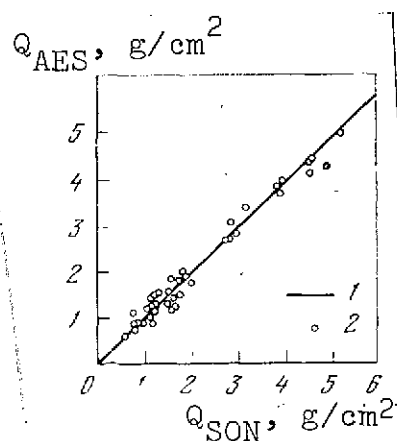

Fig. 6.27. Comparison of satellite and radiosonde determinations of moisture content Q
1. Ideal agreement
2. Experimental data /17/

If one considers that Q in the ocean can vary at the same station by 2-2.5 g/cm^2 /25/, an error of 0.2 g/cm^2 is admissible, and satellite measurements to the accuracy already attained during the experiment on Kosmos 243 can yield useful information on the water vapor content over the oceans, over whose extensive expanses virtually no quantitative measurements of atmospheric parameters are made.

3-4) The set of the results of brightness temperature measurements at the wavelength 0.8 cm and 1.35 cm made from the

satellite and the Q values calculated from these measurements can be regarded as a stochastic ensemble. To describe the random variables, it is natural to use probability distributions and the simplest characteristics of these distributions: mean values and root-mean-square deviations. This statistical approach permits generalizing the set of measurements and representing their results in a compact, graphical form. In this section we will examine several statistical generalizations of the results of measurements made on Kosmos 243 pertaining to determining the water vapor content in the atmosphere.

One of the key parameters of the probability distributions will be the latitude of the location or the quantities associated with it, for example ocean surface temperature. In Fig. 6.28 is shown the probability distribution for brightness temperatures at the wavelength 1.35 cm; latitude is the parameter of the family of curves. In Fig. 6.29 is shown the latitudinal dependence of the probability of the brightness temperature deviating at the wavelength 0.8 cm from the mean-climatic value. This function /166 shows that in spite of the closeness to the fall equinox, the distribution of brightness temperatures is asymmetric relative to the equator. This asymmetry is evidently associated with the thermal inertia of the oceans. Besides the interest that these distributions represent for designers of future satellites, several more conclusions can be drawn from them.
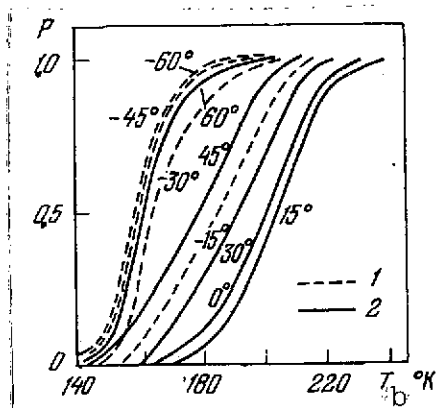
Fig. 6.28. Empirical probability distributions for brightness temperatures measured from Kosmos 243 at the wavelength
λ = 1.35 cm over the ocean /12/
Numbers by curves represent latitudes:
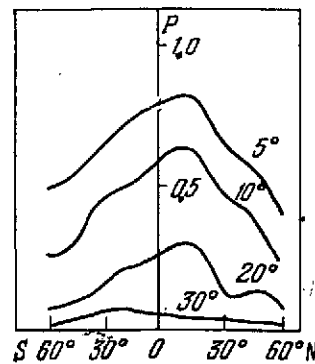1. Southern hemisphere
2. Northern hemisphere

Fig. 6.29. Probability of brightening compared with mean climate at the wavelength λ = 0.8 cm as a function of latitude based on Kosmos 243 measurements Numbers by curves represent brightening in °K /12/

In roughly 30-40 percent of the cases (averaged over all latitudes), the increment in brightness temperature is less than 5° K -- the minimum level detectable in the experiment. This agrees closely (considering the relative duration of the experiment -- several days) with the modern concept of the covering of the globe by clouds. Small brightening not exceeding 10° and not representing in practice a barrier to the determination of Q is observed in roughly 50 percent of the cases and in only 5 percent of the cases does the brightening exceed 30°. With such a high excess, it is highly probable that considerable precipitation will fall, and careful analysis is required to obtain information on the water vapor content.

Fig. 6.30 is a histogram of the distribution of Q in the polar regions and in the lower latitudes. Ocean temperature is the histogram parameter. Cases of cloud-free situations are shown in the histogram or, to be more exact, cases in which cloud cover was not scanned at the wavelength 0.8 cm. Curiously, in the lower latitudes there is a very broad range of variation /167 in Q and, as was noted in Section 3 of Chapter Three, this parameter over the ocean correlates poorly with the humidity of the near-water air. Smaller variations, compared with the mean value, are observed also in the high latitudes.

Observations made globally make it possible to estimate the distribution of water vapor over the oceans. If one considers that about 30 percent of solar heat received by the Earth is expended in evaporation, and that the influx of latent heat of evaporation in the atmosphere is 15 times greater than the rate of generation of kinetic energy /27/, study of the distribution of water vapor over the oceans is, in addition to all else, a problem in finding the energy reserves in the atmosphere at the site of their origination. In Fig. 6.31 is presented the latitudinal distribution of precipitable water over three oceans, and in Fig. 6.32 the globally averaged distribution of precipitable water over the oceans. Fig. 6.32 also shows the limits of the variations in the water vapor content. The data in Fig. 6.31 indicate that the latitudinal trend over all the oceans on the average is the same and that, in spite of the fall equinox, there is more water vapor in the northern hemisphere. Evidently, this is also a consequency of the inertia of the system active ocean layer-atmosphere. An estimate of the total mass of water vapor in the entire Earth's atmosphere /26/ obtained by a reasonable extrapolation of the data in Fig. 6.32 leads to an Earth-mean amount of precipitable water equal to 2.4 g/cm^2, in agreement with the estimates given in /27/.

3-5) Besides the statistical analysis of the results of measurement over the ocean, it is also possible to analyze individual realizations in a set with all the available meteorological information.

Fig. 6.33 shows the variation in moisture content along an orbit from the equator up to 70° N. Lat. The variation in Q is not monotonic and in general reflects a complicated pattern of movement of dry and moist air masses. Since satellite measurements proceeded continuously, by using both the ascending as well as the descending sections in subsequent orbits, one can enter on the plot Q values along an orbit and consider this field as the basis for compiling a humidity map, bearing in mind some degree of nonsynchronicity in the data obtained.

When Q values were plotted on the map of the southern hemisphere where the oceans occupy a greater surface, it was found that there is a fairly well-defined delimiting line between the dry air of the polar and middle latitudes and the moister air characteristic of the tropical latitudes /1 /. Analysis of baric fields in this region /28/ showed a definite relationship between the distribution of moisture content and the synoptic situation in this region. The interfaces of dry and moist air were plotted on the synoptic map (Fig. 6.34), with the latitude of the transition from $Q \leqslant 1$ g/cm^2 to $Q \geqslant 4$ g/cm^2 indicated. An examination of the interfaces in the western hemisphere showed they run between cyclone sweeping masses of tropical air toward /168 the south, and the anticyclone carrying masses of polar air toward the north. In the eastern hemisphere the interface also extends north of an extensive anticyclone. Thus, circulation of the baric systems is reflected in the distribution field of moisture content Q.
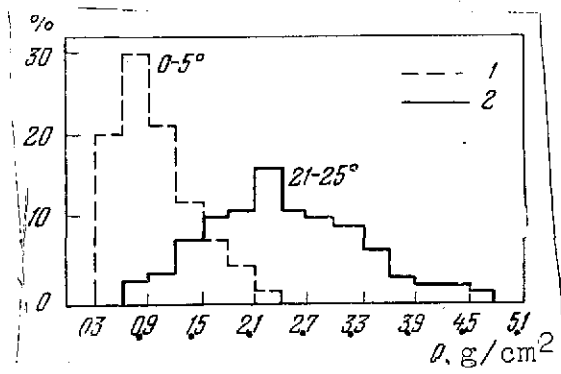

Fig. 6.30. Histograms of the distribution of Q in polar regions (1) and in the lower latitudes (2) in conditions of low cloud cover (W < 0.2 kg/m^2) Numbers by curves (distribution parameter) represent temperature of ocean surface in °C /26/
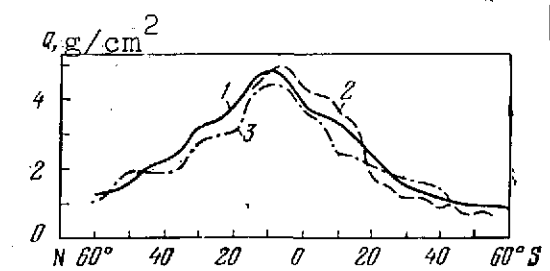

Fig. 6.31. Latitudinal distribution of mean values of Q based on Kosmos 243 measurements over the ocean
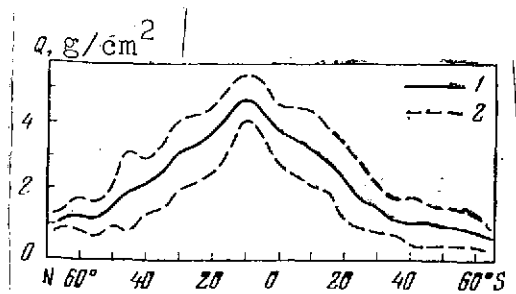1. Pacific
2. Indian
3. Atlantic /26/

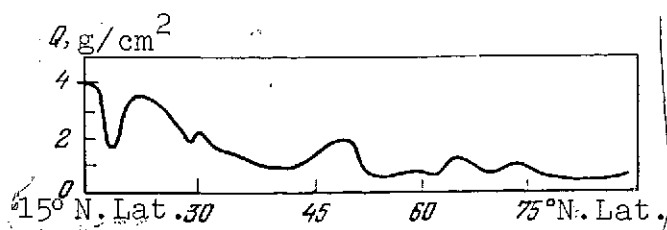Fig. 6.32. Latitudinal distribution of mean moisture content over all bodies of water (1) and its variation (2) /26/

Fig. 6.33. Variation in moisture content Q along one of the orbits of satellite trajectory over the Atlantic Ocean /1_7

Analysis of the moisture content field in the northern hemisphere together with the synoptic information and the use of satellite television cloud-cover pictures was made for the Pacific Ocean in /29, 30/ and for the Atlantic Ocean in /30, 31/.

The fact that the most reliable data on Q were obtained over extensive bodies of water is of special interest, since quantitative data on the condition of the atmosphere over the oceans are extremely scanty. At the same time owing to the presence of cloud cover the use of infrared band for quantitative measurements throughout the entire atmosphere proves to be extremely difficult. /169
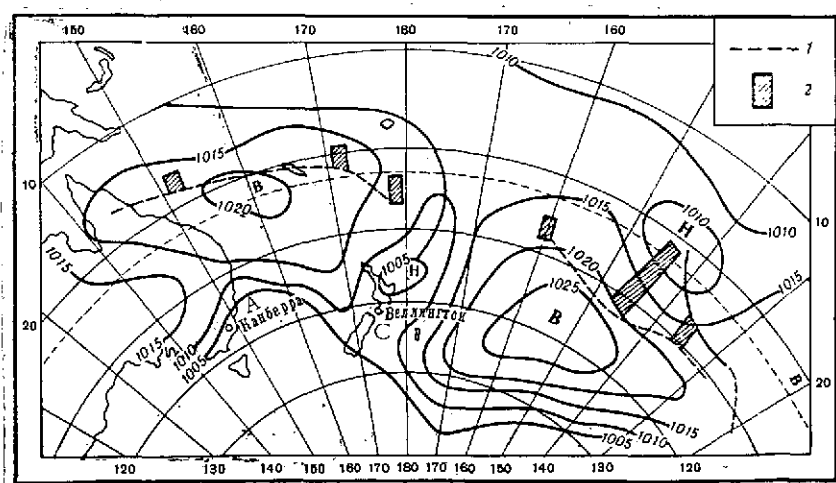

Fig. 6.34. Comparison of ground baric field with dry air-moist air interfaces determined from satellite measurements /28/
1. Boundary between dry air and moist air
2. Width of boundary
KEY: B = High; H = Low; A = Canberra; C = Wellington

Maps of total moisture content in /29, 30/ were plotted as follows: Projections of satellite orbital planes were entered onto a map of the ocean body of water in four to five subsequent orbits. Values of the total moisture content of the atmosphere Q in g/cm^2 with gradations 0.5 g/cm^2 were denoted at the points lying along the projections of the orbits at a distance from each other of approximately 200 km (Fig. 6.35). Radiosonde data at the stations noted by the points on the map revised the position of the Q isolines between projections of the satellite orbit.

A certain amount of nonsynchronicity of the data plotted is a distinguishing feature of the moisture content maps thus constructed. Data along one orbit in the region of the equator and in the area of 70° N. Lat. differed from each other in time by about 15 min. The time of measurement in a single orbit differed from the time of measurement in the subsequent (at the same lati- /170 tude) orbit by 1.5 hr. Therefore, in plotting the moisture content map based on data from five orbits, the time for measuring the moisture content over the western part of the ocean will differ from the time required to measure it over the eastern part, by 6 hr. However, as shown by a comparison of the data for three subsequent orbits over the same regions, the total moisture content is a quite conservative quantity, when the synoptic situation in the given region remains unchanged: the maximum variation in Q over the period of a day was 1.5 g/cm^2 at several points of the ITCZ (intratropical convergence zone), while it was 0-0.5 g/cm^2 in the mid- and high latitudes, as a rule. Therefore this moisture content map can to the first approximation be interpreted and analyzed as an integral whole.

All the remaining forms of information resorted to in the analysis (synoptic maps, baric topography maps, and maps of nephanalysis) were taken for the time periods so that the discontinuity in time between them was within 6 hr.

In the combined analysis, use was also made of the synoptic map for 15:00 (Moscow Time) on the same day as the nephanalysis data plotted on it from meteorological satellites ESSA-6 and ESSA-7. By comparing this map shown in Fig. 6.35, it became clear that well-defined narrow tongues of moist air bounded by a zone with increased moisture content gradients correspond to the atmospheric fronts -- one associated with the cyclone in the Gulf of Alaska, and the other associated with the cyclone along the coasts of Chukotka.

Sources of dry air correspond to a high-pressure ridge south of Kamchatka, the anticyclones south of the Aleutian Islands, and the anticyclone along the coasts of the United States, as well as a ridge oriented from the first of the anticyclones listed toward the southwest.

In the south, in the equatorial zone sources of maximum moisture content were observed, associated with the ITCZ, one branch of which stretched from 150° E. Long. to 170° W. Long. (5-9° N. Lat.), and the other -- from 170° to 140° W. Long. (6-7° N. Lat.). A belt of relatively dry air with minimum integrated moisture content of 2 g/cm^2 in the area of 170° W. Long. stretched along the equator itself.

The two above-listed anticyclones (the one south of the Aleutian Islands and the one along the coasts of the United States) on the moisture content maps are characterized by dry air sources. The weather conditions in these sources are different on the synoptic maps. A thick continuous cloud cover is observed in the anticyclone south of the Aleutian Islands, while limited cumuloid cloud cover is observed in the cyclone along the coast of the United States. The specific moisture content at the ocean surface (based on ground meteorological observations) in the latter anticyclone is higher than in the former (10-14 and 6-9 g/kg, respectively).

The resulting maps of total moisture content refine the position of the atmospheric front associated with the cyclone in the Gulf of Alaska on the synoptic map. From the data of the total moisture content maps, this front extends somewhat to the south. This is further confirmed by the fact that on the synoptic maps and the total moisture content maps, on subsequent days it was displaced southward. The revised front position is entered onto the map in Fig. 6.35 with a dashed line.

Analysis of the integrated moisture content field over the 3 days 23-25 September 1968, made by drawing upon aerial synoptic material, revealed the following.

In the northern part of the Pacific Ocean (north of the equator) three latitudinally oriented regions can be readily traced, differing from each other both in total moisture content as well as by the nature of the sources of dry and moist air. From 60° to 40° N. Lat. is a belt of reduced moisture content (the minimum moisture content of the central parts of the dry air sources is ⁓ 0.5 g/cm^2). Sources of driest air are stretched in the meridional direction and correspond to the central parts of the anticyclones at these latitudes. It should be noted that sources of dry air correspond to the anticyclones, regardless of what weather is observed in this anticyclone. From 20° to 5-4° N. Lat. is a belt of moist air. Sources of maximum moisture content (Q = 5.5 g/cm^2) are quite narrow, latitudinally elongated regions. These sources of elevated moisture content lie along the ITCZ and correspond to cloud formations in this zone. The equatorial dry zone (Q = 2 g/cm^2) can be readily traced along the
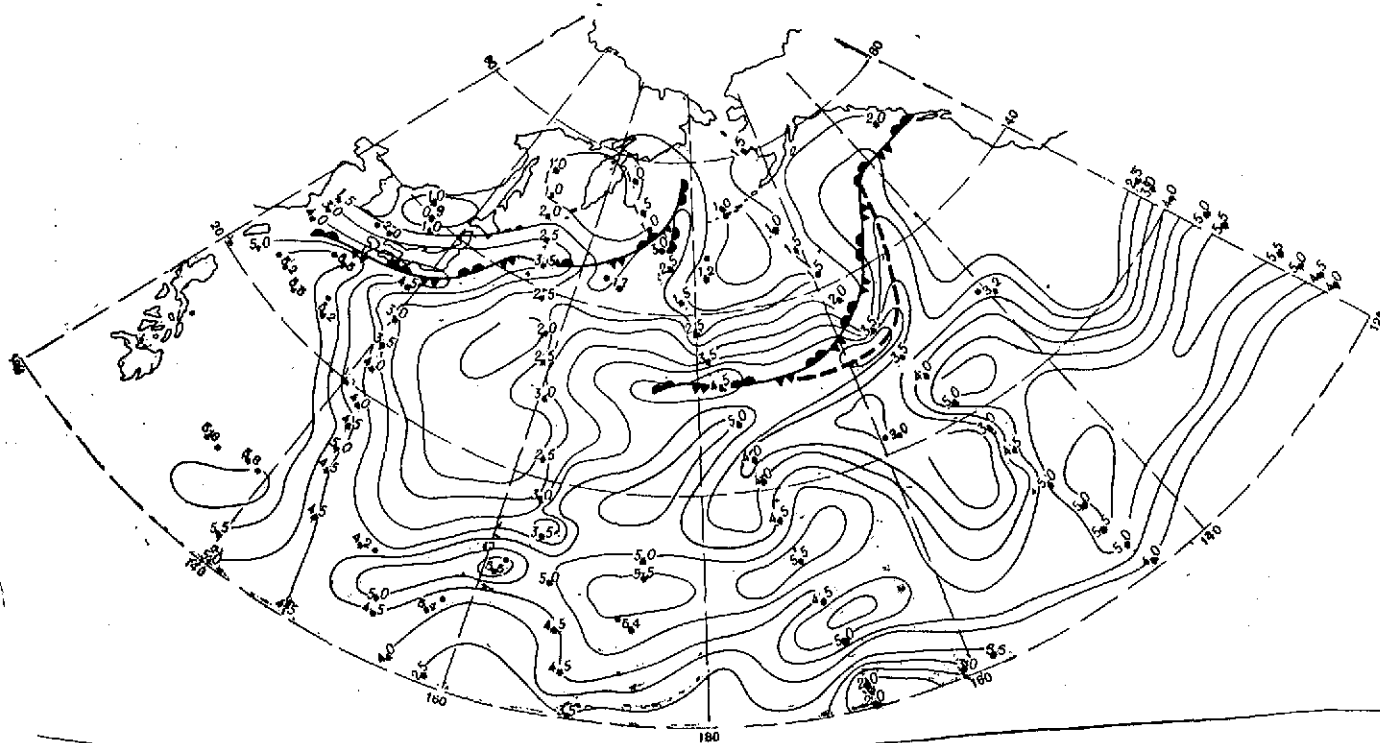
Fig. 6.35. Field of moisture content Q over the northern part of the Pacific Ocean on 23 Sep 1968 with atmospheric fronts plotted on it

Broken curve denotes refinement of front position in the area of Alaska from satellite observations /29/

equator. Part of the Pacific Ocean from 40° to 20° N. Lat. is a zone where in general there is an exchange between the dry northerly and moist southerly air masses. In this region tongues of moist air directed south-to-north alternate with tongues of dry air oriented in the opposite direction. The moist air tongues can propagate farther to the north and penetrate the northern dry belt, just as the dry tongues can penetrate the moist southern belt.

Penetration of significant drier masses far to the south leads to the disappearance of the narrow belt of maximum moisture content. At the same time the cloud cover of the ITCZ is observed to break up. Narrow tongues of moist air correspond to frontal interfaces in the moisture content maps, and the transition to the narrow tongues of moist air from regions of dry air is characterized by high gradients of integrated moisture content. Regions of reduced moisture content correspond to high pressure ridges in the moisture content maps.

Over the ocean the warmer air masses are also more moist. This conclusion is well confirmed by averaged maps of total atmospheric moisture content. However, as can be seen in the daily maps of integrated moisture content obtained from data of measurements made on Kosmos 243, a smooth rise in the total moisture content from north to south is disrupted as a result of the /173 formation of atmospheric perturbations and their displacement in a particular direction. The redistribution of dry and moist air masses can be accounted for by the inception of descending and ascending air movements. Descending movements are accompanied by considerable settling, adiabatic compression, and streaming (divergence of air masses) in the lower layers in anticyclones and regions of elevated pressure, while the ascending movements lead to the opposite results in cyclones and at atmospheric fronts.

The dynamics of the buildup of synoptic processes can be readily traced in maps of total moisture content over the three-day period. Narrow tongues of elevated total moisture content are displaced along with the corresponding atmospheric fronts. Propagation of the high pressure ridge is accompanied by broadening of the source of relatively dry air.

Owing to the fairly well-defined correspondence between the narrow moist air tongues and the atmospheric fronts, and between the dry air sources and the anticyclone and the elevated-pressure regions, and also due to the above-noted conservation of integrated moisture content when there is no change in the synoptic situation, the moisture content maps can be of major assistance in tracing the history of the buildup of synoptic processes and in frontological analysis. This assistance is especially marked when the near-ground front is not sufficiently well defined in temperature fields, parametric trend fields, or wind fields, or when the synoptic map lacks sufficient data for a detailed determination of the position of the front.

A comparison of the integrated moisture content maps with the synoptic maps and the baric topography maps showed that in the moisture content maps the atmospheric fronts are more clearly and graphically pronounced than on the Pacific Ocean $\frac{500}{1000}$ maps. Evidently, this is associated with the fact that at the present time there are very limited data for drawing contour lines over the oceans.

In $\overline{/331/}$ are presented the results of a combined analysis of the synoptic situation and the Q field plotted from radiometric measurements taken on Kosmos 243 over the Atlantic Ocean over three successive days (23-25 September 1968).

Besides the results of radiometric measurements from Kosmos 243 and synoptic maps, altitude maps and nephanalytic maps as well as daily weather bulletins of Great Britain and radiosonde data of nine weather ships of the North Atlantic were brought into the analysis.

Fig. 6.36 shows the Q fields, and on them are entered the results of the synoptic analysis and the analysis of cloud fields from the ESSA and Meteor satellites. Dry air sources (A, B, E, H, and I) and moist air sources (C, D, F, and G) are marked on the map. The figures pertain to 23 and 25 September 1968. The evolution of all fields entered on the map can be traced over two days.

From the standpoint of the correspondence between the Q field elements and specific synoptic formations, the following can be stated: /174

1) sources of reduced moisture content correspond to anti-cyclones and ridges characterized by the presence in their regions of descending air movements; and not only cyclones with clear or sparse-cloudy weather are characterized by reduced moisture content, but also anticyclones with solid subinversional cloud cover (for example, the drier source B in Fig. 6.36 a lies in the region of sparse-cloudy weather, while in Fig. 6.36 b -- in a zone of continuous stratiform cloud cover);

2) corresponding to frontal interfaces, in whose zone as a rule ascending air movements are observed, are narrow sources of increased moisture content; and

3) the moisture content field shifts along with the corre-sponding synoptic formations.

Moist formations in the frontal zone are more clearly reflected in the maps of integrated moisture content Q. At the
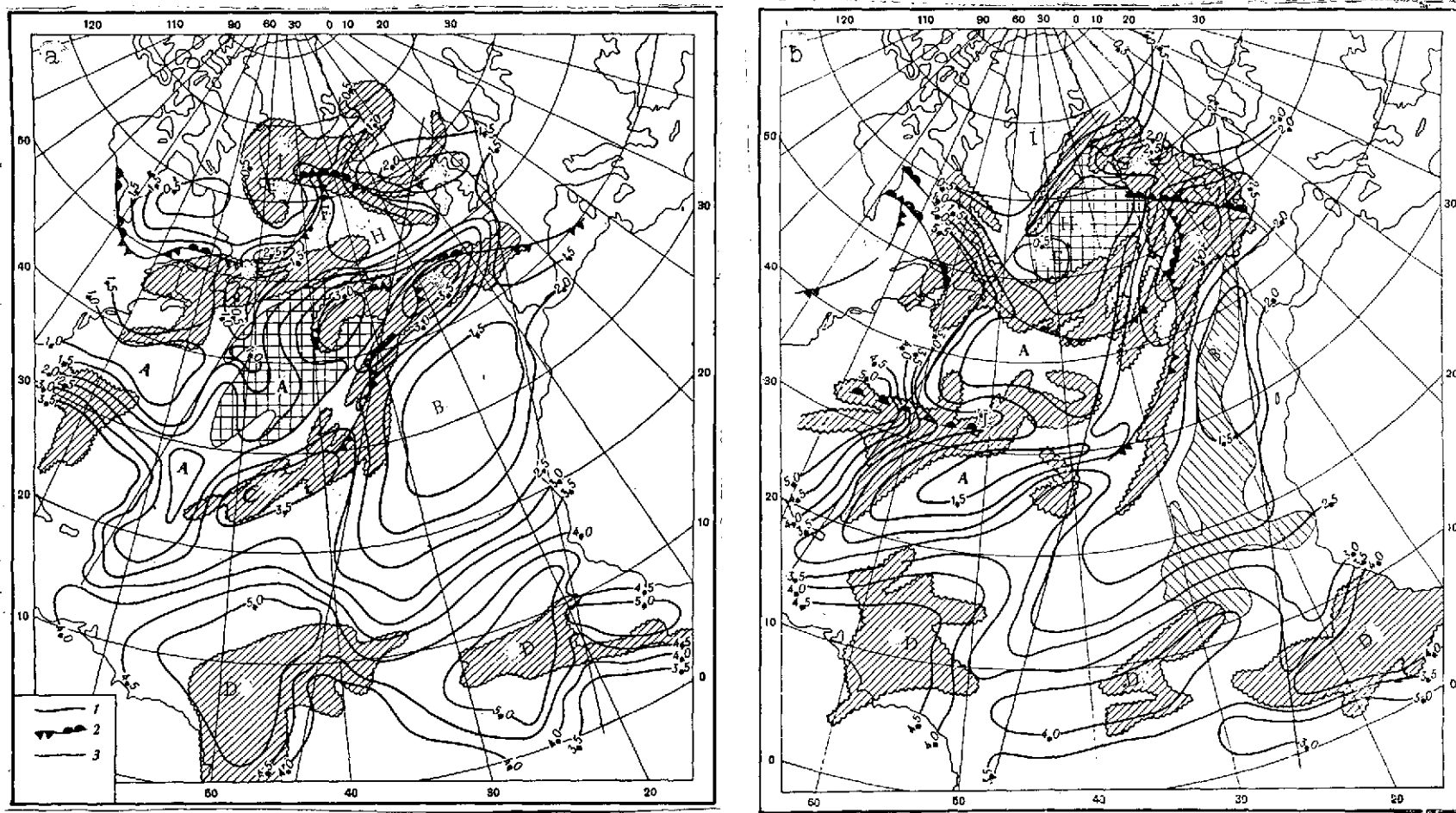
Fig. 6.36. Field of moisture content over the northern part of the Atlantic Ocean on 23 September 1968 (a) and 25 September 1968 (b) from satellite data, with synoptic situation plotted on it /31/

1. Q isolines   2. Frontal interfaces
3. Projections of satellite orbit
Cloudy areas are hatched (from nephanalytic data)

same time the deepening and filling of cyclones, and the buildup and breakdown of anticyclones can be traced in the Q maps much more poorly on the maps of Q which were, it must be admitted, obtained over a short period -- 3 days.

Analysis of the fields of air moisture content in relation /176 to the synoptic situation is still in its initial stage, however the first experiment furnished encouraging results. The prognosticatory value of Q fields doubtless will rise when the latent heat of condensation of water vapor is included in the prognostic scheme.

3-6) Determining the parameters of water vapor distribution by altitude is of particular interest. In principle, these estimates can be made in the absence of cloud cover based on measurements in the resonance λ = 1.35 and in the "window" -- at the wavelength 0.8 cm /32/. However, in order to detect variations in the characteristic altitude of water vapor from these measurements without bringing in any additional information, high accuracy of measurements is necessary. As an example that enables us to estimate the required accuracy of measurements, we present calculated estimates for Q = 5.0 g/cm^2. At this Q that is optimal for the estimates, the variation in the characteristic altitudes of water vapor from 2.1 km to 5 km leads to a change in the brightness temperature at the wavelength λ = 1.35 cm of $T_{b,\lambda}$ = = 10° K. But in order to confidently relate this change in the brightness temperature to the change in the vertical distribution of the water vapor and not the change in Q, we must measure the brightness temperature at the wavelength λ = 0.8 cm to an error smaller than 2° K. This precision of measurement was beyond the capability of the experiment performed on Kosmos 243[4].

Several estimates of the characteristics of vertical water vapor distribution based on satellite measurements are given in /33/, based on the correlations between Q and the vertical distribution of water vapor.

---

[4] With reference to the foregoing and given the inevitable variations in ocean emission that cannot be monitored accurately enough, data on variations in the vertical distribution of water vapor presented in /32/ are not due to the precision of the starting experimental material.

4. Characteristics of Clouds and Precipitation

4‐1) The results shown in Chapter Four indicate that given the microwave radiometer parameters on the Kosmos 243 and Kosmos 384 satellites, reliable determinations of the moisture reserve in clouds and estimates of precipitation intensity are possible only over bodies of water $\underline{/4}$, 12, 3$\underline{4/}$.

Determining the moisture reserve of clouds W, delineating the precipitation zones, and estimating their intensity from satellite measurements was carried out in two stages. In the first stage, the tracings of radiobrightness temperatures at four wavelengths used in the satellite measurements were inspected.

An example of a tracing of radiobrightness temperatures is shown in Fig. 6.37 $\underline{/7\_/}$. Based on these tracings, the precipitation zones which are characterized by high values of brightness /177 temperatures at the wavelength $\lambda = 0.8$ cm[5] exceeding 180–185° K were delineated, as well as the "sawtooth" appearance of the tracing, due to local structure of intensive precipitation. As can be seen from Fig. 6.37, this "sawtooth" structure in heavy precipitation appeared also at the wavelength $\lambda = 3.4$ cm. In the case of marked brightening at the wavelength 3.4 cm, a check was made of the observance of the law $\tau_{\lambda_1}/\tau_{\lambda_2} = (\lambda_2/\lambda_1)^2$, that is valid for the Rayleigh approximation applied in describing absorption in clouds.

In the second stage, outside the delineated precipitation zones, from the brightness temperatures at the wavelength $\lambda = 0.8$ cm and $\lambda = 1.5$ cm based on Eq. (6.10), the absorption coefficients are determined at these same wavelengths and then absorption in the droplet water is determined (see Chapter Four, and also Eqs. (6.6), (6.7), and (6.8)). To determine the moisture content of a cloud, we must know the temperature or the effective cloud alti- /178 tude H_W. These values were not determined in the experiment and to estimate them it was necessary to bring in characteristic values either of altitude, or of the temperature of the cloud cover, as well as measurements in the infrared band.

The noise sensitivity of the receivers limited the precision of the measurements of W to 0.1 kg/cm^2. An additional air source consisted of the changes in the blackness factor of the surface

---

[5] The increment in radiobrightness temperature at wavelength $\lambda = 0.8$ cm greater than 30° K with respect to the mean-climatic value was taken as the conditional criterion for delineating precipitation zones. See also Subsection 3–4 of the preceding section.
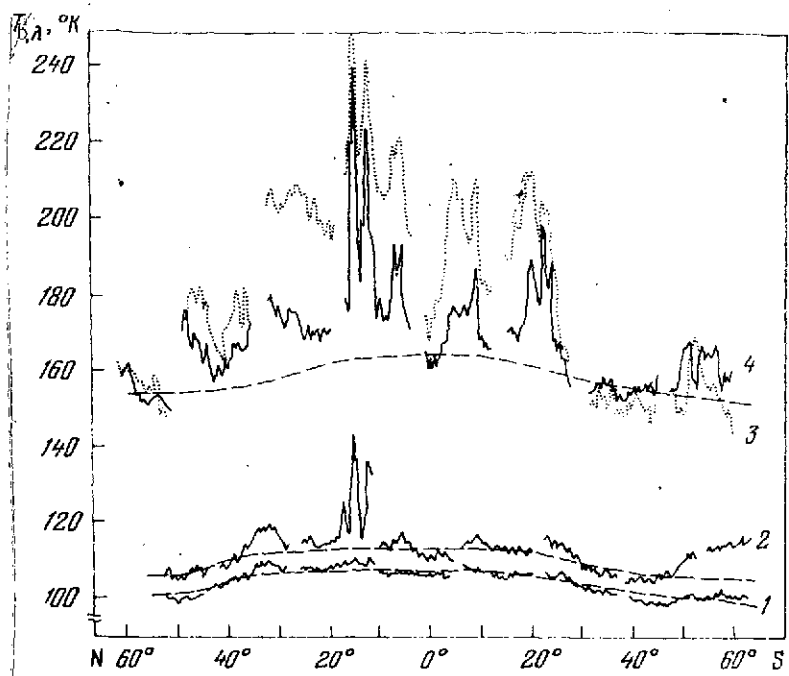
Fig. 6.37. Latitudinal profiles of radio-
brightness temperatures of the atmosphere
over the Pacific Ocean on 23 September
1968 /7_7
1. Measurements at the wavelength 8.5 cm
2. 3.4 cm
3. 1.35 cm
4. 0.8 cm
The broken lines correspond to calculated
values based on mean-climatic data; the
breaks in the lines correspond to instru-
ment calibrations during the flight\

of the bodies of water
and the nonuniformity
of the moisture content
in the field of view of
the radiometer antenna.
With these components
taken into account, it
can be assumed that the
total error in the
determination of the
moisture reserve of
clouds W based on
measurements made on
Kosmos 243 and Kosmos
384 is 0.15-0.2 kg/m^2.

Fig. 6.38 is the
profile of the radio-
brightness temperature
at the wavelength 0.8
cm over the Pacific
Ocean for 10 December
1970, when the region
of the ocean was cloud-
covered based on data
of television pictures,
to a large extent.

The cloud cover
in the subsatellite
zone can be judged from
standard symbols of
nephanalytic maps plotted
in the lower part of
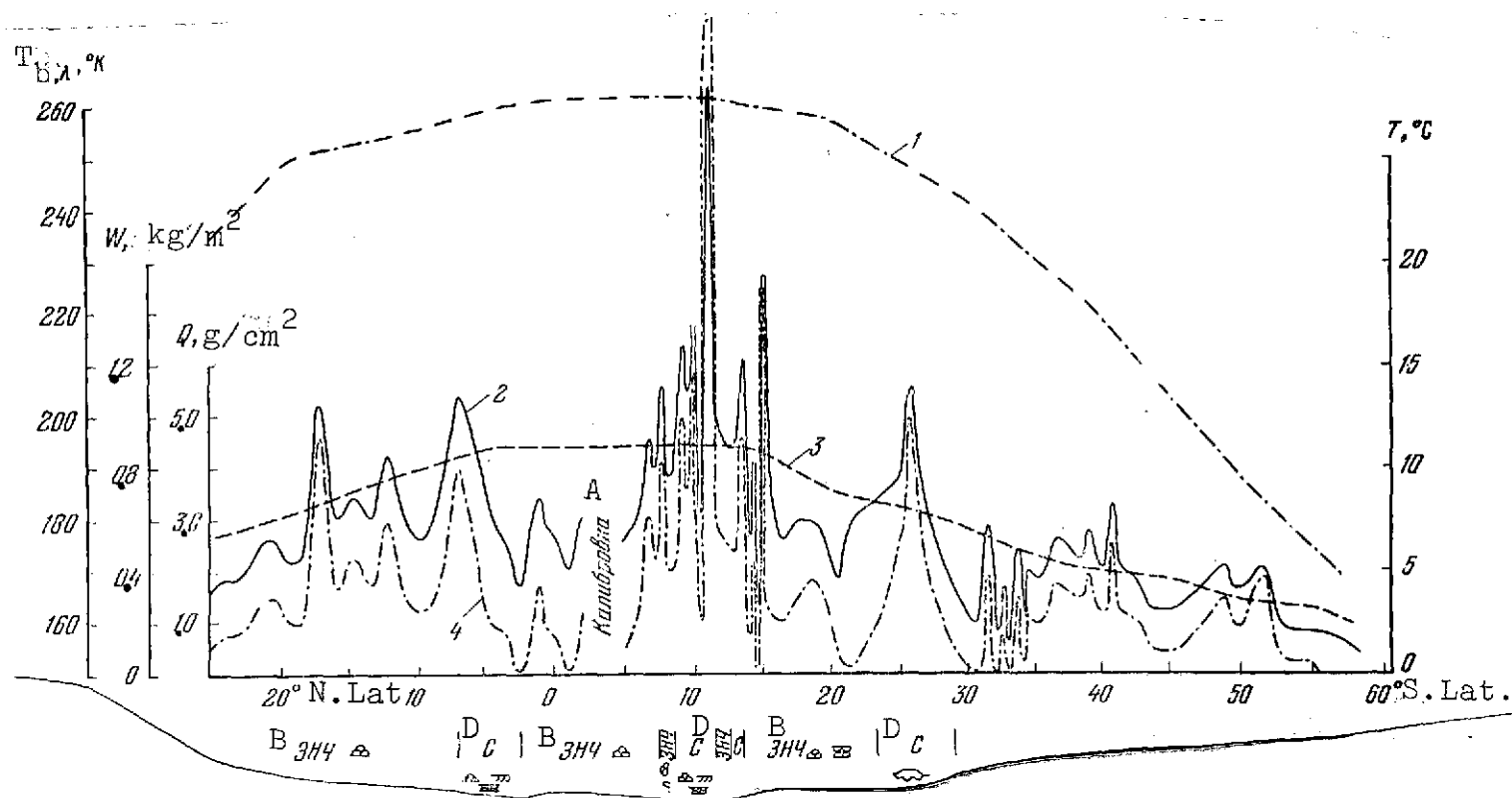Fig. 6.38.

In converting from
the absorption values
to moisture reserve W, when processing this profile use was made
of Eq. (4.24) that is valid for clouds, but not for precipitation.
However, in the zones of precipitation where the absorption is
high, calculation of W using the Rayleigh approximation for χ_λ
gives an overstated value (see Table 7), therefore W values in
these zones are only of conditional significance, correct to a
precision of the cofactor G. As already noted, the values of
$T_{b,\lambda} > 185°$ K for $\lambda = 0.8$ cm and thus $W > 0.7$ kg/m^2 very probably
indicate the presence of precipitation.

4-2) About 50 cases of interception of atmospheric front
lines were examined to analyze the variations in the radiobrightness

Fig. 6.38. Altitudinal profile of radiobrightness temperature over the Pacific Ocean at the wavelength λ = 0.8 cm (10 Dec 1970)
1. Mean-climatic ocean surface temperature T
2. Profile of radiobrightness temperatures $T_{b,\lambda}$

3. Estimate of integrated moisture content Q based on Eq. (6.6), (6.7), and (6.8)
4. Estimate of moisture content of droplet clouds W based on Eq. (4.24)
KEY: A. Calibration
      B. ZNCh /transliterated/   D. S /transliterated/

temperature of the atmosphere over the ocean in the zones of warm
and cold fronts. In all cases of intersections of fronts, marked
variations in the radiobrightness temperature associated with the
emission of cloud formations were observed. In several cases,
when the fronts intersected variations were also observed at the
wavelength 1.35 cm associated with frontal changes in the content
of vaporous moisture.

Radiobrightness profiles at the wavelengths 0.8 cm and 1.35
cm obtained upon the intersection of a wavefront are shown in
Fig. 6.39. The position of the front is noted by intense peaks
at both wavelengths, indicating that intensive condensation of
moisture in the frontal zone is associated with a rise in the
content of vaporous moisture. A similar situation was observed
in the intersection of a cold front in the Indian Ocean (Fig.
6.40). A continuous frontal cloud cover containing cirrus, stratus,
and cumulus clouds was observed in this region in the nephanalytic
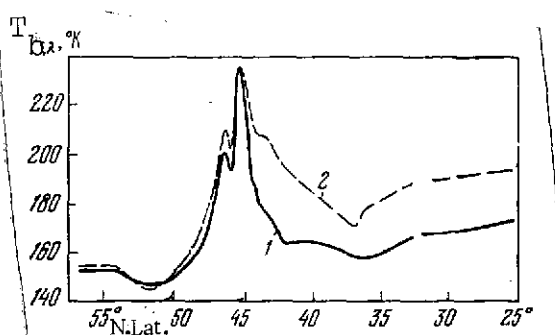maps, from Kosmos 226 data.

However, there were cases   /180
when an increase in the moisture
reserve in a frontal cloud cover
zone was not accompanied by a rise
in the moisture content in the
vaporous phase. For example,
Fig. 6.41 shows profiles of
change in content of vaporous
and droplet moisture along the
projections of the field of view
of the Kosmos 243 radiotelescopes
in the northwest Pacific Ocean
on 25 September 1968 when the
satellite track intersected two
fronts: a cold front (about 50°
N. Lat.) and a warm front (about
42° N. Lat.). Behind the warm
front the vaporous moisture
content rose to 4.5 g/cm^2, while
in the cold front region, with
just as intense condensation,
the moisture content in the

Fig. 6.39. Latitudinal pro-
files of radiobrightness
temperature in cold front
zone, 23 Sep 68
1. Radiobrightness tempera-
   ture at wavelength
   λ = 0.8 cm
2. Radiobrightness tempera-
   ture at wavelength
   λ = 1.35 cm

vaporous phase did not exceed 2 g/cm^2.

Analysis of the duration of radiobrightness temperature peaks
upon intersecting front lines showed that the width of the frontal
cloud cover zone with moisture content greater than 0.2 kg/m^2 is
in the range 100-1300 km.

4-3) Simultaneous observations of radiation characteristics
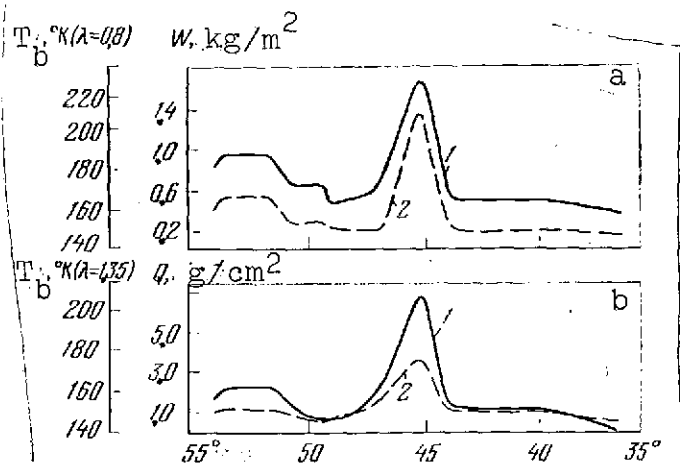of cloud formations in the microwave and infrared ranges

Fig. 6.40. Latitudinal profiles of radiobrightness temperature in a zone of the Indian Ocean upon intersection of frontal cloud cover, 24 Sep 68
a: 1. Radiobrightness temperature at wavelength $\lambda = 0.8$ cm
2. Profile of cloud moisture reserve
b: 1. Radiobrightness temperature at wavelength $\lambda = 1.35$ cm
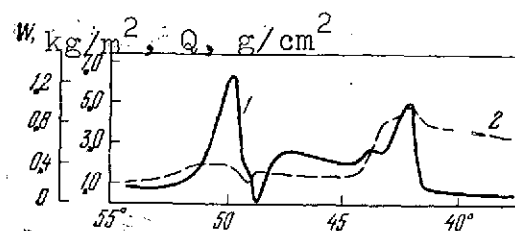2. Profile of integrated vaporous water content

Fig. 6.41. Latitudinal profiles of moisture reserve of clouds W (1) and moisture reserve Q (2) of atmosphere based on radiometric measurements upon intersection of /radiotelescope/ field of view by cold and wet fronts over the Pacific Ocean, 25 Sep 1968

considerably expanded our information on cloud structure by combined estimates of the cloud top altitude and cloud moisture content. The technique of estimating the cloud top altitude from radiation temperature measurements in the infrared range was developed in /35/.

Fig. 6.42. Example of realization of synchronous measurements of radiobrightness temperature at wavelength $\lambda = 0.8$ cm and radiation temperature at wavelength $\lambda = 10$ m of cloud formations over the ocean, 10 Dec 1970 /4_/
1. T_r
2. $T_{b,\lambda}$

Fig. 6.42 is an example of the synchronous recording of radiobrightness temperatures at the wavelength 0.8 cm and radiation temperatures at the wavelength of about 10 m /4_/.
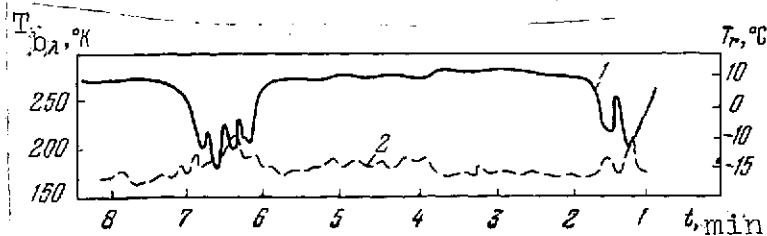
In Section 1, the decrease in the radiation temperature T_r is accompanied by a rise in the radiobrightness T_b. In this region a high cloud moisture reserve W corresponds to high cloud-top altitudes. In section 2 the variation in the cloud-top altitude is not always accompanied by a variation in cloud moisture reserve, and in several cases an increase in altitude occurs simultaneously with a reduction in moisture content. There is no upper tier cloud cover between sections 1 and 2, but judging from the variations in $T_{b,\lambda}$, here warm lower-tier clouds with /182 moisture content $W \leqslant 0.1$ kg/cm^2 can be present.
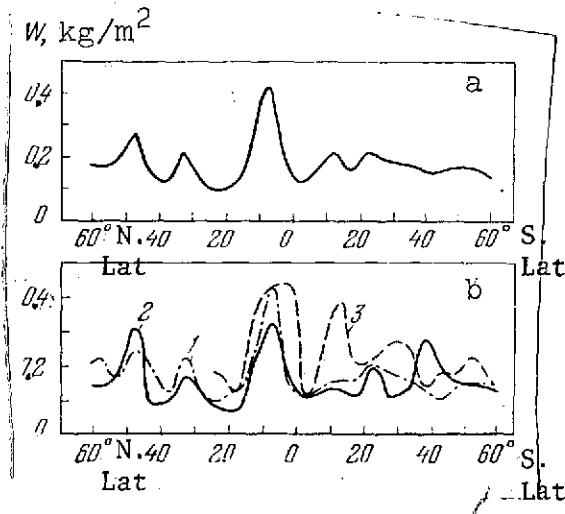

Fig. 6.43. Latitudinal distri-
bution of cloud moisture reserve
over globe based on radiometric
experimental data from Kosmos 243
(Sept.1968)
a. Averaged over bodies of water
b. 1, 2, 3 -- over the Pacific,
    Atlantic, and Indian oceans,
    respectively
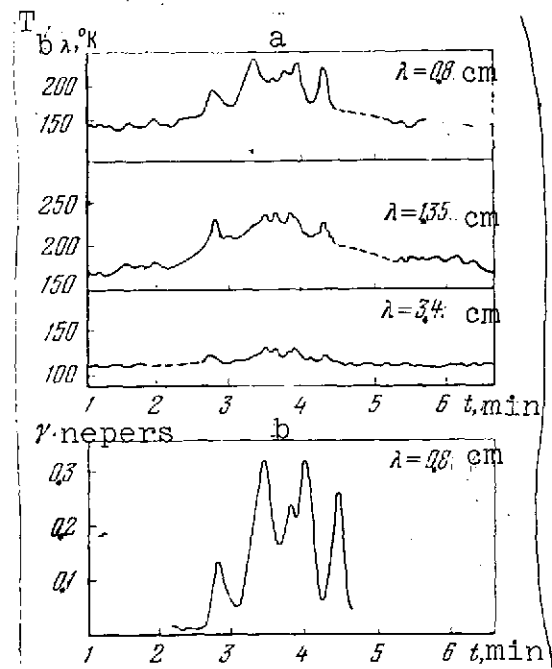
Fig. 6.44. Latitudinal profiles
of the radiobrightness tempera-
ture in an extensive precipita-
tion zone over the ocean (at
wavelength λ = 0.8, 1.35, and
3.4 cm) (a) and absorption in
the atmosphere at the wave-
length λ = 0.8 cm (b)

4-4) Grouping and averaging of radiometric data on cloud
moisture reserve by latitudinal belts yielded characteristics of
the latitudinal distribution of water content in the droplet phase.

195

The mean latitudinal distribution of the droplet moisture content is shown in Fig. 6.43 a. Fig. 6.43 b gives characteristics of the latitudinal distribution of the droplet moisture content over the Pacific, Atlantic, and Indian oceans for the period 24-26 September 1968. The maximum content values of vaporous and droplet moisture occur in the 5°-10° N. Lat. latitudinal belt. Data for Fig. 6.43 were used in determining the total mass of droplet water in the Earth's atmosphere[6]. The estimate of the total mass of droplet water is $8.7 \cdot 10^{16}$ g; 54 percent is in the northern hemisphere, and 46 percent in the southern. The ratio of the mass of droplet water to vaporous water mass is about 0.7 percent.

4-5) Besides delineation of the precipitation zones, rain intensity can also be estimated from measurements of the emission spectrum. Rain showers over the oceans are characterized by an extremely narrow distribution in space. For example, in Fig. 6.38 the appearance of rain showers can be noted from the considerable brightening at the wavelength 3.4 cm in the region 10°-20° S. Lat. Elongated precipitation zones showed up upon observations at three wavelengths (Fig. 6.44). A large values of total absorption in the atmosphere for emission at $\lambda = 0.8$ cm calculated from measurements of brightness temperatures suggest the conclusion that during the measurement period the satellite was passing over an extensive precipitation zone where rain intensity reached 10-20 mm/hr.

It should be noted that in spite of the relatively low precision of the determination of cloud moisture reserve in this experiment, the resulting data are of great value, since they permit the determination of several gradations in cloud moisture reserve. Similar determinations made from satellites equipped with microwave radiometers are evidently the only direct method of remote determination of cloud moisture reserve. The possibility of delineating precipitation zones and estimating their intensity also heightens the interest in investigations of cloud systems based on their microwave emission.

---

[6] The estimate of the total mass of droplet water in the Earth's atmosphere was made on the assumption that the mean values of the droplet water content over the oceans and the continents are the same within the particular latitudinal belt selected.

REFERENCES

1. Basharinov, A. Ye., Gurvich, A. S., and Yegorov, S. T., Dokl. AN SSSR 188/6, 1973 (1969).

2. Basharinov, A. Ye., Gurvich, A. S., and Yegorov, S. I., Proceed. of the Seventh Intern. Symp. on Remote Sensing of Environment. Ann Arbor, Michigan, 119 (1971).

3. Basharinov, A. Ye., Gurvich, A. S., Tuchkov, L. T., and Shifrin, K. S., Izv. AN SSSR, seriya FAO 6/4, 366 (1970).

4. Akvilonova, A. N., Basharinov, A. Ye., Gorodetskiy, A. K., and Gurvich, A. S., et al., Izv. AN SSSR, seriya FAO 9/2, 187 (1973).

5. Basharinov, A. Ye., Gurvich, A. S., Yegorov, S. T., Zhukov, V. I., et al., Kosmicheskiye issledovaniya 9/2, 268 (1971).

6. Basharinov, A. Ye., Gorodetskiy, A. K., Gurvich, H. S., Yegorov, S. I., Kurskaya, A. A., Matveev, D. T., and Shutko, A. M., Proc. of the Eighth Intern. Symp. on Remote Sensing of Environment, 214, 1972. /184

7. Basharinov, A. E., Yegorov, S. I., Gurvich, A. S., and Oboukhov, A. M., Space Res. 11, 593 (1971), Akad.-Verlag Berlin

8. Matveyev, D. T., Izv. AN SSSR, seriya FAO 7/10, 1070 (1971).

9. Marzinkevich, L. M., and Matveyev, D. T., Meteorologiya i gidrologiya, 8, 50 (1971).

10. Basharinov, A. Ye., and Shumko, A. M., Issledovaniye vzaimos-vyazi kharakteristik polya teplovogo radioizlucheniya s sostoyanpem poverkhnosti akvatoriy /Analysis of Relationship Between Characteristics of Thermal Radio Emission Field and Surface State of Bodies of Water/, Preprint of the Institute of Radioelectronics, USSR Academy of Sciences, Moscow, 1971.

11. Gurvich, A. S., Kalinin, V. I., and Matveyev, D. T., Izv. AN SSSR, seriya FAO 9/12, 1247 (1973).

12. Obukhov, A. M., Basharinov, A. Ye., Vasil'yev, Yu. V., Gurvich,
    A. S., Demin, V. V., et al, Kosmicheskiye issledovaniya 9/1,
    66 (1971).

13. Basharinov, A. Ye., Gorodetskiy, A. K., Gurvich, A. S.,
    Yegorov, S. T., et al., Izv. AN SSSR, seriya FAO 9/183
    (1973).

14. Basharinov, A. E., Gurvich, A. S., Yegorov, S. T., and
    Kurskaya, A. A., Space Res. 11, 713 (1971), Akad.-Verlag.
    Berlin.

15. Belyakova, G. M., Gurvich, A. S., Matveyev, D. T., and
    Mironov, B. P., Dokl. AN SSSR 201/4, 837 (1971).

16. Barkov, N. I., Shel'fovyye ledniki Antarktidy /Ice Shelfs of
    of the Antarctic/, Leningrad, Gidrometeoizdat, 1971.

17. Gurvich, A. S., and Demin, V. V., Izv. AN SSSR, seriya FAO
    6/ 771 (1970).

18. Dombkovskaya, Ye. P., Meteorologiya i gidrologiya, 8, 8 (1969).

19. Basharinov, A. Ye., and Kutuza, B. G., Trudy GGO, 222, 100
    (1968).

20. Shifrin, K. S., and Chernyak, M. M., Trudy GGO, 222, 74
    (1968).

21. Demin, V. V., Izv. AN SSSR, seriya FAO 8/811 (1971).

22. Mitnik, L. M., Trudy TsAO, 103, 64 (1972).

23. Gorodetskiy, A. K., Malkevich, M. S., Orlov, A. P., and
    Timofeyeva, V. I., Izv. AN SSSR, seriya FAO 6/5, 477 (1970).

24. Gurvich, A. S., Yuferev, V. N., Izv. AN SSSR, seriya FAO
    6/5, 523 (1970).

25. Plechkov, V. M., Gurvich, A. S., and Snopkov, V. G., Dokl.
    AN SSSR 193/5, 1041 (1970).

26. Basharinov, A. Ye., and Mitnik, L. M., Meteorologiya i
    gidrologiya, 12, 13 (1970).

27. Monin, A. S., Prognoz pogody kak zadacha fiziki /Weather
    Forecasting as a Problem in Physics/, Moscow, Nauka Press,
    1969.

28. Obukhov, A. M., and Tamarskaya, M. S., _Meteorologiya i gidrologiya,_ 11, 36 (1969).

29. Gurvich, A. S., Demin, V. V., and Dombkovskaya, Ye. P., _Meteorologiya i gidrologiya,_ 8, 30 (1970).

30. Dombkovskaya, Ye. P., and Mimnik, L. M., _Meteorologiya i gidrologiya,_ 6, (1972).

31. Demin, V. V., and Dombkovskaya, Ye. P., _Trudy GMTs_ /Transactions of the State Meteorological Center/, 73, 134 (1970).

32. Mimnik, L. M., _Meteorologiya i gidrologiya,_ 8, 22 (1971).

33. Boldyrev. V. G., Dombkovskaya, Ye. P., Gurvich, A. S., and Krasil'nikova, T. G., _Trudy GMTs,_ 73, 126 (1971).

34. Kumuza, B. G., _Trudy GGO_ /Transactions of the State Geophysical Observatory/, 222, 11 (1968).

35. Gorodetskiy, A. K., Malkevich, M. S., and Syachinov, V. I., _Dokl. AN SSSR_ 200/3, 588 (1971).

199

The results of the experiments performed on the reception of the Earth's radiothermal emission by satellite showed the sizable potentialities of microwave radiometry for meteorology, oceanology, and geophysical studies.

For meteorology, the possibility of determining the water vapor content over the oceans is ofggreat value. The virtually synchronous data obtained on the water vapor content over the entire planet will make it possible to determine the global distribution of energy reserves in the atmosphere concentrated in the latent heat of condensation of water vapor.

Microwave radiometry at the present is the most reliable method of remote determination of cloud moisture reserve and delineation of precipitation zones from satellites.

Observations of the ocean surface temperature and the determination of storm regions independently of whether cloud cover is present is of direct interest to oceanology and of immediate consequence to such sectors of the national economy as fisheries and navigation. To a large extent, the capabilities of ice monitoring are greater due to the ability to detect ice and to estimate its continuity in the polar basins regardless of conditions of illumination and cloud cover.

Measurements performed over continents revealed a definite relationship between microwave emission and soil temperature and moisture content. For glaciology, the possibility of obtaining information on the structure of glaciers by measuring radio-brightness spectra is of interest.

Experiments performed on the Kosmos 243 and the Kosmos 384 satellites are the results of a definite stage in theoretical calculations, ground-based, and aircraft experiments investigating the thermal radio emission of the Earth. The results of the satellite experiments have laid the foundation for the broad use of thermal radio emission for practical purposes, especially in meteorology. Still, these results make it possible to outline several further problems in extending the methods of remote sensing of the Earth using the microwave band.

Major opportunities unfold if the band range is extended. The use of shorter waves, down to 1 mm, will permit more exact determination of cloud cover characteristics and will solve the problems of reconstructing the vertical profiles of temperature

and moisture even when cloud cover is present. Moving into the submillimeter region will permit diagnostics of water vapor and impurity gases above the tropopause. On the other hand, use of decimeter waves can yield information on soil conditions. Additional information can be forthcoming from measurements of radiation polarization.

The possbilities of successfully solving problems of the use of microwave radiometer instruments in regular observations of the Earth's radiothermal emission are to a large extent bound up with improvements in aircraft and satellite radiometers.

Among the main indicators of onboard microwave radiometers is temperature sensitivity and spatial resolution, determined by the size of the instantaneous field of view and the width of the scanning zone. The required temperature sensitivity of 0.3-0.5° K can be realized in present-day radiometers only for an observational period exceeding tenths of a second.

Improvement in spatial resolution in satellite observations is a very difficult problem. Possible avenues for extending the spatial resolution include the use of inflated and deployable antennas and methods of filming artificial apertures. Extending the scanning zone can be achieved by using multichannel (mosaic) radiometer systems or by transverse scanning of the direction of the axis of the antenna's instantaneous field of view.

The possibilities of remote sensing grow when synchronous measurements are taken in the microwave, infrared, and visible bands. The large spread over wavelengths can yield mutually supplementary information on cloud systems, temperature, and water vapor content, surface conditions, and so on.

At the present time, the wide use of thermal radio emission of the Earth for remote sensing from satellites has only begun and therefore it is difficult to give a reliable prognosis of further developments and the use of microwave radiometry methods in meteorology, geophysics, and the national economy. However, we can state with confidence that further scientific research and design developments will enable the microwave region to figure prominently in the spectrum of emission used for remote sensing of the Earth.